UNIVERSITAT ROVIRA I VIRGILI

# THEORETICAL STUDIES OF SELECTIVE PROCESSES IN HETEROGENEOUS CATALYSIS

## Mónica García Mota

ISBN: 978-84-693-5424-7
Dipòsit Legal: T-1415-2010

**ADVERTIMENT**. La consulta d'aquesta tesi queda condicionada a l'acceptació de les següents condicions d'ús: La difusió d'aquesta tesi per mitjà del servei TDX (www.tesisenxarxa.net) ha estat autoritzada pels titulars dels drets de propietat intel·lectual únicament per a usos privats emmarcats en activitats d'investigació i docència. No s'autoritza la seva reproducció amb finalitats de lucre ni la seva difusió i posada a disposició des d'un lloc aliè al servei TDX. No s'autoritza la presentació del seu contingut en una finestra o marc aliè a TDX (framing). Aquesta reserva de drets afecta tant al resum de presentació de la tesi com als seus continguts. En la utilització o cita de parts de la tesi és obligat indicar el nom de la persona autora.

**ADVERTENCIA**. La consulta de esta tesis queda condicionada a la aceptación de las siguientes condiciones de uso: La difusión de esta tesis por medio del servicio TDR (www.tesisenred.net) ha sido autorizada por los titulares de los derechos de propiedad intelectual únicamente para usos privados enmarcados en actividades de investigación y docencia. No se autoriza su reproducción con finalidades de lucro ni su difusión y puesta a disposición desde un sitio ajeno al servicio TDR. No se autoriza la presentación de su contenido en una ventana o marco ajeno a TDR (framing). Esta reserva de derechos afecta tanto al resumen de presentación de la tesis como a sus contenidos. En la utilización o cita de partes de la tesis es obligado indicar el nombre de la persona autora.

**WARNING**. On having consulted this thesis you're accepting the following use conditions: Spreading this thesis by the TDX (www.tesisenxarxa.net) service has been authorized by the titular of the intellectual property rights only for private uses placed in investigation and teaching activities. Reproduction with lucrative aims is not authorized neither its spreading and availability from a site foreign to the TDX service. Introducing its content in a window or frame foreign to the TDX service is not authorized (framing). This rights affect to the presentation summary of the thesis as well as to its contents. In the using or citation of parts of the thesis it's obliged to indicate the name of the author.

Mónica García Mota

# THEORETICAL STUDIES OF SELECTIVE PROCESSES IN HETEROGENEOUS CATALYSIS

DOCTORAL THESIS

supervised by Dr. Nuria López Alonso

INSTITUT CATALÀ D'INVESTIGACIÓ QUÍMICA (ICIQ)

ICIQ
Institut
Català
d'Investigació
Química

UNIVERSITAT ROVIRA I VIRGILI

TARRAGONA
2010

Institut Català d'Investigació Química
Avgda. Països Catalans 16
43007-Tarragona (Spain)

NURIA LOPEZ ALONSO, jefa de grupo en el Institut Català d'Investigació Química, y profesora asociada de Química Física de la Universitat Rovira i Virgili,

CERTIFICO:

Que la presente memoria, titulada “Theoretical studies of selective processes in heterogeneous catalysis”, que presenta Mónica García Mota para la obtención del título de Doctora, ha sido realizada bajo mi dirección en el Institut Català d'Investigació Química (ICIQ), dentro del programa de doctorado en Química Teórica y Computacional de la Universitat Rovira i Virgili, y que cumple los requisitos para poder optar a la Mención Europea.

Tarragona, Abril de 2010

Nuria López Alonso

*A mi familia,*

*"Jamás el esfuerzo desayuda a la fortuna"*

*Fernando de Rojas*

# Agradecimientos

La presente memoria es el fruto de cuatro años de investigación. Tengo mucho que agradecer a mi Directora de Tesis, la Dra. Núria López. Bajo su tutela he disfrutado con cada uno de los proyectos a los que nos hemos enfrentado durante estos cuatro años.

Mis años de doctorado no habrían sido los mismos sin la presencia de mi compañero y amigo Jaime Gómez. Con su llegada, el despacho dejó de estar vacío y pasó a estar lleno de consejos, confidencias y debates. También darle las gracias al resto de nuestro creciente grupo, que junto con todos los miembros del grupo del Prof. Carles Bo y del Prof. Feliu Maseras, han contribuido a crear un espacio de trabajo alegre y agradable. En especial, quiero darle las gracias a Elena Herrero por sus útiles consejos y a Núria Vendrell porque siempre ha estado presente resolviendo múltiples dificultades que se han planteado en estos años.

I would like to acknowledge the hospitality of Prof. Nørskov, who was my host during my stay at the Technical University of Denmark, DTU. Thanks for giving me that opportunity to grow as a scientist, and thanks to everyone at DTU because they made me feel at home.

Mi tesis tiene mucho que agradecer a Eduardo. Sus ánimos me empujaron a comenzar mi carrera en la investigación y su apoyo constante durante estos cuatro años ha sido vital, contagiándome siempre con su entusiasmo por la ciencia y su ansia de conocimiento.

Finalmente, quiero agradecer el apoyo constante de mi familia.

Gracias a todos.

El trabajo desarrollado en esta tesis doctoral ha sido posible gracias a la financiación del Institut Català d'Investigació Química (ICIQ) y se ha desarrollado en el marco del proyecto Diseño de Catalizadores para una Química Sostenible: Una Aproximación Integrada (CONSOLIDER CSD2006-0003) perteneciente al programa CONSOLIDER-INGENIO 2010, y del proyecto CTQ2006-00464/BQU del Ministerio de Ciencia e Innovación.

ICIQ
Institut
Català
d'Investigació
Química

intecat

Consolider Ingenio 2010
CSD2006-0003
Diseño de Catalizadores
para una Química Sostenible:
**una Aproximación Integrada**

Consolider

# Contents

UNIVERSITAT ROVIRA I VIRGILI
THEORETICAL STUDIES OF SELECTIVE PROCESSES IN HETEROGENEOUS CATALYSIS
Mónica García Mota
ISBN:978-84-693-5424-7/DL:T-1415-2010

# Chapter 1

# Introduction

## 1.1 Gold Chemistry, poisoned Pd and PdAu alloys

Gold is the most noble of all metals.[1] The inertness of gold has been related to two factors: the degree of filling of the antibonding states on adsorption, and the degree of orbital overlap with the adsorbate. These two factors operate together to determine the adsorbate binding, and subsequent reactivity on gold. Even if gold was known to shown the lowest activity of all transition metals, in the eighties the group of Prof. Haruta discovered that the catalytic performance of gold depends on the size of the nanoparticles.[2] The nobility of gold disappears for nanometric-size structures. In order to be active, gold is deposited as nanoparticles with diameter smaller than 5 nm on different supports ($TiO_2$, $CeO_2$, $MgAlO_4$, $FeO_x$...). In those cases gold can be active in low-temperature CO oxidation,[2, 3] partial oxidation of hydrocarbons,[4] selective hydrogenation of unsaturated hydrocarbons,[5] and selective reduction of nitro groups in complex molecules,[6] just to name a few reactions. But, this list is not exhaustive, and in the last five years the number of potential applications has raised enormously.[7]

A particular case is that of the selective hydrogenation of alkynes in the presence of alkenes.[5] This reaction is industrially relevant in the upgrading of alkene fractions coming from the cracking units.[8] The traditional catalyst is based on Pd and provides good activity, selectivity and stability if a selectivity enhancer, such as CO is added. For Au, it was determined that thermodynamics was the driving force for selectivity in the alkyne-alkene hydrogenation pairs. However, the selectivity properties of Pd for this reaction, in the presence of selectivity modulators, i.e. CO, that convert the properties of Pd into those of Au nanoparticles were not clear, and have been addressed in the present work. In addition, alkynes are activated both in the presence of gold nanoparticles and gold-based organometallic compounds. This has been denoted as alkynophilicity, and has been subject of the research described in this Thesis.

However, the applications of gold catalysis are not restricted to its use as nanoparticles: organometallic gold species,[7] impurities in oxide lattices,[9, 10] and gold in bimetallic systems,[11] can also be active and selective in different reactions. In alloys, several roles have been proposed for Au. Despite the inert character of Au it can act as an active species by binding reactants or products.[12] It has been proposed that gold can also work as a spacer (due to its inert nature), and thus is perfectly suited to study ensemble effects in catalysis. An increasing number of examples of the use of gold-based alloys in technologically relevant processes has been reported in the last years. For instance, NiAu alloys were found to be active in the steam-reforming process where hydrocarbons and water are converted into $H_2$ and CO.[13] The industrial catalyst is based on Ni but it also catalyses the formation of graphite and then, the deactivation of the catalyst. Experimental results [13] confirmed that Au alloyed into the surface layer of a Ni catalyst increases the effectiveness of the catalyst in the steam-reforming process, but, even if NiAu alloys are more resistant to the formation of graphite, the alloy is less resistant to the elimination of Ni from the catalyst due to the formation of volatile $Ni(CO)_4$ species, and this has prevented its introduction in industrial processes.[14]

A second group of alloys that has been quoted by its tantalising chemistry is PdAu. Mixtures of Pd and Au are used as catalysts for a number of applications.[11, 15, 16] The addition of Au to Pd can greatly enhance Pd catalytic activity, selectivity and stability. For instance, Behm *et al.*[16] evaluated the electrochemical properties of defined atomic ensembles in atomically flat PdAu(111) electrodes with variable surface stoichiometry that were prepared by controlled electrodeposition on Au(111). Palladium monomers were identified as the smallest ensemble for carbon monoxide adsorption and oxidation, setting the differences in the ensembles needed by protons and CO on the electrode surface.

The composition and structure in a bimetallic system have a strong influence on its catalytic properties.[17] These interactions are known as the ligand and ensemble effects:

- The **ligand effect** refers to the modification in the catalytic activity and selectivity caused by the electronic interaction between components of a bimetallic system.
- The **geometric effect** is the modification in the catalytic activity and selectivity due to changes in the structure, and can be divided in two terms:
  - **ensemble**: considers different sets and local distribution of active atoms.
  - **stress/strain**: considers changes in the distances.

In order to determine the local structure and stoichiometry of an alloy, it is important to know the relative interactions between the metal atoms. The most characteristic phenomena can be summarised as aggregation and segregation effects. Both are schematically represented in Figure 1.1.

- The **segregation energy** can be defined as the energy cost to move an impurity from the bulk to the surface. If this energy has a negative value it means that the concentration of impurity is enriched in the surface (segregation), while a positive value means than the impurity is more stable in the bulk (antisegregation).

UNIVERSITAT ROVIRA I VIRGILI
THEORETICAL STUDIES OF SELECTIVE PROCESSES IN HETEROGENEOUS CATALYSIS
Mónica García Mota
ISBN:978-84-693-5424-7/DL:T-1415-2010

- The **aggregation energy** indicates how much energy is needed to aggregate, i.e. form a ensemble, of impurity atoms on the surface. A negative aggregation energy means that the formation of impurity islands in the surface is favourable.

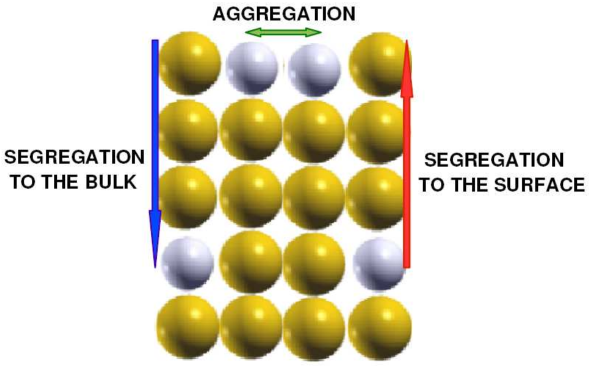

Figure 1.1: Yellow spheres represent host atoms, and blue ones impurity atoms. The two main effects, aggregation and segregation effects, are schematically represented. Adapted from ref.[18].

Advances in Density Functional Theory, DFT, make it possible to describe catalytic reactions at surfaces with such accuracy that the theoretical results can be compared with experiments.[19] The purpose of this Thesis is shed light on some experimental evidences in which Au, in homogeneous or heterogeneous version, is involved, and compare to Pd for some key reactions. To this end I will first describe the tools to analyse the surface composition and ensemble stoichiometry for PdAu systems with different annealing procedures. Then, a set of reactions with special emphasis on the activity: CO oxidation; and selectivity: direct $H_2O_2$ formation and vinyl acetate synthesis, will be explored. Complementary, homogeneous-heterogeneous gold and palladium parallelisms will be described for alkynophilicity and vinyl acetate synthesis. Finally, the way to reach the ultraselective character of Au in alkyne-alkene hydrogenation mixtures from poor Pd catalyst by employing selective modulators is analysed in detail.

## 1.2 CO vibrational spectra

The role of ensembles is fundamental to understand the chemical and electrochemical properties observed, and the detailed knowledge of the local (short-range) structure of surface alloys combined with an understanding of the relation between the surface composition and reactivity, are needed to achieve atomistic catalyst design. Thus, the detailed knowledge of the structure and stoichiometry of the alloy surface is needed. One of the simplest ways to investigate the surface state is by using a probe molecule CO.[20] The very sensitive nature of CO vibrational frequency to the local environment is employed as a precise measure of the electronic properties of a given metallic system, and serves as fingerprint of the adsorption site.[21] Experimentally, a detailed group of studies on CO adsorption on the PdAu alloys generated under different experimental conditions are available.[11, 22, 23, 24, 25, 26, 27]

If a molecule sits on the surface has a dipole moment, the molecule can adsorb infrared light but only at certain frequencies. Hence, an infrared spectrum of light reflected from the surface will show adsorption peaks which are characteristic of the molecule, and these peaks will depend on the adsorption site. This is the basis of the Infrared Reflection Absorption Spectroscopy, IRAS.[28] For thin-films on reflective surfaces the incidence angle is large, and the technique is known as grazing incidence experiment. The intensity of the reflected waves are given by the Fresnel equations, and in this particular case, the intensity of the light reflected is almost cancelled for $s$-polarised light and almost doubled for $p$-polarised light. Therefore, the observation of vibrational modes of adsorbates on metallic substrates is subject to the *surface dipole selection rule*: only vibrations with a component of the dynamic dipole that is polarised in the direction normal to the surface can be observed in IRAS, see Figure 1.2.

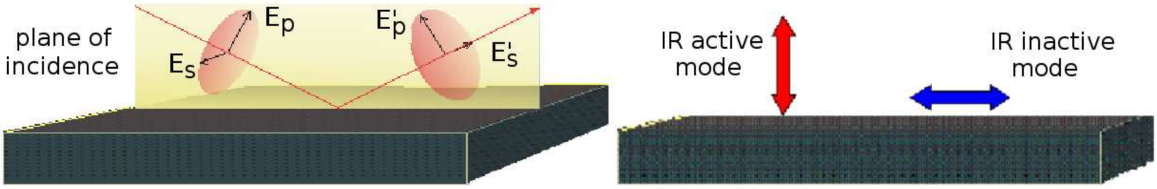

Figure 1.2: Left: Schematic representation of the components of the radiation in the IRAS experiment. $E_p$ and $E_s$ are the incident components parallel and perpendicular to the plane of incidence of the radiation, and $E'_p$ and $E'_s$ are the reflected components. Right: Schematic representation of IR active and inactive modes.

The phase diagram of the bimetallic system PdAu is shown in Figure 3.1.[29] The diagram presents different stable structures. At high temperatures ($>$ 1400 K) the liquid is present. At low temperatures, the disordered phase with an fcc structure where both Au and Pd atoms can be in all positions is observed. This configuration exists for the whole composition range and although it only shows a short range order. At lower temperatures, in the 1:3 ranges two ordered phases exist $Pd_3Au$ and $PdAu_3$. Both of them are fcc while for the equiatomic composition the structure is still under discussion.[29]

The vibrational spectra of CO adsorbed on PdAu alloys have been employed to titrate the ensembles present on differently prepared surfaces in order to establish their nature.[24, 30] In these experiments different ways to prepare the bimetallic alloy have been employed. Surface composition analysis,[31] indicates that for a 5 ML Pd grown on 5 ML Au/Mo(110), the surface concentration of Au gradually increases from 4 to 80% with increasing annealing temperature up to 700 K, see Figure 1.4. Between 700 and 1000 K, the surface composition $Pd_{0.2}Au_{0.8}$ remains constant. Above 1000

UNIVERSITAT ROVIRA I VIRGILI
THEORETICAL STUDIES OF SELECTIVE PROCESSES IN HETEROGENEOUS CATALYSIS
Mónica García Mota
ISBN:978-84-693-5424-7/DL:T-1415-2010

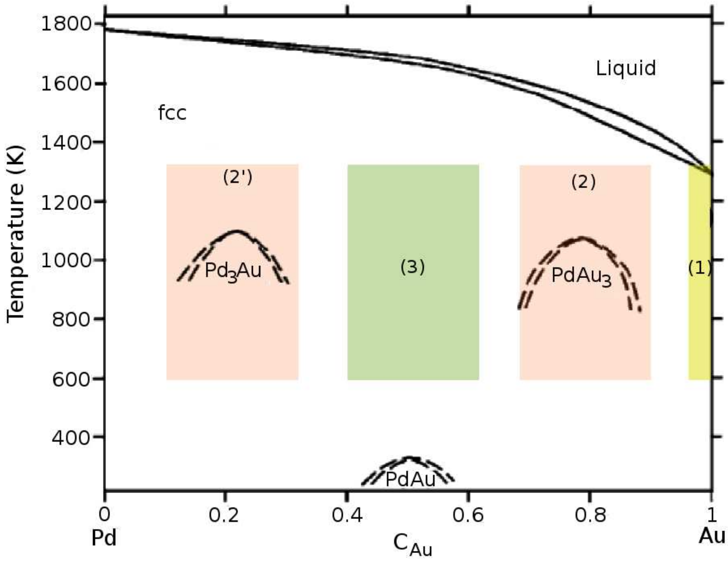

Figure 1.3: PdAu phase diagram. Dashed lines are speculative. Taken from ref. [29].

K, the Au surface concentration abruptly decreases because of Au desorption, and Pd becomes dominated on the surface. For the inverse system, 5 ML Au grown on 5 ML Pd/Mo(110), the Pd surface concentration gradually increases from 0 to 20% up to 700 K, where an alloy surface, $Pd_{0.2}Au_{0.8}$, forms and remains stable up to 1000 K.

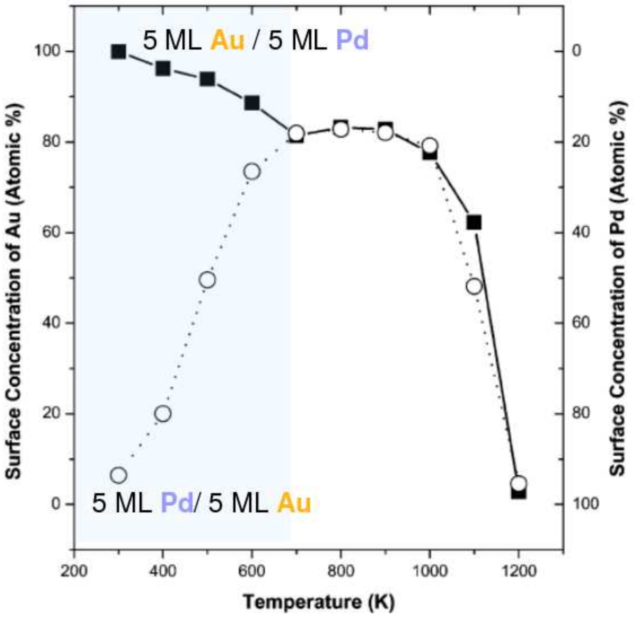

Figure 1.4: Surface concentration of Au and Pd of 5 ML Pd/5 ML Au/Mo(110), and 5 ML Au/5 ML Pd/Mo(110), open circle and dashed line, as function of annealing temperature. Taken from ref. [31].

Goodman *et al.*,[24] used IRAS to study CO adsorption on 5 ML Pd/5 ML Au/Mo(110) alloy system annealed at different temperatures. One alloy was well-annealed at 800 K, and a second was annealed at 600 K, see Figure 1.5. The alloy surface is smooth and well ordered after annealing at 800 K, and as a consequence, the IR intensities at high temperature annealed samples are greatly enhanced respect to at low temperature ones. The CO pressure of 5x10$^{-8}$ Torr employed for this spectra, is not enough to provoke the formation of contiguous Pd in the surface. There is only a single feature at 2088 cm$^{-1}$ at all CO coverages, that can be attributed to CO residence on Pd monomers. With additional CO dosage, a second peak emerges at 2112 cm$^{-1}$. This shoulder disappears at a lower temperature (between 150 and 200 K). The authors attribute this shoulder to CO residence on-top Au sites.[24]

The alloy is not completely ordered at annealing temperature of 600 K. The presence of Pd dimers in the surface is manifested by three features, at 2013, 2078 and 1940 cm$^{-1}$, with the low CO dosage regime ($<$ 0.1 L). All these bands show no frequency shift with further CO exposure. When CO saturates the surface, the IRAS spectrum is dominated by a feature at 2078 cm$^{-1}$, and there is a shoulder at 2103 cm$^{-1}$, which is attributed to CO residence on-top Au sites by the authors.

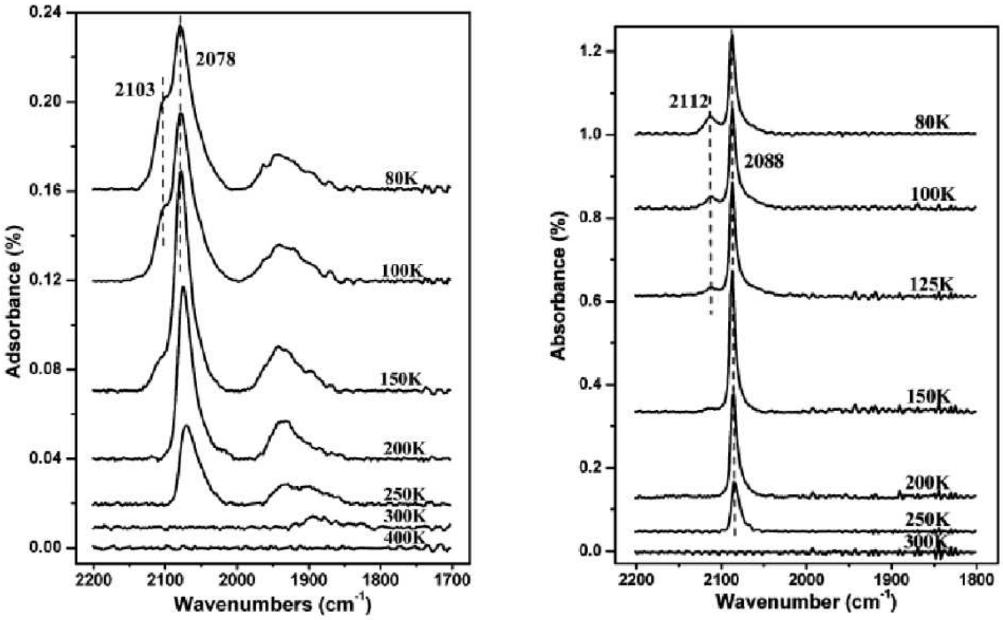

Figure 1.5: Temperature-dependent IRAS spectra for CO adsorption on the 5 ML Pd/5 ML Au/Mo(110) system. The alloy film was annealed at 600 K for 30 min prior to the CO adsorption (left) and at 800 K for 45 min (right). Taken from ref. [24].

More recently, CO adsorption experiments have been performed at much higher CO pressures, close to the ambient regime. In the few-Torr pressures, the surface composition can be modulated by the CO presence. This is because, the energy of CO on a surface Pd atom is lower that that of CO in gas and a Pd atom in the bulk. Thus, CO adsorption can induce the enrichment of Pd in the surface layer.[32] For instance, on a well-annealed sample, CO pressures of ∼ 0.1 Torr, are required for the formation of a significant population of contiguous Pd sites at the surface PdAu(100),[26, 27] see Figure 1.6.

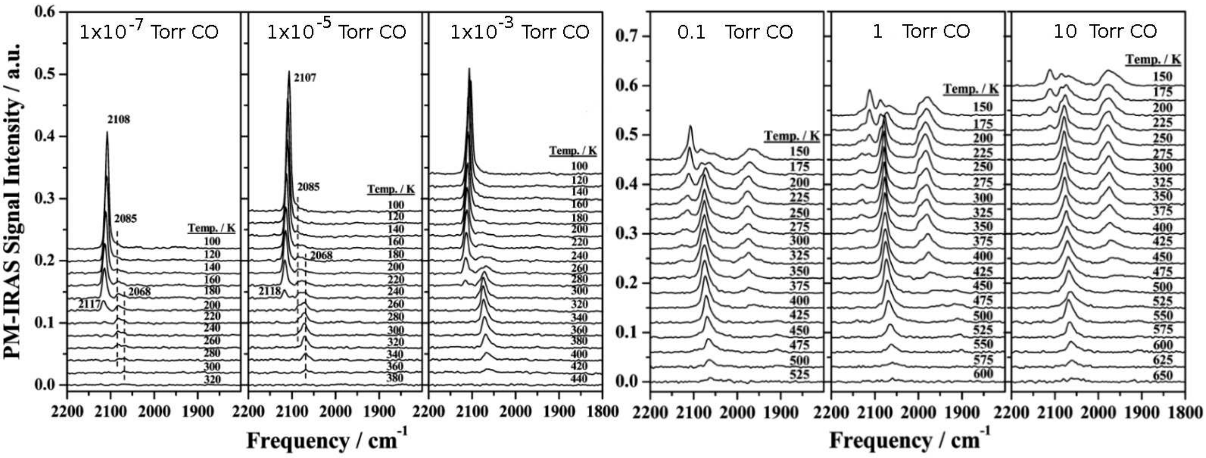

Figure 1.6: PM-IRAS spectra for CO on a well-annealed PdAu(100) sample as a function of temperature. Sample temperatures are marked adjacent to each spectrum. Taken from ref. [27].

In order to study the PdAu bimetallic systems, several structures will be built to model several positions in the phase diagram, it will be structures placed in the zones labelled as (1), (2) and (3) in Figure 3.1. Density Functional Theory, DFT, coupled to ab initio thermodynamics will be employed to analyse the vibrational spectra of CO on different $Pd_xAu_{100-x}$, $0< x <50$, alloys under different temperatures and pressures in order to identify the fingerprints for adsorption of the Figures 1.5, and characterise the ensembles, see Chapter 3.

## 1.3 Model reaction: CO oxidation

CO oxidation belongs to the most fundamental reactions in heterogeneous catalysis. It is an exceptionally well studied reaction due to two main reasons. Scientifically, it is one of the simplest catalytic reactions, and thus is widely used as a model system to understand heterogeneous catalysis. CO oxidation is present in some industrial applications as in car-exhaust emission control, $CO_2$ lasers and air purification.[33] In the literature the origin of the catalytic activity of gold nanoparticles for low-temperature CO oxidation has been studied,[34, 35, 36] and the CO oxidation has been reported mainly on transition metals like Pt, Pd, Ru and Rh. [37, 38, 39, 40]

CO oxidation takes place in two possible ways: in the first channel, the adsorbed carbon monoxide, $CO^*$, reacts directly with molecular oxygen, $O_2^*$, and the final state is $CO_2$ with a remaining atomic oxygen on the surface. This channel will finish with CO reacting with that remaining atomic oxygen.

$$CO^* + O_2^* \longleftrightarrow CO_2 + O^* + * \tag{1.1}$$

$$CO^* + O^* \longleftrightarrow CO_2 \tag{1.2}$$

In the second channel, molecular $O_2$ dissociates to provide active O atoms before the reaction can occur.

$$O_2^* \longleftrightarrow 2O^* \tag{1.3}$$

$$CO^* + O^* \longleftrightarrow CO_2 \tag{1.4}$$

Therefore, $O_2$ dissociation plays an important role in the CO oxidation but it is also relevant to other oxidation processes, formation of the oxide and $O_2$ reduction in electrocatalysis. The adsorption and dissociation of $O_2$ in transition metals have been extensively reported.[41, 42, 43, 44] In oxygen reduction reactions, ORRs, the strength of the metal-O interaction, and the ease of $O_2$ dissociation will be the two criteria for choosing possible candidates.[45, 46]

Lahr and Ceyer identified a new CO oxidation route at low temperatures, 77 K, in AuNi surface alloys containing about 20-25% of Au in the surface although no nanoparticles are present.[9] In that set of experiments, saturation coverage of $O_2$ is adsorbed on the 0.24 ML Au/Ni surface alloy at 77 K. The vibrational spectrum, measured by HREELS, is shown in Figure 1.7. The dominant feature, at 865 $cm^{-1}$ is assigned to the O-O stretch mode of molecular oxygen whose bond axis is parallel to the surface, indicating the shoulders at 790 and 950 $cm^{-1}$ molecular $O_2$ adsorbed at multiple sites. In contrast, $O_2$ dissociatively adsorbs on Ni(111) at a temperature as low as 8 K.

In this Thesis, the aim will be to shed some light on the catalytic reactivity of surface Au-based catalyst using the well known CO oxidation as test reaction. By means of Density functional Theory, DFT, the CO oxidation on Ni, and on $AuNi_3$ surface alloy, will be studied in Chapter 4.

## 1.4 Selective reaction: Direct $H_2O_2$ formation

Hydrogen peroxide is a strong oxidant. $H_2O_2$ is regarded as a *green* oxidant since it decomposes to give water and oxygen as reaction products.[47] $H_2O_2$ is more efficient than others oxidants, such as sodium hypochlorite, and shows a oxidative power slightly below that of ozone. Its dissociation products, hydroxyl radicals, have an oxidative power below fluorine. Nowadays hydrogen peroxide is mainly employed in chemical synthesis and paper bleaching,[48] see Figure 1.8. In fine chemistry, water peroxide is used to

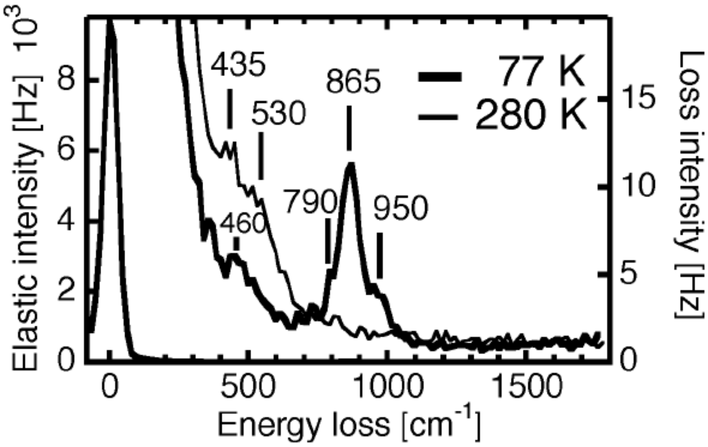

Figure 1.7: Specular HREEL spectrum of saturation coverage $O_2$ measured at 77 K on 0.24 ML of Au/Ni(111), and after heating to 280 K. Incident electron energy is 6.4 eV with 55 $cm^{-1}$ fwhm. Taken from ref. [9].

obtain ultraselective oxidation processes [49, 50] where other catalytic systems fail.[51] However, the use of $H_2O_2$ is expected to grow exponentially provided that economically and ecological route is found.[48] $H_2O_2$ manufacturing is currently almost exclusively via the environmentally unfriendly anthraquinone oxidation, AO,[47] in which hydrogen, atmospheric oxygen, and an anthraquinone derivative are employed in the reaction cycle. The advantage of the AO process is the very high yield of hydrogen peroxide per cycle. However, this process exhibits important drawbacks, including gradual loss of expensive anthraquinone, deactivation and massive use of organic solvents that imply high cost and high waste per cycle. One alternative route to $H_2O_2$ that avoids the use of anthraquinone is the direct synthesis from hydrogen and oxygen in the presence of a catalyst. The earliest work on direct formation of $H_2O_2$ was done by the group of Pospelova.[52, 53, 54] The fact that O–O bond does not dissociate during $H_2O_2$ formation was experimentally confirmed by Dissanyake and Lunsford,[55] and the presence of hydroperoxide on catalyst surface during the reaction was discovered by Sivadinarayana *et al.*[56]

The direct reaction has been known to take place on Pd containing catalysts,[55, 57] however the process shows many severe limitations: first, $H_2$ and $O_2$ mixtures are explosive in large composition ranges; second, the $H_2O_2$ product activity and selectivity on Pd is low due to the complex reaction network involved, and third; the stability of the product depends on the environment. The first problem can be mitigated by the incorporation of membranes to avoid the explosive ranges.[58, 59, 60] With respect to $H_2O_2$ decomposition, working in acid media can avoid the process which is known to take place under basic conditions. Chlorine or bromine species are known to improve the selectivity of the process, decreasing the $H_2O_2$ decomposition, and blocking active sites for $O_2$ dissociation.[61, 62, 63] On other hand, because the reaction takes place

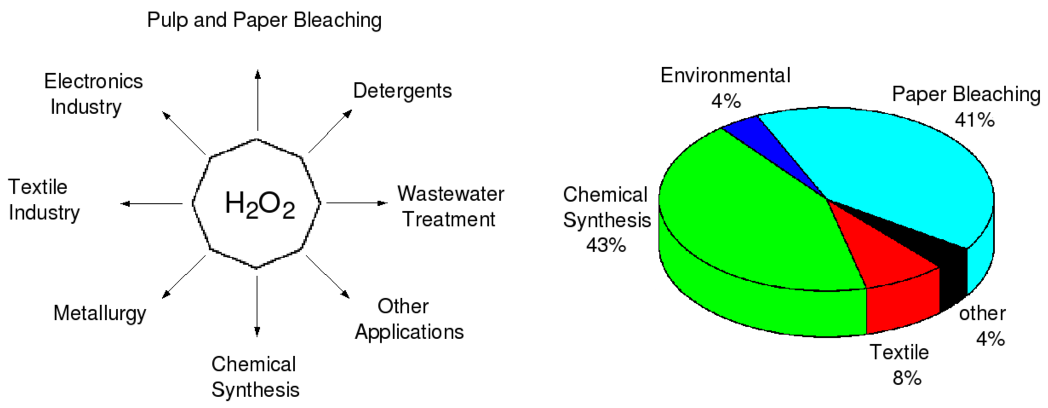

Figure 1.8: Left: Principal uses of hydrogen peroxide. Right: Distribution of hydrogen peroxide consumption in Europe. Taken from ref. [48].

in a three-phase system (the reagent gases, the palladium catalyst and a solvent) the rates may be transport-limited. The replacement of water by methanol or ethanol is proposed to improve the solubility of $O_2$ and $H_2$ [57, 60, 64] and thus increase the activity of Pd. The theoretical limit for selectivity of the reaction process is governed by the competitive reaction networks on the catalyst surface.

Recently, Hutchings and coworkers have indicated that alloying of Pd with Au might be a suitable option to improve the activity and selectivity of the catalyst.[65, 66, 67] These works have been complemented by Boccuzzi *et al.*[68] while gas-phase studies indicate that there is an optimum content for Au on the alloy to achieve this effect.[69]

To explain the better performance experimentally found for the gold containing alloys in direct $H_2O_2$ synthesis, Pd monometallic system and $MPd_3$ bimetallic alloys (with M=Pt,Ag and Au) on the most stable surface (111) will be considered. By Density Functional Theory, DFT, I will study the reaction mechanisms that drive to the formation of hydrogen peroxide from its elements, and the competitive formation of water or hydroxyl groups.

## 1.5 Selective reaction: Vinyl acetate synthesis

Another interesting reaction that can be carried out in PdAu alloy is that of the acetoxylation of ethylene, the route for the synthesis of vinyl acetate, $CH_3COOCHCH_2$, VA.[70] Vinyl acetate is an important monomer precursor to polyvinyl alcohol and polyvinyl acetate, which are wide spread polymers employed as paints, adhesives, coatings and fibres.[70] VA is synthesised from ethene and acetic acid, and although initially the synthetic process was based on homogeneous palladium catalysts,[71] nowadays VA is mostly based on silica supported Pd-Au alloys, $PdAu/SiO_2$, which are additionally modified with potassium acetate, KOAc.[15, 72, 73, 74] The reaction takes place between 130-200°C and 5-10 atm and the yield is 96% or higher of VA in terms of ethene conversion.[72] The preference for the heterogeneous process is based on the better performance against corrosion and poisoning by chlorides and water.

The reaction process in the synthesis of VA is given by the following equation

$$CH_3COOH + C_2H_4 + \frac{1}{2}O_2 \rightarrow CH_3COOCHCH_2 + H_2O \tag{1.5}$$

Two basic mechanisms were proposed for the palladium catalysed synthesis of the VA. In the first, suggested by Samanos *et al.*,[15] oxygen is employed in the reaction to drive acetic acid dehydrogenation, and ethene can be adsorbed in a neighbouring Pd centre and then the C-O coupling takes place. The resulting intermediate, hydrogenated VA, evolves via $\beta$-hydrogen elimination to vinyl acetate and a water molecule. This can be summarised as follows

$$\begin{gathered} CH_3COO^* - C_2H_4^* \rightarrow CH_3COOCH_2CH_2^{**} \\ CH_3COOCH_2CH_2^{**} + OH^* \leftrightarrow CH_3COOCHCH_2 + H_2O + 3^* \end{gathered} \tag{1.6}$$

The second mechanism was proposed by Moiseev *et al.*,[71, 75] as well as by Nakamura and Yasui.[73] They supported that ethene could first dehydrogenate to form a vinyl-palladium intermediate, which then couples with the coadsorbed acetate species to form directly VA. Nowadays the mechanism proposed by Samanos has been verified both experimentally [76] and theoretically,[77] and the acetate-ethene coupling was found to be the rate-liming step.

Detailed experimental studies exist on the ensemble effects found for VA synthesis over Pd-Au alloys.[24, 25, 30, 78, 79] Isolated Pd dimers on Au surfaces have been found to be active and selective catalysts for the VA synthesis but a strong dependence on the local structure of the ensemble is observed.[24, 78, 79] The experimental evidences showed that the rate of VA formation on Pd/Au surfaces as a function of the Pd coverage was significantly enhanced on PdAu(100) compared to PdAu(111). Figure 1.9 shows the VA rate dependence on the local structure of the ensembles.[78] The rate on the Au(100) surface increases significantly with a decrease in the Pd coverage until a maximum is reached at a Pd coverage of 0.07 ML. The corresponding VA formation rates for Pd on Au(111) rise steadily as the Pd coverage is decreased, nevertheless the rates on Au(111) are significantly lower compared with the rate for the corresponding Pd coverage on Au(100) at all Pd coverages.

The aim the work will be to explain the strong dependence on the local structure of the ensemble found in the experimental results. By means of Density Functional Theory, several Pd dimer configurations on both Au(100) and (111) will be used as models for the different intermediates involved on the VA synthesis. All elementary steps according to the Langmuir-Hinshelwood mechanism [80] will be taken into account to figure out the apparent activation energy of the reaction. Those steps are oxygen dissociation, O-assisted dissociative adsorption of acetic acid, ethylene adsorption, acetate-ethylene approximation, hydrogenated VA formation, and $\beta$-H elimination.

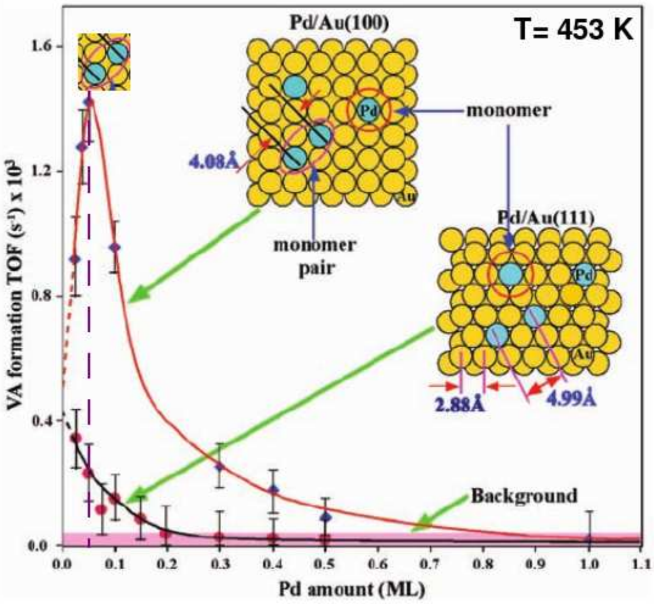

Figure 1.9: Vinyl acetate formation rates, TOFs, as a function of Pd coverage on Au(100) and Au(111). The two insets show Pd monomers and pairs on the Au(100) and Au(111) surfaces. Taken from ref. [11].

### 1.5.1 VA synthesis on homogeneous Pd-based catalysts

Initially the VA synthesis from ethene and acetic acid was based on homogeneous palladium catalysts.[71] The homogeneous process was described by Moiseev around 1960,[71, 81, 82] and it belongs to the family of oxidative acyloxylation reactions.[83] Acyloxylations can be carried out in acetic acid at moderate temperatures (50-60°C).[84] The mechanism shows the following steps;[85, 86] First, the alkene coordinates to Pd(II) catalyst. Then, the C-O bond is formed by nucleophilic addition of the acetate to the alkene. The next step is the C-H cleavage that results in formation of the C-C double bond. Finally, regeneration of the catalyst by a redox system takes place. The first description of the mechanism was developed by Van Helden *et al.*, who assumed that the elimination of the $\beta$-hydrogen atom was the rate-limiting step.[87] Both the homogeneous and the heterogeneous routes are reproduced in Figure 1.10. The benzoquinone/hydroquinone (BQ/HQ) pair is used as external oxidant for the homogeneous reaction. Since the same metal is employed in both homogeneous and heterogeneous version of the catalyst, the similarities and differences on the reaction mechanisms in both cases will be analysed by DFT in Chapter 6.

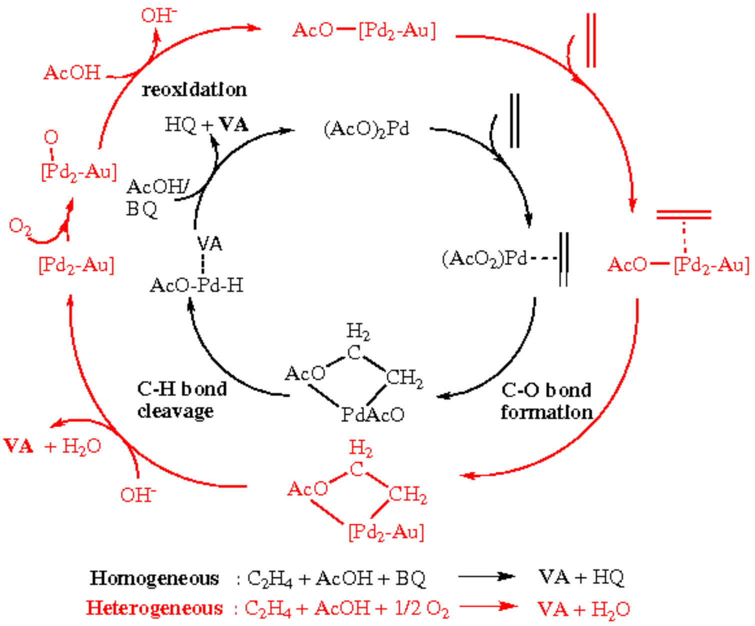

Figure 1.10: Reaction scheme for the synthesis of vinyl acetate from ethene and acetic acid for both homogeneous and heterogeneous versions of the catalyst.

## 1.6 Selective homogeneous and heterogeneous gold catalysis with alkynes and alkenes

In recent years, homogeneous and heterogeneous gold systems have emerged as active and extremely selective catalysts in a wide range of reactions. Some of them are only active as heterogeneous catalysts, such as the chemoselective reduction of substituted nitroarenes,[6] or the hydrochlorination of ethyne to vinyl chloride.[88] However, homogeneous and heterogeneous gold catalysts have been reported to be active for several important reactions, for example low temperature CO oxidations,[9, 89] selective oxidation of alcohols,[90, 91] C-C bond formation,[92, 93], and alkyne hydrogenation.[5, 94] As a consequence, the use of homogeneous gold catalysts has give rise to the extension to heterogeneous version and vice versa.[94, 95, 96] For example, in homogeneous catalysis, $Au^{I}$ and $Au^{III}$ species are employed for C-C and C-heteroatom bond formation from alkynes and alkenes,[7] while in the heterogeneous case, supported gold nanoparticles on different oxides ($CeO_2$, $Fe_2O_3$, $TiO_2$) are active and selective in the partial hydrogenation of alkynes.[5, 97, 98]

The preference shown by alkynes to react with gold catalysis in the presence of other functional groups,[94, 7] has been termed as alkynophilicity. The transferability of the chemical properties from isolated single metal catalysts to nanoparticles is far from being well established and, *a priori*, it is not possible to attribute alkynophilicity to the same mechanistic origin. Understanding the gap between *hetero-* and *homogeneous* catalysis worlds has been recognised as one of the major challenges in chemistry.[99]

In Chapter 7, in a combined theoretical and experimental study, the fundamental reasons behind the selective alkyne activation in homogeneous and heterogeneous gold catalysis will be unravelled. It will be also checked if the well established reactivity of enynes, with a variety of homogeneous $Au^{I}$ and $Au^{III}$ systems, could be extrapolated to heterogeneous gold catalysts, as has been made for other reactions.[94, 95, 96]

## 1.7 Interplay between CO, hydrides, and carbides in selective alkyne hydrogenation on palladium

Alkyne hydrogenation, also known as hydrorefining, is a widely-used procedure in industry to purify olefin streams by removing highly unsaturated impurities.[100, 8] On the other hand, it is also a prototype reaction to understand selectivity in heterogeneously catalysed reactions. Selective hydrogenation of alkynes and alkadienes in the presence of alkenes over Pd-based catalysts is one of the best playgrounds to identify the control parameters for selectivity.[101, 102]

Palladium chemistry has been found to be extremely sensitive to the presence of subsurface species. Teschner *et al.*[101, 103] proposed that a substoichiometric carbide phase is responsible for the selectivity towards alkenes, on the basis of in situ XPS studies Palladium also forms hydrides, even at low hydrogen pressures,[104] which are reported to be unselective [105] and which indicate the high hydrogenation activity of subsurface species as found for nickel.[106] The possible formation of carbide and hydride phases, and their relationship with the selectivity of the catalysts has been speculated and discussed vividly during several decades.[8, 100, 103]

In addition to alkene and alkane products, oligomers have to be taken into consideration, in fact, the selectivity of pure palladium catalysts is very low.[107, 108] In practise, promotion by a second metal like Ag, or continuous feeding of CO, is required to increase the alkene selectivity and to explain the successful their implementation in industry.[107] In commercial plants average ethene selectivities of 40% have been reported in ethyne hydrogenation over promoted $Pd/SiO_2$.[109] In previous theoretical studies, the reaction pathway for hydrogenation has been studied on pure Pd surfaces,[102, 110, 111, 112] gold nanoparticles [5] and on Pd-Ag alloys.[113]

The aim of this work will be to establish new structure-selectivity relationships for alkyne hydrogenation on Pd-containing catalysts based on the detailed knowledge of the state of the catalyst under reaction conditions, with or without CO. All components will be considered: alkynes, alkenes, alkanes, and oligomers. The partial hydrogenation of C2 and C3 alkynes will be studied by Density Functional Theory, DFT, and the results will be directly compared with the catalytic tests over $Pd/Al_2O_3$ that are shown in this section.

### 1.7.1 Catalytic tests

Three types of catalytic tests were carried out by Prof. Pérez-Ramírez' group, see details in ref. [114], over a 1wt.% Pd/$\gamma$-$Al_2O_3$ (Aldrich, ref:205702).

- Influence of the $H_2$:alkyne ratio (1-10): the inlet alkyne concentration was kept at 2.5 vol.% and the inlet $H_2$ concentration was increased every 2h from 2.5 to 25 vol.%.
- Influence of the CO:$H_2$ ratio (0-0.2): the inlet alkyne and hydrogen concentrations were kept at 2.5 vol.% and 12.5 vol.%, respectively ($H_2$:alkyne=5), and the CO concentration was increased every 2h from 0 to 2.5 vol.%.
- Influence of the pretreatment in the absence or presence of carbon monoxide. The catalyst was tested without pretreatment or after pretreatment in (a) 2.5 vol.% alkyne in He, (b) 5 vol% $H_2$ in He, and (c) 2.5 vol% alkyne and 3.75 vol% $H_2$ in He (reaction mixture). The pretreatments were carried out at 473 K for 30 min using a total gas flow of 42 $cm^3min^{-1}$. Afterwards, the catalyst was cooled down in the same gas mixture to 348 K (5 K $min^{-1}$), and evaluated in two feed mixtures: alkyne:$H_2$:He=2.5:3.75:93.75, and alkyne:CO:$H_2$:He=2.5:0.1:3.75:93.65. A fresh catalyst was loaded for each pretreatment.

The alkyne conversion, $\chi$, was determined by the amount of reacted alkyne,

$$\chi = 100\frac{Inlet_{alkyne} - Outlet_{alkyne}}{Inlet_{alkyne}} \tag{1.7}$$

and the selectivity to the alkene, $S_{alkene}$, (alkane, $S_{alkane}$) was determined as the amount of alkene (alkane) formed divided by the amount of reacted alkyne,

$$S_{alkene} = 100\frac{Outlet_{alkene}}{Inlet_{alkyne} - Outlet_{alkyne}} \tag{1.8}$$

$$S_{alkane} = 100\frac{Outlet_{alkane}}{Inlet_{alkyne} - Outlet_{alkyne}} \tag{1.9}$$

The selectivity to oligomers, $S_{oligomers}$, was obtained as

$$S_{oligomers} = 1 - S_{alkene} - S_{alkane} \tag{1.10}$$

#### Influence of the $H_2$:alkyne ratio

The influence of the $H_2$:alkyne ratio is shown in Figure 1.11. The observations are the following:

- The alkyne conversion at 348 K is complete at all $H_2$:alkyne ratios, except for the stoichiometric ratio of 1, with values around $\chi$(alkyne)= 90%.

UNIVERSITAT ROVIRA I VIRGILI
THEORETICAL STUDIES OF SELECTIVE PROCESSES IN HETEROGENEOUS CATALYSIS
Mónica García Mota
ISBN:978-84-693-5424-7/DL:T-1415-2010

- The selectivity to ethene and propene, with $H_2$:alkyne = 1, is 42% and 62%, respectively. These values decrease steadily upon increasing the inlet partial $H_2$ pressure. The same trend described for the selectivity to the olefin is followed by the selectivity to oligomers, starting at *ca.* 30-40%, with $H_2$:alkyne=1.
- The selectivity to the alkane exhibits an opposite trend, increasing from 10-20% at $H_2$:alkyne = 1 to 80-90% at $H_2$:alkyne = 10.
- At $H_2$:alkyne>4, the selectivity to products remained essentially constant: no production of the alkene, and *ca.* 90% to the fully hydrogenated alkane, but still oligomerisation represents *ca.* 10% of the total conversion.

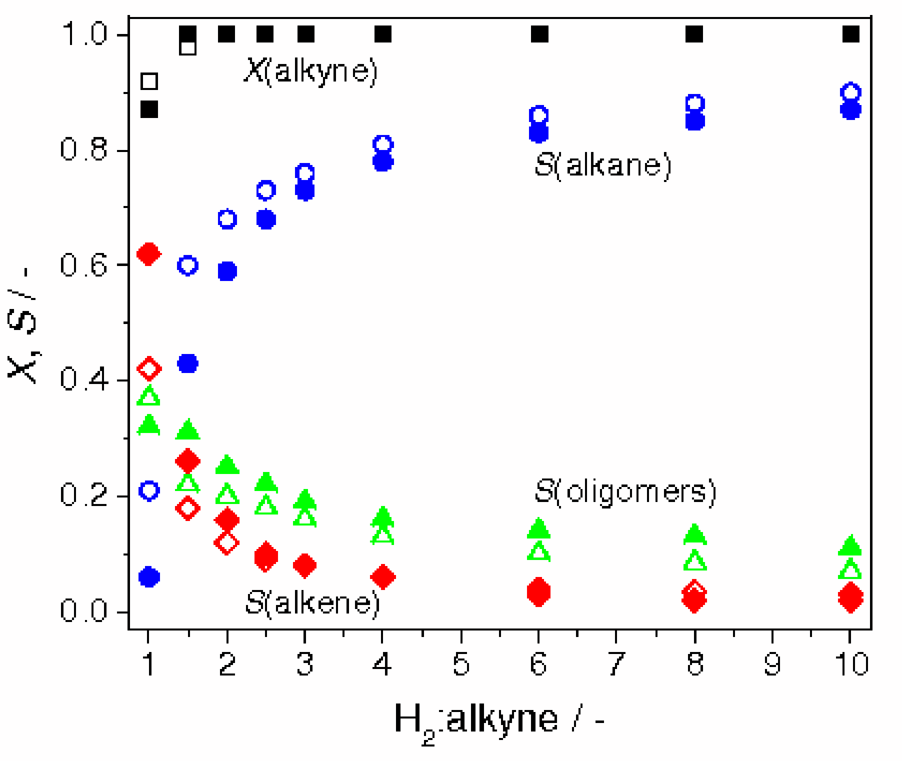

Figure 1.11: Conversion of ethyne and propyne, $\chi$(alkyne), and selectivity to the alkene, $S$(alkene), alkane, $S$(alkane), and oligomers, $S$(oligomers), over Pd/$Al_2O_3$ as a function of the $H_2$:alkyne ratio. Ethyne (propyne) and the derived products are represented by open (solid) symbols. Other conditions: T=348 K, SV=16,800 $cm^3g^{-1}h^{-1}$, and p=1 bar.

The loss of alkene selectivity upon increasing the $H_2$:alkyne ratios has been typically explained by the formation of the $\beta$-PdH phase at high partial $H_2$ pressures, which is selective to the over-hydrogenated product.[100, 105] In qualitative terms, the dependencies of the product distribution on the $H_2$:alkyne ratio are very similar for C2 and C3. But it can be observed that at low $H_2$:alkyne ratios, the selectivity to propene is slightly higher than to ethene by more than 10%. This difference smooths out when increasing the inlet partial $H_2$ pressure. About selectivity to the alkane it is higher for C2 than for C3 at all $H_2$:alkyne ratios.

As summary, the most likely path under low hydrogen pressure, hydrogen:alkyne<1, is oligomerisation whereas alkane is the main product at hydrogen:alkyne>2. The ratio of 1.5 corresponds to a switch for alkene:alkane selectivity. The very narrow window under which selective hydrogenation is observed on palladium, stresses the major role of surface modifiers in the industrial process, where $H_2$/alkyne ratios can be as high as 100 (front-end conditions).

### Influence of the CO:$H_2$ ratio

The influence of CO as selectivity moderator is studied setting the $H_2$:alkyne=5, and gradually increasing the CO:$H_2$ ratio. The selected $H_2$:alkyne ratio in the feed is relatively high in order to evidence more clearly the decrease of alkane production upon CO addition. Figure 1.12 shows as CO acts a external switch of the alkene:alkene:oligomers selectivity, and by optimisation, it enables to adjust the partial hydrogenation depending on the inlet $H_2$:alkyne ratio. The conclusions from these experiments are:

- Addition of very low amounts of carbon monoxide, CO:$H_2$<0.002, led to a marked decrease of the alkane selectivity at the expenses of an increased production of the alkene and oligomers.

- A further increase of the inlet partial CO pressure, CO:$H_2$=0.04, completely suppressed the over-hydrogenation product, and led to a maximum alkene selectivity, *ca.* 30% ethene and *ca.* 60% propene. Oligomers are formed extensively and the selectivity is much higher for C2 than for C3. Within this range of CO:$H_2$ ratios, the degree of alkyne conversion was >90%.

- Excess of carbon monoxide, CO:$H_2$ >0.1, is detrimental, producing a decrease of the alkyne conversion, down to 30%, and alkene selectivity: *ca.* 30% propene, and *ca.* 20% ethene. The pathway to the alkane is zero, and oligomers compounds are the major byproduct, reaching a selectivity of *ca.* 85% for C2 and *ca.* 75% for C3.

### Influence of the pretreatment

A third type of experiments is dedicated to study the influence of CO on alkyne hydrogenation over differently pretreated catalysts, see Figure 1.13. The pretreatment conditions influence the state of palladium (clean, H-rich, C-containing) prior to reaction. In general the results are parallel for C2 and C3. The main differences observed are more likely to appear in presence of CO, this, points out to the intrinsic properties of the insaturated C3 when compared to the C2 counterparts in terms of oligomerisation. Oligomers are more likely to be formed in the presence of C2 (*ca.* 40% for C2 compared to *ca.* 20% for C3). The main results can be summarised as follows:

- For ethyne and the unpretreated catalyst, CO addition lowers the conversion, suppresses ethane production, and increases both the ethene and oligomer selectivity.

- If the catalyst is pretreated in ethyne, ethene selectivity does not change upon CO addition, and the oligomer selectivity increased at the expense of ethane. However, the introduction of CO in the feed results in a large increase (about 30% more) for alkene selectivity in the C3 case.

- If the sample is prepared under high $H_2$ pressures, conversion is high and the alkane is the major product (75% selectivity), the second product being oligomers (24%), and minor ethene production. When CO is added to this preparation, ethyne conversion decreases, then the major products are oligomers, ethene production is enhanced, and the complete quenching of ethane is observed.

- If the pretreatment is carried out under reaction condition, the hydrogenation behaviour of C2 and C3 is similar to the results observed for the unpretreated catalyst. Oligomers and alkanes are obtained for C2, and alkanes are the major products for C3. After CO addition, alkene production is enhanced, but the olefin is the major product only in the case of C3.

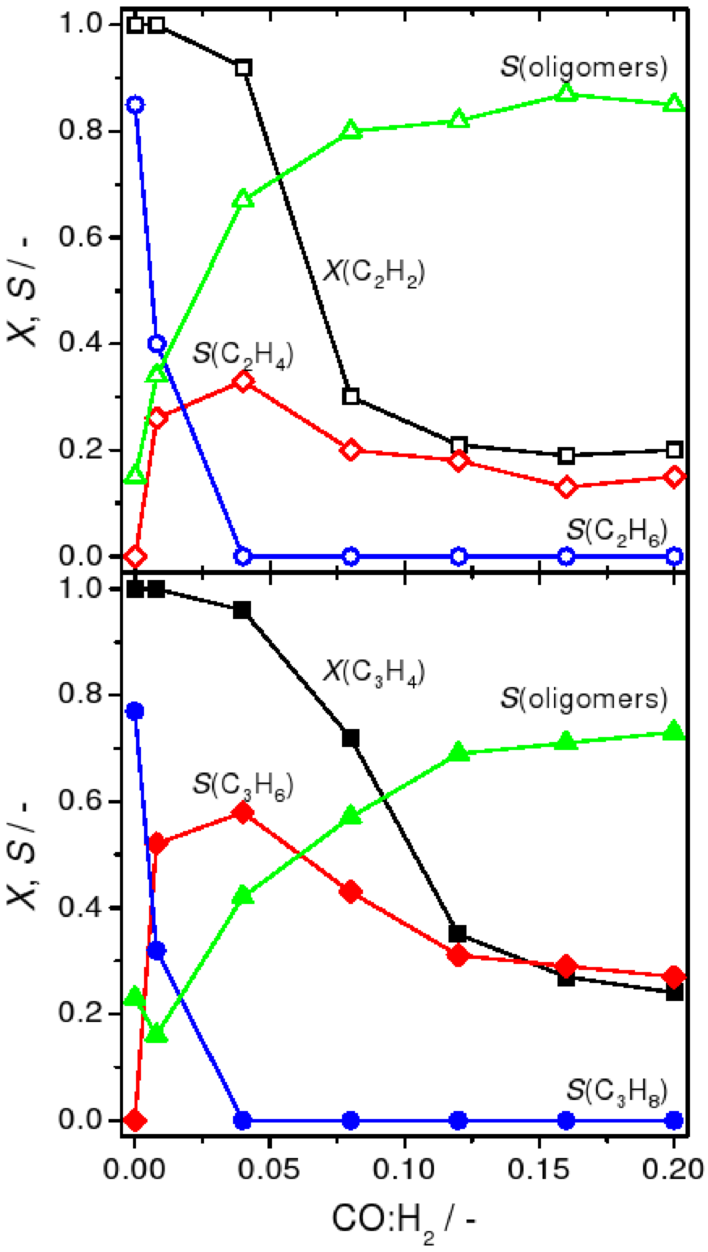

Figure 1.12: Conversion of ethyne, $\chi(C_2H_2)$, and propyne, $\chi(C_3H_4)$, and selectivity to the alkene, $S(C_2H_4)$ and $S(C_3H_6)$, alkane, $S(C_2H_6)$ and $S(C_3H_8)$, and oligomers, $S$(oligomers), over $Pd/Al_2O_3$ as a function of the $CO$:$H_2$ ratio. Ethyne (propyne) and the derived products are represented by open (solid) symbols. Other conditions: $H_2$:alkyne = 5; T=348 K; SV=16,800 $cm^3 g^{-1} h^{-1}$; and p=1 bar.

UNIVERSITAT ROVIRA I VIRGILI
THEORETICAL STUDIES OF SELECTIVE PROCESSES IN HETEROGENEOUS CATALYSIS
Mónica García Mota
ISBN:978-84-693-5424-7/DL:T-1415-2010

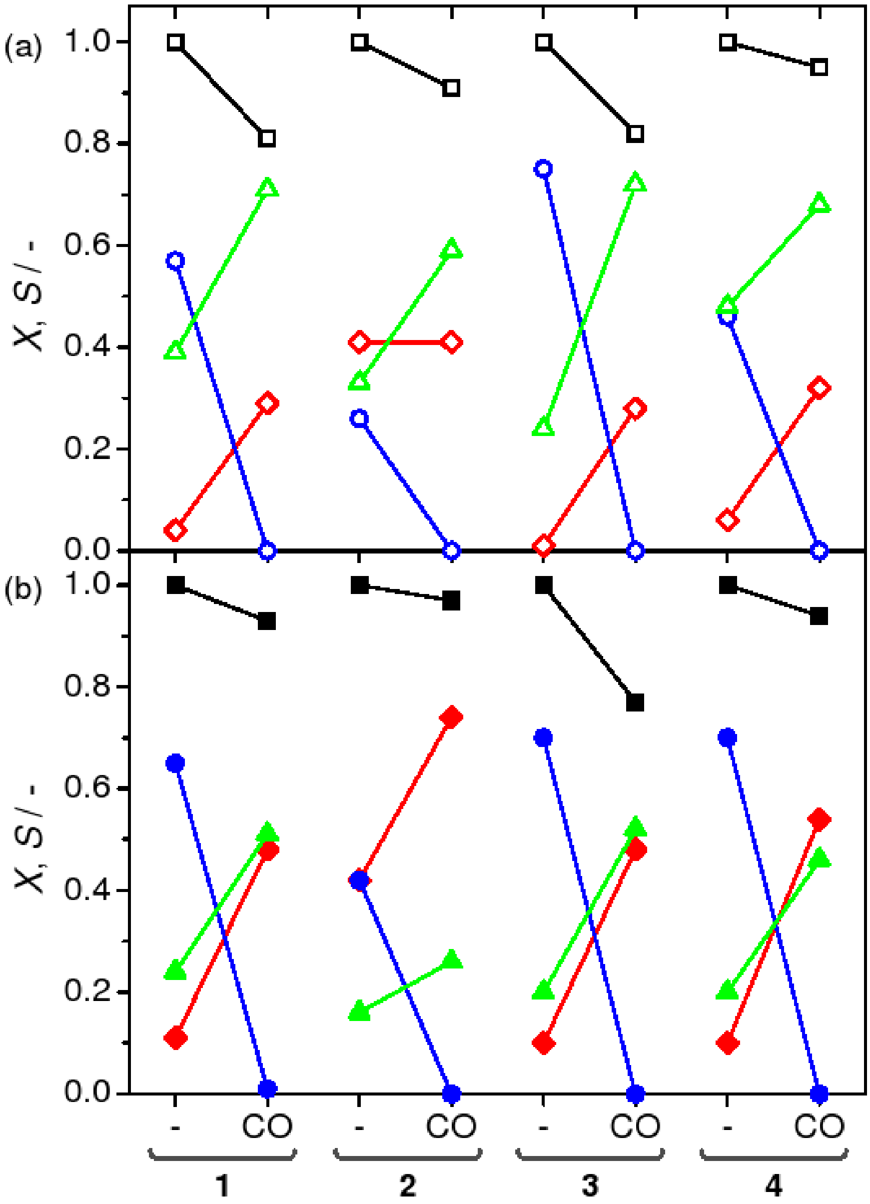

Figure 1.13: Influence of the pretreatment of $Pd/Al_2O_3$ on the hydrogenation of ethyne (a) and propyne (b) in the absence or presence of CO. Ethyne (propyne) and the derived products are represented by open (solid) symbols. Black line is for the alkyne conversion. Red and blue lines are for alkene and alkane selectivity respectively. Green line is for selectivity to oligomers. Pretreatments: (1) no pretreatment; (2) alkyne; (3) $H_2$; and (4) alkyne+$H_2$. Conditions: $H_2$:alkyne = 1.5; CO:$H_2$ = 0 or 0.03; T=348 K; SV=16,800 $cm^3g^{-1}h^{-1}$, and p=1 bar.

## 1.8 Outline

The outline of the Thesis is as follows:

In Chapter 2, the most important theories and tools in the field of first principles atomistic heterogeneous catalytic simulations will be revised.

In Chapter 3, Density Functional Theory, DFT, coupled to ab initio thermodynamics will be employed to analyse the vibrational spectra of CO on different $Pd_xAu_{100-x}$, $0< x <50$, alloys under different temperatures and pressures in order to identify the fingerprints for adsorption and characterise the ensembles.

In Chapter 4, CO oxidation on transition metal surfaces, Ni, Pd and Pt, and bimetallic alloys with a 0.25 ML of the surface atoms replaced by Au, is studied by means of Density functional Theory, DFT. The objective will be explain the reason behind the low temperature CO oxidation experimentally found when an AuNi surface alloy is used, and how this extrapolates to other transition metals.

In Chapter 5, the reaction mechanism that drives the selective conversion of hydrogen peroxide from its elements will be unravelled by means of Density Functional Theory, DFT, applied to slabs for Pd monometallic system, and $MPd_3$ bimetallic alloys (with M=Pt, Ag and Au) on the most stable surface face (111).

In Chapter 6, an extensive analysis of the vinyl acetate, VA, synthesis on heterogeneous Pd-based catalysts will be exposed in order to explain the strong dependence on the local structure of the ensemble experimental observed. VA can be synthetised by both homogeneous and heterogeneous processes involving Pd atoms as reaction centres, and the similarities and differences on the reaction mechanisms on both cases will be analysed.

In Chapter 7, experimental and theoretical methods are employed to find the similarities and differences in the performance of homogeneous and heterogeneous gold catalysts.

In Chapter 8, a systematic study on the effect of the catalyst state on the reaction network for the clean Pd surface, and the carbide, hydride, and CO-covered models is carried out. The state of the catalyst under experimental conditions is determined by first principles thermodynamics.

In Chapter 9, the main conclusions of this Thesis are discussed.

# Chapter 2

# Theoretical background

In this chapter the most important theories and tools in the field of first principles atomistic simulations in heterogeneous catalytic will be revised. Density Functional Theory, DFT, as the method to investigate the ground state of many-body systems will be shortly reviewed introducing the main approximations, LDA and GGA, used to describe the exchange-correlation energy. Some practical aspects will be also described: Basis set, $k$-point sampling, pseudopotentials and supercells. In a second term, Surface reactivity and Chemical bonding will be addressed (Section 2.4). The essence of the Statistical Thermodynamics, and the function role to introduce temperature and pressure effects will be discussed in Section 2.3. Some relations between trends in chemical reactions can often be approximately described by a linear relationships, this technique is analysed in Section 2.5. The microkinetic model of a simple reaction is described in Section 2.6.

## 2.1 Electronic structure calculations

In 1926, Erwin Schrödinger proposed an equation aimed at finding the state of any system. The time-independent Schrödinger equation for a particle of mass $m$ with energy $E$ is

$$\widehat{H}\Psi = E\Psi \tag{2.1}$$

where $\Psi$ represents the state and $\widehat{H}$ is the hamiltonian operator for the system:

$$\widehat{H}\Psi = -\frac{\hbar^2}{2m}\nabla^2 + \widehat{V} \tag{2.2}$$

The first term in Equation 2.2 is the kinetic energy, and the second is the potential. To obtain the evolution of a system with time, it is necessary to solve the time-dependent Schrödinger equation:

$$\widehat{H}\Psi(t) = i\hbar\frac{\partial\Psi(t)}{\partial t} \tag{2.3}$$

In many-body electronic structure calculations, the nuclei of the treated molecules or clusters are usually seen as fixed, (Born-Oppenheimer approximation) generating a static external potential, $V$, in which the electrons are moving. A stationary electronic state is then described by a wave function $\Psi(\mathbf{r}_1,\ldots,\mathbf{r}_n)$ satisfying the many-electron stationary Schrödinger equation:

$$\widehat{H}_{elec}\Psi = \left[\widehat{T} + \widehat{V} + \widehat{U}\right]\Psi = \left[\sum_i^N -\frac{\hbar^2}{2m}\nabla_i^2 - \sum_i^N V(\mathbf{r}_i) + \sum_{i<j} U(\mathbf{r}_i,\mathbf{r}_j)\right]\Psi = E\Psi \quad (2.4)$$

where $\widehat{H}$ is the electronic molecular Hamiltonian, $\widehat{T}$, $\widehat{V}$ and $\widehat{U}$ are the kinetic energy, the external potential, and the electron-electron interaction respectively. $N$ is the total number of electrons. The operators $\widehat{T}$ and $\widehat{U}$ are so-called universal operators as they are the same for any system, while $\widehat{V}$ is system dependent or non-universal. The difference between a single-particle problem and the many-particle problem just arises from the interaction term, $\widehat{U}$.

There are many methods to solve the many-body Schrödinger equation based on the expansion of the wave function in Slater determinants. The simplest one is the Hartree-Fock method and more sophisticated approaches are usually categorised as post-Hartree-Fock methods. However, the problem with these methods is the huge computational effort that they require, which makes it virtually impossible to apply them efficiently to large, complex systems. Instead, Density Functional Theory, DFT, provides an appealing alternative.

### 2.1.1 Density Functional Theory

Density Functional Theory, DFT, is a quantum mechanics theory employed to determine the ground state of many-body systems, in particular atoms, molecules and condensed phases. In DFT the key variable is the particle density n($\mathbf{r}$) which is given by

$$n(\mathbf{r}) = N\int \mathrm{d}^3r_2 \int \mathrm{d}^3r_3 \ldots \int \mathrm{d}^3r_N \Psi^*(\mathbf{r},\mathbf{r}_2,\ldots,\mathbf{r}_N)\Psi(\mathbf{r},\mathbf{r}_2,\ldots,\mathbf{r}_N) \quad (2.5)$$

The main idea behind DFT is that the electron density, n($\mathbf{r}$), is the basic variable, instead of the many-body wave function. Whereas the many-body stationary wave function, $\Psi$ ($\mathbf{r}_1$, $\mathbf{r}_2$, ..., $\mathbf{r}_n$), is dependent on 3N variables, three spatial variables for each of the N electrons (without considering the spin), the density is only a function of three variables and is a simpler quantity to deal with both conceptually and practically. Moreover, the electronic density, n($\mathbf{r}$), is a physical observable thus simplifies its interpretation when compared to $\Psi$ ($\mathbf{r}_1$, $\mathbf{r}_2$, ..., $\mathbf{r}_n$).

#### History

The theory of DFT was developed by Hohenberg and Kohn [115] and a possible way for its practical application was settled by Kohn and Sham.[116] DFT roots its basis on the Thomas-Fermi method developed in 1927 which is a prototypical description of the ground-state properties of a many-electron system.

The Thomas-Fermi method employed a statistical model to approximate the distribution of electrons in an atom. The mathematical basis postulated that electrons are distributed uniformly in phase space with two electrons in every $h^3$ of volume, where h, the Planck constant, is a physical constant that is employed to describe the sizes of quanta. For each element of coordinate space volume, $d^3\mathbf{r}$, we can fill out a sphere, Fermi sphere, the radius called Fermi momentum, $\mathbf{p}_f$, and its volume is

$$V_{Fermi} = (4/3)\pi \mathbf{p}_f^3(\mathbf{r}) \tag{2.6}$$

making equal the number of electrons in coordinate space to that in phase space gives

$$n(\mathbf{r}) = \frac{\mathbf{p}_f^3}{3\pi^2} \tag{2.7}$$

solving for $\mathbf{p}_f$ and substituting in the classical kinetic energy formula then leads directly to a kinetic energy, $T_F(n)$, represented as a functional of the electron density, $n(\mathbf{r})$,

$$T_F(n) = C_F \int n^{5/3}(\mathbf{r}) d^3\mathbf{r}. \tag{2.8}$$

As such, they were able to calculate the energy of an atom using this kinetic energy functional combined with the classical expressions for the nuclear-electron and electron-electron interactions, which can both also be represented in terms of the electron density.

Although this was an important first step, the accuracy of the Thomas-Fermi model is limited both because the resulting kinetic energy functional is only approximate and because the method does not include the exchange energy that arises from the Pauli principle. An exchange energy functional was added to the model by Paul Dirac in 1928.[117] However, the Thomas-Fermi-Dirac theory remained rather inaccurate for most applications. The largest source of error was in the representation of the kinetic energy, followed by the errors in the exchange energy, and due to the complete neglect of electron correlation. Edward Teller,[118] showed that Thomas-Fermi-Dirac theory cannot describe molecular bonding. This was overcome by improving the kinetic energy functional as done by Carl Friedrich in 1935,

$$T_W(n) = \frac{1}{8}\frac{\hbar^2}{m} \int \frac{|\nabla n(\mathbf{r})|^2}{n(\mathbf{r})} dr \tag{2.9}$$

In 1965 Pierre Hohenberg and Walter Kohn developed the existence of a one-to-one correspondence between the ground state electron density, $n_0(\mathbf{r})$, and the ground state wavefunction of a many-particle system, $\Psi_0(\mathbf{r}_1,\ldots,\mathbf{r}_N)$. They proved that the energy of a quantum mechanical system is a unique function of the electron density, $n(\mathbf{r})$, and that the correct ground-state density minimises it. The original Hohenberg-Kohn theorems hold only for a non-degenerate ground state in the absence of magnetic field, although they have been generalised to the ground states of each symmetry.

### Derivation and formalism

Hohenberg and Kohn proved in 1964 that the Equation 2.5 can be reversed, i.e. to a given ground state density $n_0(\mathbf{r})$ it is in principle possible to obtain the corresponding ground state wavefunction $\Psi_0(\mathbf{r}_1,\ldots,\mathbf{r}_N)$. In other words, $\Psi_0$ is a unique functional of $n_0$, $\Psi_0{=}\Psi(\mathrm{n}_0)$.

This means that all other ground state observables are also functionals of $n_0$. In particular, the ground state energy, $E_0$, can be expressed as a functional of $n_0$.

$$E_0 = E(n_0) = \langle \Psi_0(n_0) \left| T(n_0) + V(n_0) + U(n_0) \right| \Psi_0(n_0) \rangle \tag{2.10}$$

The functionals $T(n)$ and $U(n)$ are called universal functionals while $V(n)$ is non-universal, as it depends on the system under study (i.e. the tridimensional structure of the nuclei). The state energy, $E(n)$, can be expressed as:

$$E(n) = T(n) + U(n) + \int V(\mathbf{r}) n(\mathbf{r}) d^3\mathbf{r} \tag{2.11}$$

Having specified a system, $V$ is known, a successful minimisation of the energy functional with respect to $n(\mathbf{r})$ will yield the ground state density, $n_0(\mathbf{r})$, and thus other ground state observables.

The variational problem of minimising the energy functional, E(n), can be solved by applying the Lagrangian method of undetermined multipliers, which was done by Kohn and Sham in 1965. Hereby, one uses the fact that the functional in the equation above can be written as a fictitious density functional of a non-interacting system

$$E_s(n) = \langle \Psi_s(n) \left| T_s + V_s \right| \Psi_s(n) \rangle \tag{2.12}$$

where $T_s$ denotes the non-interacting kinetic energy and $V_s$ is an external effective potential in which the particles are moving.

If $V_s$ is chosen to be

$$V_s = V + U + (T - T_s) \tag{2.13}$$

then $n_s(\mathbf{r}) \overset{\mathrm{def}}{=} \mathrm{n}(\mathbf{r})$. Thus, one can solve the so-called Kohn-Sham equations of this auxiliary non-interacting system

$$\left[ \frac{\hbar^2}{2m} \nabla^2 + V_s(\mathbf{r}) \right] \phi_i(\mathbf{r}) = \epsilon_i \phi_i(\mathbf{r}) \tag{2.14}$$

which yields the molecular orbitals, $\phi_i$, that reproduce the density, $n(\mathbf{r})$, of the original many-body system

$$n(\mathbf{r}) \overset{\text{def}}{=} n_s(\mathbf{r}) = \sum_i^N |\phi_i(\mathbf{r})|^2 \tag{2.15}$$

The effective single-particle potential, $V_s$, includes the external potential, the effects of the Coulomb interactions between the electrons, and the exchange and correlation interactions. $V_s$ can be written in more detail as

$$V_s = V + \int \frac{e^2 n_s(\mathbf{r}')}{|\mathbf{r}-\mathbf{r}'|}\mathrm{d}^3 r' + V_{\mathrm{XC}}(n_s(\mathbf{r})) \tag{2.16}$$

where V is the external potential, the second term denotes the so-called Hartree term describing the electron-electron Coulomb repulsion, and the last term, $V_{\mathrm{XC}}$, is known as the exchange correlation potential. Usually, one starts with an initial guess for $n(\mathbf{r})$, then calculates the corresponding $V_s$ through Equation 2.16, and solves the Kohn-Sham equations, Equation 2.14 for the $\phi_i$. From these one calculates a new density and starts again. This procedure is then repeated until self-consistency is reached. Therefore, the intractable many-body problem of interacting electrons in a static external potential, $V$, has been reduced to a tractable problem of non-interacting electrons moving in an effective potential, $V_s$. It shall be noticed that the KS equations are formally equivalent to the HF ones, only the potential is different.

### 2.1.2 Exchange-correlation approximations

The exchange energy is the reduction of the energy of the electronic system which results from the anti-symmetry of the wave function under permutation of electrons. The correlation contribution to the energy arises because the motion of an electron depends also on the movements of other electrons. The major problem of DFT is that the exact functionals for exchange and correlation are not known except for the free electron gas. However, approximations exist which permit the calculation of many physical quantities quite accurately.

#### The Local Density Approximation, LDA

The lower level of approximation to the exchange-correlation interaction is the local-density approximation, LDA. It was originally introduced by Kohn and Sham.[116] In LDA, the functional depends only on the density, n($\mathbf{r}$), at the position where the functional is evaluated. In order to find the exchange-correlation energy, $E_{XC}$, for an inhomogeneous electron gas, it is assumed that the contribution from each point in the electron gas is the same as in a homogeneous electron gas with the same density n($\mathbf{r}$).

$$E_{XC}^{LDA} = \int n(\mathbf{r})\varepsilon_{XC}^{hom}(n)\mathrm{d}\mathbf{r} \tag{2.17}$$

The spin-polarised version of LDA is termed as Local-Spin Density Approximation, LSDA,[119] and allows difference between the spatial parts of $n_\uparrow$ and $n_\downarrow$. It is needed for atoms and molecules with unpaired electrons and for magnetic condensed materials.

$$E_{XC}^{LSDA}(n_\uparrow, n_\downarrow) = \int \varepsilon_{XC}(n_\uparrow, n_\downarrow) n(\mathbf{r}) \mathrm{d}^3\mathbf{r} \tag{2.18}$$

### The Generalised Gradient Approximation, GGA

Generalised Gradient Approximations, GGA, are still local but also take into account the gradient of the charge density at the same coordinate

$$E_{XC}^{GGA}(n(\mathbf{r})) = \int n(\mathbf{r}) \varepsilon_{XC}(n(\mathbf{r}), \nabla n(\mathbf{r})) \mathrm{d}\mathbf{r} \tag{2.19}$$

GGA can also be extended to spin-polarised systems

$$E_{XC}(n_\uparrow, n_\downarrow) = \int \varepsilon_{XC}(n_\uparrow, n_\downarrow, \nabla n_\uparrow, \nabla n_\downarrow) n(\mathbf{r}) \mathrm{d}^3\mathbf{r} \tag{2.20}$$

Several groups have constructed functionals, of which the most commonly used in chemistry are BP86,[120] BLYP,[121] and in solid state problems PW91,[122] PBE,[123] and RPBE.[124] Geometries are good with LDA while thermochemistry demands at least GGA type functionals. Complex structures with strongly correlated electrons *d* and *f* electrons need *on-site* effects (L(S)DA+U methods and derived). In the present work GGA functional are used; RPBE (Chapters 3, 4, 5 and 6), PW91 (Chapter 8), and B3LYP (Chapter 7). RPBE is extremely sensitive to density gradients, and provides better thermochemistry data than other GGAs.[124] In Chemistry, other functionals like hybrid B3LYP [125, 126] constitutes the standard. B3LYP contains a part of the HF exchange and provides good thermochemistry data, but it has two drawbacks. First, they do not fulfill the requirements for homogeneous gas (i.e. the only system for which an exact functional exists), and second they are difficult to implement in plane wave calculations.

## 2.2 Practical aspects

### 2.2.1 Basis set

For a numerical description of the Kohn-Sham wave functions, a basis set has to be chosen. In DFT calculations for solid surfaces, a plane wave basis set is often chosen due to the periodicity of the systems.

The expansion of the wave functions is based on Bloch's theorem.[127] A *Bloch state* is the wave function of a particle, usually an electron, placed in a periodic potential. Then the *Bloch state* can be expressed as the product of a plane wave envelope function, $e^{i\mathbf{kr}}$, and a periodic function, $U_n(\mathbf{r})$, which has the same periodicity as the potential.

$$\psi_n(\mathbf{r}) = e^{i\mathbf{kr}} U_n(\mathbf{r}) \tag{2.21}$$

The periodic part of the wave function can be expanded using a basis set consisting of a discrete set of plane waves whose wave vectors are reciprocal lattice vectors of the crystal,

$$U_n(\mathbf{r}) = \sum_{\mathbf{G}} c_{n,\mathbf{G}} e^{i\mathbf{G}r} \tag{2.22}$$

where the reciprocal lattice vectors $\mathbf{G}$ are defined by $\mathbf{Gl} = 2\pi m$ for all $\mathbf{l}$. $\mathbf{l}$ is a lattice vector of the crystal and $m$ is an integer.

Therefore, each electronic wave function can be written as sum of plane waves,

$$\psi_n(\mathbf{r}) = \sum_{G} c_{n,\mathbf{k}+\mathbf{G}} e^{i(\mathbf{k}+\mathbf{G})\mathbf{r}} \tag{2.23}$$

where $k$ is the wave vector limited to the first Brillouin zone (multiplied by the reduced Planck's constant, this is the particle's Crystal momentum) and $\mathbf{G}$ is a reciprocal lattice vector. The corresponding energy eigenvalue is periodic, $E_{nk}= E_{n(k+\mathbf{G})}$, with periodicity of a reciprocal lattice vector, $\mathbf{G}$. All distinct values of $E_n$ occur for $k$ values within the first Brillouin zone of the reciprocal lattice.

The plane wave wavevector, or Bloch wavevector, $\mathbf{k}$, is unique only up to a reciprocal lattice vector, so one only needs to consider the wavevectors inside the first Brillouin zone.

Therefore, using plane waves with periodic boundary conditions, we get rid of the infinite number of atoms and electron wave functions but end up having an infinite number of $\mathbf{G}$-vectors. However, the coefficients $c_{n,\mathbf{k}+\mathbf{G}}$ for the plane waves with small kinetic energy $(\frac{\hbar^2}{2m})|\mathbf{k}+\mathbf{G}|^2$ are typically more important that those with large kinetic energy. Thus the number of plane waves can be safely truncated by introducing the cutoff energy, $\mathrm{E}_{cut}$,[128] which is given as a kinetic energy of the largest $\mathbf{G}$-vector.

For a given wavevector and potential, there are a number of solutions, indexed by $n$, to Schrödinger's equation for a Bloch electron. These solutions, called bands, are separated in energy by a finite spacing at each k; if there is a separation that extends over all wavevectors, it is called a band gap. In short the band structure is the collection of energy eigenstates within the first Brillouin zone, see Figure 2.1.

All the properties of electrons in a periodic potential can be calculated from this band structure and the associated wave functions, at least within the independent electron approximation.

### 2.2.2 k-point sampling

Although Bloch's theorem gives the electronic states for a set of $k$-points, the size of the set is infinite. However, the wave functions at $k$-points close to each other are very similar, therefore when performing integrations, only a discrete set of $k$-points is needed to represent the $k$-space.

The electronic structure calculations of metals are more demanding than those of semiconductors and insulators, since more $k$-points are needed to describe reliably the

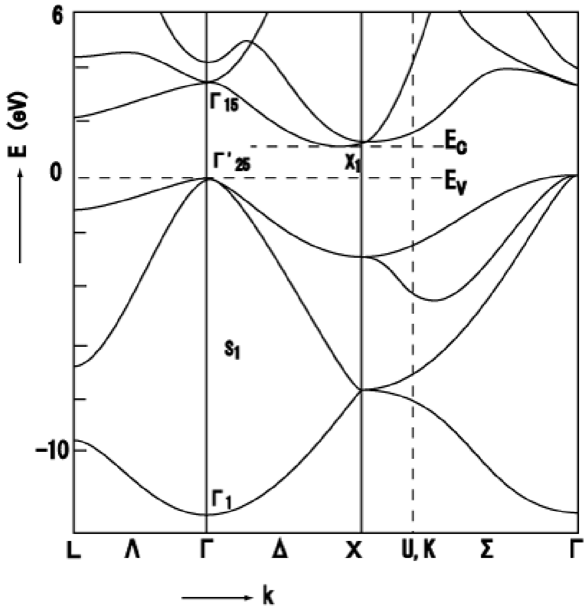

Figure 2.1: Calculated band structure of crystalline Si. Taken from ref. [129].

Fermi surface. Unlike metals, insulators and semiconductors have a gap between occupied and unoccupied states, and the shape of the Fermi surface is simple, see Figure 2.2. For metals, the $k$-space integrals converge slowly with increasing number of $k$-points.

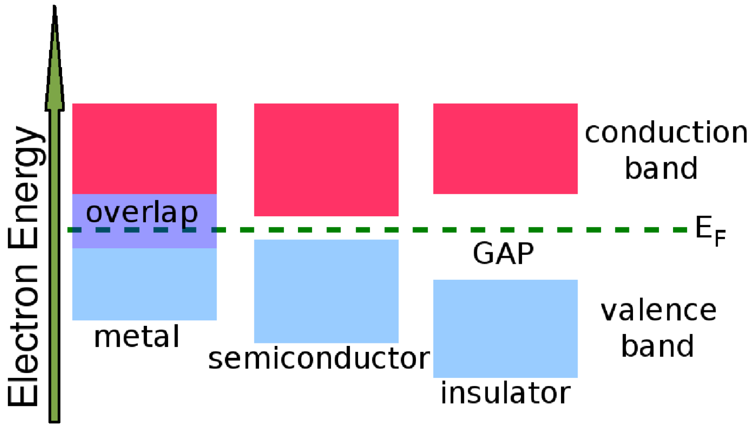

Figure 2.2: Comparison of the electronic band structures of metals, semiconductors and insulators.

To decrease the number of $k$-points further, special $k$-points are often used where the symmetry of the system is exploited. The Monkhorst-Pack grid,[130] is usually used for rectangular systems. In Figure 2.3 the first Brillouin zone for a face centred cubic, fcc, structure is represented.

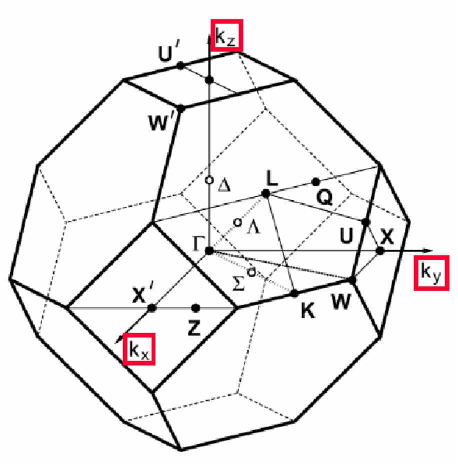

Figure 2.3: Some important symmetry points on the Brillouin zone of a fcc crystal. Taken from ref. [131].

### 2.2.3 Pseudo-potentials

Although Bloch's theorem states that the electronic wave functions can be expanded using a discrete set of plane waves, PW, a plane wave is usually very poorly suited to describe electronic wave functions. This is because a very large number of PW are needed to expand the tightly bound core orbitals and to follow the rapid oscillations of the wave functions of the valence electrons in the core region. An extremely large plane wave basis set would be required to perform an all electron calculation, and a vast amount of computational time would be required to calculate the electronic wave functions. However, only the outermost electrons in an atom normally influence the chemical properties of matter, while electrons in the inner shells are almost inert. Therefore, the distribution of the core electrons basically does not change when the atoms are placed in a different chemical environments. It is thus justified to assume the core electrons to be *frozen*,[132] and to keep the core electron distribution of the isolated atom in the crystal environment. The pseudopotential approximation exploits this by removing the core electrons, and by replacing them and the strong ionic potential by a weaker pseudopotential that acts on a set of pseudo wave functions rather than the true valence wave functions. An ionic potential, a valence wave function and the corresponding pseudopotential and pseudo wave function are illustrated schematically in Figure 2.4. The pseudopotential approximation [133] allows the electronic wave functions to be expanded using a much smaller number of plane wave basis states.

The valence wave functions oscillate rapidly in the region occupied by the core electrons due to the strong ionic potential in this region. These oscillations maintain the orthogonality between the core wave functions and the valence wave functions, which is required by the exclusion principle. The pseudopotential is constructed so that its scattering properties or phase shifts for the pseudo wave functions are identical to the scattering properties of the ion and the core electrons for the valence wave functions,

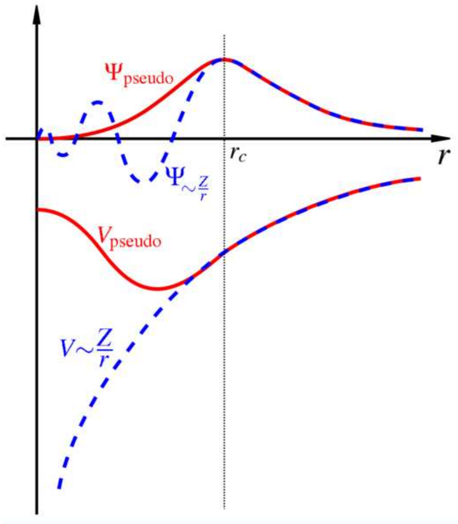

Figure 2.4: Schematic illustration of all electron (blue lines) and pseudoelectron (red lines) potentials and their corresponding wave functions. The radius at which all electron and pseudoelectron values match is known as cutoff radius, $r_c$. Taken from ref. [128].

but in such a way that the pseudo wave functions have no radial nodes in the core region. Outside the core region, the two potentials are identical and the scattering from the two potentials is indistinguishable.

The pseudopotentials must be as transferable as possible, because although they are always constructed for a single atom, they are applied in various chemical environments. Furthermore, the pseudopotential should be as *soft* as possible. It means that the number of plane waves required to expand the pseudo wave functions should be as small as possible. Both properties, transferability and softness, are closely related to the cutoff radius, $r_c$ and compete with each other. Low cutoffs give pseudopotentials with a very good transferability. However, increasing $r_c$ makes the pseudopotentials softer. Usually one has to find a compromise between the two requirements.

### 2.2.4 Supercells

When using plane waves as basis functions, the system has to be periodic in all directions in space because Bloch's theorem only applies for such systems. Atoms and molecules in vacuum, as well as clusters and surfaces, are not periodical as such, therefore in calculations these systems have to be surrounded by enough empty space to prevent artificial or cell-to-cell interactions, which are due to periodic boundary conditions. The supercell for a surface calculation is illustrated schematically in Figure 2.5. A surface may have periodicity in the plane, but it cannot have periodicity perpendicular to the surface. This leads to the creation of the slab, a geometry where the surface is modelled with few atomic layers and a vacuum region, which separates the slabs in the z-direction, see Figure 2.6. To ensure that the results of the calculation accurately represent an isolated surface, the vacuum region must be wide enough, each slab has to be several atomic layers thick so that faces of adjacent crystal slabs do not interact across the vacuum region, and the crystal slab must be thick enough so that the two surfaces of each crystal slab do not interact through the bulk crystal.

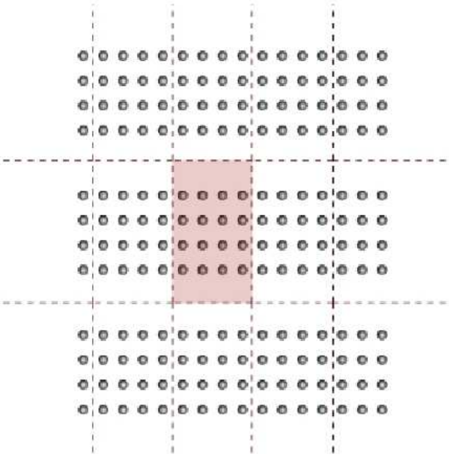

Figure 2.5: Schematic illustration of a supercell geometry for a surface of a bulk solid. The supercell is the area enclosed by the dashed lines.

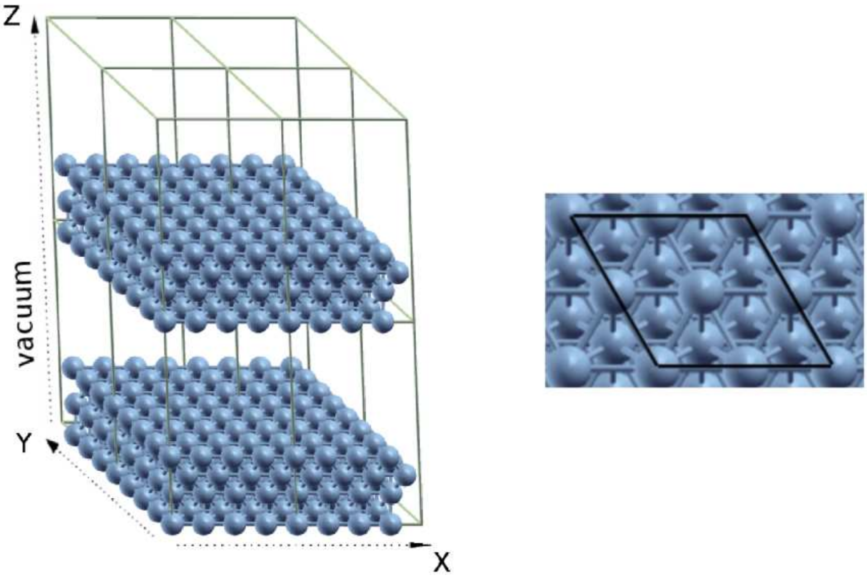

Figure 2.6: Side view of a four atomic layer-thick metallic slab (left). A top view of a $p$(2x2) unit cell (right).

## 2.3 Statistical Thermodynamics

However, all the descriptions DFT are restricted to 0 K temperature and 0 bar pressures. The introduction of pressures and temperatures is fundamental to retrieve interesting properties and to compare to experiments. To this end, statistical thermodynamics techniques can be employed very efficiently.

The essential problem in statistical thermodynamics is to determine the distribution of a given amount of energy $E$ over $N$ identical systems. The goal of statistical thermodynamics is to understand and to interpret the measurable macroscopic properties of materials in terms of the properties of their constituent particles and the interactions between them. This is done by connecting thermodynamic functions to quantum-mechanic equations. Two central quantities in Statistical Thermodynamics are the Boltzmann factor and the partition function.[134]

One of the most important approximations to be aware of throughout this analysis is that all the equations assume non-interacting particles and therefore apply only to an ideal gas. This limitation will introduce some errors, depending on the extent that any system being studied is non ideal.

### 2.3.1 Partition functions

In statistical mechanics, the partition function, $Q$, is the important quantity that encodes the statistical properties of a system in thermodynamic equilibrium. It is a function of temperature and other parameters, such as the volume enclosing a gas. Most of the thermodynamic variables of the system, such as the total energy, $E$; Gibbs free energy, $G$; entropy, $S$; and pressure, $p$; can be expressed in terms of the partition function or its derivatives. When the number of available quantum states is much greater than the number of particles, the partition function of the entire system can be written in terms of the individual atomic partition functions, then the partition function of a system of independent indistinguishable atoms or molecules can usually be written as

$$Q(N,T,V) = \frac{[q(T,V)]^N}{N!} \tag{2.24}$$

where $N$ is the number of particles and $q(T,V)$ is the molecular particular function

$$q(T,V) = \sum_j e^{-\varepsilon_j/k_BT} \tag{2.25}$$

The number of translational states alone is usually sufficient to guarantee that the number of energy states available to any atom or molecule is larger than the number of particles in the system. Therefore, this procedure yields an excellent approximation in many cases. The criterion that the number of available states exceeds the number of particles so that Equation 2.24 can be used is

$$\frac{N}{V}\left(\frac{h^2}{8mk_BT}\right)^{\frac{3}{2}} \ll 1 \tag{2.26}$$

This criterion is favoured by large particle mass, high temperature, and low density. If Equation 2.24 is valid, we say that the particle obeys *Boltzmann statistics.* Furthermore, when treating diatomic or polyatomic molecules, we use the rigid rotator-harmonic oscillator approximation and we can write the total energy of the molecule as a sum of its translational, $\varepsilon_{trans}$, vibrational, $\varepsilon_{vib}$, rotational, $\varepsilon_{rot}$, and electronic energies, $\varepsilon_{elec}$.

$$\varepsilon = \varepsilon_{trans} + \varepsilon_{vib} + \varepsilon_{rot} + \varepsilon_{elec} \tag{2.27}$$

Equation 2.26 is particularly applicable to ideal gases because the molecules are independent and the densities of gases that behave ideally are low enough that the Equation 2.24 is satisfied. Furthermore, Equation 2.27 allows us to write

$$q(V,T) = q_{trans}q_{rot}q_{vib}q_{elec} \tag{2.28}$$

so the partition function of a molecular ideal gas is given by

$$Q(N,V,T) = \frac{(q_{trans}q_{rot}q_{vib}q_{elec})^N}{N!} \tag{2.29}$$

We can calculate the average translational energy, $\varepsilon_{trans}$, of an ideal diatomic gas molecule from this partition function [134]

$$q_{trans}(V,T) = [\frac{2\pi(m_1+m_2)k_BT}{h^2}]^{\frac{3}{2}}V \tag{2.30}$$

so we have that

$$<\varepsilon_{trans}>= \frac{3}{2}k_BT \tag{2.31}$$

We can calculate the average vibrational energy from q$_{vib}$(T),[134] where we can introduce the quantity $\Theta_{vib} = \frac{h\nu}{k_B}$, called the *vibrational temperature*,

$$q_{vib}(T) = \frac{exp^{-\frac{\Theta_{vib}}{2T}}}{1-exp^{-\frac{\Theta_{vib}}{T}}} \tag{2.32}$$

so we have that

$$<\varepsilon_{vib}>= Nk_B\Theta_{vib}[\frac{1}{2} + \frac{1}{exp^{(\frac{\Theta_{vib}}{T}}-1)}] \tag{2.33}$$

In order to calculate the rotational partition function is useful introduce a quantity that has units of temperature and is called the *rotational temperature*, $\Theta_{rot}$

$$\Theta_{rot} = \frac{\hbar^2}{2\mathbf{I}k_B} \tag{2.34}$$

where **I** is the momentum of inertia of the molecule. The rotational partition function in the high temperature limit, $\Theta_{rot} \ll$ T, (it is the case for most molecules at room temperature) can be written as,[134]

$$q_{rot}(T) = \frac{T}{\Theta_{rot}} = \frac{8\pi^2 \mathbf{I} k_B T}{h^2} \tag{2.35}$$

and the average rotational energy is

$$< \varepsilon_{rot} >= N k_B T \tag{2.36}$$

Last, we take the zero of the electronic energy to be the separated atoms at rest in their ground electronic states, and the electronic partition function is

$$q_{elec} = g_{e1} exp^{\frac{-\varepsilon_{e1}}{k_B T}} + g_{e2} exp^{\frac{-\varepsilon_{e2}}{k_B T}} \tag{2.37}$$

Where $g_{e1}$ and $g_{e2}$ are the degeneracy of the energy levels, $\varepsilon_{e1}$ is the energy of the ground electronic state and $\varepsilon_{e2}$ is the energy of the first excited electronic state. If we assume that the first electronic excitation energy is much larger than $k_B$T then the first excited state is assumed to be inaccessible at any temperature. If the energy of the ground state is set to zero, these assumptions simplify the electronic partition function to

$$q_{elec} = g_{e1} \tag{2.38}$$

Since there are no temperature dependent terms in the partition function, the internal thermal energy due to electronic motion is zero.

$$< \varepsilon_{elec} >= 0 \tag{2.39}$$

Summing up, the average translational, $\varepsilon_{trans}$, vibrational, $\varepsilon_{vib}$, rotational, $\varepsilon_{rot}$ and electronic energies, $\varepsilon_{elec}$, of the molecule are

$$\begin{aligned} < \varepsilon_{trans} > &= \frac{3}{2} k_B T \\ < \varepsilon_{vib} > &= N k_B \Theta_{vib} [\frac{1}{2} + \frac{1}{exp^{(\frac{\Theta_{vib}}{T}} - 1)}] \\ < \varepsilon_{rot} > &= N k_B T \\ < \varepsilon_{elec} > &= 0 \end{aligned} \tag{2.40}$$

## 2.4 Surface reactivity

Gas-surface interactions and reactions on surfaces play a crucial role in many technologically important areas such as corrosion, adhesion, synthesis of new materials, electrochemistry and heterogeneous catalysis.[135] This section aims to describe the role of the catalyst and the interaction of gases with metal surfaces in terms of chemical bonding. Molecular orbital and band structure theory are the basic tools for this.

### 2.4.1 The role of the catalyst

A catalyst accelerates a chemical reaction. It does so by forming bonds with the reacting molecules and by allowing these to react to a product, which detaches from the catalyst and leaves it unaltered so that it is available for the next reaction cycle. The potential energy diagram, Figure 2.7, compares the non-catalytic and the catalytic reaction, and shows how the catalyst accelerates the reaction. Catalysis is a cycle, which starts with the adsorption of reactants on the surface of the catalyst. When an atom or molecule approaches the surface it feels the potential energy set up by the metal atoms in the solid. The interaction is usually divided into two regimes, namely physisorption and chemisorption. The physisorption is a weak interaction, a chemical bond is not formed and the interaction is due to polarisation or van der Waals forces. This problem is not well-treated in the present DFT functionals. The chemisorption is when molecules or atoms form a chemical bond with the surface upon adsorption, this bond is correctly reproduced by DFT.

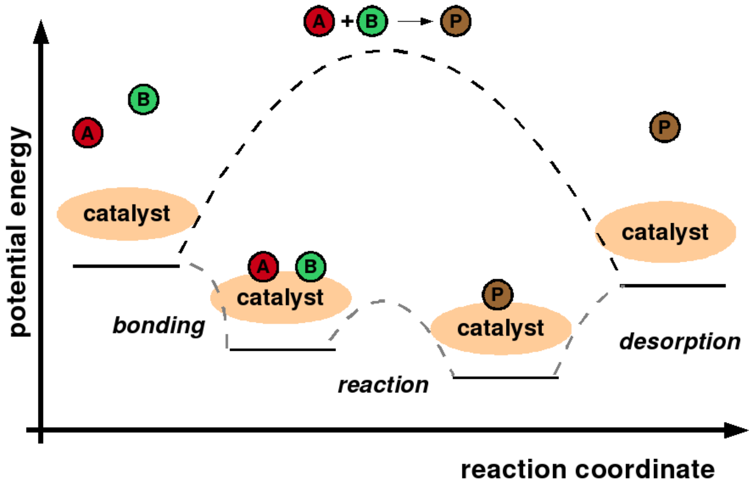

Figure 2.7: Potential energy diagram of a heterogeneous catalytic reaction, with gaseous reactants and products and a solid catalyst. Adapted from ref. [135].

### 2.4.2 Chemical bonding

The essence of catalytic action is that it assists in breaking strong intramolecular bonds at lower temperatures than those needed in the direct gas-phase reaction. Chemisorbed adsorbate binds to a surface through a chemical bond. This bond is formed due to the coupling of the adsorbate molecular orbitals to the metal electron bands. Simple models can be used to analyse the coupling. A model has been proposed by Hammer and Nørskov [136] where the interaction of the adsorbate orbitals with the metal bands is divided into two parts, one describing the coupling with the $s$ and $p$ valence electrons and another the coupling with the $d$ valence bands.

To describe the chemisorption bond it is necessary to review briefly a simplified form of molecular orbital theory and summarise major results of solid state theory that are relevant to understand the adsorption on surfaces.

### The solid surface

All metals have extended outer *s* or *p*-orbitals, which ensure large overlap. The orbitals are very close in a metal and form an almost continuous band of levels. The *d*-orbitals have pronounced shapes and orientations that are largely retained in the metal. Hence, the overlap between the individual *d*-orbitals of the atoms is much smaller than that of the outer *s* and *p* electrons. The latter are strongly delocalised and they form an almost free electron gas that spreads out over the entire metal. Then, the atomic *sp* electron wave functions overlap to a great extent, and consequently the band they form is much broader, see Figure 2.8.

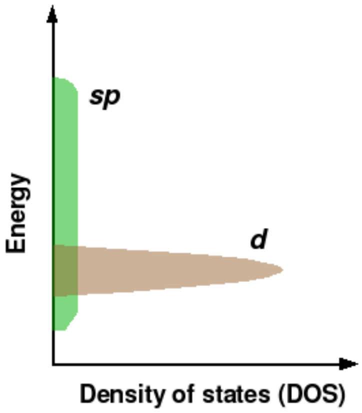

Figure 2.8: Schematic representation of the broad *sp*-band and the narrow *d*-band. Adapted from ref. [135].

A knowledge of the behaviour of *d*-orbitals is essential to understand the differences and trends in reactivity of the transition metals. The width of the *d*-band decreases as the band is filled when going to the right in the periodic table since the molecular orbitals become ever more localised and the overlap decreases. Thus, a band is simply a collection of many molecular orbitals. The lower levels in the band are bonding, the upper ones antibonding and the ones in the middle non-bonding. Each energy level in the band is called a state and an important quantity to look at is the density of states, DOS, at a given energy. The density of states curves of transition metals show complicated structures, due to crystal structure and symmetry, see Figure 2.9.

The bands are filled with valence electrons of the atoms up to the Fermi level, $\epsilon_F$. In a molecule this is known as highest occupied molecular orbital or HOMO.

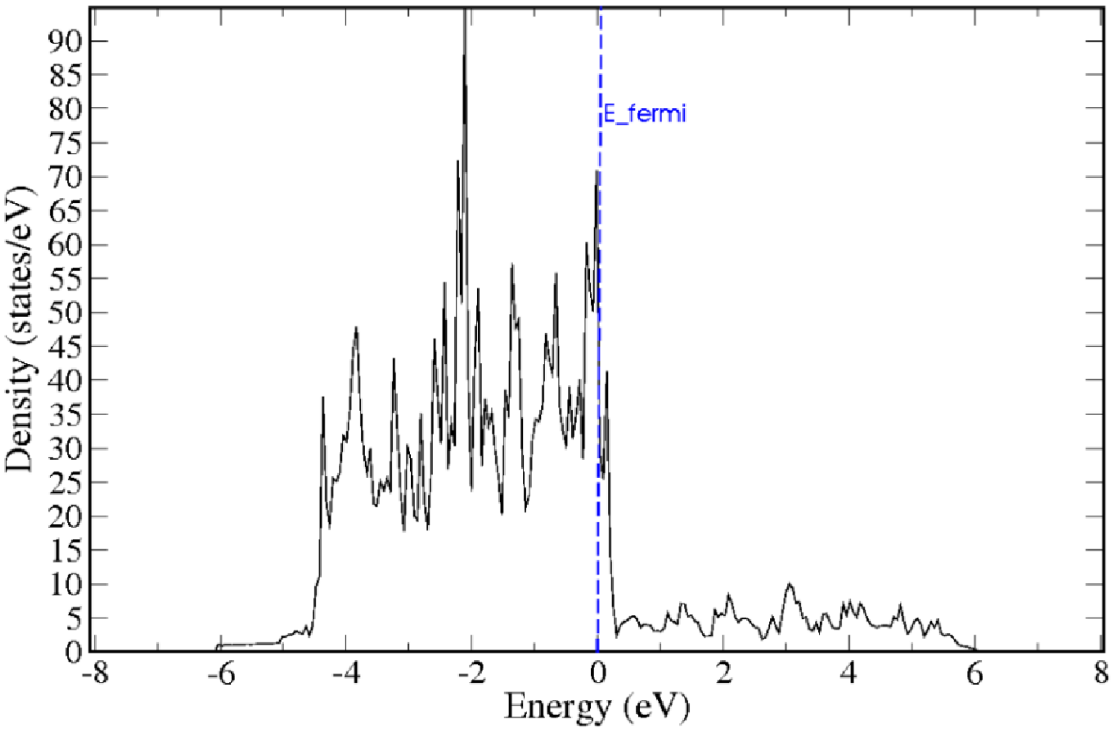

Figure 2.9: Calculated electronic density of states, DOS, of Pd(111).

## Important trends in surface reactivity

### Trends in atomic chemisorption energies

The total bonding energy between an atom and a metal surface has two contributions; one due to the *sp* interaction, $E_{sp}$, and one from *d*-band, $E_{d-hyb}$.

#### sp-interaction

When an atom with a filled level at energy $\varepsilon_a$ approaches a metal surface it chemisorbs due to the interaction with the *sp* electrons of the metal. Consider for example an oxygen atom, the 2*p* level contains four electrons when the atom is isolated, but as it approaches the metal the 2*p* levels broaden and shift down in energy through the interaction with the *sp*-band of the metal. All levels below the Fermi level are filled with additional electrons, the *sp* valence electrons can move freely leading to a strong *sp*-induced bonding, which amounts to about -5 eV.[135]

The coupling to the *s* and *p* valence electrons gives information about the bond energy, the preferred bond lengths and the binding sites of the adsorbate, but the O-*sp* interaction can not explain the trends in bonding through the transition metals, since the *sp*-bands of these metals are very similar. To understand the trend the *d*-valence bands have to be taken into account.

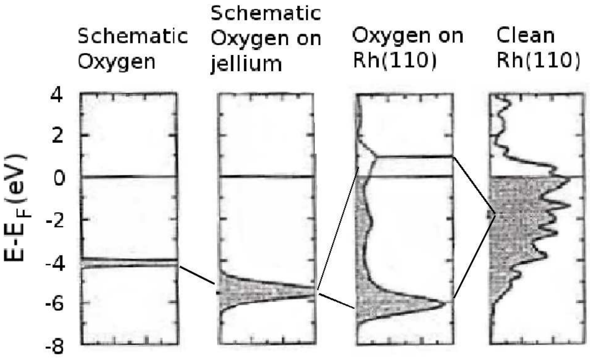

Figure 2.10: Schematic representation of the change in local electronic structure of an oxygen atom adsorbing on rhodium. Taken from ref. [135].

### d-interaction

The $d$-orbitals are more localised than the extended $sp$-bands. The bands they form are therefore much narrower. The small extension of the $d$-bands, means that this interaction with the molecular orbitals can be treated as done before, giving rise to bonding and anti-bonding states.

The three parameters that play a role in determining the bond strength between the metal $d$-band and the atomic adsorbate are:

- The degree of filling of the $d$-band, $f$.
- The interaction matrix element, $\beta$, between the wave functions of the electron on the atom and those for the $d$-states of the metal. This term varies with the metal for a fixed adsorbate and adsorption site on the surface.
- The energy difference, $\delta$, between the original electron level of the adsorbate, $\varepsilon_a$, and the centre of the $d$-band, $\varepsilon_d$.

The variation between different adsorbates only needs to be included by a proportionality constant, $V^2_{xrad} = \lambda_a \beta^2$, where $a$ labels different adsorbates. Figure 2.11 shows that $\beta^2$ decreases with the filling degree $f$ and increases when going from the $3d$ series to the $5d$ series, since the geometrical extent of the $d$-orbitals decreases with filling degree and the geometrical extent increases when going up through the series.

### Trends in molecular chemisorption energies

In diatomic molecules, such as $N_2$, $O_2$, and CO, the valence electrons are located on the $5\sigma$, $1\pi$ and $2\pi$ orbitals. The $5\sigma$ level is below the $1\pi$ level due to interaction with the $4\sigma$ level. In general, the $1\pi$ level is filled and sufficiently low in energy so that the interaction with a metal surface is primarily though the $5\sigma$ and $2\pi$ orbitals.

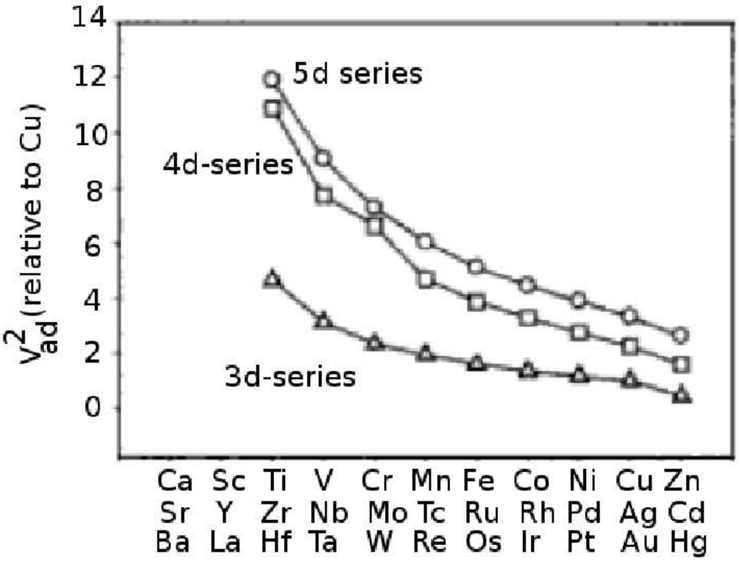

Figure 2.11: The matrix element $V^2_{ad}$ expresses how the *d*-band of the metal couples with the *s* or *p* level of the atomic adsorbate, for the three transition metal series. Taken from ref. [135].

The adsorption of CO on d metals can be described with two terms, *sp*-interaction and *d*-interaction

### sp-interaction

Upon adsorption, there is a strong interaction of the $5\sigma$ and $2\pi$ orbitals and the metal *sp* electrons, resulting in a downward shift and broadening of these two levels. In Figure 2.12, it is shown that the $5\sigma$ and $2\pi$ levels of CO are first allowed to interact with the *sp*-band of the free-electron metal aluminium. Both levels are seen to shift down and broaden. The additional structure in the downshifted $5\sigma$ orbital is due to interaction with the $4\sigma$ orbital of CO, which was not included in the figure, making things more complicated without changing the overall effect.

A very similar result is obtained if one lets the CO orbitals interact with the *sp*-band of platinum. The interaction of the $5\sigma$ and $2\pi$ orbitals with the *sp*-band again gives a large and negative contribution, $E_{sp}$, to the bond.

### d-interaction

In Figure 2.12 it is shown that the interaction of $5\sigma$ and $2\pi$ levels of CO with the *d*-electrons leads to the expected splitting into bonding and antibonding orbitals.

The diagram for CO on Pt(111) reveals that the contribution from the $5\sigma$ orbital to the chemisorption bond is small, as $5\sigma$-$5d$ interaction yields a combination of a filled bonding orbitals, and an almost filled antibonding orbital for the chemisorption.

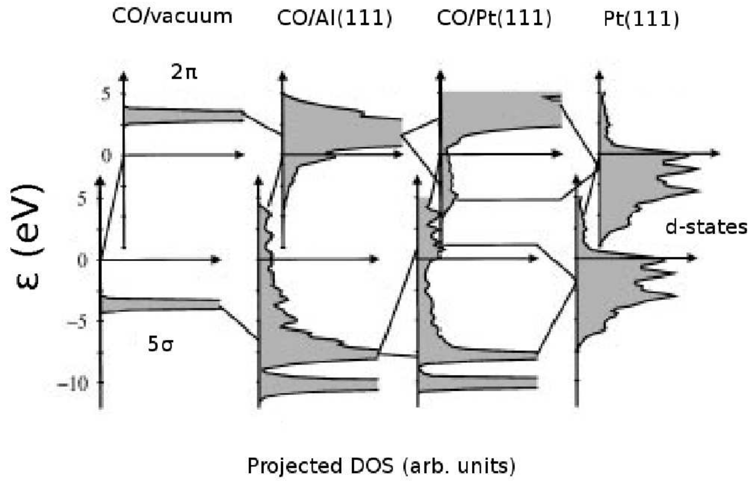

Figure 2.12: Projection of the bonding and antibonding orbitals on the adsorbate levels. Taken from ref. [136].

Whereas the $2\pi$-$5d$ interaction strengthens the bond, as only the bonding region of this orbital is occupied.

With respect to the adsorption energy, it can be estimated in a similar way to that in the case of atomic adsorbates. The hybridisation energy, $\Delta E_{d-hyb}$, includes two terms

$$\Delta E_{d-hyb} = \Delta E^{5\sigma}_{d-hyb} + \Delta E^{2\pi}_{d-hyb} \tag{2.41}$$

The first term of the interaction is attractive, as before adsorption the $2\pi$ orbital is empty, and upon adsorption only the bonding region of the orbital becomes occupied.

The bond strength increases towards left in periodic table, in part because the centre of the $d$-band moves up in energy.

## 2.5 Linear energy relationships

A relation between trends in chemical reactions can often be approximately described by a linear relationship. A very useful procedure to analyse transition state in heterogeneous catalysis relates changes in activation energy for a particular elementary reaction step, $E_a$, with changes in the overall reaction enthalpy for that step, $\Delta H$, over a family of similar catalytic materials. This is the Bell-Evans-Polanyi, BEP, relationships.

$$E_a = a\Delta H + b \tag{2.42}$$

with $a$ and $b$ constants that describe the linear correlation. Recently such linear energy relations have also been called Brønsted-Evans-Polanyi relations, acknowledging the fact that Brønsted was the first to introduce linear free-energy relations in chemistry.[137, 138]

The Hammond Principle [139] is a way of thinking about the connection between transition barrier and reaction enthalpy. In highly exothermic reactions, the transition state is structurally similar to the reactants and in highly endothermic reactions the product is a better model of the transition state. The postulate has been rationalised by different methods, often based on curve-crossing models or valence-bond descriptions.[140] For instance, Marcus equation derives the Hammond postulate specifically for electron transfer reactions,[141, 142] see Figure 2.13.

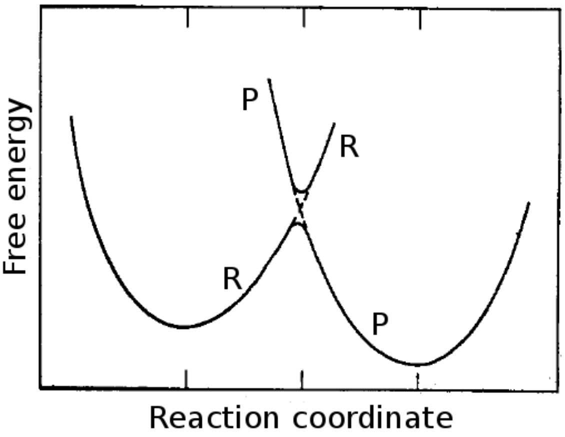

Figure 2.13: Free energy of reactants and products (R and P curves respectively) versus the reaction coordinate. The three vertical lines on the abscissa denote, from left to right, the value for reactants, for the transition state, and for the products. Taken from ref. [142].

A good catalyst is characterised by a low activation energy and weak bonding of the intermediates. When the interaction between product molecules and catalyst becomes too strong, the desorption of product molecules becomes rate limiting. The rate will then decrease with increasing interaction energy of product with the catalysis. Because $E_a$ and $\Delta E$ are often correlated, the best catalyst is a compromise between both factors. This is known as the Sabatier principle.

Calculations based on Density Functional Theory, DFT, shed light on the reasons behind Sabatier's principle in reactions when dissociation is the essential step in the reaction mechanism. These reactions have two main parts: the dissociation of the reacting molecules and the removal of the dissociation products. The rate of dissociation is determined by the activation barrier for dissociation, $E_a$, while the rate of product removal is given largely by the stability, $\Delta E$, of the intermediates on the surface.

This balance results in a volcano-type plot of rate against reaction-interaction strength whereby the rate increases up to a particular interaction strength known as the Sabatier maximum and then decreases, see Figure 2.14. The rate of a catalytic reaction is maximised at an optimum interaction strength of the reactants with catalyst. This provides a rational strategy for the optimisation of catalytic rates, being possible select surface that might improve catalytic performance.

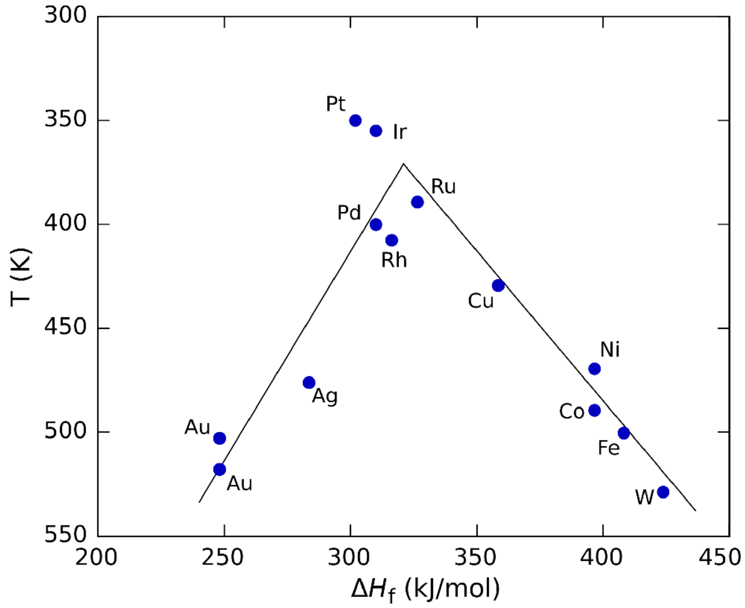

Figure 2.14: Volcano plot for the decomposition of formic acid on transition metals. Adapted from ref. [143].

Nørskov and coworkers proved that the activation energy for dissociation, $E_a$, versus the adsorption energy of the dissociated atoms, $\Delta E$, give a straight line for small $N_2$, CO, NO and $O_2$ molecules.[144] The transition states for the heterogeneously catalysed dissociation of $N_2$, CO, NO and $O_2$, determined by nudged elastic band DFT calculations, resemble each other for all the diatomic molecules, and all strongly resemble the dissociated final state. The consequence is that the correlation between transition state potential energy, and the dissociative chemisorption energy turns out to be the same for all the diatomic molecules for a given surface geometry. Figure 2.15 shows the universal BEP-relationships both for close packed surfaces and for stepped surfaces.

The universality principle has significant implications for the understanding of optimal catalysts. The microkinetics of different heterogeneous catalytic reactions which include the dissociation of diatomic molecules could be closely related.

More recently, Abild *et al.* found that the adsorption energy of the molecules $AH_x$ ($CH_x$, with $x$= 0,1,2,3, $NH_x$ with x= 0,1,2, $OH_x$ with $x$= 0,1, and $SH_x$ with $x$= 0,1), $\Delta E^{AH_x}$, scales approximately with the adsorption energy of the central atom, $\Delta E^A$ (A is C, N, O or S atom), on a range of close packed and stepped metal surfaces.[145]

$$\Delta E^{AH_x} = \gamma \Delta E^A + \xi \tag{2.43}$$

The scaling constant is found to depend only on x, $\gamma$(x)

$$\gamma(x) = \frac{x_{max} - x}{x_{max}} \tag{2.44}$$

where $x_{max}$ is the maximum number of H atoms that can bond to the central atom

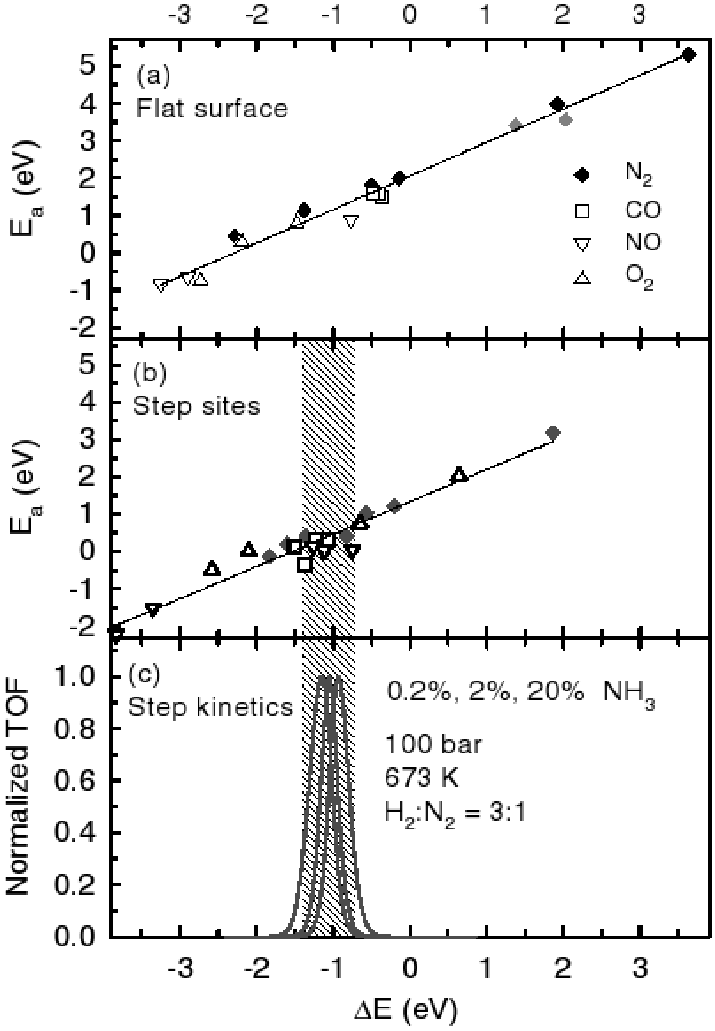

Figure 2.15: Calculated activation energies, $E_a$ for $N_2$, CO, NO and $O_2$ dissociation on a number of different metals plotted as a function of the calculated dissociative chemisorption potential energy for the dissociation products, $\Delta E$. Taken from ref. [144].

A ($x_{max}$= 4 for A = C, $x_{max}$= 2 for A = O, S). By combining this model with the Bell-Evans-Polanyi correlations between activation barriers and reaction energies for surfaces reactions, Equation 2.42, it is possible to estimate the full potential energy diagram for a surface catalysed reaction for any transition metal on the basis of the C, N, O and S chemisorption energies. A similar scaling relationships was found on the adsorption of O, OH, S, SH, N, NH, and $NH_2$ on a range of transition metals oxide, sulfide, and nitride surfaces.[146] The Equation 2.43 is verified, with A = O, S or N. The scaling constant depends on x, through the Equation 2.44, with $x_{max} = 2$ for A = O, S, and $x_{max} = 3$ for A = N. Several groups have been focused on the extensive development of BEP-like relationships, for instance, Honkala *et al.* studied the reaction pathways for different processes involving the the hydrogenation-dehydrogenation, decomposition and isomerisation of organic moieties derived from ethylene on two Pd surfaces (111) and (211). In this study was found that the dehydrogenation steps of ethylene on Pd, seem to follow the Brønsted-Evans-Polanyi type of behaviour.[147] The similar slope of the linear relationships seems to indicate that the reaction is not strongly dependent on the surface, while differences in the reaction energies for particular steps might indicate some kind of structure sensitivity.

## 2.6 Microkinetic Models

In this section the kinetics of the general catalytic reaction will be analysed:

$$A + B \longrightarrow AB \tag{2.45}$$

In Langmuir-Hinshelwoods kinetics it is assumed that all species are adsorbed and accommodated with the surface before they take part in any reaction. This is the prevailing situation in heterogeneous catalysis, and the kinetic reaction will be described according to this behaviour. The catalytic reaction must be thermodynamically and stoichiometrically consistent. For instance the number of active sites ($*$ in the Equations 2.46-2.49) consumed in the adsorption and dissociation steps must be equal to the number of sites liberated in the formation and desorption steps.

Writing out the catalytic reaction between $A$ and $B$ in elementary steps we obtain.[80]

$$A^{gas} + * \longleftrightarrow A^* \qquad (k_1^+, k_1^-) \tag{2.46}$$

$$B^{gas} + * \longleftrightarrow B^* \qquad (k_2^+, k_2^-) \tag{2.47}$$

$$A^* + B^* \longleftrightarrow AB^* + * \qquad (k_3^+, k_3^-) \tag{2.48}$$

$$AB^* \longleftrightarrow AB^{gas} + * \qquad (k_4^+, k_4^-) \tag{2.49}$$

Each step can be characterised by $K_i=k_i^+/k_i^-$ ($i$=1,..., 4), where $k_i^+$ describes the adsorption and $k_i^-$ the desorption of each step. The corresponding rate for Equations 2.46-2.49 can be written as function of that constants

$$r_1 = k_1^+ p_A \Theta^* - k_1^- \Theta_A \tag{2.50}$$

$$r_2 = k_2^+ p_B \Theta^* - k_2^- \Theta_B \tag{2.51}$$

$$r_3 = k_3^+ \Theta_A \Theta_B - k_3^- \Theta_{AB} \Theta^* \tag{2.52}$$

$$r_4 = k_4^+ \Theta_{AB} - k_4^- p_{AB} \Theta^* \tag{2.53}$$

Where $p_A$, $p_B$ are the pressures of the reactants, $p_{AB}$ is the pressure of the product, and $\Theta^*$ is the fraction of the active sites that are free. The number of sites ($*$) on a catalyst is constant and hence all coverages should always add up to unity, as expressed by the following balance of sites:

$$\Theta^* + \Theta_A + \Theta_B + \Theta_{AB} = 1 \tag{2.54}$$

To solve the kinetics for the most general case is necessary solve numerically the full set of differential equations describing the coverage of all species participating in the reaction, without making any approximations in the system. But some approximations can be applied:[80]

- *The steady state approximation.* A constant flow of reactants leads to a constant output of products therefore the differential equations describing the coverage of all species are equal to zero.

- *The quasi-equilibrium approximation.* One elementary step is assumed to determine the rate while all others steps are sufficiently fact that they can be considered as being in quasi-equilibrium.

- *The irreversible step approximation.* The reverse reaction of one of several steps is neglected.

- *The MARI approximation.* One of the intermediates adsorbs so strongly in comparison to the other participants that it completely dominates the surface. This intermediate is called the MARI.

- *Nearly empty surface.* The intermediates are bound very weakly or the temperature is high enough for the equilibrium to be shifted sufficiently towards the gas phase. The surface is mostly empty, $\Theta^* \simeq 1$.

The constants $k_i^+$ and $k_i^-$ can be obtained with the Transition State Theory, TST. Transition State Theory is based on the concept that reacting molecules acquire energy by collisions with surrounding molecules, reaching an activate state, the transition state, located at the top of the energy barrier between reactants and products, from which the products forms. While collision theory treats reacting molecules as hard spheres for which the activation barrier is determined only by the kinetic energy upon collision, transition state theory includes the vibrations and rotations of reacting molecules, and also the degrees of freedom that are excited when a reacting complex passes over the activation barrier. The reaction event is described by a single parameter, called the reaction coordinate, which is usually a vibration. The recta's, $R$, are in equilibrium with the transition state, $R^\sharp$, with an equilibrium constant $K^\sharp$. Crossing the barrier, towards the product, $P$, is only possible in the forward direction.

$$R \longleftrightarrow R^\sharp \longrightarrow P \tag{2.55}$$

The rate of reaction from the transition state to the product is taken as the frequency of the reaction coordinate, h$\nu$. The rate of the overall reaction can be expressed in terms of the partition functions of both the reactant, q, and the transition state, $q'^\sharp$, see Section 2.3.

$$\frac{d[P]}{dt} = K^\sharp[R] = \nu\frac{q'^\sharp}{q}[R] \tag{2.56}$$

We can express the partition function of the transition state, $q'^\sharp$, taking the partition function of the reaction coordinate separately, $q_v$.

$$q'^\sharp = q_v q^\sharp \tag{2.57}$$

Therefore,

$$\frac{d[P]}{dt} = \nu q_v \frac{q^\sharp}{q}[R] = \nu\frac{\exp\left(-\frac{h\nu}{2k_BT}\right)}{1-\exp\left(-\frac{h\nu}{k_BT}\right)}\frac{q^\sharp}{q}[R] \tag{2.58}$$

Because the frequency of a weakly bonded vibrating system is relatively small, h$\nu$ $\ll$ k$_B$T we may approximate its partition function by the classical limit k$_B$T/h$\nu$, and arrive at the rate expression in transition state theory

$$\frac{d[P]}{dt} = \frac{k_BT}{h}\frac{q^\sharp}{q}[R] = k_{TST}[R] \tag{2.59}$$

with

$$k_{TST} = \frac{k_BT}{h}\frac{q^\sharp}{q} \tag{2.60}$$

The partition function of transition state can be refereed to its own electronic ground state as

$$q'^{\sharp} = q_v q^{\sharp} = q_v q_0^{\sharp} \exp(-\frac{E_a}{k_B T}) \tag{2.61}$$

Therefore, $k_{TST}$ can be calculated as

$$k_{TST} = \frac{k_B T}{h} \frac{q_0^{\sharp}}{q} \exp{(-\frac{E_a}{k_B T})} \tag{2.62}$$

where $E_a$, is the energy difference between the ground state and the transition state. With the Equation 2.62 the rate expression for elementary surface reactions, such as adsorption, desorption and dissociation can be derived. In Equation 2.62, the term $\frac{k_B T}{h} \frac{q_0^{\sharp}}{q}$ is known as the pre-exponential factor. If the transition state resembles the ground state, a prefactor of desorption of the order of $10^{13}$ s$^{-1}$ is expected ($\frac{k_B T}{h} \frac{q_0^{\sharp}}{q} \simeq 10^{13} s^{-1}$ ). If the adsorbates are mobile in the transition state, the prefactor increases by one or two orders of magnitude. For desorbing molecules, free rotation in the transition state increases the prefactor even further,[135] see Figure 2.16.

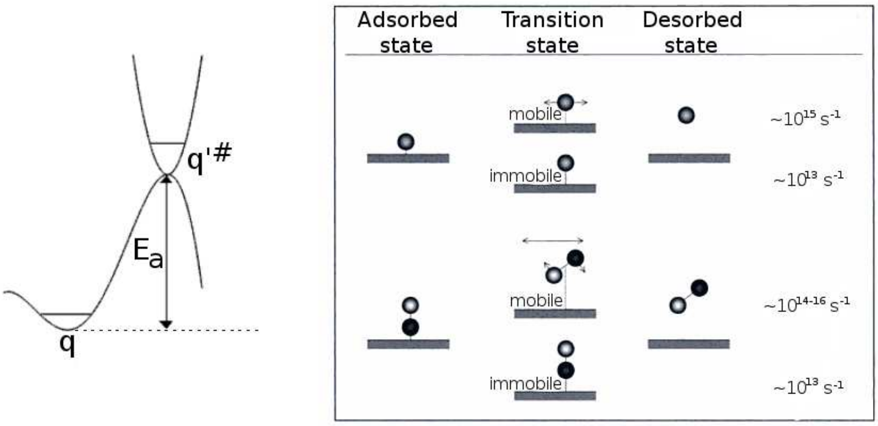

Figure 2.16: Left: The electronic ground state of $q'^{\sharp}$ is shifted $E_a$ upwards respect to $q$. Right: Microscopic pictures of the desorption of atoms and molecules via mobile and immobile transition states. The prefactor expected in each case is indicated in s$^{-1}$. Taken from ref. [135].

# Chapter 3

# CO vibrational spectra: Searching for the right ensemble

Density Functional Theory, DFT, and *ab initio* thermodynamics have been employed in this chapter to analyse the vibrational spectra of CO on different $\mathrm{Pd}_x\mathrm{Au}_{100-x}$, 0< $x$ <50, alloys under different temperatures and pressures. The aim is to identify the fingerprints for adsorption and characterise the ensembles.

## 3.1 Computational details

Density Functional Theory, DFT, applied to slabs has been used to determine the adsorption energies and the stretching frequencies of CO adsorbed on Pd(111) and Au(111) surfaces, and on different $\mathrm{Pd}_{100-x}\mathrm{Au}_x$(111) alloys, 0< $x$ <50. DFT calculations were performed using the Vienna Ab-initio Simulation Package, VASP.[148, 149, 150] The Revised Perdew-Burke-Ernzerhof, RPBE,[124] was employed as exchange-correlation functional to obtain the energy. Monoelectronic states corresponding to valence electrons were expanded in plane waves with a kinetic cut-off energy of 400 eV, while core electrons were represented by Projector Augmented Wave, PAW, pseudopotentials. [151, 152] A dipole layer was placed in the vacuum region separating the slabs, in order to avoid the artificial electrostatic field between the two side of slabs, it appears by the only adsorption on one side of the slab. A finite temperature of $k_BT$= 0.2 eV was used in order to avoid the discontinuous jump in the occupancy of states at the Fermi level at 0 K. All total energies were extrapolated to $k_BT$= 0 eV. No spin polarisation is needed for these systems. The calculated cell parameters needed to this study are compiled in Table A.1 of Appendix A. The (111) monometallic surfaces of Pd and Au were modelled by four-layer slabs with a $p$(2x2) supercell, separated by a 12 Å thick vacuum layer. The top two metal layers were allowed to relax, and the third and fourth layers were fixed to the bulk values in order to represent the bulk of the material. Brillouin zone integrations were performed on a grid of 5x5x1 Monkhorst-Pack $k$-points.[130]

## 3.2 Bimetallic systems

### 3.2.1 Description of the models

In order to study the PdAu bimetallic systems, several structures have been built to model several positions in the phase diagram. The positions have been labelled in Figure 3.1.

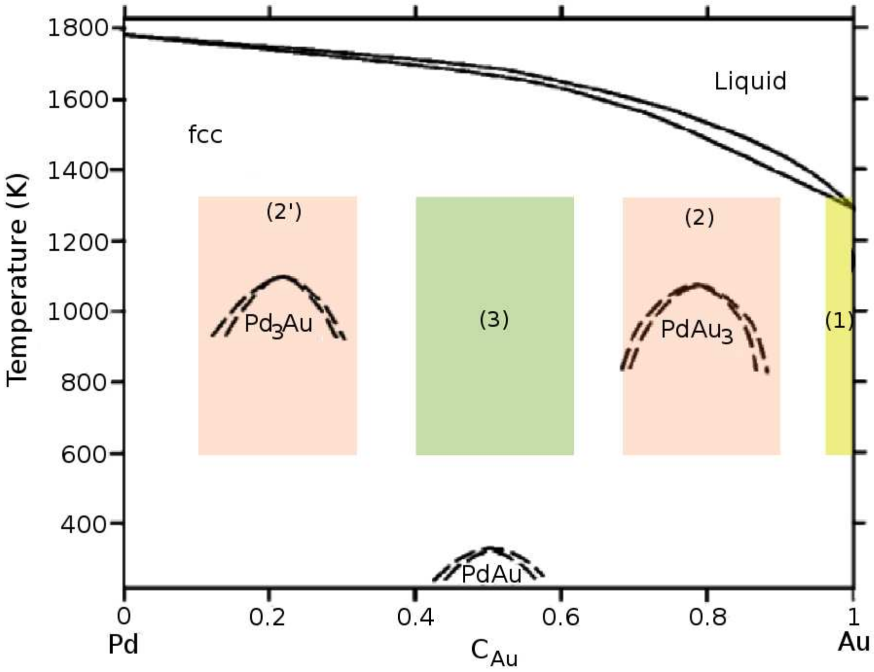

Figure 3.1: PdAu phase diagram, taken from ref. [29]. The positions of the models built have been coloured.

The structures have been represented through three families of models:

- Impurity models where one or a few Pd atoms are immersed in the bulk of Au. Area (1) in Figure 3.1.
- Alloys with $Pd_3Au$ bulk composition (area (2')). Due to the different surface energies of Au and Pd, the $Pd_3Au$ surface is enriched in Au, formally being $PdAu_3$ (area (2)).
- Medium Pd content with 50:50 alloy composition and fcc structure. Area (3).

Impurity models and 50:50 alloys were built with a $p(3x3)$ supercell, and Brillouin zone integrations were performed on a grid of 3x3x1 Monkhorst-Pack $k$-points.[130] Whereas a $p(4x4)$ reconstruction was employed for $PdAu_3$ surface with integrations on a grid of 2x2x1 Monkhorst-Pack $k$-points.

### 3.2.2 Low content Pd alloys: Impurity models

The first family of models for the PdAu(111) system is that of impurities, and represents low Pd concentration alloys. In order to do this, different Pd ensembles have substitute Au atoms on the gold slabs. The structures are represented in Figure 3.2, and show: a subsurface Pd atom: $Pd_{ss}$@Au; surface monomers like: an isolated atom on the surface: Pd@Au; a structure formed by a surface and a subsurface Pd as nearest neighbours: Pd-$Pd_{ss}$@Au; or next-nearest neighbours: Pd+$Pd_{ss}$@Au. Surface dimers like: $Pd_2$@Au; a next-nearest neighbours configuration on the surface: Pd+Pd@Au; a dimer with a subsurface Pd atom: $Pd_2$-$Pd_{ss}$@Au; or next-nearest neighbours with a subsurface Pd atom: Pd+Pd-$Pd_{ss}$@Au. Larger ensembles consisting of three Pd atoms can be formed on the surface: like trimers, $Pd_3$@Au.

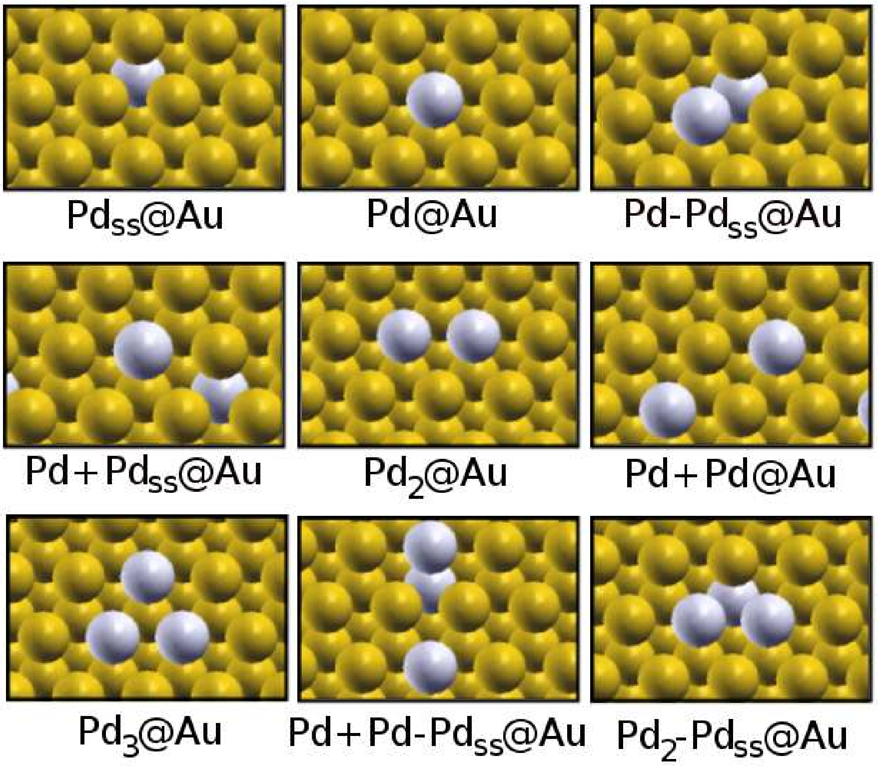

Figure 3.2: Schematic representation of the models representing the Pd impurities on Au. Yellow spheres stand for Au and blue for Pd.

### 3.2.3 $PdAu_3$ surfaces

The low temperature annealing of 5 ML Pd on top of 5 ML Au produces an alloy with a bulk composition for the top layers close to $Pd_3Au$. The calculated cell parameter for $Pd_3Au$ is 4.043 Å. Due to the different surface energies of Au and Pd, the $Pd_3Au$ surface is enriched in Au, formally being $PdAu_3$.[31] This surface, shows isolated Pd

UNIVERSITAT ROVIRA I VIRGILI
THEORETICAL STUDIES OF SELECTIVE PROCESSES IN HETEROGENEOUS CATALYSIS
Mónica García Mota
ISBN:978-84-693-5424-7/DL:T-1415-2010

atoms denoted as Pd@PdAu$_3$. The formation of islands for this alloy has been considered, with configurations including: a dimer: Pd$_2$@PdAu$_3$; and two trimers: triangular Pd$_{3t}$@PdAu$_3$, and linear Pd$_{3l}$@PdAu$_3$, see Figure 3.3.

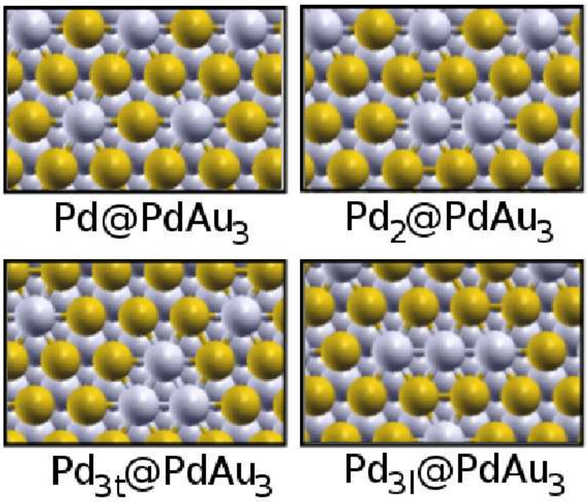

Figure 3.3: Schematic representation of PdAu$_3$(111) surfaces, considering Pd aggregation and island formation. Colour code is that of Figure 3.2.

### 3.2.4 Medium Pd content alloys with 50:50 composition

**Monometallic surfaces, and completely ordered stoichiometric Pd$_{50}$Au$_{50}$ alloys**

The 50:50 alloy composition is studied with different models formed by a layer-by-layer growth, see Figure 3.4. The first model contains two Pd overlayers on a Au surface, 2Pd/2Au, denoted as Pd/Au (Au cell); while the second is the opposite, 2Au/2Pd, indicated as Au/Pd (Pd cell). In these cases, the Pd or Au overlayers have been adapted to follow the lattice constant of the metal underneath. The third model shows an alternated Pd/Au/Pd/Au alloy, a-Pd/Au, for which the average lattice constant, 4.099 Å, has been employed. Finally, has been studied an ordered alloy, o-PdAu, in which Pd and Au atoms are alternated, and the cell parameter is that of the average lattice constant.

**Pd ensembles on the Pd$_{50}$Au$_{50}$ surfaces**

The 50:50 alloy composition is also studied with different models formed by a layer-by-layer growth allowing tridimensional rearrangements, see Figure 3.5. The first model consists on two Pd layers sandwiched with two external Au layers, Au/2Pd/Au denoted as PdAu (A); and the second contains two gold layers on palladium, 2Au/2Pd, indicated as PdAu (B). In both cases the average cell parameter, 4.099 Å, was employed. Different

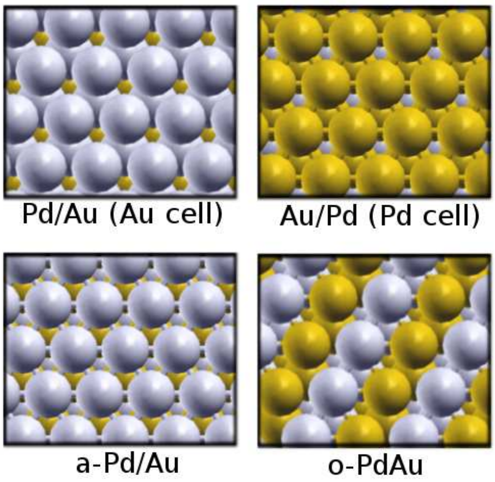

Figure 3.4: Schematic representation of layer-by-layer, and completely ordered stoichiometric $Pd_{50}Au_{50}$ (111) alloys.

Pd ensembles can be modelled on the PdAu surface on both (A) and (B) alloys: isolated Pd atoms: Pd@PdAu; dimers: $Pd_2$@PdAu; and trimers: $Pd_3$@PdAu.

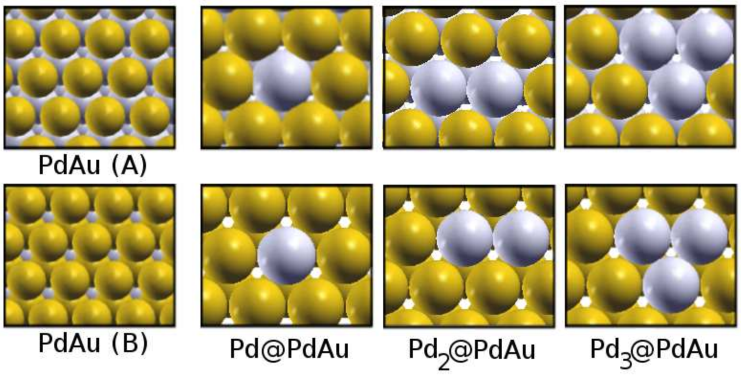

Figure 3.5: Schematic representation of $Pd_{50}Au_{50}$ alloys. Top panel: PdAu (A), and lower panel: PdAu (B). Tridimensional alloys containing singletons, Pd@PdAu; dimers, $Pd_2$@PdAu; and trimers, $Pd_3$@PdAu; are represented.

### 3.2.5 Surface relaxation

The surface relaxation for monometallic and bimetallic models is compiled in Table 3.1. Appendix A, deals in depth with surface energy, $\gamma$, and surface relaxation, %, calculated for the monometallic surfaces.

| System | % |
|---|---|
| Pd | -0.78 |
| Au | -0.38 |
| Pd@Au | -5.24 |
| Pd-Pd$_{ss}$@Au | -4.42 |
| Pd+Pd$_{ss}$@Au | -3.99 |
| Pd$_2$@Au | -4.38 |
| Pd+Pd@Au | -5.77 |
| Pd$_3$@Au | -5.82 |
| Pd+Pd-Pd$_{ss}$@Au | -5.78 |
| Pd$_2$+Pd$_{ss}$@Au | -5.23 |
| Pd@PdAu$_3$ | -0.29 |
| Pd$_2$@PdAu$_3$ | -0.91 |
| Pd$_{3t}$@PdAu$_3$ | -1.90 |
| Pd$_{3l}$@PdAu$_3$ | -1.79 |
| Pd/Au (Au cell) | -15.32 |
| Au/Pd (Pd cell) | +20.19 |
| a-Pd/Au | -1.11 |
| o-PdAu | +0.18 |
| Pd@PdAu (A) | -3.24 |
| Pd@PdAu (B) | +6.21 |
| Pd$_2$@PdAu (A) | -3.51 |
| Pd$_2$@PdAu (B) | +6.44 |
| Pd$_3$@PdAu (A) | -3.70 |
| Pd$_3$@PdAu (B) | +6.69 |

Table 3.1: Relaxation calculated as, $\frac{Z_{s-relax}-Z_{s-unrelax}}{d_{(111)interplanar}} * 100$, for each alloy.

The results show that the relaxation way is related to the strain and stress effects. When the overlayer is strained (Pd low-content alloys, Pd/Au (Au cell), a-Pd/Au, and the medium Pd content alloys PdAu(B)), the surface relaxation is outwards, otherwise the relaxation is inwards.

### 3.2.6 Stability of the bimetallic systems

The study of the relative stability of each alloy has been analysed through different energy parameters including: formation, segregation and aggregation energies, and $d$-band shift.

### Formation energy

The study of the relative stability of the alloys can be performed through the analysis of the formation energy per atom, $\Delta E^f$.

$$\Delta E^f = (E_{alloy} - N_{Pd}E_{bulkPd} - N_{Au}E_{bulkAu})/(N_{Au} + N_{Pd}) \tag{3.1}$$

Alloy stability results are shown in Table 3.2. $\Delta E^f$ of the different alloys is always positive due to the formation of both surfaces in the slabs. $\Delta E^f$ ranges from 0.08 to 0.20 eV/atom depending on the composition and configuration.

The relative stability for the low-content Pd alloys is very similar, and the formation energy lays in narrow energy interval: from 0.12-0.14 eV/atom. The formation energy for alloys containing the $PdAu_3$ surface is found to be 0.14 eV/atom. For the tridimensional alloys containing singletons: Pd@PdAu; dimers: $Pd_2$@PdAu; and trimers: $Pd_3$@PdAu, the stability results are strongly dependent on the subsurface layer composition. The most likely configurations are those where Pd atoms are surrounded by Au atoms: alloys labelled (B) have higher $\Delta E^f$ values with respect to alloys labelled (A). In the same way, layer-by-layer alloys present higher $\Delta E^f$ values than completely ordered stoichiometric $Pd_{50}Au_{50}$ alloys.

## 3.2.7 Electronic structure

Both the presence of heterogeneous metal neighbours, and mechanical perturbations (stress or strain) of the Pd atoms in the alloys with gold, affect the overlap of the electronic orbitals, and therefore modify the electronic properties of the surface and its reactivity. Although the degree of $d$-band filling remains the same, the width of the $d$-band, and the energy of its centre, $\varepsilon_d$, changes as the overlap is perturbed.

The centre of $d$-band is calculated as the average of the integration of the density of states below Fermi level weighted by their energy. The units are number of states/unit cell. The shifts of the Pd $d$-band centre, $\Delta\varepsilon_d$, for each alloy respect to pure Pd have been calculated as the difference between $\varepsilon_d$ for metal surface alloy, $\varepsilon_{d-alloy}$, and $\varepsilon_d$ for pure Pd, $\varepsilon_{d-Pd}$=-1.54 eV. This is:

$$\Delta\varepsilon_d = \varepsilon_{d-alloy} - \varepsilon_{d-Pd} \tag{3.2}$$

$d$-band shifts are reported in Table 3.2. The shift is almost always positive (towards the Fermi level) and amounts between 0.05 and 0.30 eV. This means that the binding of CO will be more favourable than to the same ensemble on the clean Pd surface. The only exceptions are $Pd_2$@PdAu (B) and $Pd_3$@PdAu (B) for which a small negative (stabilising) value is found.

## 3.2.8 Segregation energies

The segregation energy, $E_{seg}$, measures how much energy it costs that one Pd atom emerges from the bulk to the surface. The segregation energy for the Pd impurity is

| Alloy | $\Delta E^f$ | $\Delta\epsilon_d$ | $E_{seg}$ | $E_{agg}$ |
|---|---|---|---|---|
| Pd@Au | +0.12 | +0.07 | +0.29 | – |
| Pd-Pd$_{ss}$@Au | +0.12 | +0.08 | – | +0.10 |
| Pd+Pd$_{ss}$@Au | +0.12 | +0.05 | – | +0.06 |
| Pd$_2$@Au | +0.13 | +0.08 | – | +0.10 |
| Pd+Pd@Au | +0.13 | +0.06 | – | +0.05 |
| Pd$_3$@Au | +0.14 | +0.15 | – | +0.18 |
| Pd+Pd-Pd$_{ss}$@Au | +0.13 | +0.14 | – | +0.09 |
| Pd$_2$-Pd$_{ss}$@Au | +0.13 | +0.07 | – | +0.17 |
| Pd@PdAu$_3$ | +0.14 | +0.02 | +0.0 | – |
| Pd$_2$@PdAu$_3$ | +0.14 | +0.14 | – | -0.02 |
| Pd$_{3t}$@PdAu$_3$ | +0.14 | +0.06 | – | +0.06 |
| Pd$_{3l}$@PdAu$_3$ | +0.14 | +0.02 | – | +0.04 |
| Pd/Au | +0.20 | +0.30 | – | – |
| Au/Pd | +0.15 | – | – | – |
| a-Pd/Au | +0.13 | +0.23 | – | – |
| o-PdAu | +0.12 | +0.20 | – | – |
| Pd@PdAu (A) | +0.08 | +0.17 | +0.01 | – |
| Pd@PdAu (B) | +0.18 | +0.05 | -0.17 | – |
| Pd$_2$@PdAu (A) | +0.09 | +0.10 | – | +0.12 |
| Pd$_2$@PdAu (B) | +0.17 | -0.01 | – | +0.03 |
| Pd$_3$@PdAu (A) | +0.09 | +0.15 | – | +0.41 |
| Pd$_3$@PdAu (B) | +0.17 | -0.04 | – | +0.12 |

Table 3.2: Alloy formation energies, $\Delta E^f$, with respect to bulk Au and Pd metals; shift of the Pd *d*-band, $\Delta\epsilon_d$; and segregation energies and aggregation, $E_{seg}$ and $E_{agg}$. See text for definitions. All the energies are in eV except for $\Delta E^f$, in eV/atom.

calculated as

$$E_{seg} = E_{Pd@Au} - E_{Pd_{ss}@Au} \tag{3.3}$$

The segregation value obtained is +0.29 eV. For the formation of monomers on the surface, Pd@PdAu(A) and Pd@PdAu(B), the segregation energy has been obtained as

$$\begin{aligned} E_{seg} &= E_{Pd_N@PdAu(A)} - E_{Pd_{ss}@PdAu(A)} \\ E_{seg} &= E_{Pd_N@PdAu(B)} - E_{Pd_{ss}@PdAu(B)} \end{aligned} \tag{3.4}$$

where $E_{Pd_N@PdAu}$ is the energy of the slab containing a dimer (or trimer) on the surface and $E_{Pd_{ss}@PdAu}$ is the energy of the slab with a single Pd atom on the subsurface. A negative segregation energy suggests surface segregation, while positive segregation energy implies a tendency to sink into the bulk. For the alloy Pd@PdAu (A), (Au/2Pd/Au), the segregation energy is positive, +0.01 eV, while it is negative, -0.17 eV, for the alloy Pd@PdAu (B), (2Au/2Pd). This effect can be explained by the fact that the number of heterometallic (Au-Pd) contacts in the segregated structures of (B) composition is larger than that of (A). The segregation energies obtained are compiled in Table 3.2. Our surface energy results are in agreement with the study of surface segregation energies in transition-metal alloys developed by Ruban *et al.*[153]

### 3.2.9 Aggregation energies

Aggregation energy, $E_{agg}$, measures the tendency of the alloy to generate Pd ensembles on the surface. For low-content Pd alloys, the aggregation energies for the impurity on the surface are also reported in Table 3.2. The aggregation energy is obtained as

$$E_{agg} = E_{Pd_N@Au} + (N_{Pd} - 1)E_{Au} - N_{Pd}E_{Pd@Au} \tag{3.5}$$

where $E_{Pd_N@Au}$ is the energy of the configuration with the dimer (trimer), $E_{Au}$ is the energy of the gold slab, and $E_{Pd@Au}$ is that of the slab with the Pd impurity on the surface. The aggregation of isolated Pd atoms on Au(111) surfaces is an endothermic process between 0.06-0.18 eV/atom. Therefore, the formation of singletons on the Au surface is thermodynamically favoured. This is in agreement with experimental observations,[30] and with recent theoretical results.[154]

For the layer-by-layer surfaces, PdAu(A) and PdAu(B), the aggregation energy for the formation of dimer and trimer ensembles on the surface, $Pd_2$@PdAu and $Pd_3$@PdAu, has been obtained as

$$E_{agg} = E_{Pd_N@PdAu} + (N_{Pd} - 1)E_{PdAu} - N_{Pd}E_{Pd@PdAu} \tag{3.6}$$

The formation of aggregates is found to be more energy demanding for the alloys with (A) configuration than for those with (B) configuration. This effect can be explained by the fact that the number of heterometallic (Au-Pd) contacts in the segregated structures of (B) composition is larger than that of (A), up to 0.41 eV.

For $PdAu_3$ models, in the normal termination more than a single Pd atom is found in the supercell surface. Therefore, aggregation energies have been calculated as

$$E_{agg} = E_{Pd_N@PdAu_3} - E_{Pd@PdAu_3} \tag{3.7}$$

where the first energy, $E_{Pd_N@PdAu_3}$ corresponds to the island, and the second, $E_{Pd@PdAu_3}$ to the initial configuration with 4 surface Pd atoms per $p$(4x4) supercell. The formation of dimer on the surface stabilizes the alloy by 0.02 eV, while the formation of larger ensembles, $Pd_{3t}$@$PdAu_3$ and $Pd_{3l}$@$PdAu_3$, is endothermic by 0.04-0.06 eV.

## 3.3 Molecular CO

The isolated CO molecule was calculated in an asymmetric box of 7.0 x 7.5 x 8.0 Å$^3$ size, at Γ point only.[130] The C-O distance is 1.144 Å in comparison to an experimental

UNIVERSITAT ROVIRA I VIRGILI
THEORETICAL STUDIES OF SELECTIVE PROCESSES IN HETEROGENEOUS CATALYSIS
Mónica García Mota
ISBN:978-84-693-5424-7/DL:T-1415-2010

value of 1.128 Å.[155] The CO frequencies have been obtained through the harmonic approximation, these were calculated using finite differences with three displacements for each degree of freedom of CO, with a step of 0.02 Å, then the Hessian matrix were obtained and diagonalised. With this set up the harmonic calculated gas-phase CO stretching frequency is found to be $\nu$=2120 cm$^{-1}$, which is smaller than experimental estimate, 2170 cm$^{-1}$, but in reasonable agreement with previous theoretical results (2140-2112 cm$^{-1}$).[21, 156] In order to study the experimental spectra, calculated values will be scaled by 1.023, then denoted by $\overline{\nu}$, in Section 3.6. This correction factor has been chosen such that the gas-phase calculated CO stretching frequency matches the corresponding experimental value.

## 3.4 CO adsorption

This section deals the adsorption of CO on the above described monometallic and bimetallic slabs. Adsorption energies, geometric structures and frequencies were calculated with the molecule occupying different adsorption sites. The adsorption was allowed on only one side of the slab, and both CO and the two outermost metal layers were allowed to relax.

In Figure 3.6 the special adsorption sites on (111) surface are labelled with a shorthand notation: *t*, on-top; *fcc*, *hcp*, three-fold hollows.

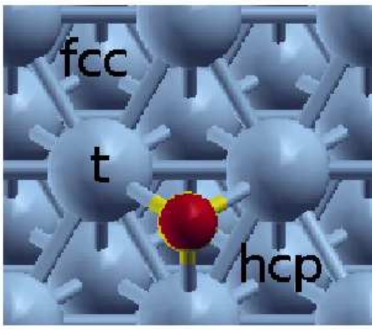

Figure 3.6: Adsorption sites on (111) surface. *t* stands for on-top, and *fcc* and *hcp* are threefold hollow sites.

### 3.4.1 CO adsorption on Pd and Au monometallic surfaces

CO adsorption on different models has been considered. For Au, the surface coverage considered is $\theta_{CO} = 0.25$ ML (CO-Au $p$(2x2)). The inertness of gold has been confirmed by the weak binding energy of CO and therefore, a model for a step (211) has been devised to obtain the corresponding CO binding energies and frequencies. In contrast, CO adsorption on Pd is rather strong and leads to the formation of low-coverage structures, $\theta_{CO} = 0.25$ ML (CO-Pd $p$(2x2)), but also other at high coverage, $\theta_{CO} = 0.75$ ML (3CO-Pd $p$(2x2)).[156]

Table 3.3 compiles adsorption energies, main distances, and the intra-molecular stretching for the CO adsorption on Pd and Au(111). The molecular adsorption energy, $E_{ads}$, has been calculated as the energy of the metal with a CO adsorbed, $E_{CO^*}$, respect to the energy of the clean surface, $E_{clean}$, and the energy of CO in gas phase, $E_{CO^{gas}}$. Negative values indicate exothermic processes.

$$E_{ads} = E_{CO^*} - E_{clean} - E_{CO^{gas}} \tag{3.8}$$

| | site | $E_{ads}$ | $d_{C-O}$ | $d_{C-X}$ | $\nu_{CO}$ |
|---|---|---|---|---|---|
| Au | top | -0.03 | 1.151 | 2.050 | 2046 |
| Au(211) | top | -0.34 | 1.152 | 2.004 | 2038 |
| Pd | *top* | -1.18 | 1.157 | 1.864 | 2046 |
| Pd | fcc | -1.72 | 1.189 | 2.085 | 1798 |
| Pd | hcp | -1.72 | 1.190 | 2.079 | 1791 |
| Pd | *bridge* | -1.43 | 1.179 | 2.004 | 1870 |
| 3CO-Pd | fcc+hcp+top | -1.12 | 1.171 | 2.055 | 2074/1864/1798 |

Table 3.3: CO adsorption energies on Pd and Au(111), $E_{ads}$, in eV/CO molecule; the molecular bond length, $d_{C-O}$ in Å; the average distance of C to the surface metal atoms, $d_{C-X}$ in Å; and the intra-molecular stretching, $\nu_{CO}$, in cm$^{-1}$. The metastable sites have been written in italics.

The theoretical results shows the preference for CO adsorption, at low coverage, on hollow sites for Pd. The adsorption is very exothermic, -1.72 eV and the CO vibrational frequency found is around 1790 cm$^{-1}$. The stronger adsorbate-surface interaction on hollow sites leads to a slightly more pronounced stretching of the C-O bond length, $\sim$ 1.190 Å, compared to its value in the gas phase molecule, $d_{CO}^{gas}$= 1.144 Å. At high coverage, a 3CO-Pd $p$(2x2) structure is found, the average CO adsorption energy is -1.12 eV/CO molecule, and fcc, hcp and top sites are simultaneously occupied. Three stretching frequencies are obtained in the 2074 to 1789 cm$^{-1}$ range. Our results are in agreement with previously reported values,[156] and with the spectrum found by Goodman *et al*,[24] shown in Figure 3.7.

On gold, CO bonds through the carbon atom to the on-top site in an upright geometry. CO is very weakly adsorbed on the Au surface, $|E_{ads}| < 0.05$ eV, while a larger value is obtained on the Au(211) step, $E_{ads}$ =-0.34 eV, and thus the stretching frequency does not change significantly from the gas-phase value, $\nu_{CO}^{gas}$= 2170 cm$^{-1}$. These theoretical results are in agreement with the spectrum shown in Figure 3.8.

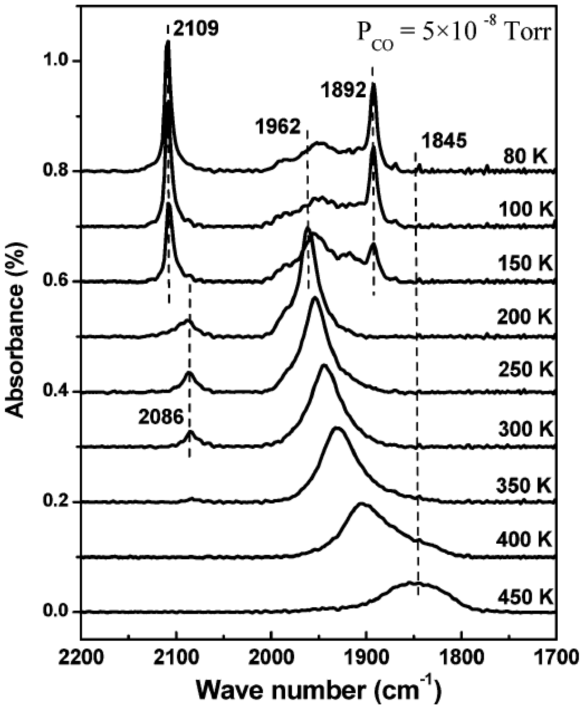

Figure 3.7: IRAS spectra for CO adsorption on a 10 ML Pd/Mo(111) surface as a function of temperature. Taken from [24].

### 3.4.2 CO adsorption on bimetallic surfaces

#### CO adsorption on the low Pd-content alloys: impurities

For the CO adsorption on the impurities, Figure 3.2, a large dispersion in adsorption energies and vibrational frequencies is found, see Table 3.4.

With respect to low CO coverages, the binding energy to the isolated impurity (singleton) is lower than to the dimer and trimer. The energies for on-top adsorption are about -0.93 eV and increase to -1.75 eV for the trimer (fcc site), thus showing the important ensemble effect that affects CO adsorption. The value for the fcc site is slightly larger than that obtained for the Pd(111) surface (Table 3.3), as expected from the *d*-band centre shift found (Table 3.2). With respect to the CO stretching frequencies, the values obtained for the impurities are lower than the CO-gas ones (blue shifted). Thus, for low CO coverages the changes in binding energies and stretching frequencies of CO to the surface are mainly due to the change of the ensemble and three different sets are observed: about 2030 (top), 1850 (bridge) and 1768 cm$^{-1}$ (three-fold).

It is important to note that the alloys with one Pd placed in the subsurface layer, Pd-Pd$_{ss}$@Au, Pd+Pd$_{ss}$@Au and Pd$_2$-Pd$_{ss}$@Au, present higher CO adsorption energy than those without Pd in the subsurface layer. However, stretching frequencies of CO are similar in both cases. Therefore, the IRAS study for these alloys would give us

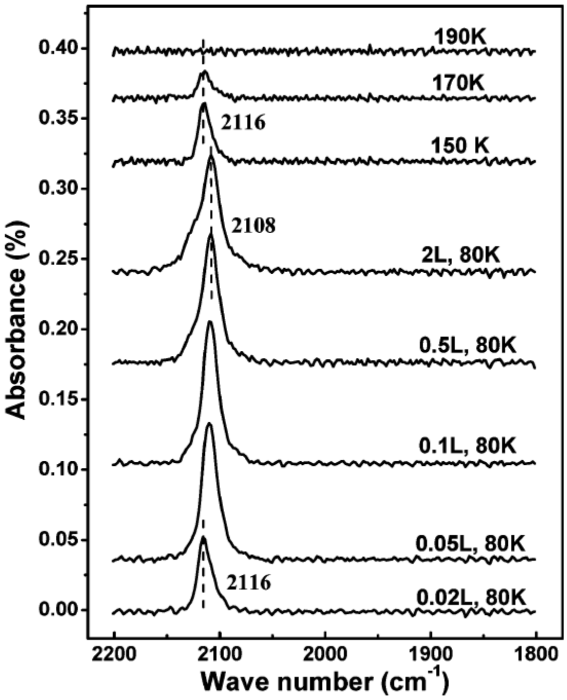

Figure 3.8: IRAS spectra for CO adsorption on a 10 ML Au/Mo(111) surface at the indicated exposures and temperatures. Taken from [24].

information about the ensembles on the surface but temperature programmed desorption, TPD, would be necessary in order to know if the subsurface atoms are present in the ensemble.

Under higher pressures, the larger ensembles might be able to adsorb more than a single CO molecule. In that case, the average binding energy per CO molecule is slightly smaller than for a single molecule at the same ensemble but the total energy gain is larger, see Table 3.4. With high CO contents, the stretching frequencies are in the range 2049-2010 cm$^{-1}$, corresponding to the vibrations for a single CO molecule on a top site. The splitting into two (or three) frequencies corresponds to the dipole-dipole interactions and amounts to about 40 cm$^{-1}$.

### CO adsorption on Pd sites at the PdAu$_3$ surfaces

In Table 3.5 it is showed the CO adsorption on Pd sites at the ordered PdAu$_3$ alloy, represented in Figure 3.3. For the Pd@PdAu$_3$ alloy only CO adsorption on Pd is possible, and the binding energy to the singleton is 0.96 eV. This value is lower that to the dimer, 1.15 eV, and trimer, 1.50 eV. The stretching frequencies of CO are 2027 (top), 1857 (bridge) and 1768 cm$^{-1}$(three-fold). Multiple CO adsorption is also possible for these alloys.

| Alloy | site | $E_{ads}$ | $d_{C-O}$ | $d_{C-X}$ | $\nu_{CO}$ |
|---|---|---|---|---|---|
| **CO low coverage** | | | | | |
| Pd@Au | top | -0.93 | 1.156 | 1.907 | 2032 |
| Pd-Pd$_{ss}$@Au | top | -1.14 | 1.157 | 1.904 | 2030 |
| Pd+Pd$_{ss}$@Au | top | -1.17 | 1.157 | 1.903 | 2031 |
| Pd$_2$@Au | *top* | -1.11 | 1.156 | 1.891 | 2041 |
| Pd$_2$@Au | bridge | -1.37 | 1.178 | 2.026 | 1850 |
| Pd$_3$@Au | *top* | -1.11 | 1.156 | 1.888 | 2035 |
| Pd$_3$@Au | fcc | -1.75 | 1.192 | 2.090 | 1768 |
| Pd$_2$-Pd$_{ss}$@Au | *top* | -1.10 | 1.155 | 1.890 | 2041 |
| Pd$_2$-Pd$_{ss}$@Au | bridge | -1.40 | 1.179 | 2.021 | 1850 |
| **CO high coverage** | | | | | |
| Pd$_2$@Au | 2*top | -0.97 | 1.156 | 1.915 | 2043/2012 |
| Pd+Pd@Au | 2*top | -1.01 | 1.156 | 1.910 | 2044/2022 |
| Pd$_3$@Au | 3*top | -0.94 | 1.156 | 1.911 | 2049/2010/2010 |
| Pd+Pd-Pd$_{ss}$@Au | 2* top | -1.05 | 1.156 | 1.898 | 2051/2030 |
| Pd$_2$-Pd$_{ss}$@Au | 2*top | -1.00 | 1.156 | 1.901 | 2045/2016 |

Table 3.4: Adsorption energy, $E_{ads}$ in eV/CO molecule; molecular bond length, $d_{C-O}$ in Å; distance of the carbon atom to the surface metal atoms, $d_{C-X}$ in Å; and intra-molecular stretching frequency, $\nu_{CO}$ in cm$^{-1}$; for CO on the available sites on the low Pd-content alloys. As previously, italics are employed for metastable adsorption sites.

| Alloy | site | $E_{ads}$ | $d_{C-O}$ | $d_{C-X}$ | $\nu_{CO}$ |
|---|---|---|---|---|---|
| **CO low coverage** | | | | | |
| Pd@PdAu$_3$ | top | -0.96 | 1.156 | 1.904 | 2027 |
| Pd$_2$@PdAu$_3$ | bridge | -1.15 | 1.179 | 2.014 | 1857 |
| Pd$_{3t}$@PdAu$_3$ | fcc | -1.50 | 1.192 | 2.074 | 1768 |
| **CO high coverage** | | | | | |
| Pd$_2$@PdAu$_3$ | 2*top | -0.88 | 1.156 | 1.910 | 2033/2012 |
| Pd$_2$@PdAu$_3$ | 2*bridge | -0.78 | 1.170 | 2.101 | 1891/1864 |
| Pd$_2$@PdAu$_3$ | 3*bridge | -0.59 | 1.169 | 2.100 | 1916/1882/1871 |
| Pd$_{3l}$@PdAu$_3$ | 3*top | -0.82 | 1.177 | 1.916 | 2032/2009/2000 |
| Pd$_{3l}$@PdAu$_3$ | 2*bridge | -1.08 | 1.174 | 2.051 | 1897/1867 |
| Pd$_{3t}$@PdAu$_3$ | 3*top | -0.83 | 1.157 | 1.909 | 2035/2006/2004 |

Table 3.5: Adsorption energy, $E_{ads}$ in eV/CO molecule; molecular bond length, $d_{C-O}$ in Å; distance of the carbon atom to the surface metal atoms, $d_{C-X}$ in Å; and intra-molecular stretching frequency, $\nu_{CO}$ in cm$^{-1}$; for CO on the available sites at the ordered PdAu$_3$ alloy.

UNIVERSITAT ROVIRA I VIRGILI
THEORETICAL STUDIES OF SELECTIVE PROCESSES IN HETEROGENEOUS CATALYSIS
Mónica García Mota
ISBN:978-84-693-5424-7/DL:T-1415-2010

### CO adsorption on the medium Pd content alloys, $\mathbf{Pd_{50}Au_{50}}$

- **CO adsorption on the layer-by-layer and completely ordered stoichiometric $\mathbf{Pd_{50}Au_{50}}$ alloys**

Table 3.6 compiles the main results for CO adsorption on layered and ordered $Pd_{50}Au_{50}$ alloy. For Au/Pd on the Au side, the binding energy of CO is reduced with respect to that of the Au(111) surface. This indicates that the reduction of the cell parameter and the formation of the heterometallic bond destabilises CO adsorption. In contrast, the adsorption energy of CO on Pd/Au on the fcc site is exothermic by -1.79 eV, thus larger than for the Pd(111) surface. The increase of the binding energy can be traced back to change in the cell parameter. In addition, other electronic effects are likely to be small since the surface Pd nearest neighbours are Pd atoms on the second layer. In the case of a-Pd/Au, CO is less adsorbed than on the clean Pd(111) surface. Electronic effects, i.e. the formation of the Pd-Au alloy, are the main contribution to this change. For the completely ordered o-PdAu structure, the binding energy for on-top adsorption is slightly larger than that found for the impurity. The main reason for such behaviour is that electronic effects (in terms of the number of different metal neighbours) are more important in the case of the impurity. With respect to the calculated frequencies, the presence of different ensembles for Pd/Au and a-Pd/Au, when compared to the completely ordered surface, are responsible for the different values obtained. The effect of lattice expansion and different number of Au neighbours affects the vibrational frequencies only by 5 $cm^{-1}$.

| Alloy | site | $E_{ads}$ | $d_{C-O}$ | $d_{C-X}$ | $\nu_{CO}$ |
|---|---|---|---|---|---|
| Au/Pd | Au | 0.19 | 1.150 | 2.069 | 2060 |
| Pd/Au | *top* | -1.27 | 1.158 | 1.871 | 2043 |
| Pd/Au | fcc | -1.79 | 1.193 | 2.089 | 1770 |
| a-Pd/Au | *top* | -1.03 | 1.158 | 1.877 | 2042 |
| a-Pd/Au | fcc | -1.62 | 1.192 | 2.085 | 1775 |
| o-PdAu | top | -1.04 | 1.157 | 1.891 | 2046 |

Table 3.6: CO adsorption energies, $E_{ads}$ in eV/CO molecule, on the layered and the ordered $Pd_{50}Au_{50}$ alloys. Molecular bond length, $d_{C-O}$ in Å; distance of the carbon atom to the surface metal atoms, $d_{C-X}$ in Å; and intra-molecular stretching frequency, $\nu_{CO}$ in $cm^{-1}$; are reported for CO on the available sites on the each alloy.

- **CO adsorption on Pd ensembles on the $\mathbf{Pd_{50}Au_{50}}$ surface**

On $Pd_{50}Au_{50}$ alloys with Pd atoms on the surface we can study CO adsorption on singletons, dimers and trimers, see Table 3.7.

For all Pd ensembles the binding energy of CO depends on the second layer metal, being larger when Pd are present. Tridimensional alloys adsorb CO more weakly

| Alloy | site | $E_{ads}$ | $d_{C-O}$ | $d_{C-X}$ | $\nu_{CO}$ |
|---|---|---|---|---|---|
| **CO low coverage** | | | | | |
| Pd@PdAu (A) | top | -0.94 | 1.156 | 1.910 | 2031 |
| Pd@PdAu (B) | top | -0.81 | 1.156 | 1.915 | 2107 |
| $Pd_2$@PdAu (A) | *top* | -0.97 | 1.156 | 1.897 | 2030 |
| $Pd_2$@PdAu (A) | bridge | -1.21 | 1.180 | 2.021 | 1835 |
| $Pd_2$@PdAu (B) | *top* | -0.76 | 1.155 | 1.902 | 2042 |
| $Pd_2$@PdAu (B) | bridge | -1.06 | 1.178 | 2.032 | 1849 |
| $Pd_3$@PdAu (A) | *top* | -0.99 | 1.157 | 1.895 | 2023 |
| $Pd_3$@PdAu (A) | fcc | -1.69 | 1.192 | 2.077 | 1765 |
| $Pd_3$@PdAu (B) | *top* | -0.81 | 1.156 | 1.904 | 2032 |
| $Pd_3$@PdAu (B) | fcc | -1.38 | 1.190 | 2.097 | 1779 |
| **CO-high coverage** | | | | | |
| $Pd_2$@PdAu (A) | 2*top | -0.89 | 1.156 | 1.913 | 2040/2010 |
| $Pd_2$@PdAu (B) | 2*top | -0.76 | 1.156 | 1.915 | 2042/2013 |
| $Pd_3$@PdAu (A) | 3*top | -0.89 | 1.157 | 1.913 | 2047/2008/2008 |
| $Pd_3$@PdAu (B) | 3*top | -0.73 | 1.156 | 1.913 | 2048/2010/2010 |

Table 3.7: CO adsorption energy, $E_{ads}$ in eV/CO molecule; molecular bond length $d_{C-O}$ in Å; average distance of the carbon atom to the surface metal atoms $d_{C-X}$ in Å; and intramolecular stretching frequency $\nu_{CO}$ in cm$^{-1}$; on Pd ensembles on the $Pd_{50}Au_{50}$ surface. Italics denote metastable adsorption sites.

than impurities ($Pd_N$@Au) with the exception of the Pd@PdAu($A$) singleton. Frequencies corresponding to on-top adsorption contribute to the band at 2031 cm$^{-1}$ (Pd@PdAu(A)), while smaller bands would appear as a consequence of bridge and three-fold hollow adsorption in the dimer, 1840 cm$^{-1}$ (d-Pd@PdAu(A)), or the trimer, 1770 cm$^{-1}$ (t-Pd@PdAu(A)). Again, ensembles rule the main position of the vibrational stretching and only a small modification is caused by the electronic structure changes in the surroundings.

As in the case of the impurities in tridimensional alloys, multiple CO adsorption is also possible, see Table 3.7. The characteristics shown by coadsorbed CO molecules on the $Pd_N$@PdAu alloy are very similar to those of the impurity dimers or trimers: lower $E_{ads}$ per CO molecule are found but total energies are larger. In addition, the vibrational frequencies resemble those of isolated Pd atoms showing a splitting (30 cm$^{-1}$) due to the dipole-dipole interactions.

## 3.5 d-band shift analysis

We have analysed the CO binding energy on different alloys (Pd impurities, Figure 3.2, and medium Pd content alloys, Figures 3.4 and 3.5), as a function of the $d$-band shift shown in Table 3.2. Only isolated CO adsorption at the most stable site is considered.

A good correlation between the adsorption energies and the local configuration to the site to which is bound is found in Figure 3.9. As expected, three different sets of data are present in the figure depending on the ensemble. This is by far the most important effect since it alters binding energies by more than 0.5 eV. Thus, geometrical effects are the leading contributions to CO binding to PdAu alloys. The second factor contributing to the binding energies electronic effects. The most important are due to the change in the number of non-homogeneous metal atoms in the surroundings of the active site. In that case modulations can reach differences of about 0.2-0.3 eV. Similar results have been found by Roudgar and Gross.[157] Still a set of points falls off the lines corresponding to their ensembles. Those points show subsurface Pd atoms in the neighboring region to the active ensemble. The reason for such behaviour is related to the changes in the Pauli repulsion that are not represented well enough by the single $\Delta\varepsilon_d$ parameter.

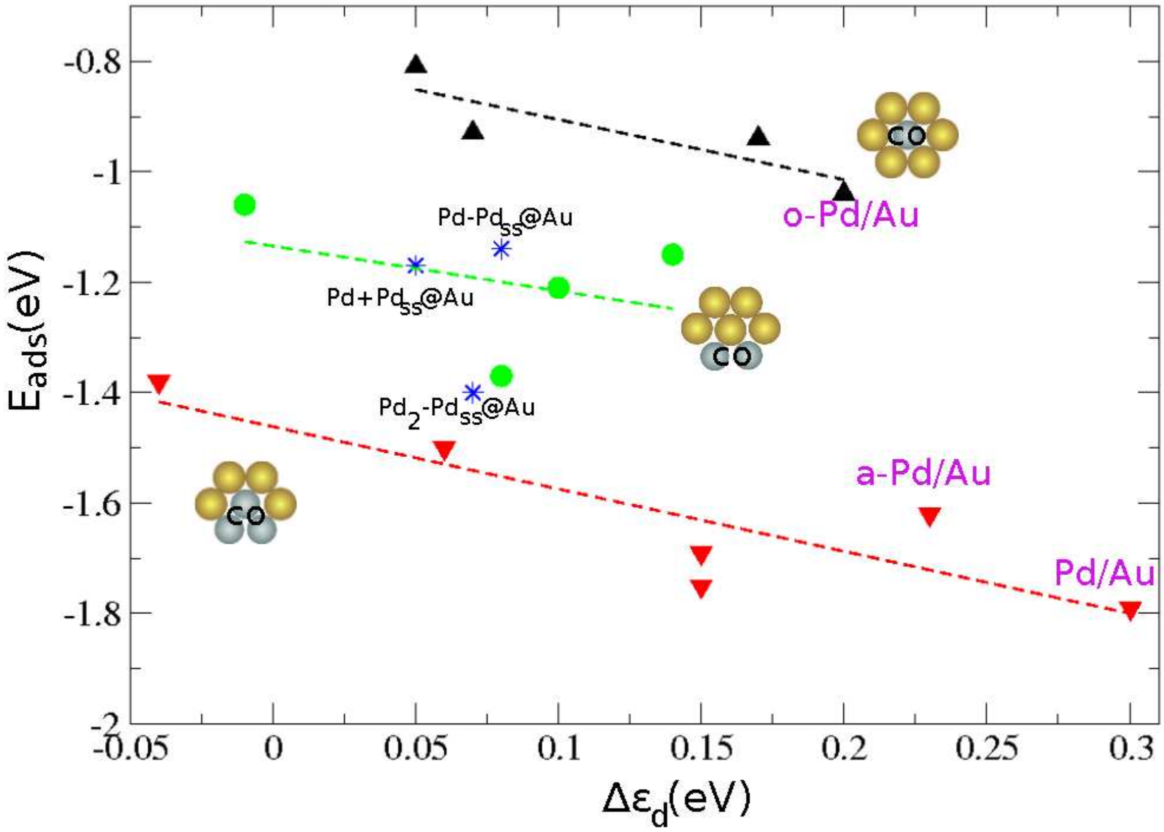

Figure 3.9: CO adsorption energy on different alloys as a function of the shift on the $d$-band centre, $\Delta\varepsilon_d$. The insets show the local configuration of the active site. Only isolated CO adsorption at the most stable site is considered.

### 3.5.1 Ab initio thermodynamics study

In order to introduce the temperature and pressure effects in the energies calculated by DFT, an *ab initio* thermodynamics study have been developed to the CO adsorption for $Pd_N$@Au models.[158, 159, 160] The excess free energy of the system, $\Delta G_{NCO}$ can be written as

$$\Delta G_{N_{CO^*}} = \frac{1}{2A}[G_{(slab+N_{CO^*})} - G_{slab} - N_{CO^*}\mu_{CO}] \tag{3.9}$$

where $G_{slab+N_{CO^*}}$ is the slab Gibbs energy when a number of CO are adsorbed, $G_{slab}$ is the clean slab Gibbs energy, $N_{CO^*}$ is the number of CO molecules, and $\mu_{CO}$ is the CO chemical potential. The Gibbs free energy can be written in terms of the Helmholtz free energy, $F$.

$$G(p,T) = F(V,T) + pV \tag{3.10}$$

For solids the last term, $pV$, is small and can be omitted. Therefore, the Gibbs and Helmholtz slab energies, $G_{slab}$ and $F_{slab}$, are rather similar

$$G_{slab} \sim F_{slab} \tag{3.11}$$

Due to the solid state nature of the slabs is verified that

$$F_{tras-slab} = F_{rot-slab} = 0 \tag{3.12}$$

then, the Helmholtz molecular partition of the slab, $F_{slab}$, can be written as the sum of its Helmholtz electronic energy, $F_{elec-slab}$, and its Helmholtz vibrational energy, $F_{vib-slab}$,

$$F_{slab} = F_{elec-slab} + F_{vib-slab} \tag{3.13}$$

and the term $F_{elec-slab}$ can be approximated by the energies obtained from DFT calculations, $E_{slab}$,

$$F_{elec-slab} \sim E_{slab} \tag{3.14}$$

with the Equations 3.11-3.14, the Gibbs free energy of the slab can be written as

$$G_{slab} \sim E_{slab} + F_{vib-slab} \tag{3.15}$$

Whereas the slab Gibbs energy when a number of CO molecules are adsorbed, $N_{CO^*}$, can be written as

$$G_{(slab+N_{CO^*})} \sim E_{(slab+N_{CO^*})} + F_{vib-(slab+N_{CO^*})} \tag{3.16}$$

$$G_{(slab+N_{CO^*})} \sim E_{(slab+N_{CO^*})} + F_{vib-(slab+N_{CO^*})} + N_{CO^*}ZPVE_{CO^*} \tag{3.17}$$

The chemical potential of the gas ideal, $\mu_{CO}(T,P)$, in Equation 3.9, can be expressed in terms of a reference pressure, $p^0$,

$$\mu_{CO}(T,p) = \mu_{CO}(T,p^0) + k_B T ln(\frac{p}{p^0}) \tag{3.18}$$

where the term $\mu_{CO}(T,p^0)$ contains entropic, $s_{CO}(T,p^0)$, and enthalpic, $h_{CO}(T,p^0)$, contributions

$$\mu_{CO}(T,p^0) = h_{CO}(T,p^0) - T s_{CO}(T,p^0) \tag{3.19}$$

and can be written as

$$\mu_{CO}(T,p^0) =$$

$$[h_{CO}(T,p^0) - h_{CO}(T=0K,p^0)] + [h_{CO}(T=0K,p^0) - E_{CO}] + E_{CO} - T s_{CO}(T,p^0) \tag{3.20}$$

therefore, the chemical potential, $\mu_{CO}(T,P)$, can be expressed as

$$\mu_{CO}(T,p) = \Delta h_{CO}(T,p^0) + ZPVE_{CO} + E_{CO} - T s_{CO}(T,p^0) + k_B T ln(\frac{p}{p^0}) \tag{3.21}$$

where $ZPVE_{CO}$ $(h^0_{CO}(T = 0K, p^0) - E_{CO})$ represents the zero point vibrational energy for the CO molecule. The entropic contribution, $s_{CO}(T,p^0)$ and the thermal correction to enthalpy, $\Delta h_{CO}(T,p^0)$, can be calculated with the average contributions to internal thermal energy, $\varepsilon_{trans}$, $\varepsilon_{rot}$ , $\varepsilon_{vib}$ and $\varepsilon_{elec}$, see Section 2.3 in Chapter 2.

If Equations 3.15, 3.17 and 3.21 are substituted in Equation 3.9 the extensive Gibbs free energy, $\Delta G_{N_{CO^*}}$, can be written as

$$\Delta G_{N_{CO^*}} \sim [E_{slab+N_{CO^*}} - E_{slab} - N_{CO^*}(E_{CO} + \Delta h_{CO} - T s_{CO} + k_B T ln(\frac{p}{p^0}))] \tag{3.22}$$

The $ZPVE$ terms ($ZPVE_{CO}$ and $ZPVE_{CO*}$) have been removed in Equation 3.22 since the difference between the adsorbed $ZPVE$ and that of the free molecule is relatively small (less than 0.02 eV). Due to the solid state nature of the slabs, the Helmholtz vibrational energy has been considered similar in both clean slab and CO-covered slab, $F_{vib-slab} \sim F_{vib-(slab+N_{CO^*})}$.

With Equation 3.22, the Gibbs energy for the CO adsorption can be calculated in any pressure and temperature conditions.

## 3.6 Vibrational spectra

The factors affecting the experimental IRAS spectra will be described in this section. Surface composition, and CO adsorption is analysed with the different annealing conditions, CO coverage and dosing temperature. First, the experimental results [24] are described:

- The vibrational spectra is found to depend on the history of the sample. Low temperature (600 K) and short time (30') annealing lead to very complex spectra in comparison to samples annealed at higher temperatures (800 K) for longer times (45').
- For the low-temperature annealed samples when dosing CO at low temperatures (80 K), a set of bands at high frequency (around 2078 cm$^{-1}$) with a second broad band in the 1950-1850 cm$^{-1}$ region are found. When increasing the CO dosage (at 80 K) a satellite at 2103 cm$^{-1}$ appears, see Figure 3.10. A similar behaviour is found when studying different temperatures at constant pressure (i.e. low coverage corresponding to high temperatures).
- For the high-temperature annealed samples the spectra consist of a single band at 2088 cm$^{-1}$ with a satellite at 2112 cm$^{-1}$ that appears at low temperatures or alternatively at very high coverages.

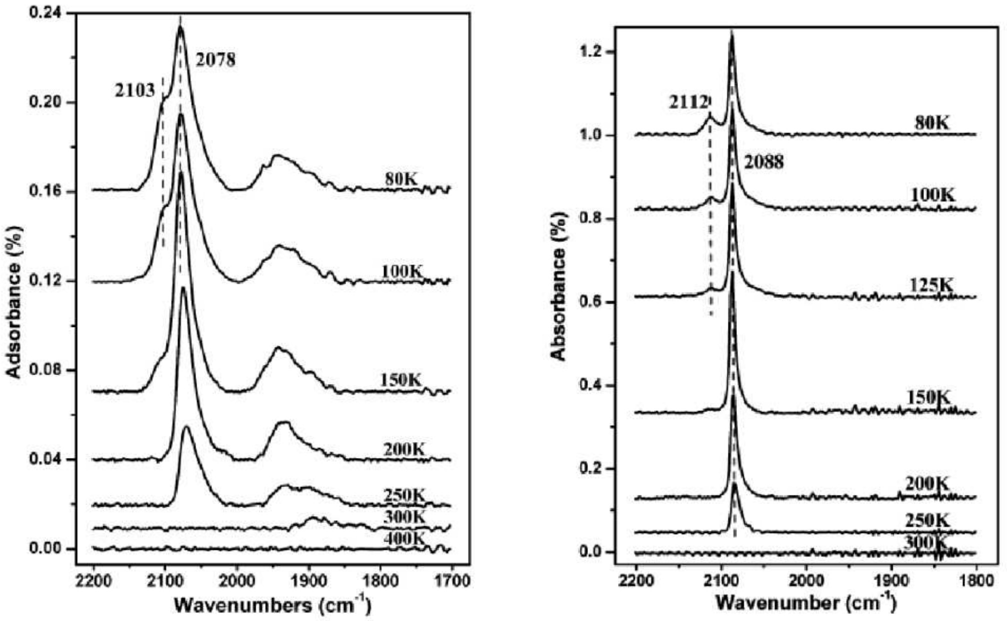

Figure 3.10: Temperature-dependent IRAS spectra for CO adsorption on the 5 ML Pd/5 ML Au/Mo(110) system. The alloy film was annealed at 600 K for 30 min (left) and at 800 K for 45 min (right). Taken from ref. [24].

### 3.6.1 Surface composition

Experimental surface composition analysis indicates that 5 ML Pd on 5 ML Au grown on Mo(110) generate an alloy with $Pd_{0.2}Au_{0.8}$ surface composition at 800 K, and $Pd_{0.25}Au_{0.75}$ at 600 K, see Figure 3.11.[31] Therefore, the alloys described in Figure

3.2 (impurity) and Figure 3.3 ($PdAu_3$), would be suitable to simulate the spectra at 800 K and 600 K annealing temperatures, respectively.

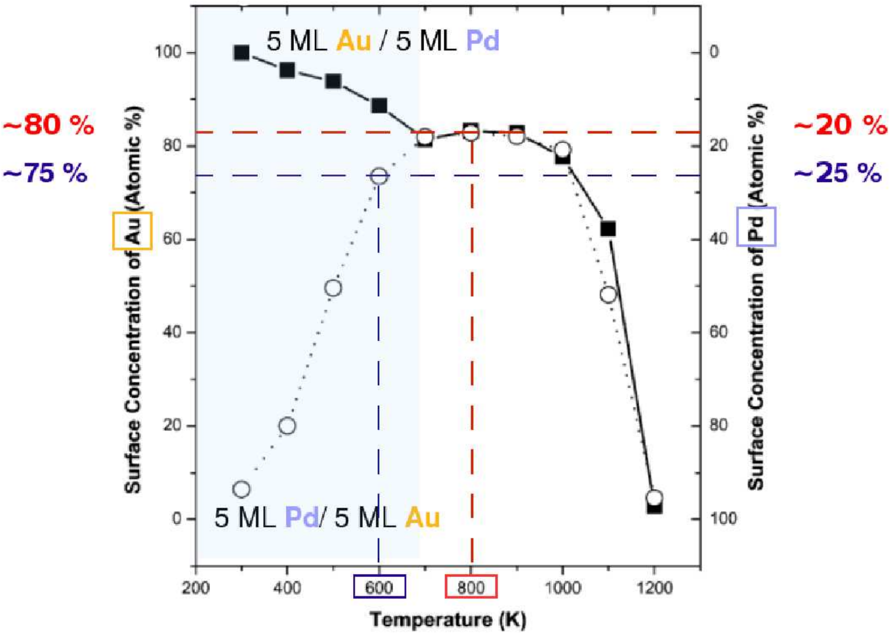

Figure 3.11: Surface concentration of Au and Pd of 5 ML Pd/5 ML Au/Mo(110) and 5 ML Au/5 ML Pd/Mo(110), open circle and dashed line, as function of annealing temperature. Taken from [31]. The surface concentrations of Au and Pd at 600 and 800 K have been marked.

Annealing conditions control the presence of each ensemble on the alloy surface. On a well-annealed sample, like the 800 K, equilibrium is reached, and thus a Boltzmann distribution considering ensemble formation energies, $E_f$, controls the probability for each configuration.

$$\mathcal{P}_{T_{ann}}^{B(alloy)} = exp(-E_f/k_BT_{ann})/\Sigma_{alloy}\exp(-E_f/k_BT_{ann}) \tag{3.23}$$

$E_f$ can be obtained as a combination of segregation and aggregation energies reported in Table 3.2. Thus, Boltzmann distributions provide a 100% of monomers on the surface at 800 K, $\mathcal{P}_{800K}^{B(imp)}$.

For the 600 K system, two limiting distribution models can be employed to analyse surface ensembles. For the Boltzmann distribution with the energies corresponding to the $PdAu_3$, the number of dimers increases up to a 15%, while monomers represent a 78% of the sample, $\mathcal{P}_{600K}^{B(PdAu_3)}$. Instead a random model distribution provides a different scenario where a 55% of the sites correspond to dimers and 27% to monomers, see Table 3.9. The probability for each ensemble in the random model can be expressed as,[30]

$$\mathcal{P}_{alloy}^{r} = m(\rho_{Pd}^{n}\rho_{Au}^{(6-n)}) \tag{3.24}$$

where $m$ is the degeneracy of a given configuration; $n$ is the number of Pd nearest neighbours; 6 comes from the surface coordination of a Pd atom; and $\rho_{Pd}$ and $\rho_{Au}$ are the surface concentrations of Au and Pd ($\rho_{Pd} \sim 0.25$ ML).

In summary, high temperature annealed samples provide 100% monodispersed Pd atoms, while a significant fraction of dimers 15-55% is expected for the low temperature annealed samples

| Ensemble | $\mathcal{P}_{800K}^{B(imp)}$ | $\mathcal{P}_{600K}^{B(PdAu_3)}$ | $\mathcal{P}^{r(PdAu_3)}$ |
|---|---|---|---|
| Monomers | 1.00 | 0.78 | 0.27 |
| Dimers | 0.00 | 0.15 | 0.55 |
| Trimers | 0.00 | 0.07 | 0.18 |

Table 3.8: Ensemble probability calculated by a Boltzmann distribution at annealing temperature of 800 K, $\mathcal{P}_{800K}^{B(imp)}$ , or 600 K, $\mathcal{P}_{600K}^{B(PdAu_3)}$, and by random distribution with $\rho_{Pd} \sim 0.25$ ML, $\mathcal{P}^{r(PdAu_3)}$.

| Alloy | $E_f$ | $\mathcal{P}_{800K}^{B}$ | $\mathcal{P}_{600K}^{B}$ | $\mathcal{P}_{alloy}^{r}$ |
|---|---|---|---|---|
| Pd@Au | +0.30 | 0.60 | 0.69 | |
| Pd-Pd$_{ss}$@Au | +0.40 | 0.14 | 0.10 | |
| Pd+Pd$_{ss}$@Au | +0.36 | 0.25 | 0.22 | |
| Pd+Pd@Au | +0.65 | 0.00 | 0.00 | |
| 2Pd+Pd$_{ss}$@Au | +0.69 | 0.00 | 0.00 | |
| **Pd monomers** | | 1.00 | 1.00 | 0.35 |
| Pd$_2$@Au | +0.69 | 0.00 | 0.00 | |
| d-Pd+Pdss@Au | +0.77 | 0.00 | 0.00 | |
| **Pd dimers** | | 0.00 | 0.00 | 0.52 |
| Pd$_3$@Au | +1.07 | 0.00 | 0.00 | |
| **Pd trimers** | | 0.00 | 0.00 | 0.13 |

Table 3.9: Ensemble formation energy, $E_f$ in eV; probability calculated by a Boltzmann distribution for the low Pd-content alloys at annealed temperature of 600 and 800 K, $\mathcal{P}_{600K}^{B}$ and $\mathcal{P}_{800K}^{B}$; and random probability, $\mathcal{P}_{alloy}^{r}$.

### 3.6.2 CO adsorption

Once known the effect of the annealing conditions in the surface alloy, in a second step, the *ab initio* thermodynamics study developed in Section 3.5.1 is employed to introduce the temperature and pressure effects on the CO adsorption.

The thermodinamic model allows us to indicate when CO-induced segregation is a favourable event as suggested theoretically,[32] and observed experimentally on the PdAu(100),[26, 27] by the following equation

$$\mu_{CO-Pd_{ss}@Au} = \mu_{CO-Pd@Au} \tag{3.25}$$

where $\mu_{CO-Pd_{ss}@Au}$ and $\mu_{CO-Pd@Au}$ are the chemical potential for the CO adsorption on Au with a subsurface Pd atom, and on an isolated Pd atom on the surface, respectively. With Equations 3.18 and 3.25, the pressure at which Pd$_{ss}$@Au can segregate to the surface to form Pd@Au, is found to be $\sim 10^{-5}$ Torr. This is in reasonable agreement with the experimental results for the PdAu(100) surface reported in ref. [27], ($p_{CO} \sim 10^{-3}$ Torr).

The Pd segregation to the surface to form Pd$_2$@Au is also study. Making equal the corresponding chemical potential for the multiple CO adsorption on the dimer Pd$_2$@Au, $\mu_{2CO-Pd_2@Au}$, and the chemical potential for the CO adsorption on the ensemble Pd-Pd$_{ss}$@Au, $\mu_{CO-Pd-Pd_{ss}@Au}$ plus the chemical potential of CO in gas phase, $\mu_{CO}$,

$$\mu_{2CO-Pd_2@Au} = \mu_{CO-Pd-Pd_{ss}@Au} + \mu_{CO} \tag{3.26}$$

Pd is found to segregate to the surface at moderate CO pressures, $p_{CO} > 270$ Torr. This pressure is higher than the experimentally reported in ref. [27] ($p_{CO} \sim 0.1$ Torr), in part to the more open character of the (100) surface.

In the following we concentrate on the low CO pressure experiments reported in ref. [24] In Table 3.10, the Gibbs energies at high (250 K) and low (80 K) CO dosing temperature, and at experimental CO pressure, $p_{CO} = 5\text{x}10^{-8}$ Torr, are presented for the impurity and PdAu$_3$ models. The conclusion for the CO adsorption at both high and low temperature are:

- At the well-annealed sample (T=800 K), monomers are the only configuration present on the surface. At high CO dosing temperature (250 K), adsorptions take preferentially place at Pd ensembles with subsurface Pd sites, Pd-Pd$_{ss}$@Au and Pd+Pd$_{ss}$@Au, see Table 3.10. At low CO dosing temperature (80 K), CO adsorption is more energetically favoured for all ensembles. Moreover, the presence of Pd atoms in the subsurface can not be distinguished by IRAS, and all Pd monomers will contribute with a single group of vibrations centred at 2079 cm$^{-1}$. In addition, neighbouring Pd atoms: Pd+Pd@Au and Pd+Pd-Pd$_{ss}$@Au can provoke the appearance of a band at 2091-2098 cm$^{-1}$, even if the number of these ensembles is relatively small according to the Boltzmann analysis. In that case, due to the IRAS selection rules, only the high frequency, symmetric mode, is active. Thus, neighbouring CO adsorption can contribute to the high frequency band in contrast to the common belief that they are due to CO on Au sites.

- When the sample is annealed at low temperatures (T=600 K), both Pd monomers and dimers are present on the surface, thus, adsorption on both ensembles has to be considered. At high CO dosing temperature (250 K), single CO adsorption on the bridge site, Pd$_2$@PdAu$_3$, is favoured, in agreement with the single broad signal around 1900 cm$^{-1}$ obtained at 300 K in the experiments.[24] At lower temperatures single and multiple adsorption on dimers, either at top or bridge positions (even at Pd-Au bridge sites), and adsorption on isolated monomers can coexist, see $\Delta G^{80K}_{NCO}$ in Table 3.10. Therefore, the spectrum is composed by a wide group of vibrations with bridge-like character centred at 1900 cm$^{-1}$, together with the top adsorption about 2075 cm$^{-1}$, plus contributions from multiple top adsorption on dimers, 2081 cm$^{-1}$. The band at low frequency is not visible in the IRAS spectra due to the cancellation of the dynamic dipole moment, see Figure 1.2 in Chapter 1

| System | $N_{CO}$ | $\Delta G^{80K}_{NCO}$ | $\Delta G^{250K}_{NCO}$ | $\overline{\nu}$ |
|---|---|---|---|---|
| **Pd monomers** (800 K) | | | | |
| Pd@Au (topAu) | 1 | 0.06 | 0.37 | 2102 |
| Pd@Au | 1 | -0.67 | -0.01 | 2079 |
| Pd-Pd$_{ss}$@Au | 1 | -0.88 | -0.22 | 2077 |
| Pd+Pd$_{ss}$@Au | 1 | -0.91 | -0.25 | 2078 |
| Pd+Pd@Au | 2 | -1.50 | -0.19 | 2091/2068 |
| Pd+Pd-Pd$_{ss}$@Au | 2 | -1.58 | -0.27 | 2098/2077 |
| **Pd monomers** (600 K) | | | | |
| Pd@PdAu$_3$ | 1 | -0.70 | -0.04 | 2075 |
| **Pd dimers** (600 K) | | | | |
| Pd$_2$@PdAu$_3$ | 1 | -0.89 | -0.23 | 1901 |
| Pd$_2$@PdAu$_3$ | 2 | -1.24 | 0.07 | 2081/ 2060 |
| Pd$_2$@PdAu$_3$ | 2 | -1.04 | 0.27 | 1936/ 1908 |
| Pd$_2$@PdAu$_3$ | 3 | -0.99 | 0.98 | 1961/1926/1915 |

Table 3.10: Gibbs free energy, $\Delta G_{NCO}$ in eV, and corrected intra-molecular stretching frequency, $\overline{\nu}$ in cm$^{-1}$, for CO adsorption in low Pd-content alloys, and in PdAu$_3$ alloys, at 80 and 250 K dosing temperatures and $p_{CO} = 10^{-8}$ Torr.

In order to extend this study at higher CO pressures, the excess free energy, $\Delta G_{NCO}$, of single and multiple CO adsorption on dimers, Pd$_2$@Au, is shown as a function of the pressure in Figure 3.12. At low temperature, the equilibrium configuration for CO adsorption on the Pd$_2$@Au is 2*CO molecules in all range of pressures, while at high temperature, a single CO bound to the bridge site is favoured at low pressures, and CO pairs are likely only at high CO pressures. The crossing between multiple and single CO adsorption is observed at $p_{CO} \sim 1.3$ Torr. High CO adsorption density on the Pd patches can be traced back to the reduced number of nearest Pd neighbours in the alloy when compared to the extended Pd surface. The number of CO-CO repulsive interactions in the Pd surface on the 3CO-Pd(111) $p$(2x2) is six for CO each molecule (for distances smaller than 2d$_{Pd-Pd}$). This is reduced in the case of dimers or trimers on the alloys (to 1 or 2). In the isolated islands, in the alloys the CO-CO repulsions calculated as $\Delta E = \overline{E} - E_{isolated}$ are smaller than for the Pd(111) surface, 0.4 eV (dimer) compared to 0.6 eV. This is similar to what has been observed for the AuNi alloy at high CO pressures [14] were preferred Ni extraction due to the increase in the

UNIVERSITAT ROVIRA I VIRGILI
THEORETICAL STUDIES OF SELECTIVE PROCESSES IN HETEROGENEOUS CATALYSIS
Mónica García Mota
ISBN:978-84-693-5424-7/DL:T-1415-2010

effective CO pressure.

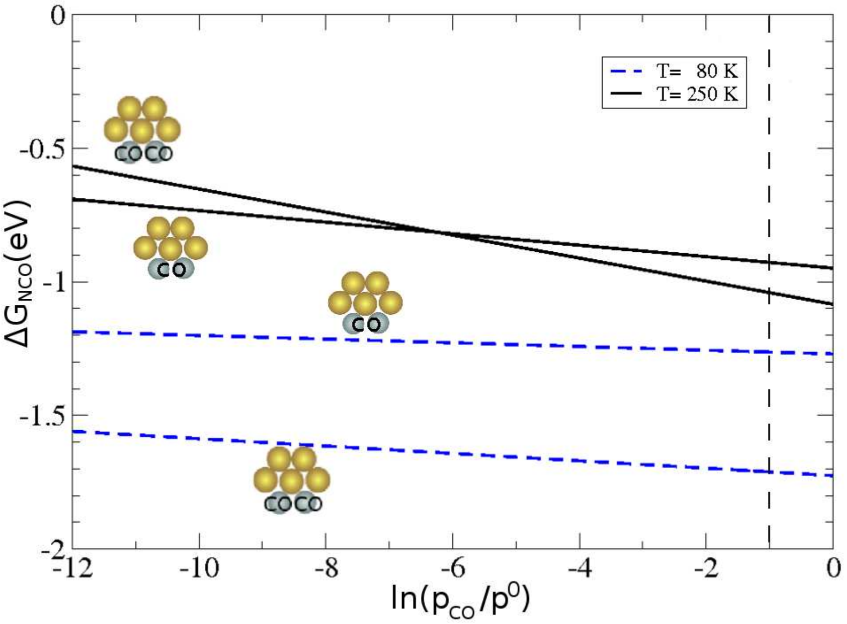

Figure 3.12: Gibbs free energy, $\Delta G_{NCO}$, at different CO dosing pressure, $p_{CO}$, and temperatures. The single or double CO adsorption on $Pd_2$@Au is shown in the insets. The vertical line indicates the pressure at which Pd+$Pd_{ss}$ would transform into $Pd_2$ on the Au(111) surface.

## 3.7 Conclusions

In the present chapter, the CO adsorption on monometallic systems, Pd and Au, and on different PdAu alloys have been analysed by means of Density Functional Theory. The conclusions from this chapter are:

- With respect to the alloy stability
    - The relative stability for low content Pd alloys, and for $PdAu_3$ models are very similar while the stability for the alloys with 50:50 alloy composition are strongly dependent on the subsurface layer composition. The most likely configurations are those where Pd atoms are surrounded by Au atoms.
- With respect to CO adsorption on monometallic surfaces
    - The theoretical results show the preference for CO adsorption on fcc site for Pd(111) at low coverage. In contrast, CO is very weakly adsorbed on the

Au surface, and sites at low coordination are needed to retrieve any bonding to the surface. The present observations are in agreement with previous experimental and theoretical results.

- With respect to CO bonding to bimetallic $Pd_{100-x}Au_x(111)$ alloys, $0<x<50$.
  - When CO is adsorbed on the low Pd-content alloys, the binding energy to the isolated impurity is lower than to the dimer and trimer. Pd atoms placed in the subsurface layer affect the alloy activity (by increasing the binding energy of CO) but do not change the stretching frequency of CO.
  - The binding energies of CO adsorbed on Pd sites at the $PdAu_3$ surface are lower than those of the Pd(111) surface.
  - Geometric effects account for the increase (decrease) of the CO binding energy for the layered Pd/Au (Au/Pd) respect to that of the Pd(111) surface.
  - Electronic effects constitute the main contribution to the reactivity change in the case of the alternate alloy, and the completely ordered o-PdAu structure.
  - CO binding energy depends on two terms: The ensemble to which CO is bound, and the *d*-band shifts of the Pd atoms in the ensemble.
  - Under high pressures, the dimer and larger ensembles might be able to adsorb more than a single CO molecule. For multiple CO adsorption on the low content Pd alloys, $PdAu_3$ and $Pd_{50}Au_{50}$ alloys, the average adsorption energy per CO molecule is slightly smaller than for a single molecule at the ensemble but the total energy gain is larger with respect to CO gas phase.
- With respect to CO vibrational spectra on the low Pd-content alloys
  - At high annealed temperature samples, $T_{ann}$= 800 K, the alloy is in equilibrium. A Boltzmann distribution of the Pd aggregation energies on the surface estimates the probability for each configuration. Pd monomers are the most common configuration present in the surface. The CO adsorption on Pd monomers contribute to the spectrum with a signal centred at 2079 $cm^{-1}$, in agreement with the experimental signal found at 2088 $cm^{-1}$.[24]
    - At high CO dosing temperature (250 K), the most favourable CO adsorption takes place in those alloys with a Pd atom in the subsurface. The CO adsorption on Pd monomers without Pd subsurface atoms, Pd@Au, is very weak, $\Delta G$=-0.01 eV
    - At low CO dosing temperature (80 K), CO adsorption is stronger than at high temperature for all ensembles. Multiple CO adsorption on the next-nearest neighbour configurations, are the most favourable ones. The CO bonding on Pd monomers without Pd subsurface atoms, Pd@Au, is now significant.

- At low annealed temperature samples, $T_{ann}$= 600 K, the equilibrium is not completely achieved. The inhomogeneity of the sample caused by a not well-annealed provokes the presence of of contiguous Pd sites on the surface together with Pd singletons.
  - At high CO dosing temperature (250 K), single CO adsorption on the bridge site is favoured, in agreement with only one experimental signal around 1900 $cm^{-1}$ at 300 K dosing temperature.[27]
  - At low CO dosing temperature (80 K), multiple CO adsorption on dimers is more likely than the single one. The peak at the highest frequency can be identified as multiple adsorption on dimers on the surfaces instead of adsorption on Au-sites.

# Chapter 4

# Catalysed CO oxidation on Au containing alloys

By means of Density Functional Theory, DFT, the atomic and molecular adsorptions (O, $O_2$ and CO), are characterised on the transition metals: Ni, Pd and Pt, and on substitutional low Au containing alloys. The CO oxidation is described on Ni and on $AuNi_3$ surface alloy. The aim of this study is unravel the reason behind the low temperature CO oxidation experimentally found when an $AuNi_3$ surface alloy is employed.[9]

## 4.1 Description of methods and models

The calculations were performed using Vienna Ab-initio Simulation Package, VASP, [148, 149, 150] with the Revised Perdew-Burke-Ernzerhof, RPBE,[124] as exchange-correlation functional to obtain the energy. Ni, Pd and Pt are the transition metals considered. The (111) surface is selected for its larger stability in faced-centred cubic structure metals, and it is modelled by a four-layer slab with a $p(2x2)$ unit cell to study the atomic and molecular adsorption, and a larger $p(4x4)$ unit cell to the $O_2$ dissociation and the CO oxidations. The top two layers are allowed to relax, and the third and fourth layers are fixed to the bulk values. The k-point sampling (Monkhorst-Pack) contains 5x5x1 k-points for the smaller cell, and reduced 3x3x1 when employing the larger ones.[130] Monoelectronic states are expanded in Bloch waves with a kinetic cut-off energy of 400 eV, while the core electrons are represented by Projector Augmented Wave, PAW, pseudopotentials.[151, 152] A dipole layer is placed in the vacuum region separating the slabs. All total energies have been extrapolated to $k_BT = 0$ eV. Spin polarised effects are included in the reported results when magnetised elements are present. The CI-NEB method is employed,[161] to locate the transition state structures. In complex cases (i.e. $O_2$ dissociation on gold alloys) CI-NEB is complemented by the dimer method.[162] The calculated cell parameters which are needed for this study are compiled in Table A.1 of Appendix A.

The alloys are represented by a substitutional model, $AuM_3@M$, where only 0.25

ML of the surface metal (M=Ni, Pd, and Pt) are replaced by Au, see Figure 4.1. In the Appendix A the cohesive energy, and the surface energy and relaxation of Ni, Pd and Pt monometallic surfaces are discussed.

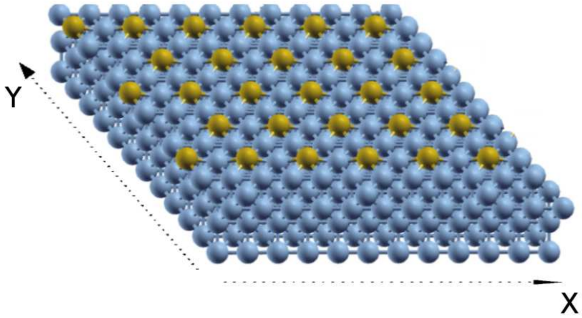

Figure 4.1: Substitutional model $AuM_3@M$. M, blue spheres, stand for Ni, Pd or Pt atoms. Yellow spheres stand for Au atoms.

## 4.2 CO adsorption

Carbon monoxide adsorption on the close packed transition metals has been extensively reported.[40, 163, 164, 165] In this work the adsorption properties are studied at low CO coverage, $\theta_{CO}$ = 0.25 ML, on Ni, Pd and Pt monometallic surfaces, and on its corresponding Au alloys. The different sites in which CO can be binding are shown in the Figure 4.2.

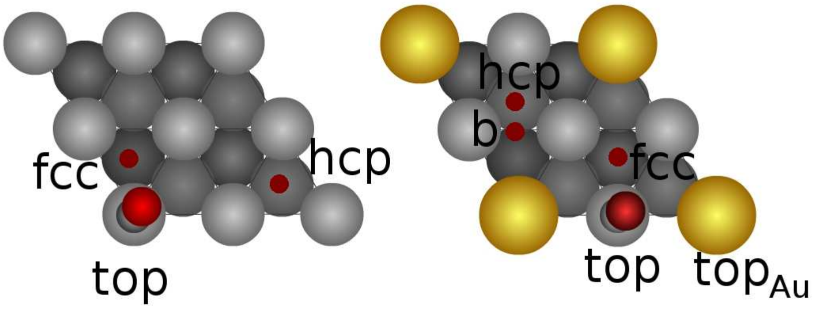

Figure 4.2: CO adsorption sites on a clean surface, and on a gold containing surface. Grey spheres stand for Ni, Pd or Pt atoms, and the yellow ones are gold. The special points in the surface cell are labelled with a short-hand notation: top$_{Au}$ corresponds to the CO adsorption above Au atoms, fcc and hcp correspond to threefold hollows, and b corresponds to the bridge position.

The adsorption is found to be very exothermic in all metals. For the CO adsorption in the most stable site, indicated in bold in Table 4.1, the strongest bond is on Pd ($E_{ads}$= -1.60 eV), and Pt is the less prone for CO adsorption ($E_{ads}$= -1.38 eV). The reactivity tend shown in Table 4.1 is in agreement with previous theoretical studies and with experimental estimates.[163]

CO hollow adsorption to the on-top position is preferred by 0.22 eV for Ni and Pd clean surfaces, in agreement with previous published calculations.[165] On Pt, although theoretically the hollow position presents a slight preference towards the CO adsorption, experimentally is known that CO adsorbs on it bonding through the carbon atom to the on-top site in an upright geometry.[166] The stronger adsorbate-surface interaction on hollow sites leads to a slightly more pronounced stretching of the C-O bond length, in the range of 1.188 (Pd)-1.194 Å (Pt), and a weaker CO vibration frequencies, 1700-1800 cm$^{-1}$, compared to its value in the gas phase molecule ($d_{C-O}^{gas}$= 1.144 Å and $\nu_{CO}^{gas}$= 2170 cm$^{-1}$).

In the alloys, the favoured adsorption site is kept but the CO adsorption energy on Au atoms, top$_{Au}$, is negligible, and the CO binding is weaker than for the monometallic metal in all adsorption sites. This shift has been ascribed to the influence of a ligand chemical interaction between the substrate and CO (mainly the back-donation of electrons from the metal $d$-band to CO antibonding orbital, $2\pi^*$ [163]). The addition of Au alters the width and position of the metal $d$-band and thus shifts the CO internal frequency. The most pronounced effect is for CO adsorption on AuNi$_3$ alloy, in that case the binding energy decreases 0.26 eV respect to the adsorption in the Ni monometallic surface. The CO adsorption increases in AuPt$_3$ alloy despite $\varepsilon_d$ decreases respect to the Pt monometallic surface. The deviation with respect expected values for systems containing Pt have been previously reported.[167]

## 4.3 Atomic and molecular oxygen adsorption

### 4.3.1 Atomic oxygen adsorption

The possible adsorption sites for the atomic oxygen on the surface are shown in the Figure 4.3.

Atomic oxygen is found to prefer fcc sites in all cases with adsorption energies in the range of -2.16 (Ni) and -0.88 eV (Pt). The difference with the hcp site is lower than 0.1 eV for the Ni surface, being larger for the Pd and Pt ones. The oxygen adsorbed in a bridge position is the less favoured site for all metals. It is a transition state between the fcc and hcp hollows and it has been characterised by a imaginary frequency, see Table 4.2.

The chemical reactivity is the main factor that determine the trends in the adsorption behaviour of oxygen on the Pt-group metals, and this reactivity according to the model introduced by Hammer and Norskøv,[168, 169] is mainly determined by the position of the centre of the metal $d$-band, $\varepsilon_d$, relative to the Fermi level. When Au

| Surface | Site | $E_{ads}$ | $d_{C-O}$ | $Z_{X-C}$ | $\nu$ | $\mu_{total}$ | $\varepsilon_d$ |
|---|---|---|---|---|---|---|---|
| Ni | top | -1.29 | 1.163 | 1.758 | 2024 | 11.377 | -1.14 |
| | **fcc** | -1.51 | 1.190 | 1.341 | 1798 | 10.598 | |
| | **hcp** | -1.55 | 1.193 | 1.322 | 1779 | 10.557 | |
| | bridge | -1.45 | 1.185 | 1.420 | 1838 | 10.760 | |
| $AuNi_3$@Ni | top | -1.06 | 1.163 | 1.767 | 2021 | 10.341 | -1.20 |
| | $top_{Au}$ | -0.06 | 1.156 | 1.999 | 2044 | 10.476 | |
| | **fcc** | -1.28 | 1.190 | 1.361 | 1.794 | 9.857 | |
| | **hcp** | -1.29 | 1.191 | 1.354 | 1779 | 9.909 | |
| | bridge | -1.17 | 1.184 | 1.448 | 1866 | 10.004 | |
| Pd | top | -1.09 | 1.157 | 1.882 | 2053 | – | -1.53 |
| | **fcc** | -1.60 | 1.188 | 1.325 | 1801 | – | |
| | **hcp** | -1.60 | 1.186 | 1.314 | 1813 | – | |
| | bridge | -1.46 | 1.180 | 1.434 | 1864 | – | |
| $AuPd_3$@Pd | top | -0.98 | 1.157 | 1.900 | 2039 | – | -1.54 |
| | $top_{Au}$ | -0.04 | 1.151 | 2.004 | 2053 | – | |
| | **fcc** | -1.52 | 1.188 | 1.328 | 1799 | – | |
| | hcp | -1.45 | 1.195 | 1.360 | 1754 | – | |
| | bridge | -1.25 | 1.177 | 1.480 | 1875 | – | |
| Pt | top | -1.34 | 1.160 | 1.858 | 2046 | – | -2.11 |
| | **fcc** | -1.38 | 1.194 | 1.322 | 1760 | – | |
| | **hcp** | -1.38 | 1.194 | 1.328 | 1768 | – | |
| | bridge | -1.39 | 1.182 | 1.453 | 1851 | – | |
| $AuPt_3$@Pt | top | -1.36 | 1.161 | 1.853 | 2040 | – | -2.15 |
| | $top_{Au}$ | -0.03 | 1.151 | 2.013 | 2055 | – | |
| | **fcc** | -1.46 | 1.195 | 1.323 | 1752 | – | |
| | hcp | -1.40 | 1.191 | 1.348 | 1789 | – | |
| | bridge | -1.35 | 1.184 | 1.484 | 1842 | – | |

Table 4.1: Adsorption energy, $E_{ads}$ in eV, calculated respect to the clean surface and the free CO molecule; CO bond length, $d_{C-O}$ in Å; average vertical distance from C atom in the CO molecule to the surface, $Z_{X-C}$ in Å; stretching frequency, $\nu$ in $cm^{-1}$; and total magnetic moment, $\mu_{total}$ in Bohr magneton; for the possible adsorption sites in each metal. Last column corresponds to the $d$-band centre, $\varepsilon_d$ in eV, of each metal. The most stable site in each metal is indicated in bold.

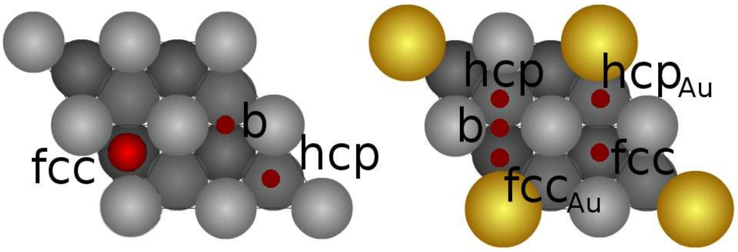

Figure 4.3: Atomic oxygen adsorption sites on a clean surface and on a gold containing surface. The special points in the surface cell are labelled with a short-hand notation: fcc and hcp are $Ni_3$ hollows, $fcc_{Au}$ and $hcp_{Au}$ are hollow sites which have one Au atom involved, and b is the bridge position. Colour code is that of Figure 4.2.

atoms are introduced in the surface metal, electronic and geometric effects provoke a down shift in the *d*-band centre, see in Table 4.2, and the *d*-band model predicts then that the reactivity of the alloy towards the O adsorption must decrease. That is the case for oxygen adsorptions in $AuNi_3$, and $AuPd_3$ surfaces in which the adsorption energies decrease around 0.3 and 0.1 eV respect to the monometallic surface Ni and Pd, respectively. However the oxygen adsorption is 0.05 eV stronger in $AuPt_3$ than in the Pt surface.

In $AuPd_3$ and $AuPt_3$ surfaces, new oxygen adsorption sites are available respect to the monometallic surface. These are hollow sites which have one Au atom involved, $fcc_{Au}$ and $hcp_{Au}$ in Figure 4.3. However, this kind of sites are found not stable in $AuNi_3$, because the Au effect confining oxygen adsorption is more pronounced in this alloy. This Au effect will be discussed in detail in Section 4.4 of this chapter.

### 4.3.2 Molecular oxygen adsorption

The possible adsorption sites for the molecular oxygen on a clean surface, and on a gold containing surface are shown in Figure 4.4. The sites in the alloys in which one Au atom is involved, $tbt_{Au}$, $tfcc_{Au}$ and $thcp_{Au}$, have been indicated in the figure, meaning that molecular adsorption does not take place in these positions.

The same trend shown by the atomic oxygen adsorbed on the metals is followed by the precursors states of $O_2$.[170] A strongly chemisorbed molecular precursor is located in a threefold hollow in the case of Nickel, with small difference between the adsorption energies in tfcc and thcp sites, see Table 4.3. The smaller Ni lattice constant compared to Pd and Pt, leads to a smaller distance between the $O_2$ molecule and the substrate atoms than for Pd and Pt metals, $Z_{O_2-X}$, and hence to a strong Ni-$O_2$ bond, -1.00 eV. This is in agreement with previous studies.[41, 42] The similarity in the lattice constants of Pt and Pd induces that the molecular oxygen adsorption on Pd behaves much more like oxygen on Pt than like oxygen on Nickel. The $O_2$ adsorption energies in Pd and Pt are -0.40 and -0.22 eV respectively if the most favourable adsorption sites

| Surface | site | $E_{ads}$ | $Z_{O-X}$ | $\nu$ | $\mu_{total}$ | $\varepsilon_d$ |
|---|---|---|---|---|---|---|
| Ni | **fcc** | -2.16 | 1.113 | 493 | 11.074 | -1.14 |
| | hcp | -2.08 | 1.113 | 490 | 11.065 | |
| | bridge | -1.62 | 1.235 | 220i | 11.301 | |
| $AuNi_3$@Ni | **fcc** | -1.84 | 1.112 | 485 | 10.008 | -1.20 |
| | hcp | -1.69 | 1.128 | 479 | 10.012 | |
| Pd | **fcc** | -1.01 | 1.122 | 432 | – | -1.53 |
| | hcp | -0.78 | 1.158 | 416 | – | |
| | bridge | -0.46 | 1.314 | 177i | – | |
| $AuPd_3$@Pd | **fcc** | -0.86 | 1.149 | 425 | – | -1.54 |
| | $fcc_{Au}$ | -0.38 | 1.160 | 424 | – | |
| | hcp | -0.64 | 1.170 | 423 | – | |
| | $hcp_{Au}$ | -0.18 | 1.208 | 422 | – | |
| | bridge | -0.22 | 1.340 | 162i | – | |
| Pt | **fcc** | -0.88 | 1.150 | 435 | – | -2.11 |
| | hcp | -0.46 | 1.192 | 430 | – | |
| | bridge | -0.25 | 1.256 | 126i | – | |
| $AuPt_3$@Pt | **fcc** | -0.93 | 1.192 | 435 | – | -2.15 |
| | $fcc_{Au}$ | -0.45 | 1.088 | 424 | – | |
| | hcp | -0.53 | 1.196 | 429 | – | |
| | $hcp_{Au}$ | -0.23 | 1.240 | 468 | – | |
| | bridge | -0.33 | 1.392 | 66i | – | |

Table 4.2: Adsorption energy, $E_{ads}$ in eV, with respect to half a free oxygen molecule and the clean surface energy; vertical average distance from O atom to the surface, $Z_{O-X}$ in Å; stretching frequency, $\nu$ in $cm^{-1}$; and total magnetic moment, $\mu_{total}$ in Bohr magneton; for the different sites in each metal. The most stable sites are indicated in bold. In last place $d$-band centre, $\varepsilon_d$ in eV, of each metal.

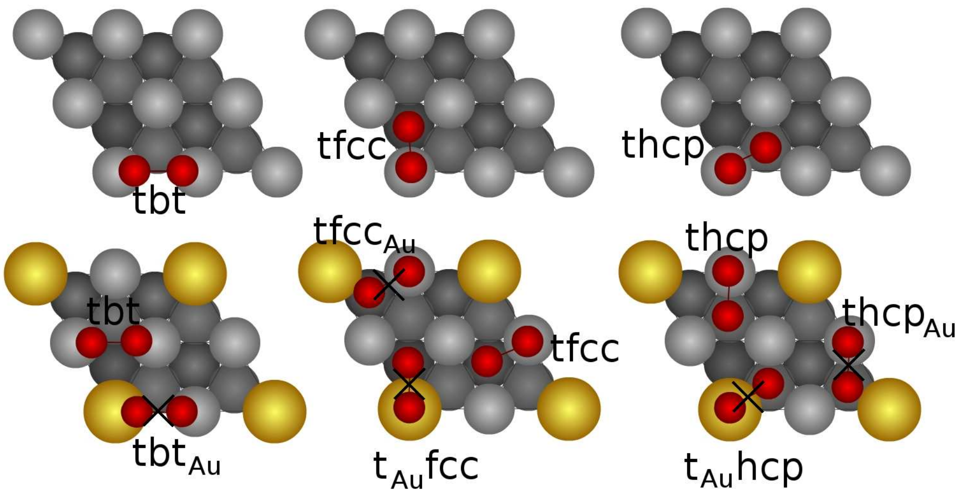

Figure 4.4: Possible adsorption sites for the molecular oxygen on a clean surface (top), and on a gold containing surface (bottom). The sites in the alloys in which one Au atom is involved, tbt$_{Au}$, tfcc$_{Au}$ and thcp$_{Au}$, have been crossed out because the molecular adsorption does not take place in them. Colour code is that of Figure 4.2.

are considered. These are the tfcc site on Pd, and a top-bridge-top, tbt, configuration on the Pt surface. At difference to Ni, for both precursors on Pd and Pt there is a pronounced preference for the tfcc over the thcp hollow.

The bond length and the magnetic moment of the adsorbed $O_2$ molecule are directly related to the $O_2$ adsorption site. During adsorption, the O-O distance increases, and the spin polarisation decreases respect to the values for the $O_2$ in gas phase ($d^{gas}_{O-O}$= 1.208 Å and $\mu^{gas}_{O2}$= 2 $\mu_B$). These differences are more pronounced for the tfcc and thcp precursors than for the tbt state. When $O_2$ is adsorbed on a tbt site shows O-O distances around 1.3 Å, with a magnetic moment in the rage of 0.5-0.7 $\mu_B$ thus compatible with a superoxo $O_2^-$ precursor, while when $O_2$ is placed in tfcc and thcp sites the O-O distances are larger than 1.4 Å, and the magnetic moment is lower than 0.3 $\mu_B$. These precursors are thus midway between superoxo $O_2^-$ state, and peroxo $O_2^{2-}$ states. The $O_2$ stretching frequencies are also dependent on the adsorption site. The highest peak corresponds to the tbt in all cases; 930 (Pt)-1058 (Pd) cm$^{-1}$. The frequencies are reduced at hollows positions; 700 (Ni)-918 (Pd) cm$^{-1}$. For the frustrated $O_2$-surface stretching mode a feature is found around 400 cm$^{-1}$. Similar frequencies have been observed for $O_2$,[42] and the precursors have also been characterised as peroxo or superoxo-like species depending on the adsorption site in previous theoretical reports.[41, 42]

When Au atoms are introduced, the $O_2$ distances on the surface are slightly longer, and the bonds are weaker than for the clean surface ones. The Au effect is very pronounced on $AuNi_3$ and $AuPd_3$ surfaces being the adsorption energy halved: from -1.00 to -0.52 eV in $AuNi_3$, and from -0.40 to -0.21 eV in $AuPd_3$. However, the introduction of Au atoms in the surface does not modify the $O_2$ adsorption energy in $AuPt_3$ respect

| Surface | Site | $E_{ads}$ | $d_{O-O}$ | $Z_{O_2-X}$ | $\nu$ | $\mu_X$ | $\mu_{O_2}$ | $\varepsilon_d$ |
|---|---|---|---|---|---|---|---|---|
| Ni | tbt | -0.85 | 1.377 | 1.771 | 906 | 0.562 | 0.622 | -1.14 |
|  | **tfcc** | -1.00 | 1.448 | 1.736/1.488 | 722 | 0.546 | 0.234 |  |
|  | thcp | -1.02 | 1.457 | 1730/1480 | 700 | 0.562 | 0.283 |  |
| $AuNi_3$@Ni | tbt | -0.41 | 1.364 | 1.795 | 932 | 0.536 | 0.692 | -1.20 |
|  | **tfcc** | -0.52 | 1.429 | 1.788/1.514 | 767 | 0.441/0.549 | 0.289 |  |
|  | thcp | -0.51 | 1.427 | 1.802/1.541 | 768 | 0.553 | 0.345 |  |
| Pd | tbt | -0.36 | 1.322 | 1.929 | 1058 | – | 0.716 | -1.53 |
|  | **tfcc** | -0.40 | 1.365 | 1.853/1.606 | 918 | – | 0.000 |  |
|  | thcp | -0.29 | 1.364 | 1.871/1.636 | 918 | – | 0.028 |  |
| $AuPd_3$@Pd | **tbt** | -0.23 | 1.318 | 1.948 | 1071 | – | 0.747 | -1.54 |
|  | tfcc | -0.21 | 1.358 | 1.879/1.637 | 939 | – | 0.000 |  |
|  | thcp | -0.13 | 1.355 | 1.894/1.667 | 945 | – | 0.056 |  |
| Pt | **tbt** | -0.22 | 1.350 | 1.931 | 930 | – | 0.617 | -2.11 |
|  | tfcc | -0.17 | 1.392 | 1.866/1.642 | 827 | – | 0.000 |  |
|  | thcp | 0.03 | 1.378 | 1.908/1.723 | 861 | – | 0.003 |  |
| $AuPt_3$@Pt | **tbt** | -0.22 | 1.359 | 1.926 | 897 | – | 0.564 | -2.15 |
|  | tfcc | -0.17 | 1.401 | 1.870/1.651 | 799 | – | 0.000 |  |
|  | thcp | -0.02 | 1.384 | 1.908/1.726 | 847 | – | 0.000 |  |

Table 4.3: Adsorption energy, $E_{ads}$ in eV; length of the $O_2$ bond, $d_{O-O}$ in Å; vertical distance of the $O_2$ molecule from the surface, $Z_{O_2-X}$ in Å; stretching frequency, $\nu$ in $cm^{-1}$; magnetic moment of the atoms below molecular oxygen, $\mu_X$ in Bohr magneton; and magnetic moment of the adsorbed oxygen, $\mu_{O_2}$ in Bohr magneton. In last place $d$-band centre, $\varepsilon_d$ in eV, of each metal.

to in Pt monometallic surface. The range at which O-O vibrations are found, 767-932 cm$^{-1}$, is in agreement with the bands reported experimentally for AuNi$_3$: 790, 865 and 950 cm$^{-1}$,[9] see Figure 4.5.

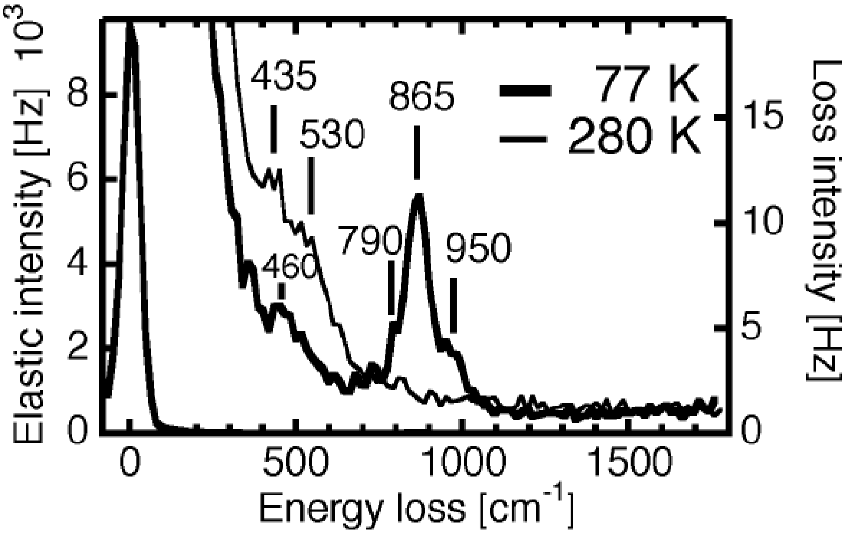

Figure 4.5: Specular HREEL spectrum of saturation coverage $O_2$ measured at 77 K on 0.24 ML of Au/Ni(111) and after heating to 280 K. Incident electron energy is 6.4 eV with 55 cm$^{-1}$ fwhm. Taken from ref. [9].

## 4.4 Potential energy surface: Atomic oxygen

To check with detail the effect of the presence of Au on the metal surface, the adsorption energy of a simple probe atomic oxygen as a function of its position on the surface has been computed on AuNi$_3$, and AuPd$_3$ surface alloys in order to be compared with the same Potential Energy Surface, PES, for the corresponding monometallic surfaces. In the calculations the oxygen atom is moved along the surface with the X and Y coordinates fixed.

The two different potential energy surfaces drawn with the atomic oxygen adsorption energy on Ni and on AuNi$_3$ surfaces, are shown in the Figure 4.6. In the Ni monometallic surface the oxygen adsorption energy ranges from -2.05 eV, with oxygen in a hollow position, to -0.32 eV, when oxygen is placed in the region above Ni atoms.

On AuNi$_3$, oxygen adsorption neither happens if O is placed above Ni nor on Au atoms. The higher adsorption energy takes place on the Ni$_3$ hollow, -1.64 eV, while in the neighbouring sites of Au the adsorption energy is lower than -0.1 eV. The larger corrugation observed in AuNi$_3$ respect to Ni, produces confinement on the O adsorption. As consequence, the normal $O_2$ dissociation path observed for the monometallic surfaces is blocked in the alloys. This will be discussed with detail in the next section.

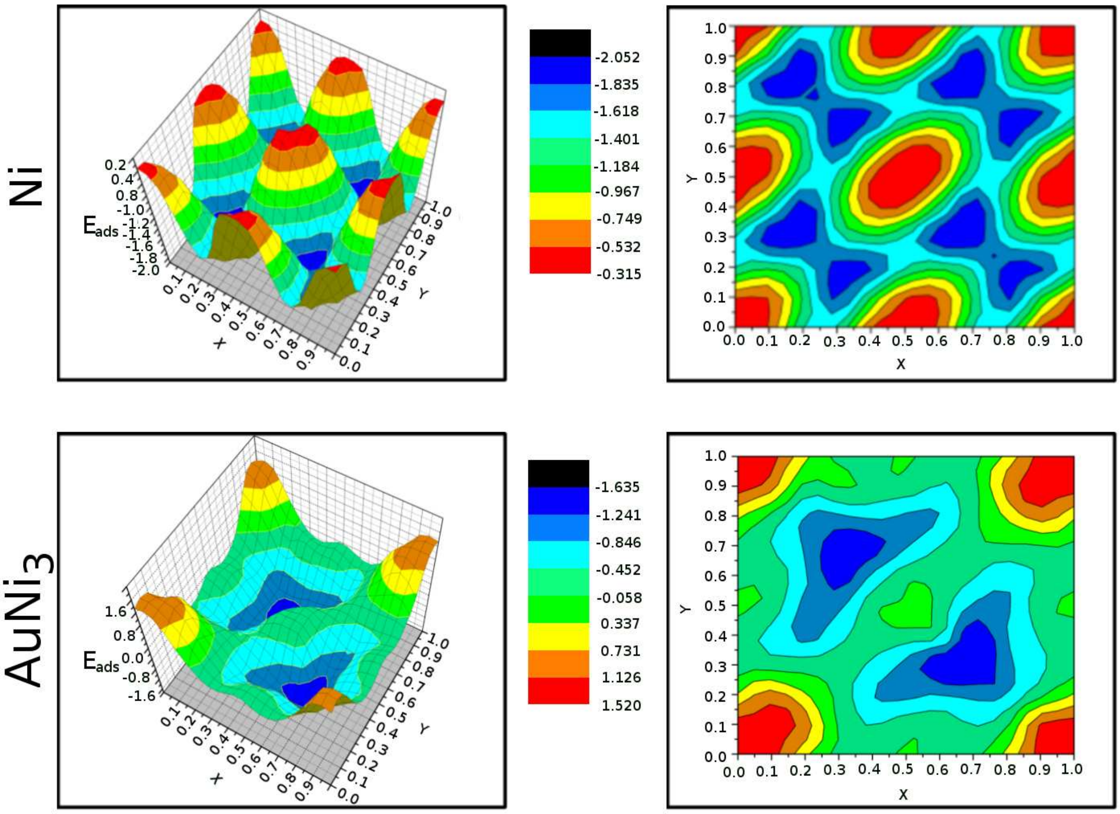

Figure 4.6: Potential energy surface of the atomic oxygen adsorption on Ni and on $AuNi_3$ surfaces drawn as two and three dimensional maps. Adsorption energy, $E_{ads}$ is shown in eV.

The PES drawn with atomic oxygen moving on Pd surface is shown in Figure 4.7. The oxygen adsorption does not take place when oxygen is on-top Pd atoms. The stronger adsorption is in the fcc site with an adsorption energy of -0.82 eV, and both hcp and fcc sites are not equivalent. For $AuPd_3$ surface, although the adsorption energies are weaker than that in the Pd monometallic surface, corrugation respect to Pd is less pronounced than in the $AuNi_3$ case. Therefore, the study of the CO oxidation will be analysed in the Ni and $AuNi_3$ surfaces, in order to clarify the gold role in the reaction path.

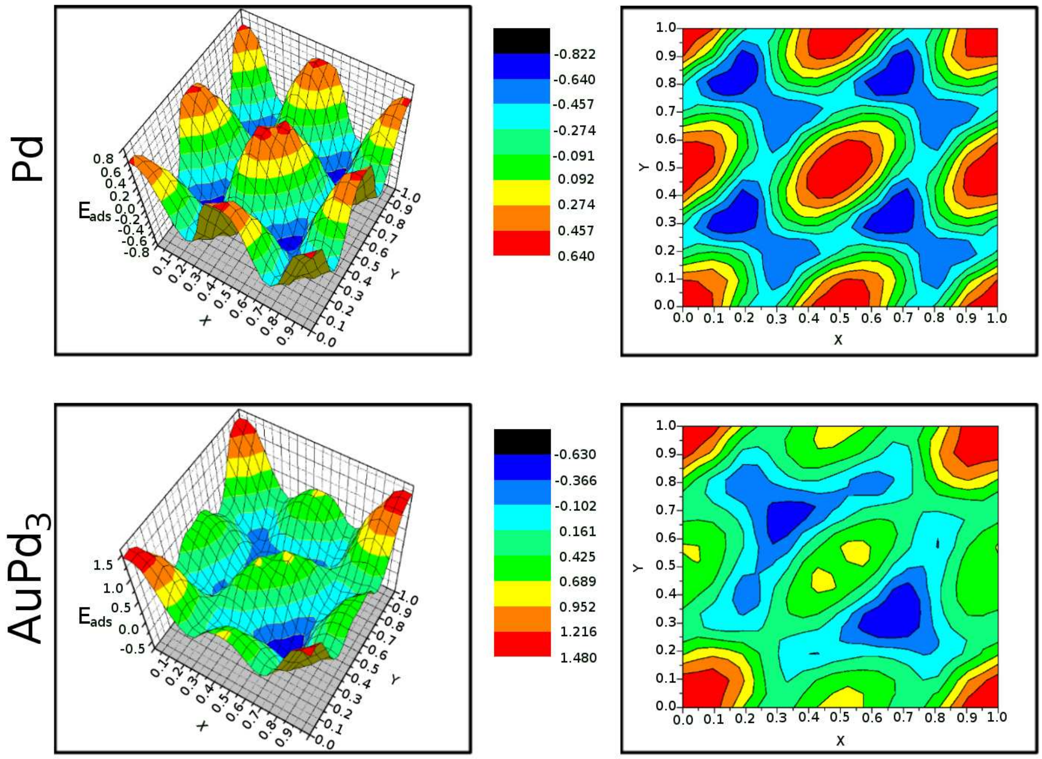

Figure 4.7: Potential energy surface of the atomic oxygen adsorption on Pd and on $AuPd_3$ surfaces drawn as two and three dimensional maps. Adsorption energy, $E_{ads}$ is shown in eV.

## 4.5 Molecular oxygen dissociation

$O_2$ dissociation has been studied from the molecular precursor in the most stable position for Pd, it is the tfcc site.

$$O_2^* + * \longleftrightarrow 2O^* \tag{4.1}$$

By a rotation, dissociation towards the formation of two atoms in the hcp sites is obtained, see Figure 4.8. This path for the $O_2$ dissociation in transition metals has been reported.[41, 42] The reaction is exothermic by 2.55 eV, see Table 4.4. A low dissociation barrier is found, 0.10 eV, this value is much lower than the binding energy of the precursor, 1.00 eV, in agreement with previous theoretical results.[41, 42, 171]

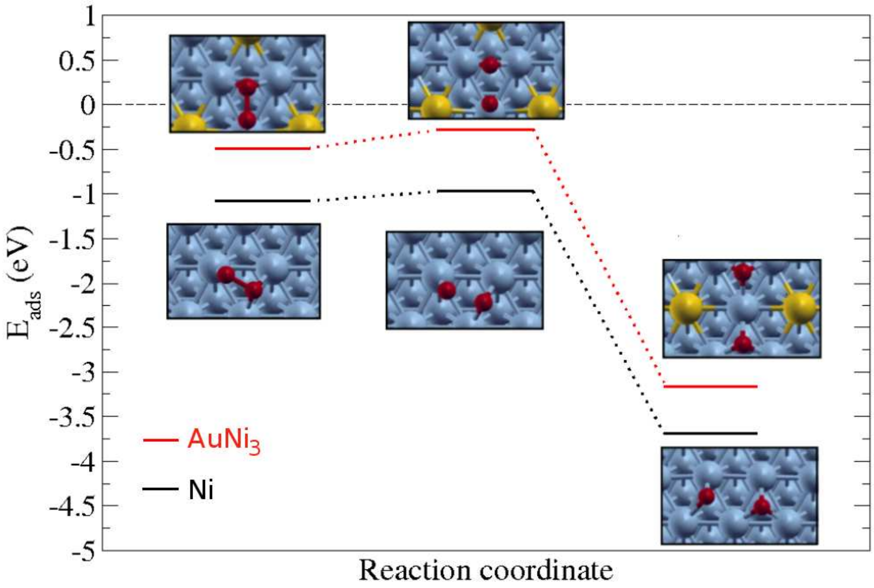

Figure 4.8: Reaction path for the decomposition of molecular oxygen on Ni and AuNi$_3$ surface alloy. Blue spheres stand for Ni, yellow for Au, and red spheres for oxygen.

In the gold containing alloy, the dissociation path is modified because of Au is blocking active reaction sites. Two oxygen atoms in neighbouring hcp and fcc sites, is the final state reached in AuPd$_3$, see Figure 4.8. The reaction presents a exothermicity close to the clean surface one, while the activation energy is found to be 0.11 eV larger. When the novel dissociation path found in the alloy is tested in the monometallic surface, the dissociation activation energy found is slightly lower than that for the dissociation path that involves oxygen rotation.

The minimum temperature, $T_m$, at which the molecular oxygen dissociation can take place in each surface can be estimated making the Arrhenius equation equal to one:

$$1 \sim \nu \exp(\frac{-E_a}{k_B T_m}) \tag{4.2}$$

where $k_B$ is the Boltzmann's constant, $E_a$ is the activation energy in eV, and $\nu$ the preexponential factor with the approximate value of $10^{13}$ s$^{-1}$. The zero point vibrational energy, ZPVE, has been included in the energy calculations.

With the previous considerations oxygen dissociation in Ni surface takes place at the estimated low temperature of 37 K. A higher temperature, 78 K, is needed for the dissociation in the $AuNi_3$ alloy. This result is in good agreement with the experimental vibrational spectrum measured by HREELS at low temperature, 77 K, on 0.24 ML of Au/Ni(111) showing that $O_2$ adsorption on this surface alloy is molecular.[9]

| | initial site | final sites | $\Delta E$ | $E_a$ | $d^{TS}_{O-O}$ | $\nu_i$ | $T_m$ |
|---|---|---|---|---|---|---|---|
| Ni | tfcc | 2hcp | -2.55 | 0.10 | 1.718 | 356 | 37 |
| | tfcc | fcc-hcp | -2.80 | 0.08 | 1.826 | 320 | 29 |
| $AuNi_3$@Ni | tfcc | fcc-hcp | -2.59 | 0.22 | 1.857 | 344 | 78 |

Table 4.4: Initial and final sites for the paths for the $O_2$ dissociation on Ni and on the corresponding $AuNi_3$@Ni alloy, together with its corresponding dissociation energies, $\Delta E$ in eV, and barriers, $E_a$ in eV. The distances at the transition state structure, $d^{TS}_{O-O}$, are reported in Å, and the imaginary frequencies that characterise the transition states in $cm^{-1}$. $T_m$ in K, is the minimum temperature calculated by Equation 4.2, at which the reaction can take place.

## 4.6 CO oxidation

There are two possible reaction paths for CO oxidation. In the first channel, the adsorbed CO reacts directly with the molecular oxygen, and $CO_2$ with a remaining atomic oxygen poisoning the surface are the products. Then $CO_2$ leaves the surface, and the remaining atomic oxygen might react with CO

$$CO^* + O_2^* \longleftrightarrow CO_2^{gas} + O^* + * \tag{4.3}$$

$$CO^* + O^* \longleftrightarrow CO_2^{gas} + 2* \tag{4.4}$$

In the second channel, firstly $O_2$ dissociates to provide active oxygen atoms before the reaction with CO takes place:

$$O_2^* \longleftrightarrow 2O^* \tag{4.5}$$

$$CO^* + O^* \longleftrightarrow CO_2^{gas} + 2* \tag{4.6}$$

The comparison of the estimated minimum temperatures for the molecular oxygen dissociation and for the CO oxidation will be the fundamental issue to determine in which of both channels the CO oxidation takes place in each surface.

### Bimolecular reaction of CO with coadsorbed $O_2$

The initial state is given by the coadsorbed molecules, CO and $O_2$, see Figure 4.9. The CO oxidation with the molecular oxygen is very exothermic on Ni (-2.59 eV) and the activation energy is found to be 1.22 eV. In the gold containing alloy, $AuNi_3$@Ni, the

UNIVERSITAT ROVIRA I VIRGILI
THEORETICAL STUDIES OF SELECTIVE PROCESSES IN HETEROGENEOUS CATALYSIS
Mónica García Mota
ISBN:978-84-693-5424-7/DL:T-1415-2010

Au effect modifies the reaction path, and CO reacts with oxygen after the unidirectional molecular oxygen splitting. The activation energies is severely reduced respect to the monometallic surface, see Table 4.5.

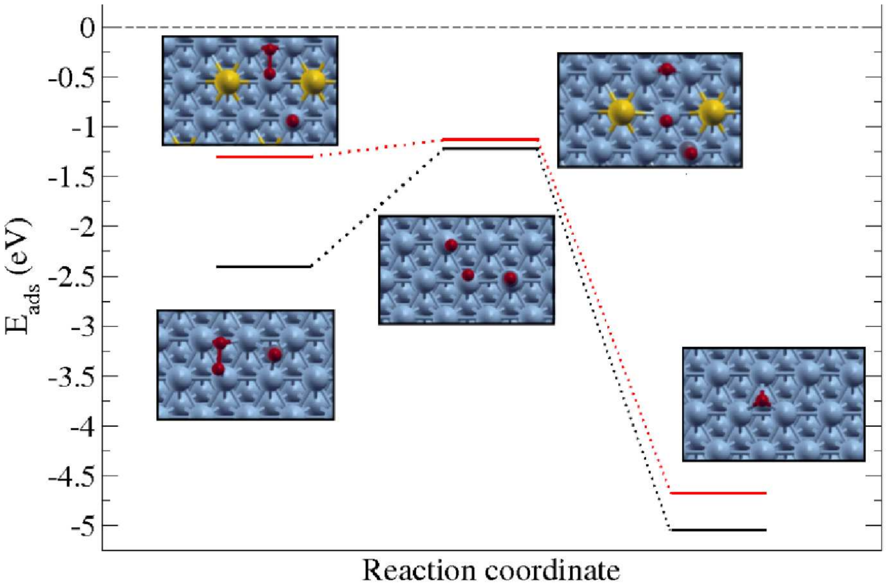

Figure 4.9: Reaction path for the reaction of CO with molecular oxygen over Ni (top) and $AuNi_3$ surfaces (bottom). Blue spheres stand for Ni, yellow for Au, and grey and red spheres for carbon and oxygen atoms respectively.

| | $\Delta E$ | $E_a$ | $d^{TS}_{O-O}$ | $d^{TS}_{CO-O}$ | $\nu_i$ | $T_m$ |
|---|---|---|---|---|---|---|
| Ni | -2.59 | 1.19 | 2.014 | 2.469 | 220 | 427 |
| $AuNi_3$@Ni | -3.32 | 0.16 | 2.052 | 2.722 | 260 | 58 |

Table 4.5: Reaction energies, $\Delta E$ in eV, and barriers, $E_a$ in eV, for the reaction of CO with molecular oxygen forming $CO_2$, and atomic oxygen on Ni and on $AuNi_3$@Ni alloy. The main distances at the transition state structure, $d^{TS}_{O-O}$ and $d^{TS}_{CO-O}$, are reported in Å, and the imaginary frequencies that characterise the transition states in $cm^{-1}$. $T_m$ in K, is the minimum temperature calculated by Equation 4.2, at which the reaction can take place.

### Reaction of CO with dissociated O

The reaction starts with the reactants in their optimal positions: The oxygen atom and the CO molecule in the fcc site. In the transition state the oxygen atom is activated from the hollow site to a bridge site, CO approaches tilting away from the O atom. Figure 4.10 gives a schematic overview of the reaction scenario on the Ni surface and on the $AuNi_3$ alloy.

The reaction with atomic oxygen is less exothermic than for the reaction of CO with molecular oxygen. The CO oxidation is endothermic of 0.30 eV, see Table 4.6, and the

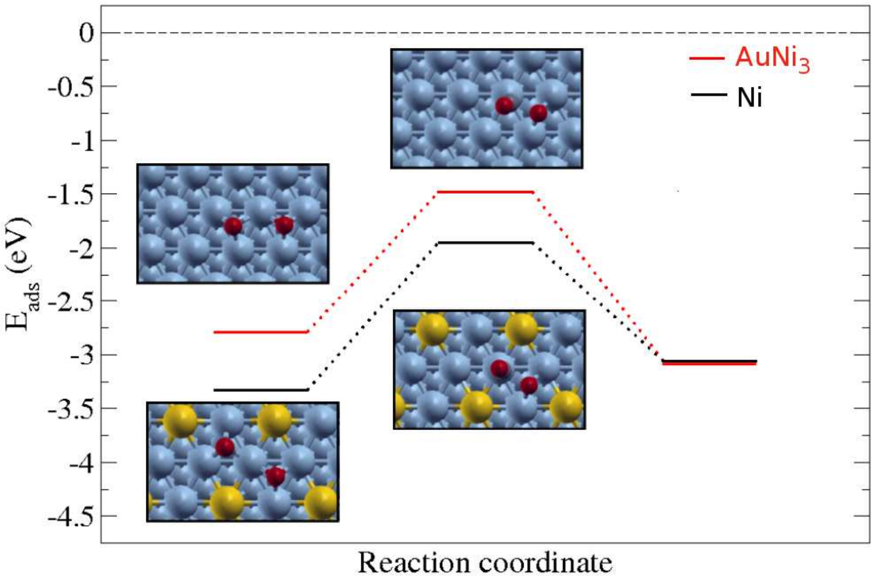

Figure 4.10: Reaction path for the reaction of CO with atomic oxygen over Ni (top) and $AuNi_3$ surfaces (bottom). Blue spheres stand for Ni, yellow for Au, and grey and red spheres for carbon and oxygen atoms respectively.

activation energy is found to be 1.38 eV. These energy barriers are in agreement with previous calculations. [37, 40]

| | $\Delta E$ | $E_a$ | $d^{TS}_{CO-O}$ | $\nu_i$ | $T_m$ |
|---|---|---|---|---|---|
| Ni | 0.27 | 1.38 | 1.769 | 438 | 498 |
| $AuNi_3$@Ni | -0.28 | 1.31 | 1.810 | 382 | 471 |

Table 4.6: Reaction energies, $\Delta E$ in eV, and barriers, $E_a$ in eV, for the reaction of CO with atomic oxygen on Ni and on $AuNi_3$@Ni alloy. The distances, $d^{TS}_{CO-O}$ in Å, and the imaginary frequencies, $\nu_i$ in $cm^{-1}$, that characterise the transition states are reported. $T_m$ in K, is the minimum temperature calculated by Equation 4.2, at which the reaction can take place.

The introduction of Au atoms in the surface provokes a decrease in the activation energy of about 0.07 eV. The minimum temperatures, $T_m$, at which the reaction of CO with atomic oxygen takes place have been calculated with Equation 4.2, and the temperature found is higher than the corresponding for the reaction of CO with coadsorbed $O_2$. Therefore, the reaction of CO with atomic oxygen never takes place at low temperatures (below 300 K).

In summary, calculations demonstrate that while the main route for CO oxidation on Ni implies $O_2$ dissociation, on the AuNi alloys, at low temperature CO oxidation path by molecular oxygen is more likely. However, the process is not catalytic since remaining O atoms on the surface can not be eliminated until high temperature, T ~ 400 K, is reached.

## 4.7 Conclusions

In the present chapter, the elementary steps involved in the CO oxidation with atomic and molecular oxygen on transition metal surfaces, Ni, Pd and Pt, and bimetallic alloys (0.25 ML Au on the surface), have been described. The conclusions from this chapter are:

- With respect to the CO adsorption ($\theta_{CO} = 0.25$ ML)
  - The CO adsorption is very exothermic. Pd is the most prone towards CO adsorption and the weakest CO bond takes place on Pt.
  - On Ni and Pd, the CO adsorption on hollow sites is favoured with respect to CO bonding on-top sites. On Pt, the theoretical binding energies on-top and on hollow sites are very similar but experimentally it is known the on-top site preference.
  - The CO adsorption is weaken on the alloys with respect to that on monometallic surfaces.
    - The effect most pronounced is observed for CO adsorption on Au-Ni alloy.
    - The CO adsorption does not take place on Au atoms in the alloys.
    - The addition of Au in the surface, alters the width and centre of the metal *d*-band and thus shifts the CO intermolecular frequency.
- With respect to the $O_2$ adsorption
  - $O_2$ is strongly chemisorbed in a threefold hollow on Ni, with small difference between the adsorption energies in tfcc and thcp sites. On Pd and Pt the $O_2$ adsorption is weaker than on Ni, and there is a pronounced preference for the tfcc over the thcp hollow.
  - The $O_2$ adsorption site has influence on the bond length and the magnetic moment of the adsorbed $O_2$ molecule:
    - $O_2$ in a tbt site is compatible with a superoxo-like $O_2^-$ precursor.
    - $O_2$ in a hollow site is midway between superoxo-like $O_2^-$ state, and peroxo $O_2^{2-}$ state.
  - The $O_2$ stretching frequencies are also dependent on the adsorption site. The highest peak corresponds to the tbt molecular adsorption.
  - The $O_2$ adsorption is weaken on the alloys with respect to that on monometallic surfaces.

    - The $O_2$ distances to the alloy are slightly longer than the clean surface ones.
    - The molecular oxygen adsorption does not take place in the sites in which one Au atom is involved.

- With respect to the atomic oxygen adsorption
  - Atomic oxygen prefers fcc sites in Ni, Pd and Pt surfaces. The difference with the hcp site is lower than 0.1 eV for the Ni surface, being larger for the Pd and Pt ones.
  - The oxygen adsorption energy decreases on all positions of the $AuNi_3$ and $AuPd_3$ surfaces compared with the Ni and Pd ones. The Au presence produces confinement on the O adsorption.
    - On $AuNi_3$ alloy, the higher adsorption energy takes place on the $Ni_3$ hollow. The adsorption energy is lower than -0.1 eV in the neighbouring sites of Au.
    - On $AuPd_3$ alloy the corrugation respect to Pd is less pronounced than the corresponding for the $AuNi_3$@Ni pair.

- With respect to the molecular oxygen dissociation
  - In Ni surface, the formation of two oxygen atoms in the hcp sites is reached by a rotation from the molecular precursor in the most stable position. The energetic barrier is much lower than the binding energy of the precursor.
  - In $AuNi_3$ surface alloy, the $O_2$ dissociation path observed for Ni is blocked. A different final state, with two oxygen atoms in hcp and fcc sites is reached in the alloy. The longer life presented on $AuNi_3$ respect to on the monoatomic surface is the origin of the low temperature CO oxidation experimentally found when an $AuNi_3$ surface alloy is used.

- With respect to the CO oxidation
  - In Ni surface, the $O_2$ dissociation is likely at low temperatures, and the atomic oxygen is strongly bound on the surface. Thus, the CO reaction with active oxygen atoms in the surface is the rate-limiting step.
  - In $AuNi_3$ surface alloy, molecular oxygen can act as oxidant at low temperatures. However, the reaction is not catalytic since remaining O atoms on the surface can not be eliminated until high temperatures are reached.

# Chapter 5

# Direct hydrogen peroxide synthesis on Pd and Pd-containing alloys

The reaction mechanisms that drive to the formation of hydrogen peroxide directly from its elements and the competitive formation of water or hydroxyl groups have been studied by Density Functional Theory, DFT, applied to slabs for Pd monometallic system and $MPd_3$ bimetallic alloys (with M=Au, Pt and Ag) on the most stable surface face (111). The essential part of this theoretical study is to explain the better performance experimentally found for gold containing alloys,[65, 66, 67] in the direct hydrogen peroxide formation. In Appendix C, a water layer has been modeled as solvent to study its role in the direct $H_2O_2$ synthesis.

## 5.1 Description of methods and models

The VASP [148, 149, 150] code was employed to obtain the energies through the RPBE functional.[124] Monoelectronic states corresponding to the valence electrons were expanded in plane waves with a kinetic cut-off energy of 400 eV, while the core electrons were represented by PAW pseudopotentials.[151, 152] With this set up the Pd unit cell parameter is calculated to be 3.987 Å, in reasonable agreement with the experimental value 3.891.[172] For the mechanistic studies the slabs contain 4 layers of Pd being interleaved by 12 Å of vacuum.

The alloys were represented by a substitutional model, $MPd_3$@Pd, where only a 0.25 ML of Pd atoms on the surface were replaced by M=Au, Pt and Ag. By this impurity model similar concentrations to the ones determined experimentally are obtained.[14] Under these conditions all impurities tend to stay on the Pd surface due to its lower surface energy; Pd provokes segregation to the surface.[173] For the gold case, a second model has also been tested where the lowest three layers correspond to bulk Au, $AuPd_3$@Au. In this case, the $AuPd_3$ surface has been adapted to follow the lattice constant of the metal underneath. The gold unit cell parameter has been calculated to be 4.208 Å, in reasonable agreement with the experimental value 4.078.[172]

In the reaction mechanism studies, the employed surface unit cell is of two types: first, a small *p*(2x2) reconstruction was performed, and in a second step larger *p*(4x2) supercells were used to test the effect of lateral interactions (hydrogen bonding). Transition state structures were determined by the Climbing Image version of the Nudged Elastic band, CI-NEB, and by the dimer algorithms.[161, 162] In all cases, the vibrational frequencies were calculated to ensure that the structure found was a transition state.

## 5.2 The possible routes involved in the direct water peroxide formation

The competitive paths involved in the direct water peroxide formation are represented in the Figure 5.1. The scheme shows not only the hydrogenation steps conducting to $H_2O_2$ formation ($O_2$, $H_2$ adsorptions and hydroperoxide formation) but also lateral decomposition paths (oxygen dissociation, water formation, $O_2H$ and $H_2O_2$ splitting and water peroxide over-hydrogenation). Each reaction will be analysed by DFT in the following sections employing the models and set up described in the previous section.

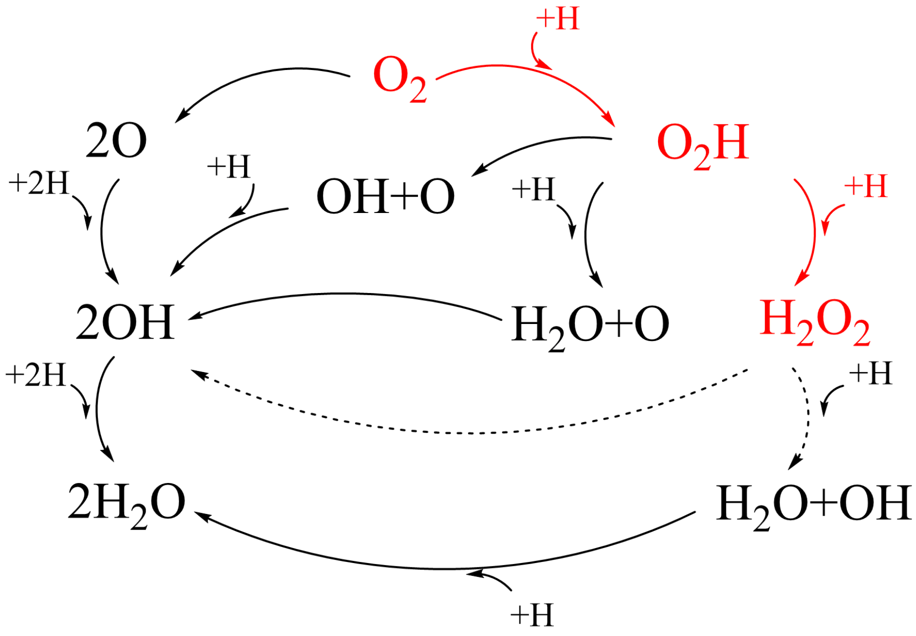

Figure 5.1: Competitive paths involved in the direct water peroxide synthesis. The reactions that drive the $H_2O_2$ formation are in red. Possible decomposition paths are dashed lines.

### 5.2.1 $O_2$ adsorption

The molecular $O_2$ precursor is adsorbed on Pd and $MPd_3(111)$ surfaces on different adsorption sites, see Table 5.1. Three different adsorption sites have been tested (tfcc, thcp and tbt). The most stable adsorption site on pure Pd is tfcc configuration where one of the oxygen atoms is directly in contact with a Pd atom while the second oxygen is in an fcc centre. In that case, the magnetic moment is completely quenched, and the binding energy to the surface is around 0.4 eV while the O-O distance is larger than in the free $O_2$ molecule, $O_2^{2-}$ (1.366 to be compared to 1.236 Å). For the alloys, $O_2$ is less bonded to the surface. The binding energies are higher for the Ag containing alloy than for the Pt and Au containing ones. A second feature of the adsorption is the possibility of changing the most stable adsorption site. This takes place for the gold and silver containing alloys, being the difference in adsorption energies from the tbt to the tfcc sites small. The tbt adsorption sites present shorter distances, higher frequencies and some magnetisation (thus closer to $O_2^-$ species) while on tfcc or thcp sites longer distances and smaller frequencies are retrieved. In the cases of Pd and $AgPd_3$@Pd no magnetisation is found (closer to properties of the peroxo $O_2{}^{2-}$ ion). The O-O bond length increases (1.31-1.37 Å) upon the adsorption with respect to the free $O_2$ molecule, a common characteristic for all surfaces.

| | site | $BE$ | $d_{O-O}$ | $\mu_B$ | $\nu$ |
|---|---|---|---|---|---|
| Pd | **tfcc** | 0.40 | 1.366 | 0.00 | 1050 |
| | tbt | 0.37 | 1.324 | 0.86 | 932 |
| | thcp | 0.28 | 1.360 | -0.08 | 914 |
| $AuPd_3$@Pd | tfcc | 0.22 | 1.357 | -0.21 | 939 |
| | **tbt** | 0.24 | 1.316 | 0.93 | 1071 |
| | thcp | 0.09 | 1.328 | 0.68 | 945 |
| $AuPd_3$@Au | tfcc | 0.23 | 1.352 | 0.88 | 934 |
| | **tbt** | 0.28 | 1.310 | 1.57 | 1121 |
| | thcp | 0.21 | 1.341 | 0.85 | 992 |
| $PtPd_3$@Pd | **tfcc** | 0.26 | 1.353 | 0.17 | 957 |
| | tbt | 0.23 | 1.314 | 0.96 | 1089 |
| | thcp | 0.14 | 1.354 | 0.03 | 953 |
| $AgPd_3$@Pd | tfcc | 0.34 | 1.369 | 0.05 | 913 |
| | **tbt** | 0.35 | 1.327 | 0.90 | 1042 |
| | thcp | 0.30 | 1.368 | -0.01 | 912 |

Table 5.1: Adsorption sites, binding energies, $BE$ in eV; distances between oxygen atoms, $d_{O-O}$ in Å; magnetic moment, $\mu_B$ in Bohr magneton; and stretching frequency, $\nu$ in cm$^{-1}$; for molecular $O_2$ adsorption on different sites of the Pd and $MPd_3(111)$ surfaces. The most stable adsorption site in each case is indicated in bold.

### 5.2.2 $H_2$ adsorption and dissociation

$$H_2^{gas} + 2* \longleftrightarrow 2H^* \tag{5.1}$$

Molecular hydrogen readily adsorbs on the Pd(111) surface.[174, 175] The barrier for the process is under reactants and therefore the process is easy under normal reaction conditions. Upon $H_2$ dissociation H atoms occupy three-fold sites on the Pd surface with a binding energy of 0.82 eV per molecular hydrogen, see Table 5.2. If the chemical potential of $H_2$ is high, i.e. high $H_2$ pressures, a surface hydride layer or even a bulk hydride can be formed, see Section 8.2 in Chapter 8.[104]

When a second metal is present the binding energies are reduced (except in the case of $AuPd_3$@Au due to the elongation of the lattice) but the adsorption sites are not perturbed. Then, the Brønsted-Evans-Polanyi relationship,[137, 138] predicts that the barrier for $H_2$ dissociation increases in the presence of a second metal. However, this effect is very small at the conditions employed in the $H_2O_2$ process. As a consequence, the presence of a second metal on the surface does not affect severely hydrogen dissociation on the surface. The largest barrier found for this process is only 0.27 eV over reactants for the $AuPd_3$@Pd and $PtPd_3$@Pd cases.

| | final site | $BE$ | $E_a$ | $d^{TS}_{H-H}$ | $\nu_i$ |
|---|---|---|---|---|---|
| Pd | 2fcc | 0.82 | 0.15 | 1.286 | 1076 |
| $AuPd_3$@Pd | 2fcc | 0.60 | 0.27 | 1.321 | 924 |
| $AuPd_3$@Au | 2fcc | 0.86 | 0.22 | 1.532 | 652 |
| $PtPd_3$@Pd | 2fcc | 0.80 | 0.27 | 1.399 | 833 |
| $AgPd_3$@Pd | 2fcc | 0.71 | 0.17 | 1.334 | 915 |

Table 5.2: Dissociative binding energies, $BE$ in eV/$H_2$; reaction barriers, $E_a$ in eV; distances between hydrogens at the transition state structure, $d^{TS}_{H-H}$ in Å; and imaginary frequencies at the TS structure, $\nu_i$ in $cm^{-1}$; for $H_2$ adsorption on Pd and $MPd_3(111)$ surfaces, (M= Au, Pt and Ag).

### 5.2.3 Hydroperoxide formation

Once the molecular $O_2$ precursor is adsorbed on the surface, the sequential hydrogenation steps can lead to the formation of hydrogen peroxide. The first step for this process is the hydroperoxide formation, schematically represented in Figure 5.2.

$$O_2^* + H^* \longleftrightarrow O_2H^* + * \tag{5.2}$$

The tbt adsorption site of $O_2$ has been taken as starting point to characterise the hydroperoxide formation. The first hydrogenation of $O_2$ takes place from a neighbouring fcc site. The hydrogen atom is activated towards the oxygen precursor and at the transition state the H is only bonded to the surface through the one of the Pd atoms where the $O_2$ molecule is adsorbed. This kind of on top activation is common to hydrogenations of organic moieties and ammonia.[176] The reaction is close to be thermoneutral for Pd and $PtPd_3$@Pd, and slightly exothermic, around 1/3 of eV, in the rest of the cases, see Table 5.3. The energy barriers are lower for the $AuPd_3$ and $AgPd_3$@Pd systems, with values close to 0.8 eV, than for the resting Pd and $PtPd_3$@Pd ones, with values close to 1 eV. In the final state, the hydroperoxide, $O_2H$, is bonded to the surface in a tbt configuration and the H atom is lying almost parallel to the surface.

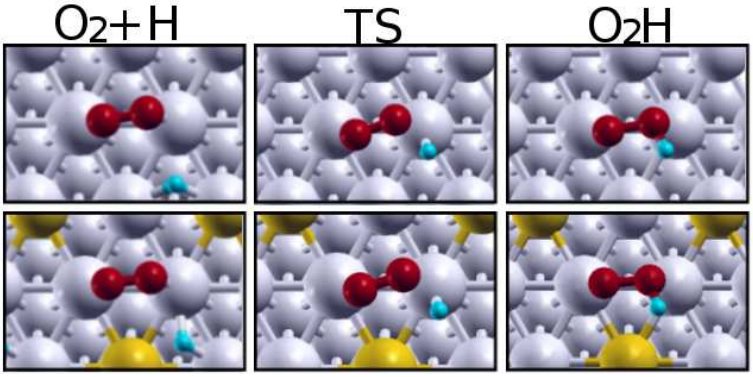

Figure 5.2: Initial, transition and final state configurations for the hydroperoxide formation on Pd (top) and $AuPd_3$ surface (bottom). Deep blue spheres stand for Pd, yellow for Au, and red and blue spheres for oxygen and hydrogen respectively.

| | $\Delta E$ | $E_a$ | $d^{TS}_{O-O}$ | $d^{TS}_{O-H}$ | $\nu_i$ | $d^{f}_{O-O}$ | $\mu_B$ |
|---|---|---|---|---|---|---|---|
| Pd | -0.07 | 0.96 | 1.339 | 1.599 | 1014 | 1.472 | 0.03 |
| $AuPd_3$@Pd | -0.34 | 0.77 | 1.330 | 1.635 | 944 | 1.465 | 0.00 |
| $AuPd_3$@Au | -0.25 | 0.76 | 1.288 | 1.585 | 782 | 1.460 | 0.10 |
| $PtPd_3$@Pd | -0.13 | 1.01 | 1.326 | 1.625 | 1071 | 1.460 | 0.00 |
| $AgPd_3$@Pd | -0.31 | 0.77 | 1.336 | 1.642 | 912 | 1.476 | 0.14 |

Table 5.3: Reaction energies, $\Delta E$ in eV; reaction barriers, $E_a$ in eV; O-O and O-H distances at the transition state structure, $d^{TS}_{O-O}$, $d^{TS}_{O-H}$ in Å; imaginary frequency at the TS, $\nu_i$ in $cm^{-1}$; O-O distances at the final structure, $d^{f}_{O-O}$ in Å; and magnetic moment; $\mu_B$ in Bohr magneton; for the hydrogenation of $O_2$ to hydroperoxide.

### 5.2.4 Hydrogen peroxide formation

Two different routes can take place in the hydrogenation of the hydroperoxide species, $O_2H^*$, one leads to the desired product, $H_2O_2$, and the other evolves towards the formation of a water molecule and an isolated O atom adsorbed on the surface. If the attack takes place on the oxygen, the final product will be the desired hydrogen peroxide.

$$O_2H^* + H^* \longleftrightarrow H_2O_2^* + * \tag{5.3}$$

To the formation of hydrogen peroxide two possible routes are open either in an *anti*-fashion , Figure 5.3, or a *syn*-fashion, Figure 5.4, with respect to the H in the hydroperoxide structure.

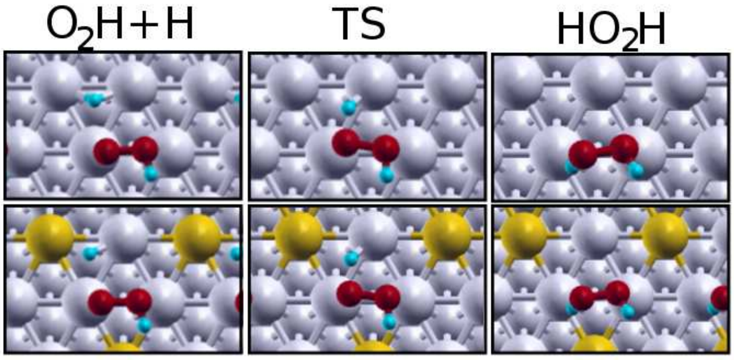

Figure 5.3: Initial, transition and final state for the hydrogenation of hydroperoxide to form hydrogen peroxide, *anti*-attack. Same colour code as Figure 5.2.

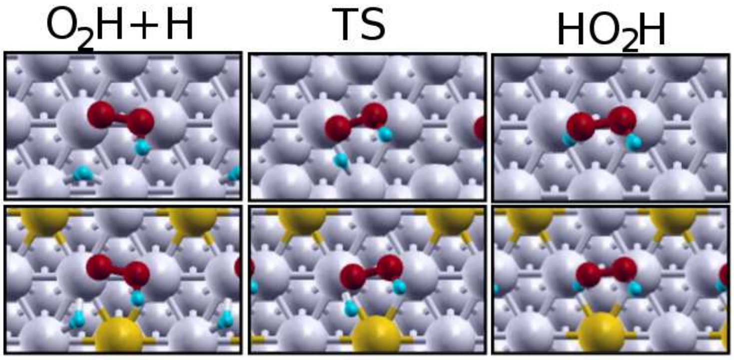

Figure 5.4: Initial, transition and final state for the hydrogenation of hydroperoxide to form hydrogen peroxide, *syn*-attack. Same colour code as Figure 5.2.

In the *anti*-attack both the H from the $O_2H^*$ and the incoming H are in a *trans*-fashion. The reaction energies are exothermic in all cases and quite large for $AuPd_3$ and $AgPd_3$ alloys, 0.8-0.9 eV, as a consequence, the barriers are very small in these cases, about 0.14 eV. For clean Pd and $PtPd_3$ the reaction is exothermic only by 0.5 eV, and the activation barriers are around 0.4 eV, see Table 5.4.

| | $\Delta E$ | $E_a$ | $d^{TS}_{O-O}$ | $d^{TS}_{O-H}$ | $\nu_i$ | $d^{f}_{O-O}$ | $\mu_B$ |
|---|---|---|---|---|---|---|---|
| Pd | -0.54 | 0.37 | 1.458 | 1.594 | 532 | 1.477 | 0.09 |
| $AuPd_3$@Pd | -0.90 | 0.13 | 1.450 | 1.730 | 356 | 1.476 | -0.07 |
| $AuPd_3$@Au | -0.80 | 0.14 | 1.448 | 1.925 | 260 | 1.474 | 0.00 |
| $PtPd_3$@Pd | -0.50 | 0.48 | 1.442 | 1.782 | 498 | 1.473 | -0.04 |
| $AgPd_3$@Pd | -0.82 | 0.12 | 1.452 | 1.731 | 286 | 1.474 | 0.01 |

Table 5.4: Reaction energies and reaction barriers, $\Delta E$ and $E_a$ in eV; O-O and O-H distances at the transition state structure, $d^{TS}_{O-O}$, $d^{TS}_{O-H}$ in Å; imaginary frequency at the TS, $\nu_i$ in $cm^{-1}$; O-O distances at the final structure, $d^{f}_{O-O}$ in Å; and magnetic moment, $\mu_B$ in Bohr magneton; for the formation of hydrogen peroxide from hydroperoxide, *anti*-attack.

For the *syn*-attack the reaction energies are in the range of 0.43-0.76 eV, that is less exothermic than the corresponding to the *anti*-mode. However, the less bounded character of the transition state structure due to the inclusion of the H along the Pd-O bond is the origin of larger barriers. Thus, the *syn*-attack is less likely than the *anti*-attack , see Table 5.5. This is reasonable due to the anti-conformer gas-phase $H_2O_2$ structure.

| | $\Delta E$ | $E_a$ | $d^{TS}_{O-O}$ | $d^{TS}_{O-H}$ | $\nu_i$ | $d^{f}_{O-O}$ | $\mu_B$ |
|---|---|---|---|---|---|---|---|
| Pd | -0.47 | 0.47 | 1.459 | 1.615 | 518 | 1.475 | 0.09 |
| $AuPd_3$@Pd | -0.76 | 0.42 | 1.450 | 1.686 | 677 | 1.476 | -0.07 |
| $AuPd_3$@Au | -0.63 | 0.54 | 1.447 | 1.700 | 686 | 1.474 | 0.00 |
| $PtPd_3$@Pd | -0.43 | 0.29 | 1.448 | 1.809 | 400 | 1.473 | -0.04 |
| $AgPd_3$@Pd | -0.65 | 0.57 | 1.453 | 1.670 | 768 | 1.474 | 0.01 |

Table 5.5: Reaction energies and reaction barriers, $\Delta E$ and $E_a$ in eV; O-O and O-H distances at the transition state structure, $d^{TS}_{O-O}$, $d^{TS}_{O-H}$ in Å; imaginary frequency at the TS, $\nu_i$ in $cm^{-1}$; O-O distances at the final structure, $d^{f}_{O-O}$ in Å; and magnetic moment, $\mu_B$ in Bohr magneton; for the formation of hydrogen peroxide from hydroperoxide, *syn*-attack.

### 5.2.5 Decomposition routes

The possible decomposition routes can be summarised in two categories: O-O bond splitting and over-hydrogenations. O-O bond splitting covers direct the $O_2$ dissociation and hydroperoxide or hydrogen peroxide splitting. Over-hydrogenations can happen in the already hydrogenated $O_2$ and in the formed hydrogen peroxide.

#### Molecular oxygen dissociation

$$O_2^* + * \longleftrightarrow 2O^* \tag{5.4}$$

$O_2$ dissociation takes place from the molecular precursor, $O_2^*$. For Pd the reaction starts at the tfcc site, leading to two atoms in the hcp sites by a rotation, see Figure 5.5.

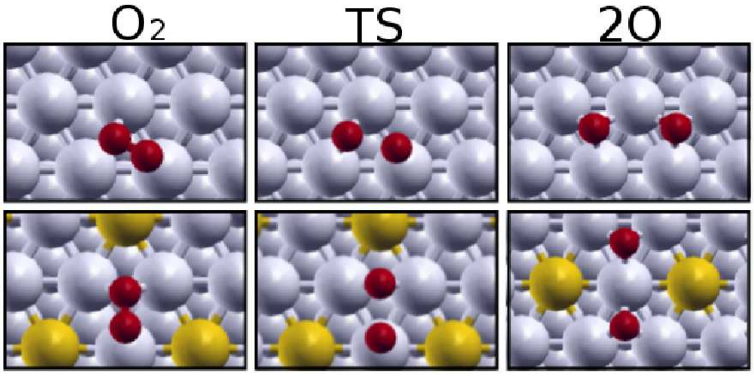

Figure 5.5: Initial, transition and final states for the decomposition of molecular oxygen into two oxygen atoms on Pd (top figure) and on $AuPd_3$@Pd surface (bottom figure).

On Pd, the barrier for dissociation is larger than the desorption energy by ∼ 0.4 eV (Table 5.1), and the reaction is exothermic by 1.0 eV, see Table 5.6.

For the alloys, the reaction also starts with molecular oxygen in a fcc site, but the final state, two atoms in the hcp sites, is reached by the unidirectional oxygen splitting, see Figure 5.5. In these alloys the barriers for dissociation are close to 0.8 eV larger than the desorption energy while the reactions present a exothermicity close to Pd ones. For the rest of the alloys, Pt and Ag containing alloys, both mechanisms (like Pd path and $AuPd_3$ ones) can be considered, and the energy barriers obtained on both are very similar, 1.04 and 0.80 eV for alloys with Pd and Ag impurities respectively. The reactions on these alloys are also exothermic and range from 0.99 eV for the $PtPd_3$ alloy to the most exothermic 1.35 eV for $AgPd_3$. In all surfaces the O-O distances at the transition state have been elongated with respect to the $O_2$ adsorbed value, and they are about 2 Å.

| | Initial site | Final sites | $\Delta E$ | $E_a$ | $d^{TS}_{O-O}$ | $\nu_i$ |
|---|---|---|---|---|---|---|
| Pd | tfcc | 2hcp | -1.07 | 0.81 | 1.983 | 335 |
| $AuPd_3$@Pd | tfcc | 2hcp | -1.04 | 1.07 | 2.121 | 294 |
| $AuPd_3$@Au | tfcc | 2hcp | -1.08 | 0.98 | 2.025 | 422 |
| $PtPd_3$@Pd | tfcc | 2hcp | -0.99 | 1.04 | 2.050 | 300 |
| $PtPd_3$@Pd | tfcc | 2hcp-Pt | -1.37 | 1.04 | 2.011 | 397 |
| $AgPd_3$@Pd | tfcc | 2hcp | -1.35 | 0.80 | 2.080 | 256 |
| $AgPd_3$@Pd | tfcc | 2hcp-Ag | 0.03 | 0.81 | 1.992 | 284 |

Table 5.6: Dissociation energies, $\Delta E$ in eV, and barriers, $E_a$ in eV; together with the initial and final sites for $O_2$ dissociation on the Pd and $MPd_3$ surfaces, (M= Au, Pt, and Ag). The distances at the transition state structure, $d^{TS}_{O-O}$, are reported in Å, and the imaginary frequencies at the transition state, $\nu_i$ in $cm^{-1}$.

Once molecular oxygen has been dissociated, it can react with hydrogen forming a hydroxyl group on the surface. However, the energy barriers found on Pd and $AuPd_3$@Pd are high, 1.02 and 1.08 eV for Pd and $AuPd_3$@Pd respectively. In Table 5.7 the main characteristics for the hydroxyl formation have been compiled.

| $O^* + H^* \rightarrow OH^* + {}^*$ | $\Delta E$ | $E_a$ | $d^{TS}_{O-H}$ | $\nu_i$ |
|---|---|---|---|---|
| Pd | -0.25 | 1.02 | 1.531 | 1240 |
| $AuPd_3$@Pd | -0.42 | 1.08 | 1.568 | 1118 |

Table 5.7: Reaction energies, $\Delta E$ in eV; and reaction barriers, $E_a$ in eV; O-H distances at the transition state structure, $d^{TS}_{O-H}$ in Å; and imaginary frequency at the TS, $\nu_i$ in $cm^{-1}$, for the hydroxyl formation on Pd and $AuPd_3$@Pd surfaces.

### Hydroperoxide splitting

One of the possible sources of unselective character lays at the centre of the synthetic route. $O_2H^*$ can be splitted into a hydroxyl group and an oxygen atom on the surface.

$$O_2H^* \longleftrightarrow OH^* + O^* \tag{5.5}$$

If the hydroperoxy species is considered sitting at the tbt site, it can rotate and break leading to adsorbed products in fcc, $O^*$, and on top, $OH^*$, which is pointing to the adsorbed oxygen in a hydrogen bonded configuration, see Figure 5.6.

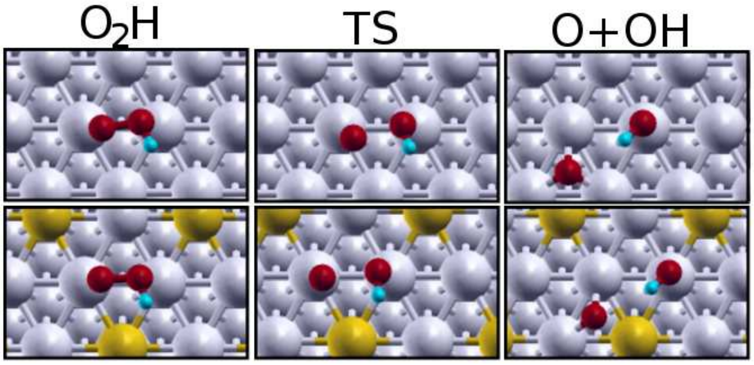

Figure 5.6: Initial, transition and final state for the decomposition of hydroperoxo intermediate in hydroxyl and oxygen fragments on Pd (top) and $AuPd_3@Pd$ (bottom) surfaces.

The reaction is exothermic, small $\Delta E$ values are found for Au and Ag containing alloys, about 1 eV, while larger energies are obtained for Pt and clean Pd. In all cases, the transition state configuration shows the hydroxyl group and oxygen atom binding to the active Pd atoms. The energy barriers are found to be in the range 0.24-0.40 eV, see Table 5.8.

| | $\Delta E$ | $E_a$ | $d^{TS}_{O-O}$ | $\nu_i$ | $d^{f}_{O-O}$ | $\mu_B$ |
|---|---|---|---|---|---|---|
| Pd | -1.68 | 0.27 | 1.911 | 304 | 3.412 | 0.00 |
| $AuPd_3@Pd$ | -0.96 | 0.37 | 2.091 | 107 | 3.471 | -0.43 |
| $AuPd_3@Au$ | -1.09 | 0.37 | 2.189 | 263 | 3.668 | 0.02 |
| $PtPd_3@Pd$ | -1.62 | 0.40 | 2.128 | 200 | 3.441 | 0.06 |
| $AgPd_3@Pd$ | -1.23 | 0.24 | 2.031 | 193 | 3.637 | -0.05 |

Table 5.8: Reaction energies, $\Delta E$ in eV; reaction barriers, $E_a$ in eV; O-O distances at the transition state structure, $d^{TS}_{O-O}$ in Å; imaginary frequency at the TS, $\nu_i$ in $cm^{-1}$; O-O distances at the final structure, $d^{f}_{O-O}$ in Å; and magnetic moment, $\mu_B$ in Bohr magneton; for the decomposition of hydrogen peroxide in hydroxyl and oxygen fragments on the surface.

This reaction pathway could be a rather important route in $O_2H$ decomposition. The initial configuration, $O_2H^*$ static sitting at the tbt site, does not correspond to the actual situation. The behaviour of $O_2H^*$ is very dynamic with two associated motions:

- $O_2H$ rotation parallel to surface plane, $(O_2H^*)_{rot}$.
- H rotation along the O-O bond, $O_2(H^*)_{rot}$.

Both movements have been studied in the Pd and the $AuPd_3@Pd$ alloy, in order to determine if they are competitive with the $O_2H$ dissociation, see Figure 5.7.

The rotation of the hydrogen is close to be thermoneutral, the energy barriers corresponding to the hydrogen rotation are 0.28 and 0.34 eV for the Pd and the $AuPd_3@Pd$

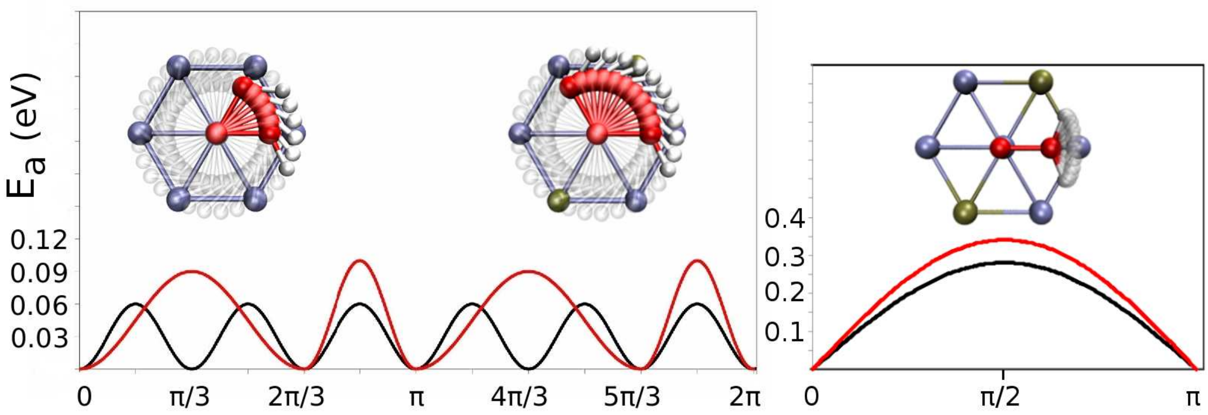

Figure 5.7: Dynamic properties of hydroperoxide on the surface. Rotation of the $O_2H^*$ intermediate (left), $(O_2H^*)_{rot}$, and H flipping around oxygen (right), $O_2(H^*)_{rot}$. Black lines represent rotations on Pd, and the red ones on $AuPd_3$@Pd(111) surface.

alloy respectively, see $O_2H^*_{rot}$ in Table 5.9. A bridge configuration transition state is found to the molecular oxygen rotation, and the activation energy required for this movement is very low, less than 0.1 eV in both surfaces, see $(O_2H^*)$(rot) in Table 5.9.

The forward rate constants, $k^+$, compiled in Table 5.9, have been calculated as function of the activation energy, $E_a$, of each reaction ($\nu = 10^{13}$ s$^{-1}$).

$$k^+ = \nu \exp(-E_a/k_B T) \tag{5.6}$$

The dynamic character of the $O_2H^*$ molecule effectively provokes that the $OH^*$ contact time with the active Pd site is shorter than that of the terminal oxygen. The order of magnitude for the $O_2H^*$ rotation rate is at least three times higher than for the $O_2H^*$ splitting. Therefore, the life-time of $O_2H^*$ on the tbt position is strongly reduced, decreasing the possibilities of $O_2H^*$ splitting. A similar effect happens with the water formation. It will be discussed in the next section.

### Water formation

$$O_2H^* + H^* \longleftrightarrow O^* + H_2O^* \tag{5.7}$$

From the hydroperoxide, the insertion of the second hydrogen atom into the molecule can drive not only to $H_2O_2$ formation. If the attack takes place in the OH fragment, the reaction leads to the formation of an adsorbed O atom on the surface, and a weakly adsorbed water molecule, see Figure 5.8.

This reaction is very exothermic due to the formation of the water molecule. Again the barriers accompanying this transformation are quite low and very similar for all the systems, between 0.26 and 0.47 eV, see Table 5.10. The lowest barrier is found for Pd followed by $AgPd_3$, thus indicating that these two systems are more prone to produce water by this route.

| | | $\Delta E$ | $E_a$ | $k^+$ |
|---|---|---|---|---|
| $O_2H^* \longleftrightarrow OH^* + O^*$ | Pd | -1.68 | 0.27 | $2.71\text{x}10^{8}$ |
| | $AuPd_3$ | -0.96 | 0.37 | $5.52\text{x}10^{6}$ |
| $O_2H^* + H^* \longleftrightarrow H_2O_2^* + {}^*$ | Pd | -2.35 | 0.26 | $4.01\text{x}10^{8}$ |
| | PdAu | -1.93 | 0.44 | $3.62\text{x}10^{5}$ |
| $(O_2H^*)_{rot}$ | Pd | -0.04 | 0.06 | $9.67\text{x}10^{11}$ |
| | $AuPd_3$ | 0.01 | 0.08/0.09 | $4.44\text{x}10^{11}$ |
| $O_2(H^*)_{rot}$ | Pd | -0.03 | 0.28 | $1.84\text{x}10^{8}$ |
| | $AuPd_3$ | 0.01 | 0.34 | $1.78\text{x}10^{7}$ |

Table 5.9: Reaction energies, $\Delta E$ in eV; reaction barriers, $E_a$ in eV; and the forward rate constants, $k^+$ in $s^{-1}$; for the $H_2O^*$ splitting, water formation and the two possible rotations of the hydroperoxide. H flipping around oxygen, $O_2(H^*)_{rot}$, and rotation of $(O_2H^*)_{rot}$ around Pd.

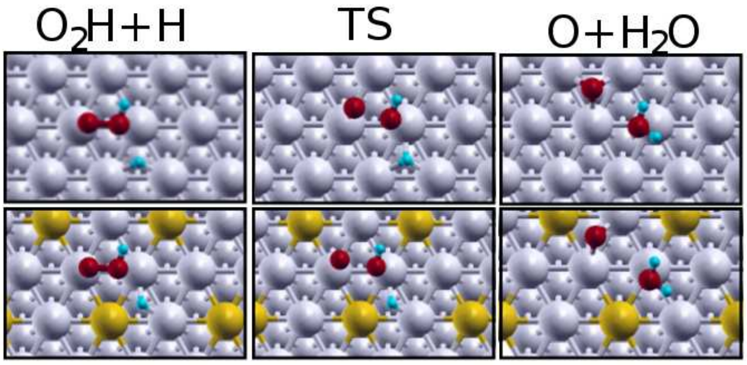

Figure 5.8: Initial, transition and final state for the hydrogenation of hydroperoxide leading to water and oxygen atoms on Pd (top) and $AuPd_3$@Pd (bottom) surfaces.

However, the transition state configuration shows that the hydroxyl group and the oxygen atom are bonded to the active Pd atoms in a similar way to the transition state of the hydroperoxide splitting. The order of magnitude for the forward rate constants, $k^+$, associated to the rotation of $O_2H^*$ around Pd, $O_2H^*$(rot), see Table 5.9, is at least three times higher than for the water formation. Therefore the dynamic properties of hydroperoxide have also as a result a lower probability of the OH hydrogenation.

| | $\Delta E$ | $E_a$ | $d^{TS}_{O-O}$ | $d^{TS}_{O-H}$ | $\nu_i$ | $d^{f}_{O-O}$ | $\mu_B$ |
|---|---|---|---|---|---|---|---|
| Pd | -2.35 | 0.26 | 1.849 | 2.507 | 332 | 3.083 | -0.05 |
| $AuPd_3$@Pd | -1.93 | 0.44 | 1.920 | 2.600 | 282 | 3.407 | -0.02 |
| $AuPd_3$@Au | -1.91 | 0.39 | 1.900 | 2.573 | 285 | 3.755 | 0.00 |
| $PtPd_3$@Pd | -2.39 | 0.47 | 1.922 | 2.492 | 297 | 3.885 | 0.04 |
| $AgPd_3$@Pd | -2.11 | 0.38 | 1.907 | 2.436 | 286 | 3.305 | 0.10 |

Table 5.10: Reaction energies and reaction barriers, $\Delta E$ and $E_a$ in eV; O-O and O-H distances at the transition state structure, $d^{TS}_{O-O}$, $d^{TS}_{O-H}$ in Å; imaginary frequency at the TS, $\nu_i$ in $cm^{-1}$; O-O distances at the final structure, $d^{f}_{O-O}$ in Å; and magnetic moment, $\mu_B$ in Bohr magneton; for the hydrogenation of hydroperoxide leading to water and oxygen atoms on the surface.

### $H_2O_2$ splitting

A second route for the deactivation is the dissociation of adsorbed hydrogen peroxide molecules. In that case, the resulting products are two hydroxyl groups adsorbed on the surface, see Figure 5.9.

$$H_2O_2^* \longleftrightarrow 2OH^* \tag{5.8}$$

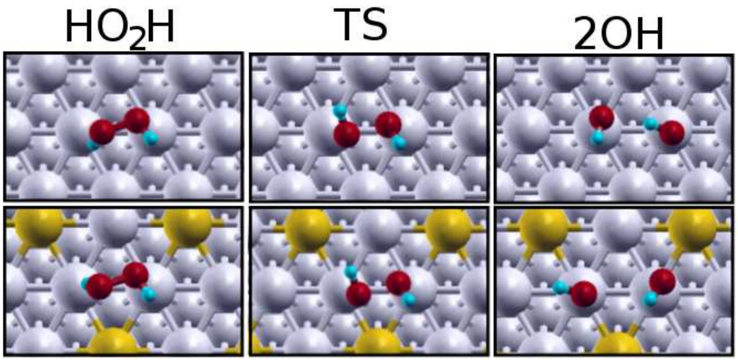

Figure 5.9: Initial, transition and final state for the decomposition of hydrogen peroxide in two hydroxyl groups on Pd (top) and $AuPd_3$@Pd (bottom) surfaces.

The binding energies of hydrogen peroxide to the surface are very weak, therefore dissociation under low water contents is likely to be show a kind of thermodynamics control.[5] However, dissociation into two hydroxyl groups has been computed and the important parameters for this reaction are shown in Table 5.11. The reaction is found to be exothermic by 1.2-1.5 eV, and the energy barriers are on the order of 0.3 eV and independent of the nature of the surface.

| | $\Delta E$ | $E_a$ | $d_{O-O}^{TS}$ | $\nu_i$ | $d_{O-O}^{f}$ | $\mu_B$ |
|---|---|---|---|---|---|---|
| Pd | -1.36 | 0.27 | 1.677 | 314 | 2.868 | -0.01 |
| $AuPd_3$@Pd | -1.24 | 0.30 | 1.680 | 331 | 3.054 | 0.01 |
| $AuPd_3$@Au | -1.22 | 0.30 | 1.750 | 510 | 2.935 | 0.00 |
| $PtPd_3$@Pd | -1.27 | 0.30 | 1.701 | 443 | 2.816 | 0.00 |
| $AgPd_3$@Pd | -1.50 | 0.25 | 1.580 | 226 | 2.816 | -0.01 |

Table 5.11: Reaction energies and reaction barriers, $\Delta E$ and $E_a$ in eV; O-O distances at the transition state structure, $d_{O-O}^{TS}$ in Å; imaginary frequency at the TS, $\nu_i$ in $cm^{-1}$; O-O distances at the final structure, $d_{O-O}^{f}$ in Å; and magnetic moment, $\mu_B$ in Bohr magneton; for the splitting of adsorbed hydrogen peroxide molecules forming two hydroxyl groups.

The presence of hydroxyl groups on the surface can be another water source; two hydroxyl groups can react forming water and atomic oxygen on the surface. However the energy barriers found on Pd and $AuPd_3$@Pd are high, see Table 5.12.

$$OH^* + OH^* \longleftrightarrow H_2O^* + O^* \tag{5.9}$$

| | $\Delta E$ | $E_a$ | $d_{O--H}^{TS}$ | $\nu_i$ |
|---|---|---|---|---|
| Pd | -0.80 | 0.26 | 1.125 | 455 |
| $AuPd_3$@Pd | -0.33 | 0.31 | 1.010 | 258 |

Table 5.12: Reaction energies and barriers, $\Delta E$ and $E_a$ in eV; O–H distances at the transition state structure, $d_{O--H}^{TS}$ in Å; and imaginary frequency at the transition state, $\nu_i$ in $cm^{-1}$; for the reaction of two hydroxyl groups on the surface driving to water and atomic oxygen

### Hydrogen peroxide over-hydrogenation

$$H_2O_2^* + H^* \longleftrightarrow OH^* + H_2O^* \tag{5.10}$$

$H_2O_2$ is very weakly adsorbed to the surface, and thus the reaction with hydrogen atoms around is unlikely. However, high hydrogen pressures or large amounts of water molecules present on the surface can increase the binding energy of the product to the surface enhancing this potential decomposition route. The important parameters for this reaction are shown in Table 5.13 and the relevant structures in Figure 5.10. The reaction is very exothermic in all surfaces, by more than 2 eV, and the reaction barriers are in the range of 0.4-0.6 eV.

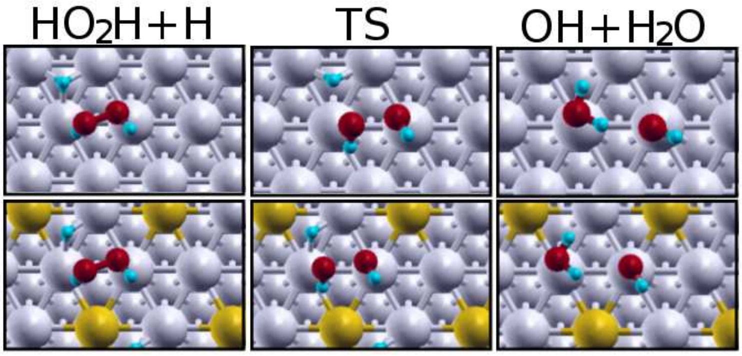

Figure 5.10: Initial, transition and final state for the hydrogen peroxide over-hydrogenation leading to water and a hydroxyl group on Pd (top) and $AuPd_3$@Pd (bottom) surfaces.

| | $\Delta E$ | $E_a$ | $d^{TS}_{O-O}$ | $\nu_i$ | $d^{f}_{O-O}$ | $\mu_B$ |
|---|---|---|---|---|---|---|
| Pd | -2.36 | 0.51 | 1.810 | 379 | 2.858 | -0.03 |
| $AuPd_3$@Pd | -2.35 | 0.60 | 1.932 | 327 | 3.004 | 0.00 |
| $AuPd_3$@Au | -2.30 | 0.37 | 2.175 | 268 | 2.997 | 0.00 |
| $PtPd_3$@Pd | -2.18 | 0.49 | 1.834 | 464 | 2.883 | 0.01 |
| $AgPd_3$@Pd | -2.42 | 0.52 | 1.787 | 546 | 3.002 | 0.20 |

Table 5.13: Reaction energies and reaction barriers, $\Delta E$ and $E_a$ in eV; O-O distances at the transition state structure, $d^{TS}_{O-O}$ in Å; imaginary frequency at the TS, $\nu_i$ in $cm^{-1}$; O-O distances at the final structure, $d^{f}_{O-O}$ in Å; and magnetic moment, $\mu_B$ in Bohr magneton; for the over-hydrogenation of $H_2O_2^*$ driving to the formation of water and a hydroxyl group.

## 5.3 Brønsted-Evans-Polanyi relationships

In order to summarise the complex chemistry for all the studied alloys and elementary steps previously showed, the relationship between the activation energies, $E_a$, and the heats of reaction, $\Delta E$, have been plotted in Figure 5.11.

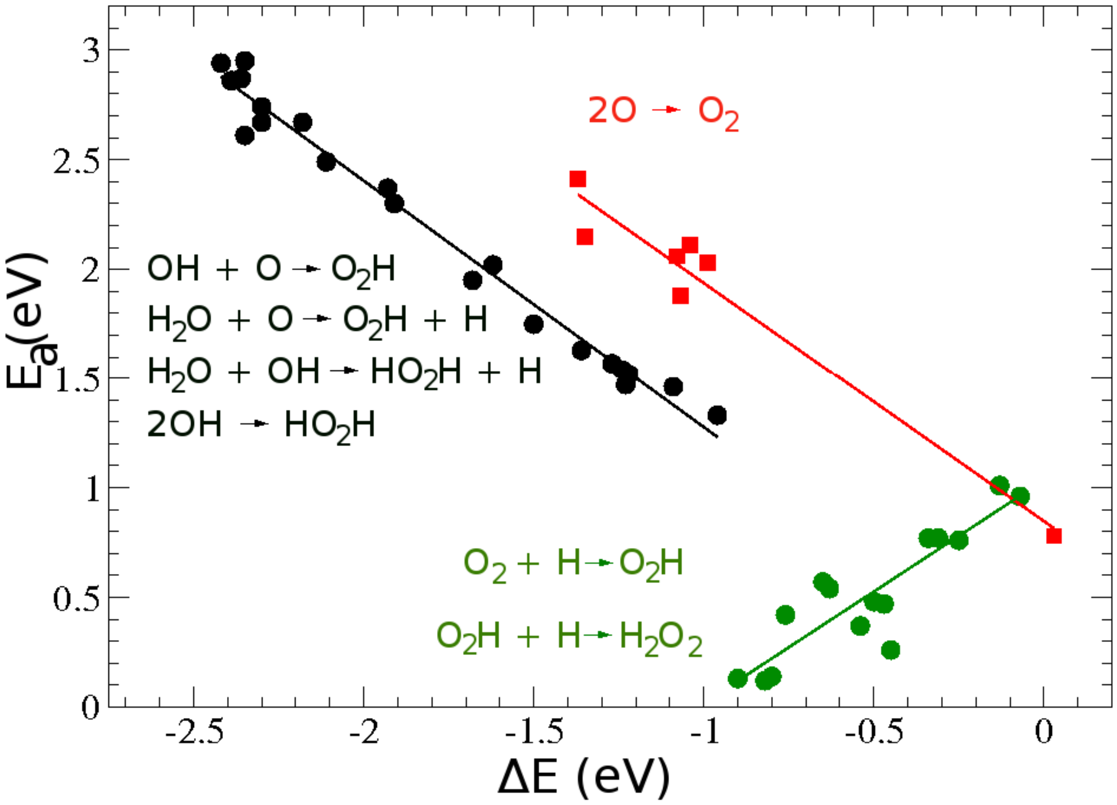

Figure 5.11: BEP relations for all the activation energy-dissociation energy pairs. The reactions corresponding with each line are written next to it in the figure. Green line: $E_a$=1.02$\Delta E$+1.03 (r=0.89). Red line: $E_a$=-1.09$\Delta E$+0.85 (r=0.98). Black line: $E_a$=-1.13$\Delta E$+0.15 (r=0.99). r is the correlation coefficient.

Three types of correlations have been reported in Figure 5.11. The green line corresponds to transformations where a $H^*$ atom is transferred to the $O_2^*$ precursor to form the intermediate $O_2H^*$, and the hydrogenation of the hydroperoxide species (both in *anti-* and *syn-* modes) to form $H_2O_2^*$, and the red line corresponds to transformations where a O-O bond is broken. The two groups have as common feature: the O-O distance at the transition state is approximately 30% elongated respect to the O-O distance at the initial state. This special characteristic makes that the relationship between the activation energy for the reverse reaction and the heats of reaction to fit better than if the energy barrier for the forward reaction is considered. Finally, the third group of data points (black line) corresponds to direct $O_2H^*$ splitting, hydrogen peroxide hydrogenation and hydrogen peroxide dissociation. In this case the O-O distance in the transition state for these points is less than 30% elongated respect to the O-O distance in the final state, that means that the transition state is like *final state*-like and the energy barrier for the forward relation is properly related with $\Delta E$. The equations of the lines of best fit for each group of points together with its correlation coefficient, r, are reported in the caption of Figure 5.11.

## 5.4 Reaction pathway

Figure 5.12 summarises the reaction paths for all reactions involved in the direct hydrogen peroxide synthesis on Pd monometallic surface and on gold containing alloy, $AuPd_3$@Pd(111). Three zones in the figure have been distinguished by colours. In the grey zone, the $O_2^*$ dissociation and the consecutive hydrogenations of the atomic oxygen formed are placed. The blue zone represents the paths associated with undesired $O_2H^*$, and $H_2O_2^*$ degradations. Finally, the white region, includes the reactions that drive to the desirable hydrogen peroxide formation. Figure 5.12 is useful to understand the better performance experimentally found when gold is added to palladium.[68, 177] Starting from the $O_2^*$ precursor molecular state and comparing dissociation and first hydrogen incorporation, the tend found in both metals is different. The suitable character of a metal for the $H_2O_2^*$ formation will be strongly depending on the relation between the activation energies for these competitive steps. On Pd, $O_2^*$ dissociation barrier, 0.81 eV, is lower than the energy barrier associated with the first hydrogenation, 1.08 eV. In the case of $AuPd_3$@Pd alloy the branching ratio changes, being the activation energy for the first hydrogenation, 0.98 eV, lower than the dissociation energy barrier, 1.07 eV.

In the next section, a simple model based on the direct rates for dissociation and first hydrogen incorporation is derived to analyse the selectivity of the direct $H_2O_2^*$ formation.

## 5.5 Selectivity study

In the previous sections, the competitive paths involve in the direct water peroxide formation were studied on Pd and $MPd_3$@Pd alloys. The goal of this section is the development of a selectivity model that allows compare catalytic activities of any transition or noble metal for the $H_2O_2$ synthesis with the knowledge of only two parameters. The adsorption energy for atomic oxygen, $E_O$, and hydrogen, $E_H$. The selectivity model is extensively described in Appendix B. In this section only main equations are written and the conclusions obtained from the selectivity study are discussed.

The starting point was consider the following elementary reactions with their respectively reaction rates:

UNIVERSITAT ROVIRA I VIRGILI
THEORETICAL STUDIES OF SELECTIVE PROCESSES IN HETEROGENEOUS CATALYSIS
Mónica García Mota
ISBN:978-84-693-5424-7/DL:T-1415-2010

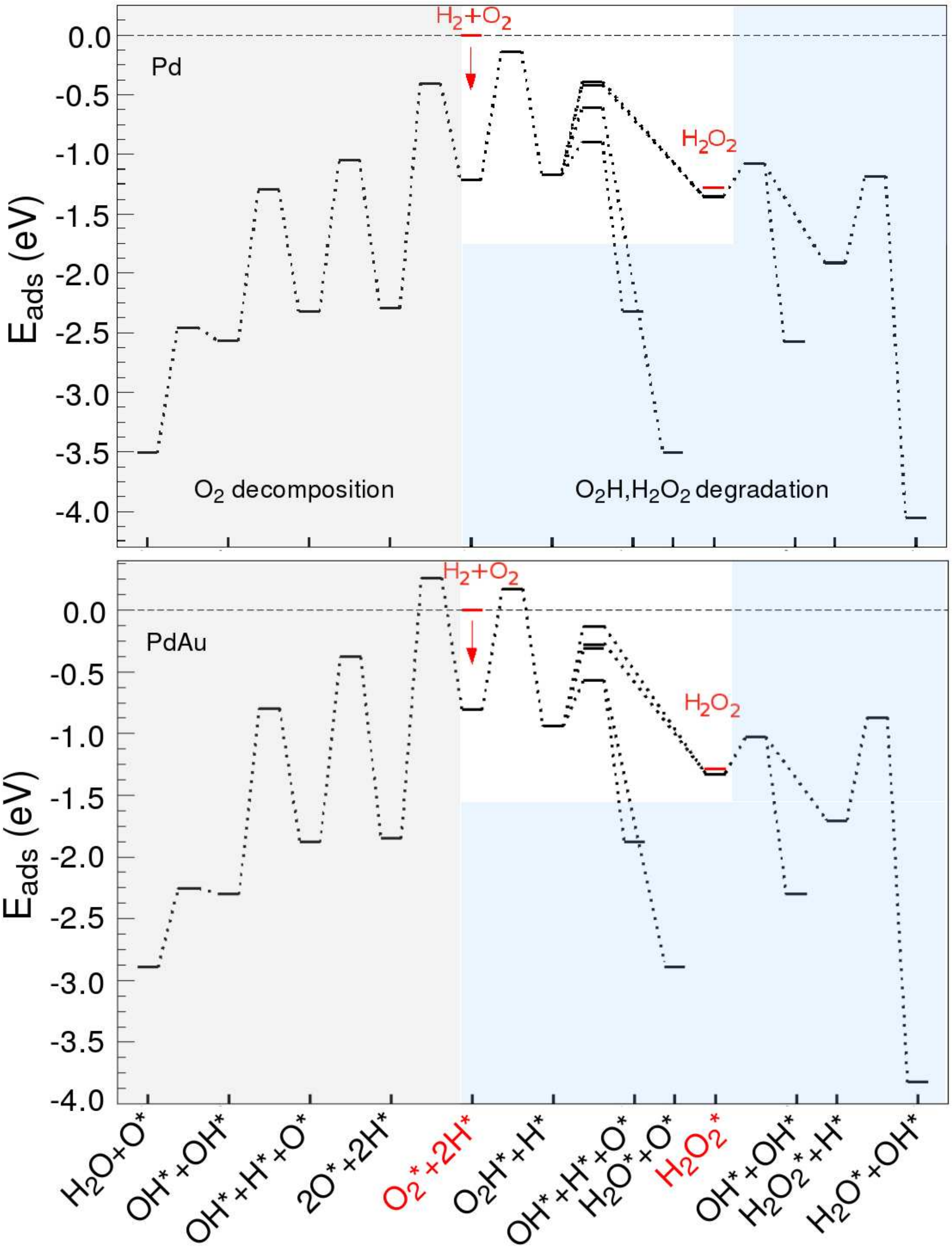

Figure 5.12: Energy profile for direct formation of $H_2O_2^*$ and for the competitive formation of water or hydroxyl groups. The catalysts employed are Pd clean surface (Top) and $AuPd_3$@Pd(111) (Bottom) The energy barriers have been calculated with respect to molecular oxygen and hydrogen placed at infinite distance.

$$H_2^{gas} + 2* \longleftrightarrow 2H^* \qquad (k_{ads,H_2}, k_{des,2H}) \tag{5.11}$$

$$O_2^{gas} + * \longleftrightarrow O_2^* \qquad (k_{ads,O_2}, k_{des,O_2}) \tag{5.12}$$

$$O_2^* + * \longleftrightarrow 2O^* \qquad (k_{3a}, k_{3b}) \tag{5.13}$$

$$O_2^* + H^* \longleftrightarrow O_2H^* + * \qquad (k_{4a}, k_{4b}) \tag{5.14}$$

$$O_2H^* + H^* \longleftrightarrow H_2O_2^* + * \qquad (k_{5a}, k_{5b}) \tag{5.15}$$

$$O_2H^* + H^* \longleftrightarrow H_2O^* + O^* \qquad (k_{6a}, k_{6b}) \tag{5.16}$$

If reactions (5.11) and (5.12) are considered in quasi-equilibrium and working at initial conditions, it is possible to focus the selectivity study on the difference between the rates associated with the oxygen dissociation, and hydroperoxide formation, $\ln(|r4-r3|)$. This parameter is the key to find the systems that drive the most selective conversion of hydrogen peroxide from its elements. The rate for the interesting steps, (5.13) and (5.14), can be expressed (after same reordering detailed in the Appendix B) as:

$$r_3 = k_{3a} K_{O_2} p_{O_2} \Theta_*^2 \tag{5.17}$$

$$r_4 = k_{4a} K_{O_2} p_{O_2} \sqrt{K_{H_2} p_{H_2}} \Theta_*^2 \tag{5.18}$$

where $k_{3a}$, and $k_{4a}$ are functions of the activation energies for the oxygen dissociation, $E_{a,3}$, and hydroperoxide formation, $E_{a,4}$, respectively. These activation energies can be written as

$$E_{a,3} = E_{TS,3} - E_{O_2} \tag{5.19}$$

$$E_{a,4} = E_{TS,4} - E_{O_2} - E_H \tag{5.20}$$

In principle, four metal dependent parameters, $E_H$, $E_{O_2}$, $E_{TS,3}$, and $E_{TS,4}$ would be needed to determine the kinetics. However, we have found the following relationships

- The $O_2$ adsorption energy, $E_{O_2}$, scales with the adsorption energy of the atomic oxygen, $E_O$.
- The transition state energy for the $O_2$ dissociation, $E_{TS,3}$, correlates with the adsorption energy of the atomic oxygen, $E_O$.

- The transition state energy for the hydroperoxide formation, $E_{TS,4}$, scales with the sum of the O and H adsorption energies, $E_O + E_H$.

The correlations corresponding with these relationships are presented in Figure B.1 on Appendix B. Therefore the interesting difference between the rates for the steps (5.13) and (5.13), $\ln(|r4 - r3|)$ can be represented in function of only two independent variables, $E_O$ and $E_H$, as is shown in Figure 5.13.

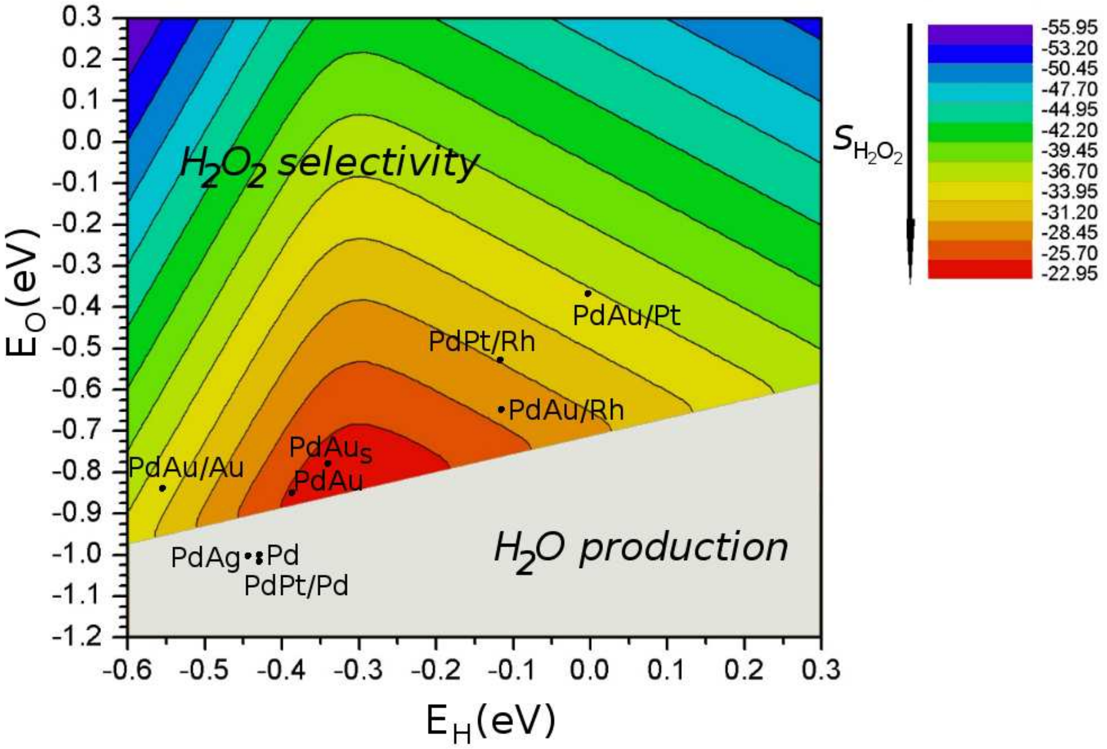

Figure 5.13: Two dimensional contour plot of $\ln(|r4 - r3|)$ as a function of $E_O$ and $E_H$. Energies are expressed in eV.

The position in the Figure 5.13 corresponding with the adsorption energy for atomic oxygen, $E_O$, and hydrogen, $E_H$, on any metal, will indicate if the surface is a suitable catalyst for the hydrogen peroxide synthesis. When the reaction rate for the step (5.13) is higher than the reaction rate for the step (5.14), the dissociation of molecular oxygen is promoted and the hydroperoxide formation does not take place. That is the case for surfaces placed in the grey area in the figure 5.13; Pd(111), and the alloys $PtPd_3$@Pd, $AgPd_3$@Pd. Because the intermediate, $O_2H^*$, is needed to form $H_2O_2^*$, suitable metals for the direct hydrogen peroxide synthesis must keep the relation $r4 - r3 > 0$. $AuPd_3$ surfaces with different metal bulk, ($AuPd_3$@M with M=Pd, Au, Rh and Pt), and $PtPd_3$ surface with Rh bulk ($PtPd_3$@Rh). The best catalyst for the hydrogen peroxide synthesis will be that with the maximum relation $r4 - r3$, and the gradient of colours for the $\ln(|r4 - r3|)$, in Figure 5.13, places the $AuPd_3$@Pd surface as the better option. If strain of 1% is applied in the surface $AuPd_3$ (it is labelled as $PdAu_s$), this surface would be also an suitable option for the direct hydrogen peroxide synthesis.

## 5.6 Conclusions

In the present chapter, the reaction mechanism that drives the selective conversion of hydrogen peroxide from its elements on Pd and Pd-containing alloys has been unravelled. All the possible reaction steps: hydrogenation, dissociation of the precursor, intermediates and products, and over-hydrogenation of intermediates and products have been considered to get a detailed picture of the chemistry in this case. The conclusions from this chapter are

- With respect to the hydrogen dissociation
    - The hydrogen dissociation is easy under normal conditions, and the presence of a second metal on the surface does not affect severely the process.
- With respect to the adsorption of the $O_2$ precursors
    - The different adsorption sites on the surface (tfcc, thcp and tbt) for the $O_2$ precursor have been tested on Pd and $MPd_3(111)$ surfaces, showing different binding energies and magnetic moments.
    - For the alloys, $O_2$ is less bonded to the surface than for pure metals. On gold and silver containing alloys, the most stable adsorption site changes respect to with that on the monometallic surfaces.
- With respect to the $O_2$ dissociation
    - The reaction takes place from the tfcc site, leading to two atoms in the hcp sites by a rotation on the Pd monometallic surface.
    - The Au presence changes the $O_2$ dissociation path. The energy barrier on $PdAu_3$@Pd is 0.2 eV higher than on Pd one.
- With respect to the hydroperoxide formation
    - The energy barriers for this process are lower for the $AuPd_3$ and $AgPd_3$@Pd systems than for the resting Pd and $PtPd_3$@Pd ones.
    - In the final state, the hydroperoxide, $O_2H$, is bonded to the surface in a tbt configuration and the H atom is lying almost parallel to the surface.
- With respect to the hydroperoxide splitting

  - $O_2H^*$ can be splitted into a hydroxyl group and an oxygen atom on the surface. In all cases the energy barriers are similar and lower than 0.4 eV.
    - Hydroxyl groups on the surface can react forming water and atomic oxygen. The energy barriers for this reaction are higher than 0.2 eV.
  - The dynamic behaviour of $O_2H^*$ reduces the life-time of the hydroperoxide on the tbt position, decreasing the probabilities of $O_2H^*$ splitting.

- With respect to the hydrogenation of the hydroperoxide species
  - Two different routes can take place. One leads to the desired product, hydrogen peroxide, through the second path the system evolves towards the formation of a water molecule.
  - If the hydrogen attack to the $O_2H$, takes place on the oxygen, the final product will be the desired hydrogen peroxide. Two possible routes are open either in a *anti-* , or an *syn*-fashion with respect to the H in the hydroperoxide structure.
    - The *syn*-attack is less likely than the *anti*. This is due to the less bounded character of the transition state structure due to the inclusion of the H along the Pd-O bond. In the *anti*-attack the reaction is less exothermic for clean Pd and $PtPd_3$ and as a consequence the energy barriers are larger for these metals.
  - In the reaction to form water
    - The barriers for this reaction are quite low and very similar for all the systems.
    - The transition state configuration shows the hydroxyl group and the oxygen atom bond to the active Pd atoms. The dynamic properties of hydroperoxide have as a consequence a decrease of probability for the OH hydrogenation.

- With respect to the hydrogen peroxide stability
  - $H_2O_2$ is very weakly adsorbed to the surface.
  - The $H_2O_2$ over-hydrogenation and the hydrogen peroxide splitting in two hydroxyl groups are unlikely.

- With respect to the selectivity study
  - The suitability of a system can be known through a simplify selectivity model by investigating the adsorption energy for atomic oxygen, $E_O$, and hydrogen, $E_H$.
  - The gold containing alloy, $AuPd_3$@Pd, is found to be the most selective catalyst, in agreement with the experimental observations done by the Hutchings' group, and further improvements by the formation of overlayers are foreseen.

# Chapter 6

# Vinyl acetate synthesis from ethene and acetic acid on Pd-based model system

Vinyl acetate synthesis from ethylene and acetic acid is mainly performed by Pd-based heterogeneous process,[15, 72, 73] The experimental evidences show that isolated Pd dimers on Au surfaces are active and selective catalysts for the vinyl acetate, $CH_3COOCHCH_2$, synthesis but a strong dependence on the local structure of the ensemble is observed.[24, 78, 79] In this chapter, by means of Density Functional Theory, DFT, several Pd dimer configurations on both Au(100) and (111) surfaces have been employed as model systems to unravel the origin of the experimental observations. Initially the synthetic process was based on homogeneous palladium catalysts,[71] and the similarities and differences on the reaction mechanisms in both homogeneous [178] and heterogeneous [179] version of the catalyst will be addressed in Section 6.6.

## 6.1 Computational details

Density Functional Theory, DFT, applied to slabs was employed to determine the adsorption energies of reactants and products involved on the VA synthesis on several Pd dimer configurations on both Au(100) and (111) surfaces. DFT calculations were performed using the Vienna Ab-initio Simulation Package, VASP.[148, 149] The Revised Perdew-Burke-Ernzerhof, RPBE,[124] was employed as exchange-correlation functional to obtain the energy. Monoelectronic states corresponding to the valence electrons were expanded in plane waves with a kinetic cut-off energy of 400 eV, while the core electrons were represented by Projector Augmented Wave, PAW, pseudopotentials.[151, 152] A dipole layer was placed in the vacuum region separating the slabs in order to avoid the artificial electrostatic field between the two sides. A finite temperature of $k_BT= 0.2$ eV was used, and total energies were extrapolated to $k_BT= 0$ eV. No spin polarisation was required for these systems.

The $k$-point sampling consisted of 2x2x1 Monkhorst-Pack points.[130] The two surface upper layers and the adsorbates were optimised while the lowest layers were kept frozen at the bulk distances. The CI-NEB method [161] was employed to locate the transition-state structures, and these transition states were characterised by a single imaginary frequency.

### 6.1.1 Pd dimer configurations

In order to explain the strong dependence on the local structure of the ensemble for the VA synthesis, several Pd dimer configurations on both Au(100) and (111) were considered, see Figure 6.1. All these configurations are likely to be present on the samples at 0.1 ML Pd coverage on Au in agreement with previous experimental and theoretical results.[11, 16, 25, 79, 180, 181] The Au theoretical cell parameter used is 4.208 Å. This value was obtained with the third-order Birch-Murnaghan isothermal equation of state.[182]

The slabs contain five layers for the (100) and four for the (111) surface in a $p$(4x4) supercell. On these surfaces, two Au atoms have been replaced by Pd atoms. For the $d_{Pd-Pd}$ distance, the configurations have been named as nearest neighbours, NN, next-nearest neighbours, NNN, with distances $d\sqrt{2}$ or $d\sqrt{3}$ for (100) and (111) surfaces respectively, and second next-nearest neighbours, 2NNN, with a Pd-Pd distance of $2d$. This notation will be used throughout this work. The relative energies to the most stable dimer for each surface are shown in Figure 6.1. In both (111) and (100) surfaces the least stable ensemble corresponds to the nearest neighbours configuration, NN, with a difference of 0.08 (111) and 0.07 eV (100) respect to the next-nearest neighbour ensemble, NNN.

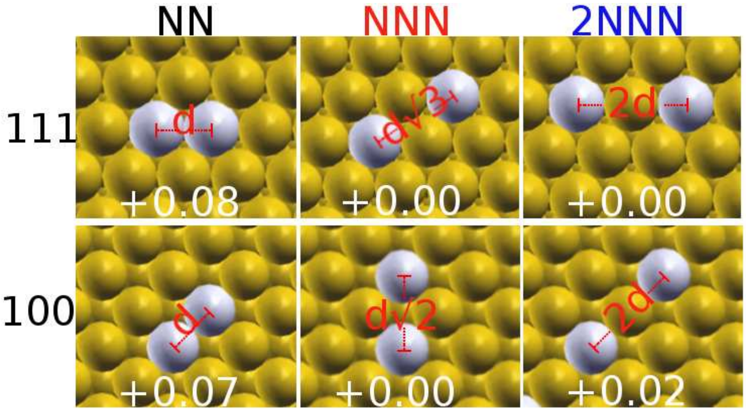

Figure 6.1: Dimer ensembles showing different local configurations on (111) and (100) Au surfaces. Yellow spheres represent Au and grey ones stand for Pd atoms. NN indicates nearest neighbours, NNN next-nearest neighbours, and 2NNN second next-nearest neighbours. The figures indicate the relative energies, in eV, to the most stable dimer on each surface. The interdimer distance is expressed in $d_{Pd-Pd}$ units.

## 6.2 Reaction Mechanism

The reaction mechanism for the vinyl acetate synthesis can be expanded in the following list of elementary steps according to a Langmuir-Hinshelwood mechanism:[80]

$O_2$ dissociation:

$$\frac{1}{2}O_2^{gas} + * \longleftrightarrow O^* \tag{6.1}$$

O-assisted dissociative adsorption of acetic acid:

$$CH_3COOH^{gas} + O^* + * \longleftrightarrow CH_3COO^* + OH^* \tag{6.2}$$

Ethylene adsorption:

$$C_2H_4^{gas} + * \longleftrightarrow C_2H_4^* \tag{6.3}$$

Acetate-ethylene approach:

$$CH_3COO^* + C_2H_4^* \longleftrightarrow CH_3COO^* - C_2H_4^* \tag{6.4}$$

Hydrogenated VA formation, VAH:

$$CH_3COO^* - C_2H_4^* \longleftrightarrow CH_3COOCH_2CH_2^{**} \tag{6.5}$$

$\beta$-H elimination:

$$CH_3COOCH_2CH_2^{**} + OH^* \longleftrightarrow CH_3COOCHCH_2^{gas} + H_2O^{gas} + 3* \tag{6.6}$$

## 6.3 Reactant adsorption

The VAH formation has been reported to be the rate-limiting step, rls, for the vinyl acetate synthesis.[76, 77] In this section, I will analyse the adsorption of the main reactants involved in the elementary steps to the VAH formation on the model systems shown in Figure 6.1.

### 6.3.1 Acetate adsorption

Adsorbed species can be classified according to their coordination to the surface, hapticity. Hapticity of a ligand is indicated by the Greek character 'eta', $\eta^X_{A,...}$, where the superscript number, X, denotes the number of contiguous atoms through which the adsorbate is bound to the surface, and the subscripted letters, A,..., represent these atoms. Figure 6.2 shows the monohapto, $\eta^1_O$, and dihapto state, $\eta^2_{O,O}$, for the acetate adsorbed on the NN-(100) dimer.

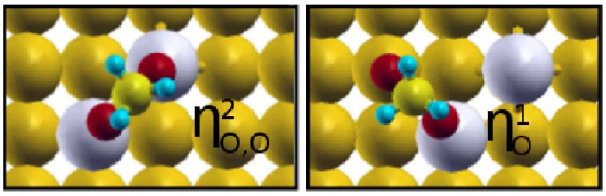

Figure 6.2: Acetate adsorbed species, $CH_3COO^*$, on the NN-(100) dimer. Left dihapto species, $\eta^2_{O,O}$, right monohapto state, $\eta^1_O$. Yellow spheres represent Au, grey Pd, red O, pale yellow C and blue H.

The adsorption energy of acetate adsorbed on the different ensembles, $E_{ads(CH_3COO)}$, has been calculated with respect to the clean surface, $E_{clean}$, and the gas phase acetate radical, $E_{CH_3COO^{gas}}$.

$$E_{ads(CH_3COO)} = E_{CH_3COO^*} - E_{clean} - E_{CH_3COO^{gas}} \tag{6.7}$$

The acetate hapticity is found to be different depending on the Pd dimer where the acetate is adsorbed, see Table 6.1. On the NN ensemble the most stable configuration is as dihaptospecies, $\eta^2_{O,O}$, for both (100) and (111) surfaces while the monohaptospecies, $\eta^1_O$, are most stable for the rest of ensembles.

| | Acetate hapticity | $E_{ads(CH_3COO)}$ | $d_{O-surf}$ | $d_{C-C}$ |
|---|---|---|---|---|
| Pd@Au(111) | | | | |
| **NN** | $\eta^1_O$ | -1.74 | 2.316 | 1.532 |
| | $\eta^2_{O,O}$ | -2.03 | 2.222 | 1.527 |
| **NNN** | $\eta^1_O$ | -1.75 | 2.302 | 1.530 |
| | $\eta^2_{O,O}$ | -1.66 | 2.348 | 1.534 |
| **2NNN** | $\eta^1_O$ | -1.78 | 2.296 | 1.530 |
| | $\eta^2_{O,O}$ | -1.33 | 2.926 | 1.516 |
| Pd@Au(100) | | | | |
| **NN** | $\eta^1_O$ | -1.92 | 2.266 | 1.529 |
| | $\eta^2_{O,O}$ | -2.15 | 2.218 | 1.530 |
| **NNN** | $\eta^1_O$ | -1.90 | 2.260 | 1.530 |
| | $\eta^2_{O,O}$ | -1.83 | 2.246 | 1.530 |
| **2NNN** | $\eta^1_O$ | -1.88 | 2.268 | 1.530 |
| | $\eta^2_{O,O}$ | -1.50 | 3.003 | 1.524 |

Table 6.1: Adsorption energy, $E_{ads(CH_3COO)}$ in eV; and average distance to the surface and C-C distance, $d_{O-surf}$ and $d_{C-C}$ in Å; of acetate adsorbed species, $CH_3COO^*$, on the different Pd ensembles on Au(111) and (100) surfaces.

### 6.3.2 Ethylene adsorption

Ethylene is weakly adsorbed to the Pd dimers through a $\pi$-Pd bond,[77] see Figure 6.3.

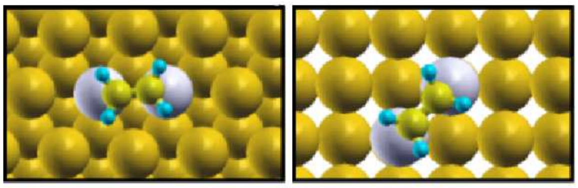

Figure 6.3: Ethylene adsorbed species, $C_2H_4^*$, through a $\pi$-Pd bond. Left: Adsorption on the NN-(111) dimer. Right: Adsorption on the NN-(100) dimer.

The adsorption energy, $E_{ads(C_2H_4)}$, has been calculated with respect to the clean surface, $E_{clean}$, and the gas phase ethene radical, $E_{CH_2CH_2^{gas}}$.

$$E_{ads(C_2H_4)} = E_{C_2H_4^*} - E_{clean} - E_{C_2H_4^{gas}} \tag{6.8}$$

The adsorption energies are around -0.2 for (100) and -0.1 eV for the (111) surfaces, see Table 6.2. Similarly, low binding energies have been reported for ethylene on Ag.[183]

| | $E_{ads(C_2H_4)}$ | $d_{C-surf}$ | $d_{C-C}$ |
|---|---|---|---|
| Pd@Au(111) | | | |
| **NN** | -0.10 | 2.360 | 1.375 |
| **NNN** | -0.09 | 2.344 | 1.376 |
| **2NNN** | -0.10 | 2.342 | 1.377 |
| Pd@Au(100) | | | |
| **NN** | -0.30 | 2.278 | 1.384 |
| **NNN** | -0.19 | 2.319 | 1.378 |
| **2NNN** | -0.20 | 2.270 | 1.384 |

Table 6.2: Adsorption energy, $E_{ads(C_2H_4)}$ in eV; average distance to the surface, $d_{C-surf}$ in Å; and C-C distance, $d_{C-C}$ in Å; of ethylene adsorbed species, $C_2H_4^*$, on the different Pd ensembles on Au(111) and (100) surfaces.

### 6.3.3 Coadsorbed state acetate-ethylene

The formation of the coadsorbed state acetate-ethylene, Ac-Et*, requires the approach of both acetate and ethylene adsorbates to neighbouring Pd atoms in the dimer, see Figure 6.4. To generate the active complex, Ac-Et, is needed the monohapto adsorption, $\eta_O^1$, of acetate. Therefore, the NN configurations on both (111) and (100) pay an energy penalty, of about 0.3 eV, to change the configuration from dihapto, in the initially separated configuration, to monohapto. In fact, strong bonding of the acetate

$\eta^2_{O,O}$ species to the NN ensembles results in poisoning of these templates under normal conditions. For NNN and 2NNN the process is almost thermoneutral, ± 0.06 eV.

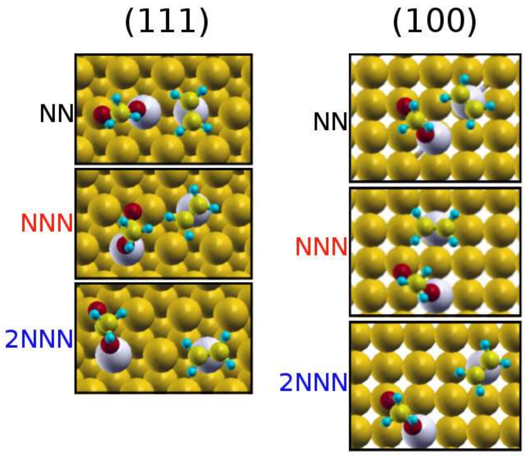

Figure 6.4: Acetate-ethylene coadsorbed state, Ac-Et*, in the most stable position at the different ensembles on Au(111) and (100) surfaces.

The adsorption energy, $E_{ads(Ac-Et)}$, has been calculated with respect to the clean surface, $E_{clean}$, and the gas phase acetate and ethene radicals, $E_{CH_3COO^{gas}}$ and $E_{C_2H_4^{gas}}$, the energy values are reported in Table 6.3. In the coadsorbed state, ethene can be in a perpendicular or parallel position respect to direction formed by Pd dimer, in any case the adsorption energy differences between both conformations have been found lower than 0.1 eV.

$$E_{ads(Ac-Et)} = E_{Ac-Et^*} - E_{clean} - E_{CH_3COO^{gas}} - E_{C_2H_4^{gas}} \tag{6.9}$$

| | $E_{ads(Ac-Et)}$ |
|---|---|
| Pd@Au(111) | |
| **NN** | -1.95 |
| **NNN** | -1.79 |
| **2NNN** | -1.85 |
| Pd@Au(100) | |
| **NN** | -2.13 |
| **NNN** | -2.12 |
| **2NNN** | -2.14 |

Table 6.3: Adsorption energies, $E_{ads(Ac-Et)}$ in eV, of ethylene and acetate coadsorbed species, Ac-Et*, with respect to the clean surface, $E_{clean}$, and the gas phase acetate and ethene radicals, $E_{CH_3COO^{gas}}$ and $E_{C_2H_4^{gas}}$ on the different ensembles for the surfaces Au(111) and (100).

## 6.4 Acetate-ethylene reaction

The VAH formation has been reported to be the rate-limiting step for the vinyl acetate synthesis,[76, 77] therefore the characterisation of the transition states connecting the coadsorbed state, Ac-Et*, is a must.

$$CH_3COO^* - C_2H_4^* \longleftrightarrow CH_3COOCH_2CH_2^{**} \tag{6.10}$$

The transition states structures together with the initial and final states in the different local configurations of dimers on the (111) and (100) surfaces are shown in Figure 6.5, and the activation energy,$E_a$, associated to the rate-limiting step on the different ensembles for both surfaces has been compiled in Table 6.4. $E_a$ is lower on the (111) surface than on (100) in any case, being the next-nearest neighbours, 2NNN, the configuration with the lowest energy barrier for each surface. The activation energies, $E_a$, compiled in Table 6.4 can be plotted in function of the reaction energies, $\Delta E$, see Figure 6.6. This is a Brønsted-Evans-Polanyi type of relationship.[137, 138] The higher activation energy found in the NNN-(100) ensemble respect to that in the NNN-(111) does not explain the higher reactivity experimentally found for the NNN-(100) structures respect to the corresponding (111), and a further analysis to explain the experimental evidence is required.

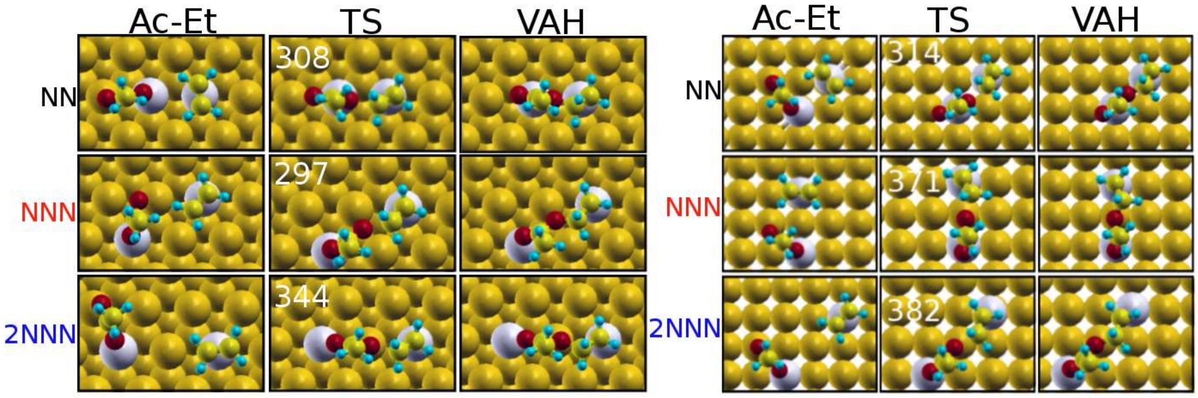

Figure 6.5: Schematic representation of initial state, $CH_3COO^*$-$C_2H_4^*$ (Ac-Et), final state, $CH_3COOCH_2CH_2^{**}$ (VAH), and transition state for the rate-limiting step in the different local configurations of dimers on the (111) (left) and (100) (right) surfaces. The figures in transition state structures correspond to the single imaginary frequency, in $cm^{-1}$.

| | $E_a$ | $\Delta E$ | $\nu$ |
|---|---|---|---|
| Pd@Au(111) | | | |
| **NN** | 1.19 | 0.64 | 308 |
| **NNN** | 1.04 | 0.40 | 297 |
| **2NNN** | 1.16 | 0.47 | 344 |
| Pd@Au(100) | | | |
| **NN** | 1.34 | 0.65 | 314 |
| **NNN** | 1.32 | 0.62 | 371 |
| **2NNN** | 1.43 | 0.91 | 382 |

Table 6.4: Activation and reaction energies, $E_a$ and $\Delta E$ in eV, for the rate-limiting step on the different Pd ensembles for the surfaces Au(111) and (100). The imaginary frequencies are reported, $\nu$ in cm$^{-1}$.

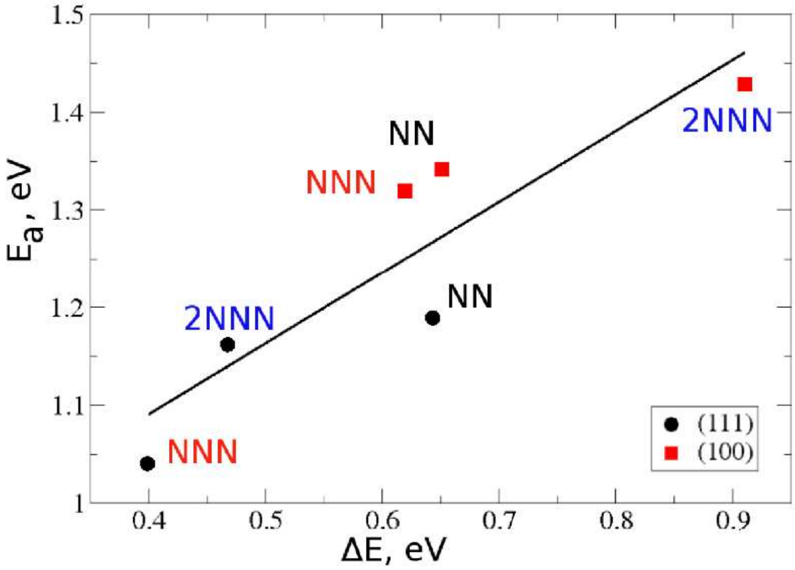

Figure 6.6: Brønsted-Evans-Polanyi, BEP, relationship between the activation energies,$E_a$, for the rate-limiting step, and the heats of reaction, $\Delta E$, ($E_a$ = 0.73$\Delta E$ + 0.80). The correlation coefficient found is 0.9. All the energies are displayed in eV.

## 6.5 Kinetic analysis

To understand the relative activity of NNN dimers, all the elementary steps previous to the rate-limiting step (the VAH formation) have to be considered. Those steps are oxygen dissociation, oxygen assisted acetic acid adsorption, ethylene adsorption, and acetate-ethylene approach. Figure 6.7 shows the reaction energy profile for the steps described in the previous sections.

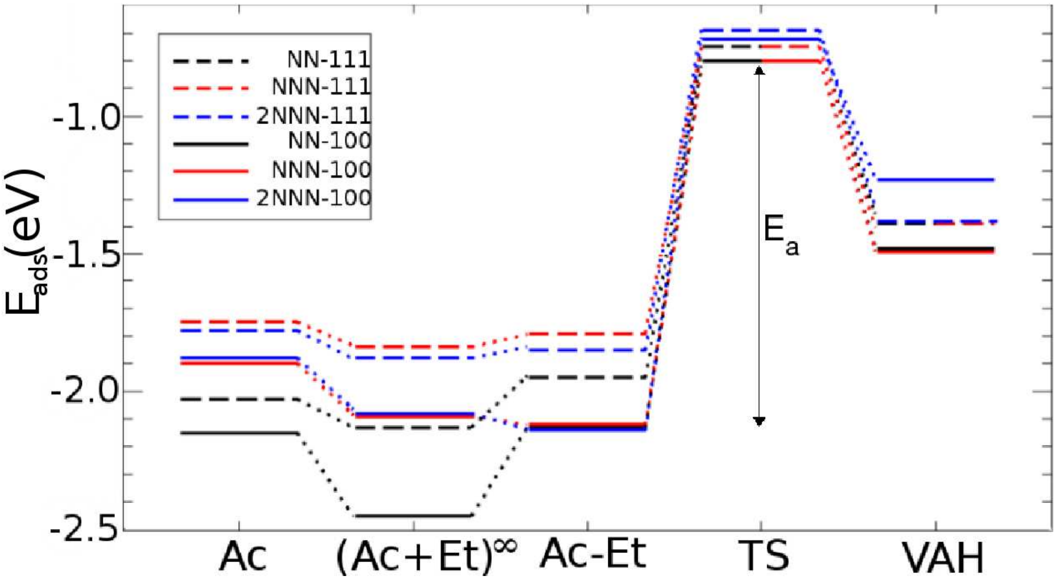

Figure 6.7: Reaction energy profiles, $E_{ads}$, (with respect to gas-phase acetate radical, ethylene, and the clean surface), for the coupling of ethylene and acetate on the models of Figure 6.1. Ac states for acetate, Et for ethylene, and the infinite sign represents adsorption in separated supercells.

We can write the VA synthesis in elementary steps according to the Langmuir-Hinshelwood mechanism,[80] and grouping the two steps dissociative $O_2$ adsorption and acetate adsorption (Equations 6.1 and 6.2) for the sake of simplicity, then we obtain

$$CH_3COOH^{gas} + \frac{1}{2}O_2^{gas} + 2* \longleftrightarrow CH_3COO^* + OH^* \qquad k_1^+/k_1^- \tag{6.11}$$

$$C_2H_4^{gas} +^* \longleftrightarrow C_2H_4^* \qquad k_2^+/k_2^- \tag{6.12}$$

$$CH_3COO^* + C_2H_4^* \longleftrightarrow CH_3COO^* - C_2H_4^* \qquad k_3^+/k_3^- \tag{6.13}$$

$$CH_3COO^* - C_2H_4^* \longrightarrow CH_3COOCH_2CH_2^{**} \qquad k_4^+/k_4^- \tag{6.14}$$

$$CH_3COOCH_2CH_2^{**} + OH^* \longleftrightarrow CH_3COOCHCH_2^{gas} + H_2O^{gas} + 3* \quad k_5^+/k_5^- \tag{6.15}$$

where $k_i^+$ and $k_i^-$ (i=1,...,5), describe reactants adsorption and desorption respectively. For each step the corresponding rates can be written as

$$r_1 = k_1^+ p_{CH_3COOH} p_{O_2}^{1/2} \Theta_*^2 - k_1^- \Theta_{CH_3COO} \Theta_{OH} \tag{6.16}$$

$$r_2 = k_2^+ p_{C_2H_4} \Theta_* - k_2^- \Theta_{C_2H_4} \tag{6.17}$$

$$r_3 = k_3^+ \Theta_{CH_3COO} \Theta_{C_2H_4} - k_3^- \Theta_{CH_3COO-C_2H_4} \tag{6.18}$$

$$r_4 = k_4^+ \Theta_{CH_3COO-C_2H_4} - k_4^- \Theta_{CH_3COOCH_2CH_2} \tag{6.19}$$

$$r_5 = k_5^+ \Theta_{CH_3COOCH_2CH_2} \Theta_{OH} - k_5^- p_{CH_3COOCHCH_2} p_{H_2O} \Theta_*^3 \tag{6.20}$$

The number of sites on a catalyst is constant and hence all coverages should add up to unity, as expressed by the following balance of sites

$$\Theta_* + \Theta_{CH_3COO} + \Theta_{C_2H_4} + \Theta_{CH_3COO-C_2H_4} + \Theta_{CH_3COOCH_2CH_2} + \Theta_{OH} = 1 \tag{6.21}$$

Because the acetate to ethylene coupling is the rate-limiting step for the VA synthesis, the overall rate, r, can be written following the rate-limiting step approximation as

$$r \sim r_{rls} = k_4^+ \Theta_{CH_3COO-C_2H_4} - k_4^- \Theta_{CH_3COOCH_2CH_2} \tag{6.22}$$

Under steady state approximation, and taking into account that initially state there are not products, the Equation 6.22 become in

$$r \sim k_4^+ \Theta_{CH_3COO-CH_2CH_2} \tag{6.23}$$

If the steps previous to the limiting step: Equations 6.11, 6.12 and 6.13 are in quasi-equilibrium, the coverages of all relevant intermediates can be expressed in terms of equilibrium constants and pressures of reactants and products.

$$\Theta_{CH_3COO} = K_1 p_{CH_3COOH} p_{O_2}^{1/2} \frac{\Theta_*^2}{\Theta_{OH}} \tag{6.24}$$

$$\Theta_{C_2H_4} = K_2 p_{C_2H_4} \Theta_* \tag{6.25}$$

$$\Theta_{CH_3COO-CH_2CH_2} = K_3 \Theta_{CH_3COO} \Theta_{C_2H_4} \tag{6.26}$$

Therefore, the overall rate can be written as

$$r = k_4^+ K_1 K_2 K_3 p_{CH_3COOH} p_{C_2H_4} p_{O_2}^{1/2} \frac{\Theta_*^3}{\Theta_{OH}} \tag{6.27}$$

where $k_4^+$ describes the adsorption of the rate-limiting step and $K_i$, with i=1, 2 and 3, is defined as

$$K_i = \frac{k_i^+}{k_i^-} \tag{6.28}$$

with

$$k_i^+ = \nu \exp(\frac{E_i^{TS} - E_i^{ini}}{k_B T}) \tag{6.29}$$

$$k_i^- = \nu \exp(\frac{E_i^{TS} - E_i^{fin}}{k_B T}) \tag{6.30}$$

where $E_i^{ini}$, $E_i^{fin}$ and $E_i^{TS}$ are the energies of initial, final and transition states of the steps labelling as i=1, 2 and 3. $\nu$ is the pre-exponential factor, and $k_B$ is the Boltzmann constant. Therefore, $K_i$ can be written as function of the reaction energy for each step, $\Delta E_i$, as

$$K_i \sim \exp(-\frac{\Delta E_i}{k_B T}) \tag{6.31}$$

The apparent activation energy, $E_a^{'}$, can be defined as

$$E_a^{'} = k_B T^2 \frac{\partial \ln(r)}{\partial T} \tag{6.32}$$

with r defined in Equation 6.27.

Therefore, the apparent activation energy, $E_a^{'}$ for the vinyl acetate synthesis can be calculated for both (100) and (111) surfaces as [80]

$$E_a^{'} = E_a + \sum_i \Delta E_i \tag{6.33}$$

where $E_a$ is the activation energy of the rate-limiting step, and the term $\sum \Delta E_i$ represents the sum of the reaction energies of the previous steps. In Table 6.5 the reaction energies, $\Delta E$, are compiled for the reaction steps in the mechanism, and the activation energy, $E_a$, for the acetate ethylene coupling (rate-limiting step).

If the apparent energy, $E_a^{'}$, is estimated with the values compiled in Table 6.5 with the Equation 6.33, the value found for the ensemble NNN(100) is found to be 0.06 eV lower than that of the (111) surface. This difference in apparent activation energies, $\Delta E_a^{'} = E_a^{'}(100) - E_a^{'}(111)$, corresponds to a relative reaction rate at the experimental temperature (453 K) of about 4-5 times faster for the (100) structure.

| $\Delta E$ | **NN-111** | **NNN-111** | **2NNN-111** | **NN-100** | **NNN-100** | **2NNN-100** |
|---|---|---|---|---|---|---|
| (6.11) | 0.01 | 0.28 | 0.26 | -0.21 | 0.12 | 0.13 |
| (6.12) | -0.10 | -0.09 | -0.10 | -0.30 | -0.19 | -0.20 |
| (6.13) | 0.18 | 0.05 | 0.03 | 0.31 | -0.03 | -0.06 |
| (6.14) | 0.64<br>(1.19) | 0.40<br>(1.04) | 0.47<br>(1.16) | 0.65<br>(1.34) | 0.62<br>(1.32) | 0.91<br>(1.43) |
| (6.15) | -1.88 | -1.88 | -1.89 | -1.68 | -1.76 | -2.02 |

Table 6.5: Reaction energies, $\Delta E$ in eV, for the reaction steps in the mechanism, (Equations (6.11)-(6.15)). For the rate-limiting step the activation energy,$E_a$ in eV, is shown in parenthesis. The first reaction summarises two steps, dissociative $O_2$ adsorption and acetate adsorption.

$$\frac{r_{100}}{r_{111}} = \exp(\frac{-\Delta E_a^{'}}{k_B T}) \sim 4.7 \tag{6.34}$$

This is in excellent agreement with the experimental evidences that show the relative activity at the (100) maximum of: $r_{100}/r_{111} \sim 4.6$ at T= 453 K.[78]

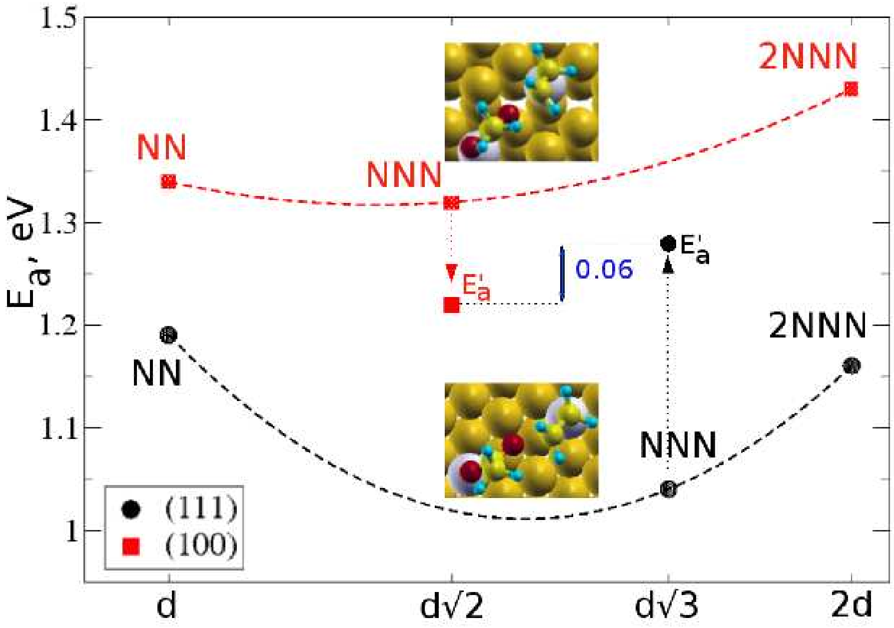

Figure 6.8: Activation energies, $E_a$, for the rate-limiting step, as function of the template Pd-Pd distance. For the NNN dimers the apparent activation energies, $E_a^{'}$ in eV, are also indicated. The insets show the transition states structures for NNN.

## 6.6 Vinyl acetate synthesis on homogeneous Pd-based model systems

In this section, the link between homogeneous and heterogeneous catalysis for VA synthesis is described through theoretical tools based on Density Functional Theory, DFT.

The reaction in homogeneous catalysis can be expressed as

$$C_2H_4 + AcOH + BQ \longrightarrow VA + HQ \qquad (6.35)$$

Homogeneous Pd is not stable against PdO formation, thus a different oxidant is required. *BQ*, benzoquinone-hydrobenzoquinone, is the external redox pair considered.[178] It is one of many oxidants that have been found to be experimentally efficient.[84] *BQ* is transformed in hydroquinone, *HQ*, after the reaction.

The reaction mechanism in homogeneous catalysis is found to have the three main steps:[85, 86] ethylene-acetate coupling (C-O formation), $\beta$-hydrogen elimination, and catalyst reoxidation. The overall profile for the reaction is presented in Figure 6.9 where both homogeneous and heterogeneous mechanisms have been overlapped.

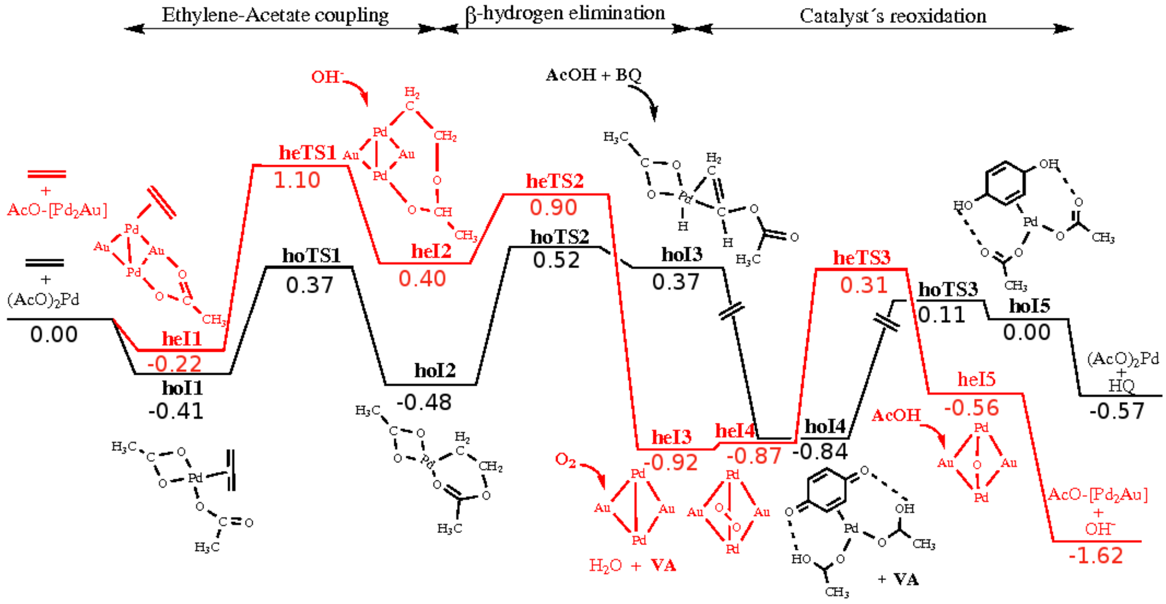

Figure 6.9: Energy profile for VA synthesis on the most active dimer of the PdAu (100) surface and with a homogeneous $(AcO)_2Pd$ complex. The energies are in eV.

For the homogeneous system, the barriers found for the three main steps are 0.78 eV for ethylene-acetate coupling, 1.00 eV for $\beta$-hydrogen elimination, and 0.95 eV for reoxidation.[178] Therefore, the rate-limiting step involves the $\beta$-hydrogen transfer, in agreement with previous experimental considerations,[87] and previous computational studies.[184] However, for the heterogeneous counterpart the rate-limiting step is associated to the formation of the C-O bond (ethylene-acetate coupling) on the surface, with a energy barrier of 1.32 eV. Hydrogen elimination is relatively easy both for acetic acid and the hydrogenated VA product. The exothermicity of the reaction, due to the presence of the oxygen-water pair, is much larger for the heterogeneous process, -1.62 eV, than for the homogeneous one, -0.57 eV.

The reoxidation process is far simpler in the heterogeneous situation, through the $O_2$ adsorption in the surface, since several steps including a external redox pair are needed in the homogeneous version, due to ligand removal, and Pd nanoparticles formation with $O_2$.[71]

## 6.7 Conclusions

In this chapter the strong dependence on the local structure of the ensemble in the vinyl acetate synthesis has been unravelled. The adsorption of the main reactants involved in the elementary steps to the VAH formation have been analysed in several Pd dimer configurations on both Au(100) and (111). The link between homogeneous and heterogeneous catalysis for the VA synthesis is described through theoretical tools based on Density Functional Theory, DFT. The conclusions from this chapter are:

- With respect to the ensemble
  - The relative energies to the most stable dimer for each surface shows that in both (111) and (100) surfaces the least stable ensemble corresponds to the nearest neighbours configuration, NN, with a difference of 0.08 (111) and 0.07 eV (100) respect to the next-nearest neighbour ensemble, NNN.
- With respect to the reactant adsorptions
  - Ethylene adsorption: Ethylene is weakly adsorbed to the Pd dimers through a $\pi$-Pd bond. The adsorption energies are very similar for all ensembles in both surfaces.
  - Acetate adsorption: The acetate hapticity depends on the Pd dimer where the acetate is adsorbed. On the NN ensemble, the most stable configuration is as dihaptospecies, $\eta^2_{O,O}$, for both (100) and (111) surfaces while the monohaptoespecies, $\eta^1_O$, are most stable for the rest of ensembles.
  - Coadsorbed state acetate-ethylene: To generate the active complex, Ac-Et, is needed the monohapto adsorption, $\eta^1_O$, of the acetate species. The NN configurations on both (111) and (100) has to pay an energy penalty, to change the configuration from dihapto, in the initially separated configuration, to monohapto. Strong bonding of the acetate $\eta^2_{O,O}$ species to the NN ensembles poisons these templates under normal conditions.

  - Acetate-ethylene approximation: The VAH formation is the rate limiting step for the vinyl acetate. The configuration with Pd next-nearest neighbours has the lowest energy barrier for each surface. The associated activation energy is lower on the (111) surface than on (100) in any case. This behaviour does not explain the higher reactivity experimentally found for the NNN-(100) structures respect to the corresponding (111).

- With respect to the kinetic analysis

  - A simplified microkinetic study in which all previous steps to the rate-limiting step have been taken into account shows as the relative activity found at the (100) curve maximum is about 4-5 times faster than the (111) in excellent agreement with experimental evidences.[78]

- With respect to the vinyl acetate synthesis on homogeneous Pd-based model systems

  - The main steps for the reaction mechanisms on both version of the Pd-based catalyst are very similar: ethylene-acetate coupling (C-O formation), $\beta$-hydrogen elimination, and catalyst reoxidation. The relative barriers are different.
  - The reoxidation process is through $O_2$ adsorption on the heterogeneous catalyst. Several steps including a external redox pair are needed in the homogeneous version.
  - For the homogeneous system, the rate-limiting step involves the $\beta$-hydrogen transfer. For the heterogeneous counterpart the hydrogen activation is relatively easy and the rate-limiting step is associated to the formation of the C-O bond (ethylene-acetate coupling) on the surface.
  - The exothermicity of the reaction, due to the presence of the oxygen-water pair, is much larger for the heterogeneous process than for the homogeneous one. The rate-limiting step is significantly higher in the heterogeneous version of the catalyst, this is the reason why the reaction takes place at lower temperatures in the homogeneous case than in the heterogeneous version of the catalyst.

# Chapter 7

# Selective homogeneous and heterogeneous gold catalysis with alkynes and alkenes

The selective activation of alkynes is a common feature for both homogeneous and heterogeneous gold catalysts. In this chapter, theoretical results are complemented with experimental evidences to assess the similarities and differences in the performance of homogeneous and heterogeneous gold catalysts.

## 7.1 Computational details

To study the interaction of C2 and C3 alkenes and alkynes with gold systems, Density Functional Theory, DFT, with the B3LYP functional,[125, 126] and localised basis sets (Gaussian 03 code,[185]) have been employed. In order to check the accuracy of the method for same systems, CCSD(T) calculations were performed on selected B3LYP structures.

Ethyne and ethene (C2), and propyne and propene (C3), were taken as representative models for alkynes and alkenes, see Figure 7.1.

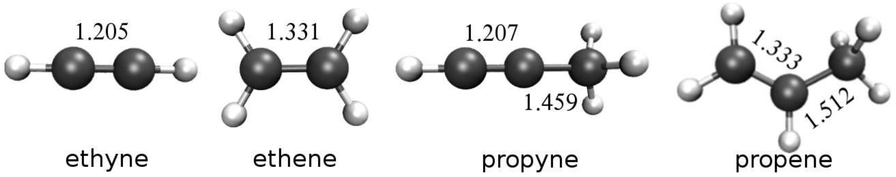

Figure 7.1: Representative models of alkynes and alkenes: ethyne and ethene, C2, and propyne and propene, C3. The calculated C-C distances are indicated in Å.

The gold systems include $Au^+$, AuCl, $AuCl_3$ (reference state $Au_2Cl_6$), and a $Au_{10}$ nanoparticle that represent gas-phase systems, homogeneous and heterogeneous catalysts respectively, see Figure 7.2. The $Au_{10}$ nanoparticle was built so as to resemble the structure of a medium size nanoparticle as was successfully done for the study of CO oxidation.[36, 186] The $Au_{10}$ nanoparticle shows the (111) and (100) facets of a fcc structure. The position of its basal plane was kept fixed in the $z$-direction, and no chemistry was allowed on it. The basis sets was 6-31G(d,p) for Cl, H, C, and LANL2DZ basis set and pseudopotential for Au, which includes the scalar relativistic part, crucial to describe the chemical properties of gold.[187, 188]

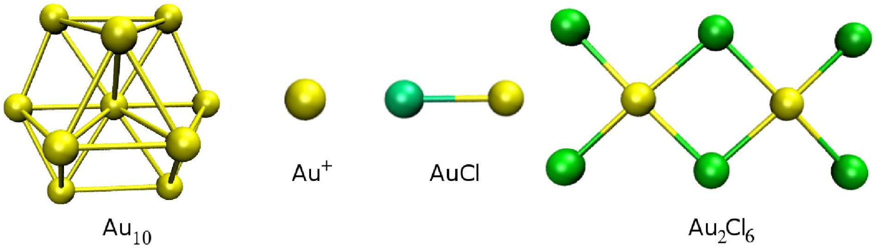

Figure 7.2: Representative theoretical models for heterogeneous and homogeneous Au catalysis: $Au_{10}$ nanoparticle, $Au^+$, AuCl, and the dimer $Au_2Cl_6$.

## 7.2 Binding of double and triple bonds to the active gold species

### 7.2.1 Heterogeneous systems

The adsorption energies for the alkynes and alkenes with the $Au_{10}$ nanoparticle have only been calculated in the B3LYP approximation because CCSD(T) calculations would be too expensive for such medium size clusters. When the interaction is analysed, significant differences in binding energies for the triple and double bond are found, see Table 7.1. The ethyne molecule is activated on $Au_{10}$ nanoparticle with an adsorption energy of -1.17 eV, and the C-C distance is elongated from 1.205 to 1.313 Å on adsorption. Ethene is much less adsorbed, -0.74 eV, and the C-C distance is 1.454 Å on adsorption, thus perturbed with respect to the C-C distance in gas phase (1.331 Å). Results are similar for propyne and propene, for which binding energies of 0.98 and 0.65 eV, and distances of 1.315 and 1.459 Å are found, see Figure 7.3. The differences in binding energies are kept for larger $Au_{19}$ nanoparticles,[5] where only triple bonds are adsorbed in the periphery, whereas double bonds are not bonded.

Qualitatively, the differences in C≡C and C=C binding energies can be traced back to the position of the HOMO and LUMO energy levels calculated for the gas phase molecules, with respect to the metal $d$-band energies.[163] For gas-phase $C_2H_2$, the HOMO is placed 0.4 eV lower than the corresponding level for $C_2H_4$, and it is degenerated. Thus, a larger coupling with the metal states and a larger binding energy to the

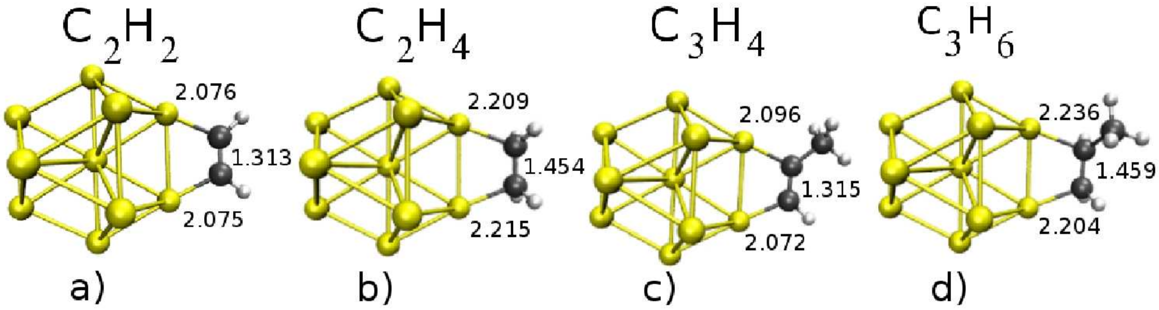

Figure 7.3: Schematic representation of gold nanoparticles, $Au_{10}$, interacting with: a) ethyne, $C_2H_2$; b) ethene, $C_2H_4$; c) propyne, $C_3H_4$; and d) propene, $C_3H_6$. Yellow spheres represent Au, green Cl, black C and grey H. Distances are in Å.

| System | $E_{(C_X H_X)_{HOMO}}$ | $E_{(C_X H_X)_{LUMO}}$ | *gap* | $E_{ads}$ |
|---|---|---|---|---|
| $Au_{10}$-$C_2H_2$ | -7.68 | 1.38 | 9.06 | -1.17 |
| $Au_{10}$-$C_2H_4$ | -7.27 | 0.47 | 7.75 | -0.74 |
| $Au_{10}$-$C_3H_4$ | -7.06 | 1.67 | 8.73 | -0.98 |
| $Au_{10}$-$C_3H_6$ | -6.76 | 0.55 | 7.31 | -0.65 |

Table 7.1: HOMO and LUMO energy levels for the C2 and C3 isolated molecules in gas phase, $E_{(C_X H_X)_{HOMO}}$ and $E_{(C_X H_X)_{LUMO}}$ in eV, and the corresponding differences between LUMO and HOMO levels, *gap*. Adsorption energies, $E_{ads}$ in eV, corresponding to gold nanoparticles interacting with ethyne, $C_2H_2$-$Au_{10}$, ethene, $C_2H_4$-$Au_{10}$, propyne, $C_3H_4$-$Au_{10}$, and propene, $C_3H_6$-$Au_{10}$.

nanoparticle is expected for the triple bond. From these results it can be inferred that the reason for selectivity in heterogeneous systems is the selective adsorption of triple bonds; thermodynamic selectivity.[189] This parameter is known to control selectivity in the sharpest way.

### 7.2.2 Homogeneous systems

$Au^+$, AuCl and $AuCl_3$ are selected as representative gas-phase system, and homogeneous catalysts respectively. When considering gas-phase chemistry, the interaction of $C_2H_2$ to $Au^+$ is -2.35 eV, and -2.73 eV for $C_2H_4$, see Table 7.2. C-C distances are elongated with respect to the gas-phase molecules to 1.240 and 1.400 Å, respectively, see Figure 7.4. Our results are similar to previous calculations indicating the larger stabilisation for the ethene complex, $Au^+$-$C_2H_4$, over the ethyne one, $Au^+$-$C_2H_2$.[190, 191] The coordination of propyne-propene to $Au^+$ is similar, the binding energies are 2.79 and 3.06 eV respectively, thus again favouring the double bond, while the C-C distances are 1.253 and 1.411 Å, see Table 7.3.

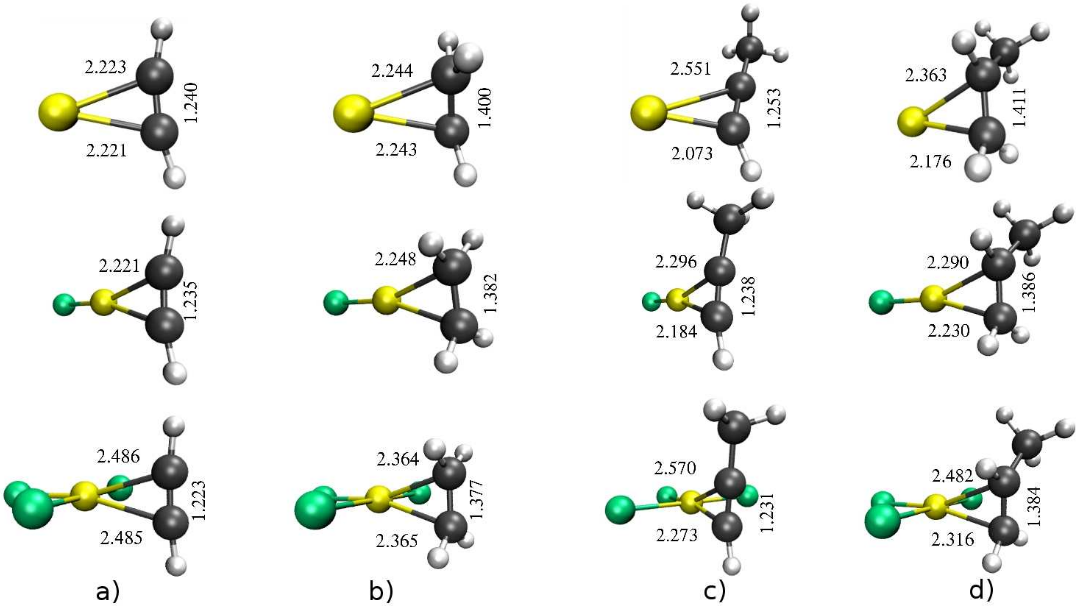

Figure 7.4: Schematic representation of gold systems: $Au^+$, AuCl, and $AuCl_3$, interacting with: a) ethyne, $C_2H_2$; b) ethene, $C_2H_4$; c) propyne, $C_3H_4$; and d) propene, $C_3H_6$. Yellow spheres represent Au, green Cl, black C, and grey H. Distances are in Å.

The calculations show that both ethyne and ethene, are activated after the coordination with AuCl. The C-C distances are enlarged to 1.235 and 1.382 Å, and the binding energies are 1.48 and 1.67 eV for ethyne and ethene respectively. If the pair propyne-propene is inspected, the coordination energies to AuCl are 1.57 and 1.77 eV, again showing preference for the molecule containing the double bond, see Table 7.3. The relevant C-C distances are 1.238 and 1.386 Å.

| System | $E_{HOMO}$ | $E_{LUMO}$ | $gap$ | $E_{coord}$ | $E_{coord(CCSD(T))}$ |
|---|---|---|---|---|---|
| $Au^+$-$C_2H_2$ | -14.14 | -9.36 | 4.78 | -2.35 | -1.74 |
| AuCl-$C_2H_2$ | -7.10 | -1.95 | 5.15 | -1.48 | -1.44 |
| $AuCl_3$-$C_2H_2$ | -7.99 | -5.32 | 2.61 | 0.07 | -0.90 |
| $Au^+$-$C_2H_4$ | -14.15 | -9.04 | 5.11 | -2.73 | -2.09 |
| AuCl-$C_2H_4$ | -7.16 | -2.12 | 5.04 | -1.67 | -1.66 |
| $AuCl_3$-$C_2H_4$ | -7.91 | -5.26 | 2.82 | -0.34 | -1.36 |

Table 7.2: Energies corresponding to HOMO and LUMO orbitals, $E_{HOMO}$ and $E_{LUMO}$ in eV, for ethyne, $C_2H_2$, and ethene, $C_2H_4$, interacting with $Au^+$, AuCl and $AuCl_3$. Coordination energies are calculated using B3LYP functional, $E_{coord}$ in eV. CCSD(T) calculations are also disclosed, $E_{coord(CCSD(T))}$ in eV.

When considering Au(III) complexes, $AuCl_3$ exists as a dimer $Au_2Cl_6$, both in gas and solid phase,[192] although the active species is $AuCl_3$. The coordination to the triple bond is endothermic by 0.07 eV, while the coordination to the double bond is exothermic by 0.34 eV with respect to $\frac{1}{2}Au_2Cl_6$. The bonding with propene is also more favourable than that to propyne. The interaction energies are of -0.14 and -0.54 eV for propyne and propene respectively. The C-C distance for $C_2H_2$ is 1.223 Å, and 1.377 Å for $C_2H_4$, and 1.231 and 1.384 Å for C3 compounds.

| System | $E_{HOMO}$ | $E_{LUMO}$ | $gap$ | $E_{coord}$ | $E_{coord(CCSD(T))}$ |
|---|---|---|---|---|---|
| $Au^+$-$C_3H_4$ | -13.17 | -8.95 | 4.21 | -2.79 | -2.07 |
| AuCl-$C_3H_4$ | -6.89 | -1.60 | 5.29 | -1.57 | -1.56 |
| $AuCl_3$-$C_3H_4$ | -7.77 | -5.09 | 2.68 | -0.14 | -1.13 |
| $Au^+$-$C_3H_6$ | -13.42 | -8.71 | 4.71 | -3.06 | -2.37 |
| AuCl-$C_3H_6$ | -7.03 | -1.82 | 5.21 | -1.77 | -1.82 |
| $AuCl_3$-$C_3H_6$ | -7.81 | -4.99 | 2.81 | -0.54 | -1.59 |

Table 7.3: Energies corresponding to HOMO and LUMO orbitals, $E_{HOMO}$ and $E_{LUMO}$ in eV, for propyne, $C_3H_4$, and propene, $C_3H_6$, interacting with $Au^+$, AuCl and $AuCl_3$. Coordinated energies calculated by B3LYP functional, $E_{coord}$, and CCSD(T), $E_{coord(CCSD(T))}$, in eV.

In order to check the accuracy for these systems, CCSD(T) energy calculations were performed on the B3LYP structures, see $E_{coord(CCSD(T))}$ in Tables 7.2 and 7.3. Both estimations are very similar for the AuCl model, with differences smaller than 0.2 eV, whereas higher differences are found for $Au^+$ and $AuCl_3$. The some trends are observed using both functionals, B3LYP and CCSD(T), which indicates that B3LYP provides reasonable estimates of binding energies for these systems.

The differential coordination energies, $\Delta\Delta E$, for C2 and C3 using both B3LYP and CCSD(T) approximations, have been compiled in Table 7.4. In contrast to the adsorption on the $Au_{10}$ nanoparticles, the binding energies for ethyne and ethene are comparable for AuCl and $AuCl_3$, and higher for C=C bonds than for $C \equiv C$ ones for the rest of interactions. Therefore, according to $\Delta\Delta E$, the Au-based homogeneous catalysts would spend most of the time coordinated to the alkene, and the reasons for the alkynophilicity observed in the experiments should be assigned to other factors but binding energies.

| | $\Delta\Delta E_{(B3LYP)}$ | | $\Delta\Delta E_{(CCSD(T))}$ | |
|---|---|---|---|---|
| System | C2 | C3 | C2 | C3 |
| $Au^+$ | 0.39 | 0.28 | 0.34 | 0.30 |
| AuCl | 0.19 | 0.20 | 0.22 | 0.26 |
| $AuCl_3$ | 0.41 | 0.40 | 0.46 | 0.46 |
| $Au_{10}$ | -0.43 | -0.33 | - | - |

Table 7.4: Differential coordination energies, $\Delta\Delta E = \Delta E_{C\equiv C}$-$\Delta E_{C=C}$ in eV, for C2 and C3. B3LYP and CCSD(T) results on different gold models.

In order to check the previous theoretical results, the $^1H$ NMR spectrum of a 1:1 mixture of the cationic $Au^I$ complex, [Au], (Figure 7.5), and 1,7-enyne, [dimethyl 2-(but-3-enyl)-2-(prop-2-ynyl)propanedioate], (Figure 7.6), was employed to check if there is any thermodynamic preference in the coordination step.[193] The 1,7-enyne, was chosen by have both terminal double and triple bond, and it is known to undergo cyclisation reactions with $Au^I$ catalysts very slowly at low temperatures.[194]

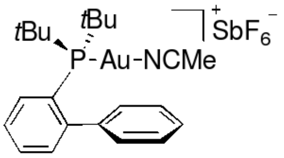

Figure 7.5: The cationic $Au^I$ complex, [Au].[195, 196]

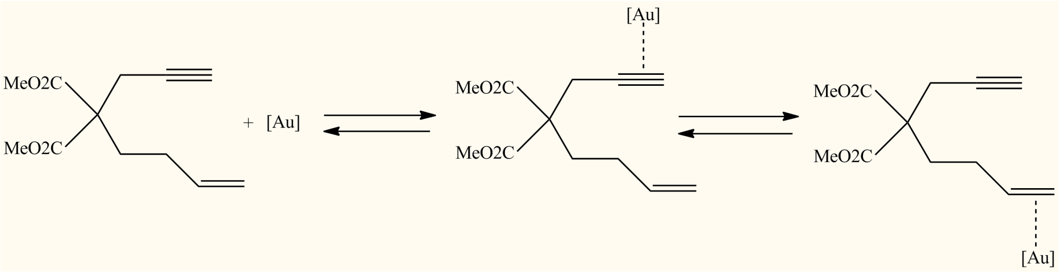

Figure 7.6: The 1,7-enyne, [dimethyl 2-(but-3-enyl)-2-(prop-2-ynyl)propanedioate], reacting with the cationic $Au^I$ complex, [Au].

In the $^1H$ NMR spectrum of the mixture, two new signals emerge at $\delta = 4.3$ and 6.15, see Figure 7.7. These are due to the alkene hydrogen atoms of the complexed $\eta^2$-alkene-gold complex.[197, 198] This experimental evidence confirms the conclusions extracted from Table 7.4; the observed selectivity in homogeneous catalysis for systems containing alkyne and alkene functions is not related to the thermodynamic preference in the coordination step.

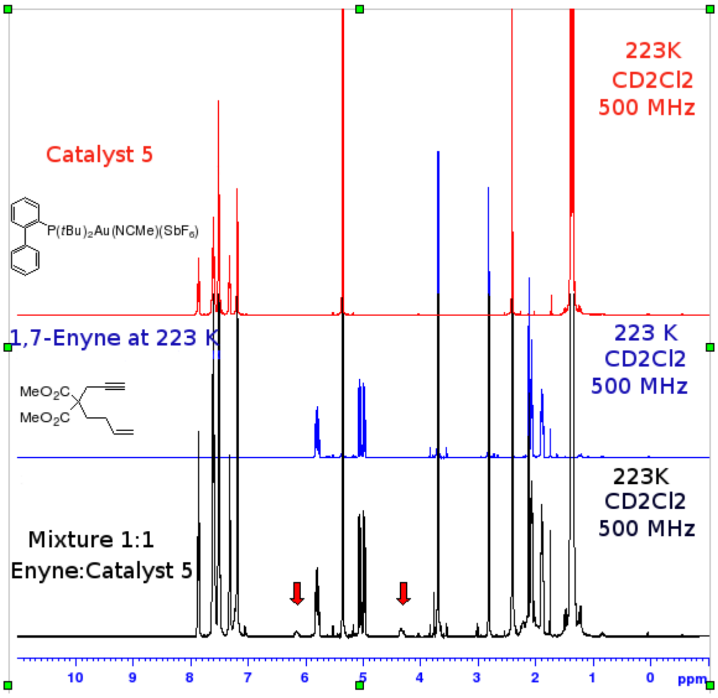

Figure 7.7: $^1$H NMR spectrum of 1,7-enyne, [dimethyl 2-(but-3-enyl)-2-(prop-2-ynyl)propanedioate], and a 1:1 mixture of this 1,7-enyne and the cationic Au$^I$ complex, [Au]. The new signals are marked with red arrows.

## 7.3 Selectivity in homogeneous gold catalysis

The experimental and theoretical results compiled in the previous section show that the coordination of the gold complex does not present any selectivity towards alkynes. The reasons for alkynophilicity in the homogeneous systems will be further explored by studying test reactions: nucleophilic ($OH^-$), and electrophilic ($H^+$) attacks, and hydration, ($H_2O$).

### Nucleophilic attack, ($OH^-$)

When the addition of the $OH^-$ is studied, the reactions are exothermic by 2.12 and 1.10 eV, for the isolated molecules $C_2H_2$ and $C_2H_4$, respectively. If these molecules are coordinated to AuCl, the exothermicity of the $OH^-$ attack increases to 6.42 (AuCl-$C_2H_2$) and 5.18 eV (AuCl-$C_2H_4$). The attack to the triple bond is thus intrinsically favoured, but the catalyst largely increases the exothermicity of the process, see Table 7.5. Similar values are found for C3. In this case, the exothermicity increases from 1.73

and 1.19 eV, for the isolated molecules $C_3H_4$ and $C_3H_6$, respectively, to 6.00 and 5.13 eV, when the molecules are coordinated to AuCl, (AuCl-$C_3H_4$ and AuCl-$C_3H_6$).

| $OH^-$-system | $E_{coord}$ | $E_{ads(CCSD(T))}$ | $\Delta\Delta E^r$ | $\Delta\Delta E^r_{(CCSD(T))}$ |
|---|---|---|---|---|
| $C_2H_2$ | -2.12 | -1.78 | -1.02 | -0.98 |
| $C_2H_4$ | -1.10 | -0.80 | - | - |
| AuCl-$C_2H_2$ | -6.42 | -6.11 | -1.23 | -1.15 |
| AuCl-$C_2H_4$ | -5.18 | -4.97 | - | - |
| $C_3H_4$ | -1.73 | -1.48 | -0.54 | -0.51 |
| $C_3H_6$ | -1.19 | -0.97 | - | - |
| AuCl-$C_3H_4$ | -6.00 | -5.78 | -0.88 | -0.82 |
| AuCl-$C_3H_6$ | -5.13 | -4.96 | - | - |

Table 7.5: Coordination energies, $E_{coord}$ in eV, and differential reaction energy of triple bonds with respect to double bonds, $\Delta\Delta E^r = \Delta E_{C\equiv C} - \Delta E_{C=C}$ in eV, for nucleophilic, $OH^-$, attack for both free and coordinated C2 (C3) to AuCl.

### Electrophilic attack, ($H^+$)

With respect to electrophilic attack, for isolated ethyne and ethene the interaction with a proton is exothermic and more favourable for $C_2H_4$ than for $C_2H_2$, (7.49 vs. 7.13 eV). Once coordinated to the AuCl catalyst, the reaction energies are smaller but the interaction with a proton is more favourable for the triple bond with respect to that for the double bond when the catalyst is present; -6.88 and -6.64 eV for ethyne and ethene respectively, see Table 7.6. The same behaviour is observed in the case of C3: for $C_3H_4$ and $C_3H_6$ coordinated to AuCl, the electrophilic attack to the triple bond is favoured by more than 0.5 eV. Thus, proton addition to the free alkene is more favoured than to the alkyne, but a selective attack on the triple bond takes places when the catalyst is present.

| $H^+$-system | $E_{coord}$ | $\Delta\Delta E^r$ |
|---|---|---|
| $C_2H_2$ | -7.13 | 0.36 |
| $C_2H_4$ | -7.49 | - |
| AuCl-$C_2H_2$ | -6.88 | -0.24 |
| AuCl-$C_2H_4$ | -6.64 | - |
| $C_3H_4$ | -8.28 | 0.14 |
| $C_3H_6$ | -8.48 | - |
| AuCl-$C_3H_4$ | -7.59 | -0.56 |
| AuCl-$C_3H_6$ | -7.03 | - |

Table 7.6: Coordination energies, $E_{coord}$ in eV, and differential coordination energies, $\Delta\Delta E^r = \Delta E_{C\equiv C} - \Delta E_{C=C}$ in eV, for electrophilic, $H^+$, attack for both free and coordinated C2 (C3) to AuCl.

### Hydration, ($H_2O$)

The hydration for the triple bond is more favourable even in the case of the isolated molecules. The reaction is exothermic by 1.83 and 0.92 eV for $C_2H_2$ and $C_2H_4$ respectively, but the presence of AuCl increases by more than 50% the differential exothermicity of the hydration reaction, being the difference between AuCl-$C_2H_2$ and AuCl-$C_2H_4$ of -1.54 eV. Similar results are observed for C3, with an increase of $\Delta\Delta E^r$ from -0.64 (isolated molecules) to -1.34 eV (AuCl coordinated molecules), see Table 7.7.

| $H_2O$-system | $E_{coord}$ | $\Delta\Delta E^r$ |
|---|---|---|
| $C_2H_2$ free | -1.83 | -0.91 |
| $C_2H_4$ free | -0.92 | - |
| AuCl-$C_2H_2$ | -2.00 | -1.54 |
| AuCl-$C_2H_4$ | -0.46 | - |
| $C_3H_4$ free | -1.62 | -0.64 |
| $C_3H_6$ free | -0.98 | - |
| AuCl-$C_3H_4$ | -1.81 | -1.34 |
| AuCl-$C_3H_6$ | -0.47 | - |

Table 7.7: Coordination energies and differential coordination energies, $\Delta\Delta E^r = \Delta E_{C\equiv C} - \Delta E_{C=C}$, in eV, for hydration of both free and coordinated C2 (C3) to AuCl.

To check the computational results corresponding to double and triple bond hydration, alkyne and alkene ((1) and (2) in Figure 7.8) have been placed with water at room temperature in the presence of the cationic $Au^I$ complex, [Au] (Figure 7.5).[193] Whereas alkyne (1) reacts with water to form a 48:1 mixture of ketone (3) and aldehyde (4),[199, 200] alkene (2) was recovered unchanged.

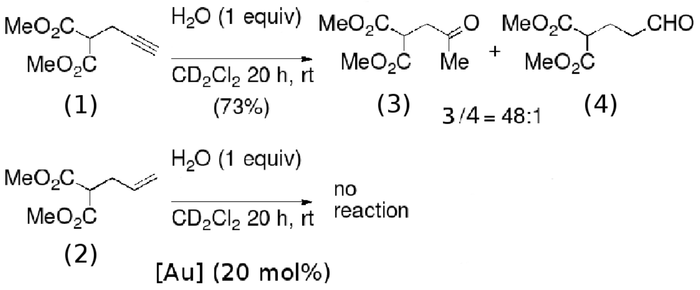

Figure 7.8: Hydration of alkyne (1) with the cationic $Au^I$ complex, [Au].[193, 195, 196]

Although our results are based on gas-phase calculations, the energy differences observed for the reactions on molecules containing double and triple bonds are large enough indicating that our conclusions do not depend on the inclusion of the solvent. Moreover, solvation would have an almost constant contribution due to the similarity of the reactants and products in both C2 and C3 systems.

## 7.4 Enyne cyclisation: Homo- versus heterogeneous Au catalysts

$Au^I$-catalysed reactions of 1,6-enynes are among the most general gold-catalysed transformations, and mechanistically reasonably well-understood,[195, 196, 201] for this reason they were chosen as test models.[193] 1,6-enyne, (5), reacts with cationic $Au^I$ catalysts, [Au], (2 mol %) in $CH_2Cl_2$ at room temperature in 5 min to form diene (6) in 98% yield, see Figure 7.9. This type of skeletal rearrangement of 1,6-enynes to give 1,3-dienes occurs readily with cationic $Au^I$ catalysts at temperatures as low as -60 °C.[201] Phenyl-substituted 1,6-enynes (7), gives the product of a formal [4 + 2] cycloaddition (8) in 86% yield, under similar experimental conditions (2% mol $Au^I$, $CH_2Cl_2$ room temperature, 1 h).[195, 196]

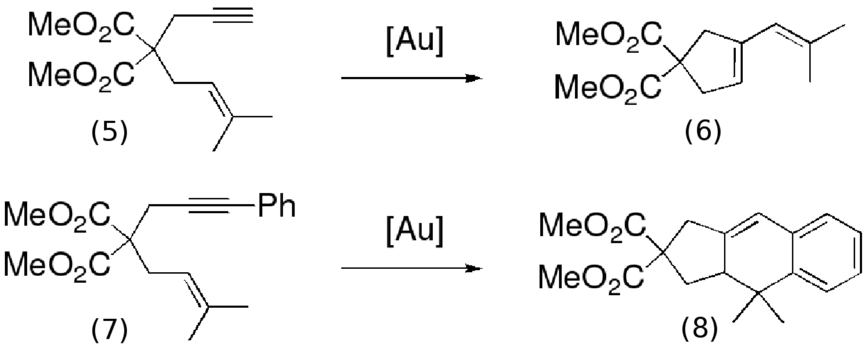

Figure 7.9: $Au^I$-catalysed reactions of 1,6-enynes.

However, reaction of (5) or (7) with heterogeneous $Au/CeO_2$ in $CH_2Cl_2$, at room temperature or at 50°C, lead only to unchanged starting materials. None of the expected products (6) or (8) are detected in these experiments. Thus, it is clear that there is a substantial difference in reactivity between homogeneous and heterogeneous (nanoparticle) gold catalysts, suggesting a gap in these particular C-C bond forming reactions.

Molecular orbital analysis can be applied to rationalise the different behaviour of homogeneous and heterogeneous catalysts with respect to enyne cyclisation. Figure 7.10 shows the energy and composition of the frontier orbitals for $Au_{10}$-$C_2H_2$, and AuCl-activated $C_2H_2$ and $C_2H_4$. The HOMO and LUMO gas-phase $C_2H_2$ and $C_2H_4$ orbitals are shown as a reference.

Upon AuCl interaction the $C_2H_2$ LUMO is downshifted by more than 3.3 eV. This is how the catalyst improves the Lewis basic character of $C_2H_2$. When interacting with $Au_{10}$ the $C_2H_2$ LUMO is much less activated (downshift is only 2.4 eV) thus, the system is less prone to electron acceptance than for AuCl (by about 1 eV). This can be traced back to the binding energies of $C_2H_2$ to AuCl and $Au_{10}$; the stronger the bond, the larger the downshift in the LUMO levels. Therefore, the smallest difference between

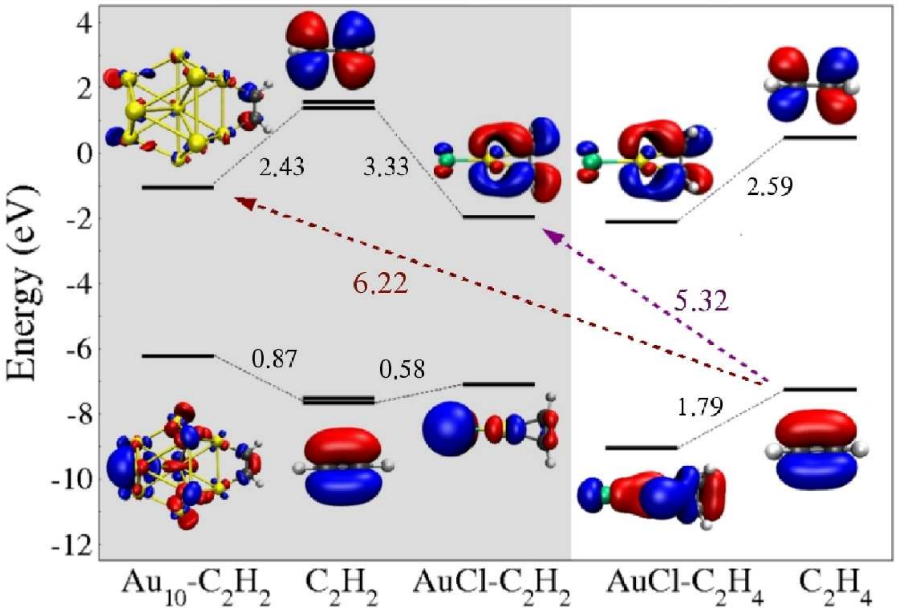

Figure 7.10: Molecular orbital diagram showing the corresponding HOMO and LUMO orbitals for $C_2H_2$ and $C_2H_4$ free, and coordinated to AuCl and $Au_{10}$.

the HOMO($C_2H_4$)-LUMO(AuCl-$C_2H_2$) orbital energies in the AuCl-catalysed reaction is 5.3 eV, while for the $Au_{10}$ system is 6.2 eV. In homogeneous systems, AuCl-$C_2H_4$ units are also present, but AuCl lowers the activity of the $C_2H_4$ by lowering the position of the HOMO state, rendering it inactive. Therefore, the increase of the Lewis acidity of C≡C by AuCl, together with the intrinsic basicity of AuCl-$C_2H_4$, are the driving forces for the enyne cyclisation. This is lower in the case of the nanoparticles than for the molecular compounds. Thus, they are less prone to C-C bond formation.

## 7.5 Conclusions

Alkynophilicity is the known preference shown by alkynes to react with homogeneous and heterogeneous gold catalysis in the presence of other functional groups. In the present chapter the fundamental reasons behind the selective alkyne activation in homogeneous and heterogeneous gold catalysis have been described. The conclusions obtained after theoretical and experimental study are

- With respect to the heterogeneous system
    - The interaction between the $Au_{10}$ nanoparticle and alkynes and alkenes shows significant difference in binding energies. The reason for selectivity in heterogeneous systems is the selective adsorption of triple bonds: thermodynamic selectivity.

- With respect to the homogeneous systems
  - The coordination energy of alkyne and alkene with $Au^+$ is always higher for the double bond. In the case of the interaction with AuCl and $AuCl_3$ binding energies are comparable both for alkyne and alkene. Therefore, the Au-based homogeneous catalysts would spend most of the time coordinated to the alkene, and the reasons for the alkynophilicity observed in the experiments should be assigned to other factors but binding energies.

- With respect to the selectivity in homogeneous catalysis
  - The reasons for alkynophilicity in the homogeneous systems have been investigate through test reactions: nucleophilic, $OH^-$, and electrophilic, $H^+$ attacks, and hydration, $H_2O$.
    - The attack to $OH^-$ to the triple bond is intrinsically favoured for the isolated molecules, but the Au-based catalyst largely increases the exothermicity of the process.
    - The electrophilic attack is exothermic and more favourable for the double bond than for the triple bond for the isolated molecules, but once coordinated to the AuCl catalyst the reaction energy order is reversed.
    - The hydration for the triple bond is more favourable even in the case of the isolated molecules. The presence of AuCl increases by more than 50% the differential exothermicity of the hydration reaction.

- With respect to the enyne cyclisation
  - Experimentally, the $Au^I$-catalysed reactions of 1,6-enynes take place at room temperature leading to 1,3-dienes products. However, the reaction with heterogeneous $Au/CeO_2$ lead only to unchanged starting materials, pointing a substantial difference in reactivity between homogeneous and heterogeneous gold catalysts.
  - The ($C_2H_2$) LUMO level interacting with AuCl is much more activated that upon $Au_{10}$ interaction. Thus, the system is more prone to electron acceptance for AuCl than for $Au_{10}$ (by about 1 eV).
  - The interaction of AuCl with $C_2H_4$ renders the HOMO level (AuCl-$C_2H_4$) inactive.
  - The increase of the Lewis acidity of C≡C by AuCl, together with the intrinsic basicity of $C_2H_4$, are the driving forces for the enyne coupling. This is lower in the case of the nanoparticles than for the molecular compounds. Thus, $Au_{10}$ nanoparticles are less prone to C-C bond formation.

# Chapter 8

# Interplay between CO, hydrides, and carbides in selective alkyne hydrogenation on palladium

The aim of this chapter is to establish new structure-selectivity relationships for alkyne hydrogenation on Pd containing catalysts. The partial hydrogenation of C2 and C3 alkynes on Pd will be studied by means of Density Functional Theory, DFT, to determine the state of the catalyst, and the whole hydrogenation path under all conditions (clean, C, H, and CO). Since the description in energy terms does not account for the effect of temperatures and pressures in hydride formation, first principle thermodynamics will be employed to describe the state of the surface under different preparations (Section 8.4). In this chapter, I will mainly focused in the theoretical description. The one-to-one comparison with the corresponding set of hydrogenation experiments, described in Section 1.7 in Chapter 1, is shown in ref. [114].

## 8.1 Computational details

The catalytic hydrogenation of ethyne and propyne on Pd was studied by means of periodic Density Functional Theory, DFT, applied to slabs, and calculated with the VASP code,[148, 149, 150] to obtain the energies through the GGA-PW91 functional.[122] Monoelectronic valence states were expanded in plane waves with a kinetic cut-off energy of 400 eV, while the core electrons were represented by PAW pseudopotentials.[151, 152] With this set up, the Pd unit cell parameter was calculated to be 3.987 Å, in reasonable agreement with the experimental value, 3.891 Å.[172] For the mechanistic studies the slabs consisted on four atomic layers interleaved by 12 Å of vacuum, a $p(2x2)$ reconstruction. The $k$-point sampling consisted of 2x2x1 Monkhorst-Pack points.[130] Four different models were employed (Figure 8.1): a) the clean Pd surface, b) a near-surface carbide with 0.25 ML carbon content, c) a fully hydrogenated Pd system containing 100% hydrogen, and d) a partially CO-covered surface with 0.25 ML CO coverage. To

UNIVERSITAT ROVIRA I VIRGILI
THEORETICAL STUDIES OF SELECTIVE PROCESSES IN HETEROGENEOUS CATALYSIS
Mónica García Mota
ISBN:978-84-693-5424-7/DL:T-1415-2010

study C-C coupling reactions (oligomerisation) was used a supercell $p(2x4)$, where two alkyne molecules were placed. Then, $k$-point meshes of 5x3x1 were considered. Transition state structures were determined by the Climbing Image version of the Nudged Elastic band, CINEB,[161] and these were proven to show a single imaginary frequency.

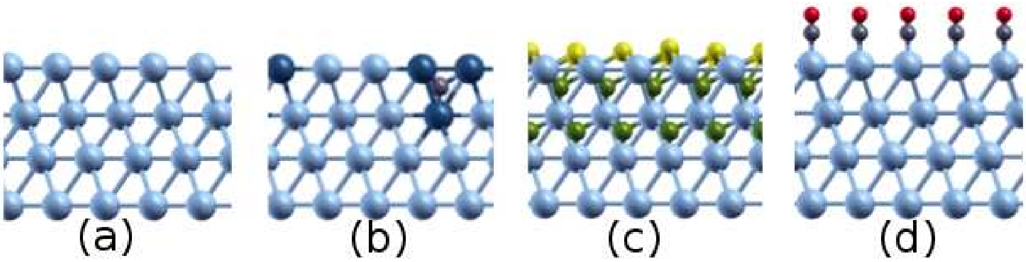

Figure 8.1: Four different models: (a) the clean Pd surface, (b) a near-surface carbide with 0.25 ML carbon content, (c) a fully hydrogenated Pd system containing 100% hydrogen, and (d) a partially CO-covered surface with 0.25 ML CO coverage.

## 8.2 States of the system

The formation of hydrides and carbides has been proposed and documented under some conditions in the past.[8, 105] In this work the hydride and the carbide formation have been analysed by DFT-based simulations.

### Hydride formation

It is known that $PdH_x$ forms both a low-content $\alpha$-$PdH_{0.02}$, and a high content $\beta$-$PdH_{0.7}$ phases.[104] In order to understand the build up of the hydride, the adsorption energies of hydrogen on the clean Pd(111) surface, both in the first layer and in the bulk, have been calculated as

$$E_{ads(N_H)}(Pd) = \frac{(E_{N_H}(Pd) - E_{Pd} - \frac{N_H E_{H_2}}{2})}{N_H} \tag{8.1}$$

where $E_{Pd}$ and $E_{H_2}$ are the energies of the Pd slab and of the molecular hydrogen in gas phase, respectively. $N_H$ is the number of incorporated hydrogens.

At low coverage ($\theta_H$= 0.25 ML), hydrogen is adsorbed exothermically by 0.58 eV/H atom. The $H_2$ dissociation is easy even at a high hydrogen coverage,[174, 175] being the average adsorption energy for the clean surface -0.54 eV/H atom, see Table 8.1.

Regarding to the hydrogen adsorption energies for the inner octahedral sites, the values found are much smaller than that for the respective surface adsorptions, around -0.1 eV/bulk H atom.

| $N_H$ | $E_{ads(N_H)}$(Pd) | $E_{ads(N_H)}$(PdC) |
|---|---|---|
| 1 | -0.58 | -0.48 |
| 2 | -0.55 | -0.46 |
| 3 | -0.53 | -0.43 |
| 4 | -0.51 | - |

Table 8.1: Adsorption energy of hydrogen on a clean Pd surface, and on a carbide surface, $E_{ads(N_H)}$(Pd) and $E_{ads(N_H)}$(PdC) in eV/H atom. $N_H$ is the number of incorporated hydrogens.

### Carbide formation

Carbide formation arises from the decomposition of organic moieties.[202, 203] Alkyne, $C_NH_{2N-2}$, and alkene, $C_NH_{2N}$, decompositions can be described by the following equations

$$Pd + \frac{1}{N}(C_NH_{2N-2})^{gas} \longrightarrow PdC + \frac{(N-1)}{N}H_2^{gas} \tag{8.2}$$

$$Pd + \frac{1}{N}(C_NH_{2N})^{gas} \longrightarrow PdC + H_2^{gas} \tag{8.3}$$

therefore, the formation energies of carbon atoms in the Pd subsurface from alkynes, $E_{f(\equiv)}$, and alkenes, $E_{f(=)}$, are calculated with respect to the alkyne (alkene) energy, $E_{(C_NH_{2N-2})^{gas}}$ ($E_{(C_NH_{2N})^{gas}}$), and the energy of Pd clean surface, $E_{Pd}$, through the equations

$$E_{f(\equiv)} = E_{PdC} + \frac{(N-1)}{N}E_{H_2^{gas}} - E_{Pd} - \frac{E_{(C_NH_{2N-2})^{gas}}}{N} \tag{8.4}$$

$$E_{f(=)} = E_{PdC} + E_{H_2^{gas}} - E_{Pd} - \frac{E_{(C_NH_{2N})^{gas}}}{N} \tag{8.5}$$

The calculated formation energies show that near-surface carbide formation is only exothermic when it is formed from the ethyne moiety, -0.56 eV. For all the rest the carbide formation is endothermic, see Table 8.2.

According to Andersin *et al.*[147] ethene dissociation into two methylene groups is hindered by 2.12 eV barrier on the (111) surface, but it is reduced to 1.69 eV at the step. Therefore, formation of C-related species takes place mainly at steps. In fact, the adsorption energy of C atoms (with respect to gas-phase $C_2H_2$ and $H_2$) is exothermic by 1.0 eV at the step (endothermic by 0.2 eV with respect to $C_2H_4$ and $H_2$).

The formation energy has been represented as function of the number of carbon atoms in Figure 8.2. The most favourable position for C atoms in Pd is the octahedral subsurface site, see model (b) in Figure 8.1, penetration towards the bulk has a thermodynamic penalty cost of 0.04 eV. The reason for near-surface carbide formation is closely related to the higher *d*-band energy of the Pd atoms on the surface and to the

| $N_C$ | 2 | 3 | 4 | 5 |
|---|---|---|---|---|
| $E_{f(\equiv)}$ | -0.56 | 0.12 | 0.35 | 0.51 |
| | - | - | 0.38 | - |
| $E_{f(=)}$ | 0.58 | 0.80 | 0.79 | 0.78 |
| | - | - | 0.85 | - |
| $E_{f(=-=)}$ | - | - | 0.44 | - |
| $\Delta E_f$ | 1.14 | 0.68 | 0.44 | 0.27 |

Table 8.2: Formation energies of carbon atoms in the Pd subsurface from alkynes, $E_{f(\equiv)}$, and alkenes, $E_{f(=)}$, in eV. $N_C$ is the number of carbon atoms in the hydrocarbon. $\Delta E_f$ is the difference between $E_{f(\equiv)}$ and $E_{f(=)}$ in eV.

fact that geometric relaxations are also easier for surface atoms than for bulk atoms. The insertion in a subsurface carbon position has calculated to be repulsive by 0.6 eV at neighbouring sites (0.1 eV at second next nearest neighbours). Therefore, the carbide phase is not very dense in C atoms in agreement with the $PdC_{0.15}$ stoichiometry reported by Ziemecki *et al.*[204]

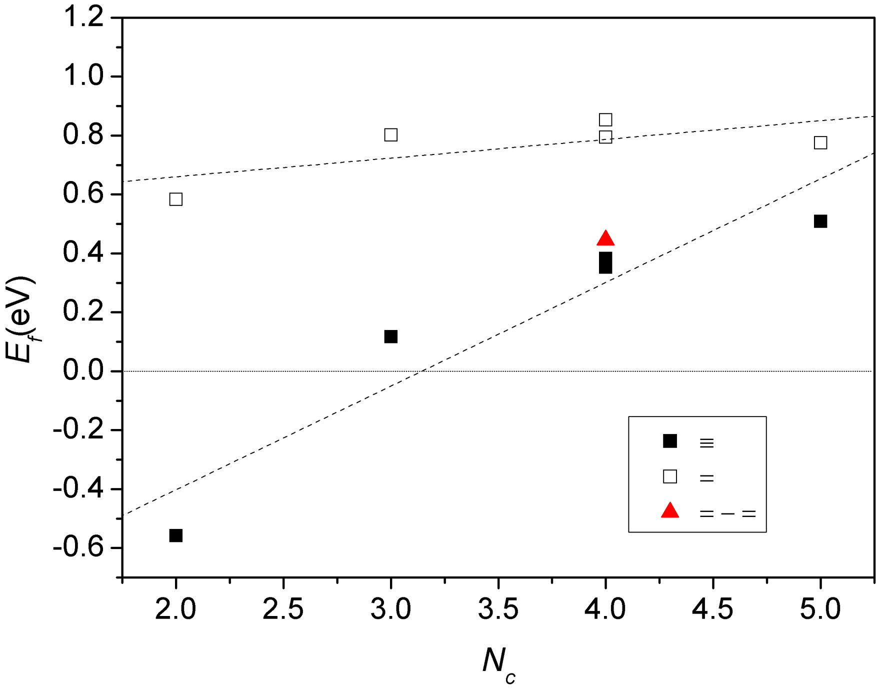

Figure 8.2: Formation energy of carbide, $E_f$ in eV, as function of the number of the carbon atoms, $N_C$, of alkyne, ≡, and alkene, =, moieties. The red triangle is associated to the butadieno formation energy, = - = .

### Carbide-hydride interplay

To analyse the interplay between the carbide and the hydride, the build up of the hydride is studied in the presence of the carbide, the adsorption energies of hydrogen, $E_{ads(N_H)}$(PdC), can be calculated as

$$E_{ads(N_H)}(PdC) = \frac{(E_{N_H}(PdC) - E_{PdC} - \frac{N_H E_{H_2}}{2})}{N_H} \tag{8.6}$$

where $E_{PdC}$ is the energy of the Pd slab with carbon atoms in the Pd subsurface, and $E_{H_2}$ the energy of the molecular hydrogen in gas phase. $N_H$ is the number of incorporated hydrogens.

Hydrogen adsorption energies are only weakly perturbed on the surface, only the position on top of the carbon atom is not favoured. The average adsorption energy of hydrogen in the first layer is slightly reduced to -0.46 eV/H atom, compared with -0.54 eV/H atom when C atom is not present, see Table 8.1. To analyse the hydrogen incorporation in the PdC bulk, the reference is a configuration in which the surface is covered by 15 hydrogen atoms, and a near-subsurface C atom is already present (inset in Figure 8.3). The insertion of H atoms on the second layer is largely hampered. The presence of carbon in the second layer impedes any other H adsorption even at distances as long as 5 Å (about 2 positions in the lattice). At smaller distances the hydrogen adsorptions are less stable than on the surface or in a subsurface layer very far away from the C position. Instead for H in the third layer, Pd atoms screen more effectively, and at 4 Å (more than one lattice position) the standard value for subsurface H adsorption is retrieved ($\sim$ -0.11 eV). In turn if we start by a situation where the hydride exists, less available step sites for dissociation will exist, thus blocking the carbide formation.

## 8.3 Reaction mechanism and kinetics

The complete reaction network starts by $H_2$ dissociation, and the adsorption of the alkyne on the surface. Both steps are exothermic under all conditions (clean, C, H, and CO). Then, the sequential addition of H to the hydrocarbon following a Horiuti-Polanyi mechanism can take place.[205] Given the symmetric nature of ethyne, the first hydrogenation (step labelled as (1) in the Figure 8.4) leads to a single product vinyl, $HC{\equiv}CH_2$.

Vinyl is a branching point intermediate since upon hydrogenation, two competitive products: ethene (2a), $H_2C{=}CH_2$, or ethylidene (2b), $HC\text{-}CH_3$, can be formed. From $H_2C{=}CH_2$ or $HC\text{-}CH_3$ further hydrogenations, (3a) and (3b), lead to a common intermediate ethyl, $H_2C\text{-}CH_3$. Finally, further hydrogenation leads to ethane (4), $H_3C\text{-}CH_3$.

For higher hydrocarbons such as C3, the number of possibilities grows, and three branching points exist in the complete hydrogenation path, see Figure 8.5. The bifurcation points can not be *a priori* eliminated from an energy point of view, and might be the main hydrogenation path for some of catalyst states as we will see later.

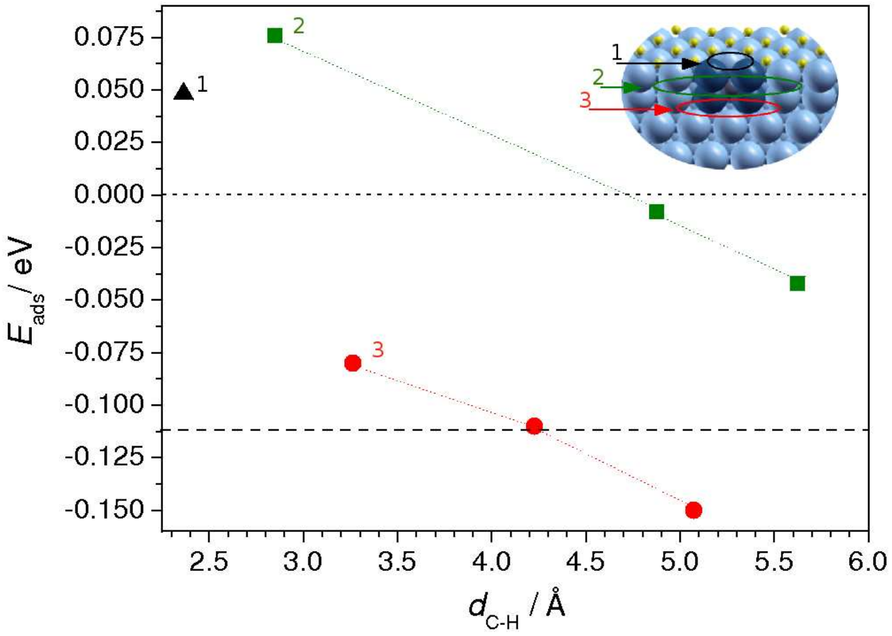

Figure 8.3: Adsorption energy of hydrogen, $E_{ads}$ in eV, with respect to gas-phase hydrogen to a palladium carbide model system covered by a H monolayer as a function of the distance between the incoming H and C, $d_{C-H}$ in Å. Position 1 stands for the surface (black point), positions 2 for the subsurface (green points), and positions 3 for the subsubsurface, (red points). The horizontal line indicates the average adsorption energy for subsurface H in clean Pd.

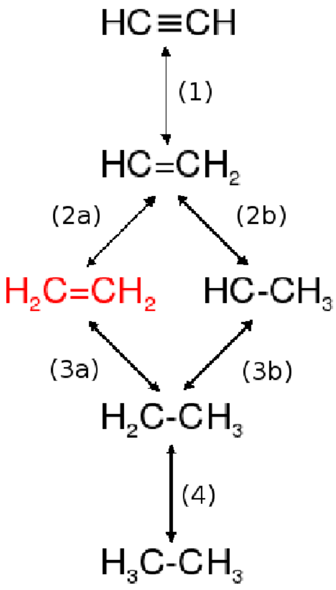

Figure 8.4: Reaction steps for the hydrogenation of ethyne following a Horiuti-Polanyi mechanism.[205]

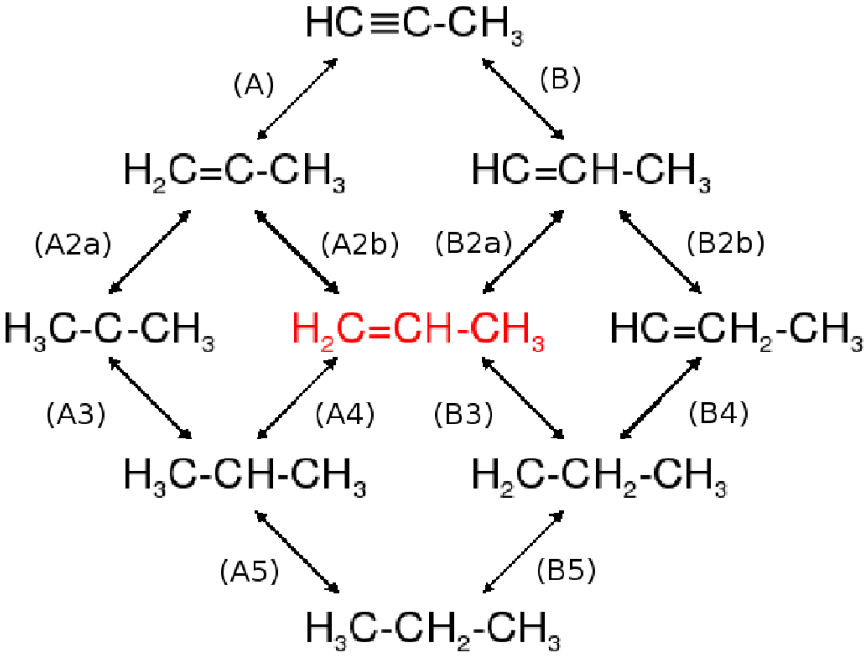

Figure 8.5: Reaction steps for the hydrogenation of propyne following a Horiuti-Polanyi mechanism.[205]

### 8.3.1 Thermodynamic factors

The adsorption energies for ethyne and ethene are calculated under all conditions: clean, C, H, and CO, see Table 8.3. A differential adsorption energy, $\Delta E_{ads}$, is defined as ethyne-ethene energy difference. $\Delta E_{ads}$ gives information about the selectivity towards the double bond for each surface: thermodynamic factor. According to this, the most effective way to obtain a good selectivity towards ethene is using a CO covered surface ($\Delta E_{ads}$ = -1.24 eV), then clean surface ($\Delta E_{ads}$ = -1.20 eV), carbides ($\Delta E_{ads}$ = -0.82 eV), and finally hydrides ($\Delta E_{ads}$ = -0.79 eV).

When the adsorption of propyne and propene is analysed, the most effective way to obtain a good selectivity towards the double bound are by order of magnitude: CO ($\Delta E_{ads}$ = -1.37 eV), then hydrides ($\Delta E_{ads}$ = -0.58 eV), carbides ($\Delta E_{ads}$ = -0.76 eV), and the most unselective system is the clean surface ($\Delta E_{ads}$ = -0.97 eV).

The trends in selectivity towards the double bound, found for both C2 and C3 molecules, is in contradiction with the experiments shown in Section 1.7 of Chapter 1. Hydride formation produces over-hydrogenated moieties even if the thermodynamic factor is more favourable than for the clean surface. Therefore, only the thermodynamic factor can not be considered as a reliable selectivity descriptor, and kinetic factors must be introduced.

| | Clean | Carbide | Hydride | CO-covered |
|---|---|---|---|---|
| $E_{ads}(C_2H_2)$ | -2.02 | -1.49 | -0.94 | -1.24 |
| $E_{ads}(C_2H_4)$ | -0.82 | -0.67 | -0.15 | 0.00 |
| $\Delta E_{ads}$-C2 | -1.20 | -0.82 | -0.79 | -1.24 |
| $E_{ads}(C_3H_4)$ | -1.57 | -1.19 | -0.59 | -0.68 |
| $E_{ads}(C_3H_6)$ | -0.60 | -0.43 | -0.01 | 0.69 |
| $\Delta E_{ads}$-C3 | -0.97 | -0.76 | -0.58 | -1.37 |

Table 8.3: Adsorption energies, $E_{ads}$ in eV, for C2 and C3 alkynes and alkenes. Differential adsorption energy, $\Delta E_{ads}$ in eV, defined as $\Delta E_{ads}$= $E_{ads}$(alkyne)- $E_{ads}$(alkene).

### 8.3.2 Kinetic factors

In this section, the activation energy for each step shown in Figure 8.4 (hydrogenation of ethyne), has been calculated for all catalyst states (clean, C, H, and CO), see Table 8.4.

On the clean surface, the first hydrogenation is exothermic by 0.17 eV, and the barrier is 0.66 eV. Formations of ethene, $H_2C{=}CH_2$, and ethylidene, $HC\text{-}CH_3$, are found to have an activation energy of 0.81 and 0.79 eV, respectively. Thus, formation of both compounds is almost equally likely. In addition, ethene can either desorb or be further hydrogenated. Both effects are responsible for the relatively low selectivity towards ethene experimentally observed for clean Pd.

If carbide is present, the second hydrogenation barriers are 0.58 and 0.68 eV to $H_2C{=}CH_2$ and $HC\text{-}CH_3$, respectively. Therefore, the presence of the carbide induces selectivity, both by destabilising ethene adsorbed on the surface, ($E_{ads}$ is -0.67 eV to be compared to -0.82 eV for the clean surface) and by improving the branching ratio in second hydrogenation. Our results explain the observations by Teschner *et al* of improved selectivity in the presence of the carbide.[101]

If CO is present, the second hydrogenation barriers are 0.88 and 0.57 eV to $H_2C{=}CH_2$ and $HC\text{-}CH_3$ at low CO coverage (0.25 ML), but at 0.50 ML CO, the barriers are reduced to 0.14 and 0.23 eV, leading to selective ethene production.

| step | | clean | C | H | CO |
|---|---|---|---|---|---|
| (1) | $\Delta E$ | -0.17 | -0.16 | -0.34 | -0.64 |
| | $E_a$ | 0.66 | 0.70 | 0.58 | 0.45 |
| (2a) | $\Delta E$ | -0.42 | -0.82 | -1.63 | -0.42 |
| | $E_a$ | 0.81 | 0.57 | 0.36 | 0.88 |
| (2b) | $\Delta E$ | 0.09 | 0.07 | -1.02 | -0.26 |
| | $E_a$ | 0.79 | 0.69 | 0.52 | 0.57 |
| (3a) | $\Delta E$ | 0.23 | 0.27 | -0.36 | -0.01 |
| | $E_a$ | 0.74 | 0.89 | 0.75 | 0.44 |
| (3b) | $\Delta E$ | -0.18 | -0.33 | -0.16 | -0.18 |
| | $E_a$ | 0.79 | 0.42 | 0.51 | 0.57 |
| (4) | $\Delta E$ | -0.33 | -0.93 | -0.77 | -1.22 |
| | $E_a$ | 0.45 | 0.30 | 0.38 | 0.20 |

Table 8.4: Reaction and activation energies, $\Delta E$ and $E_a$ in eV, for each step shown in Figure 8.4, and for all catalyst states (clean, C, H, and CO).

The situation is far more complex in presence of hydride. The first hydrogenation takes place from one of the hydrogen atoms on the surface. This leaves an H-vacancy on the Pd surface with an H in the near-surface position. This available subsurface hydrogen atom has a chemical potential that exceeds the surface hydrogen atom by 0.45 eV. Thus, once vinyl ($HC{=}CH_2$) is formed two options can be triggered, either from a H sitting on the surface (to attack the HC fragment) or an almost free H atom, closer to the $CH_2$ moiety, see Figure 8.6. The corresponding hydrogenation barriers are 0.36 and 0.06 eV, to $H_2C{=}CH_2$ and $HC\text{-}CH_3$ respectively. As a consequence, under these conditions, the major product is ethylidene, $HC\text{-}CH_3$, and the final product is ethane, $H_3C\text{-}CH_3$. Therefore, in the case of the hydride, the alkane production is controlled by H-vacancy generation after the first H transfer and the subsequent ejection of near-surface H.

As a summary, thermodynamic and kinetic factors depend on the nature of the catalyst, and both binding energies of ethyne and ethene pair (thermodynamic factors), and activation energies of the first branching reaction, are crucial to understand selectivity in alkyne hydrogenation.

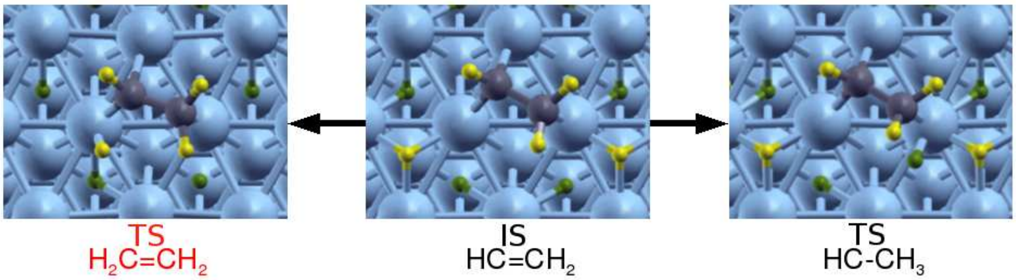

Figure 8.6: Schematic representation of the hydrogenation of vinyl, $HCCH_2$, on the palladium hydride phases. Left: transition state for the attack from a H sitting on the surface to the HC group. Right: transition state for the attack from a H in the subsurface leading to the formation of ethylidene, $HCCH_3$. Blue spheres represent Pd atoms, yellow surface H atoms, green subsurface H atoms and grey C atoms.

The adsorption of propyne on the clean surface is exothermic by 1.57 eV, (Table 8.3). Then, the first hydrogenation can take place on the primary carbon, leading to $CH_3CCH_2$ product (step (A) in Figure 8.5) with an activation energy, $E_a$, of 0.77 eV, or in the secondary carbon, leading to $CH_3CHCH$ product (B) with $E_a$ of 0.70 eV, see Table 8.5.

From each hydrogen addition, a branching point takes place that leads to the formation of $CH_3CH_2CH$ (B2b) and propene (B2a), or to propene (A2b) and $CH_3CCH_3$ (A2a), where the corresponding barriers are 0.72, 0.71, 0.77, and 0.48 eV respectively. Propene desorption is endothermic by 0.60 eV, see Table 8.3. Further propene hydrogenations to $CH_3CH_2CH_2$ (B4) or $CH_3CHCH_3$ (A4) are hindered by 0.73 and 0.83 eV barriers. Thus, the competition between propene desorption or further hydrogenation is more favourable towards desorption than for its C2 counterpart. Therefore, C3 hydrogenation to the alkene is intrinsically more selective than that of the corresponding C2. Any other hydrogenation from the rest of the intermediates in Figure 8.5 shows hydrogenation barriers between 0.93 and 0.49 eV. The effects of carbide, CO, and hydrides are parallel those found for C2, see Table 8.5.

### 8.3.3 Brønsted-Evans-Polanyi relationships

The Brønsted-Evans-Polanyi relationships, BEP, have been plotted for all reaction steps for the C-H dissociation shown in Figures 8.4 and 8.5, and for all catalyst states. Thus, all the results concerning the kinetic parameters are compiled in Figure 8.7.

Dehydrogenations of ethylene derivatives on Pd have been found to follow these kind of linear relationships independently of the degree of unsaturation of the hydrocarbon.[147] The present results extend the use of such relationships to different carbon numbers, and to all the Pd-derived substrates included in the calculations, i.e. clean surface, hydrides, carbides, and CO-covered surfaces.

| step | | clean | C | H | CO |
|---|---|---|---|---|---|
| (A) | $\Delta E$ | -0.10 | 0.21 | -0.66 | -0.52 |
| | $E_a$ | 0.70 | 0.57 | 0.39 | 0.48 |
| (B) | $\Delta E$ | -0.11 | 0.07 | -0.62 | -0.29 |
| | $E_a$ | 0.70 | 0.86 | 0.49 | 0.41 |
| (A2a) | $\Delta E$ | -0.41 | -0.23 | -0.17 | -0.27 |
| | $E_a$ | 0.48 | 0.59 | 0.97 | 0.53 |
| (A2b) | $\Delta E$ | -0.63 | -0.73 | -0.62 | -0.23 |
| | $E_a$ | 0.76 | 0.49 | 0.44 | 2.13 |
| (B2a) | $\Delta E$ | -0.29 | -0.64 | -1.31 | -0.74 |
| | $E_a$ | 0.71 | 0.54 | 0.47 | 0.78 |
| (B2b) | $\Delta E$ | 0.01 | -0.18 | -0.64 | -0.55 |
| | $E_a$ | 0.72 | 0.59 | 0.86 | 0.21 |
| (A3) | $\Delta E$ | -0.01 | -0.12 | -0.71 | -1.04 |
| | $E_a$ | 0.93 | 0.82 | 1.21 | 0.39 |
| (A4) | $\Delta E$ | 0.16 | 0.24 | 0.00 | 0.02 |
| | $E_a$ | 0.83 | 0.95 | 1.21 | 0.62 |
| (B3) | $\Delta E$ | 0.29 | 0.12 | -0.71 | -0.21 |
| | $E_a$ | 0.75 | 0.72 | 0.65 | 0.73 |
| (B4) | $\Delta E$ | 0.06 | 0.01 | -1.71 | -0.29 |
| | $E_a$ | 0.74 | 0.70 | 0.01 | 0.82 |
| (A5) | $\Delta E$ | -0.48 | -0.64 | -0.85 | -0.86 |
| | $E_a$ | 0.68 | 0.42 | 0.63 | 0.71 |
| (B5) | $\Delta E$ | -0.57 | -0.76 | 0.17 | -1.11 |
| | $E_a$ | 0.49 | 0.43 | 0.75 | 0.94 |

Table 8.5: Reaction energies, $\Delta E$, and the activation energies, $E_a$, for each step shown in Figure 8.5 on the four models shown in Figure 8.1: clean Pd surface, C in subsurface, hydride Pd and CO covered surface.

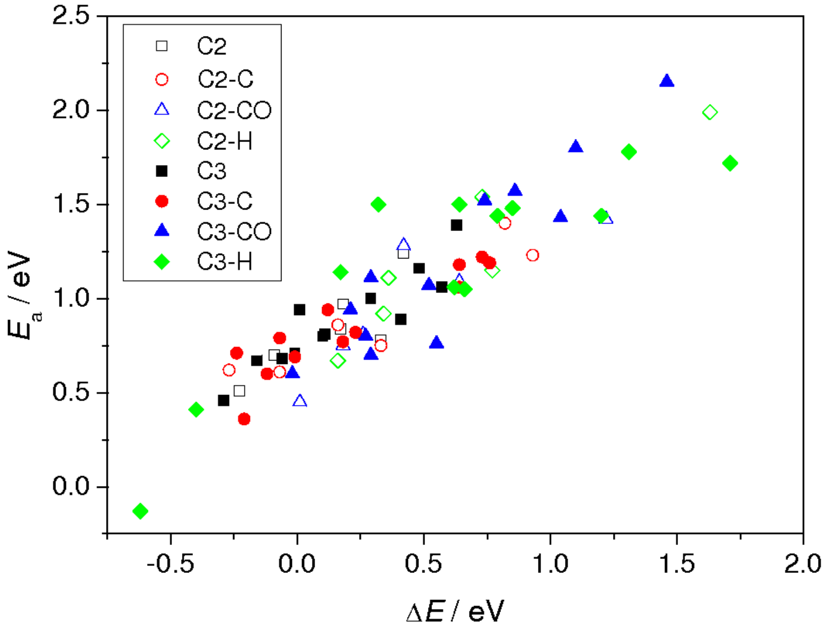

Figure 8.7: Brønsted-Evans-Polanyi relationship for the dehydrogenation of C2 and C3 compounds on the clean, carbide, hydride and CO-covered models. $E_a = 0.78\Delta E + 0.71$, r= 0.90.

### 8.3.4 Oligomerisation

The presence of oligomers is known to affect the selectivity, activity, and lifetime of the catalyst.[100] In order to keep the hydrocarbon coverage employed in the hydrogenation steps, two ethyne molecules are placed on the supercell $p(2x4)$, and the barrier for the oligomer formation are studied on the four different catalysts: clean surface, hydrides, carbides, and CO-covered surfaces.

On the clean surface, the barrier for the ethyne-ethyne coupling is 1.38 eV, see Figure 8.8. However, if very dense ethyne layers exist, the barrier can be reduced to 0.86 eV. In the presence of carbide, the reaction barriers are different depending on the local configuration; the C-C barrier increases to 1.71 or 1.99 eV, depending if the carbide is below the oligomerisation path or further away from it, see Table 8.6. Oligomerisation is energetically eased in the presence of CO, 0.91 eV, and hindered by the palladium hydride, 1.51 eV. However, effects different from those of energies, must be taken into account:

- For CO-covered surface, and to a lesser extent for hydride, the dense layer formed implies the isolation of different ensembles and thus, there is a geometric contribution that blocks preferentially oligomer formation due to reduction of the effective ensembles.
- When the barrier for C-C coupling from the partially hydrogenated HC=CH$_2$

to ethyne is calculated, it is found to be smaller than that for the ethyne-ethyne coupling, 1.19 versus 1.38 eV, which means that partially hydrogenated molecules are more energetically prone to undergo oligomerisation.

- The CO molecules adsorbed on the surface, can also react to the alkyne leading to HC=CH-CO. This energetic barrier is found to be 1.40 eV, thus, it is less likely to occur than other oligomerisation processes described above. However, the incorporation of CO to the oligomer cannot be discarded.

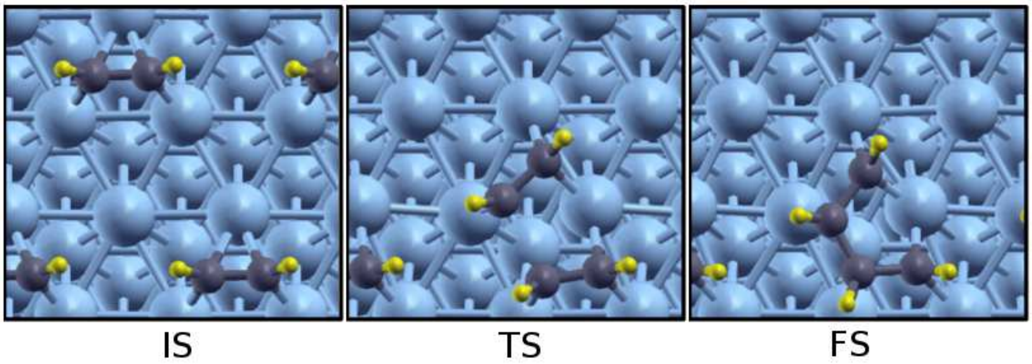

Figure 8.8: Initial, IS, transition, TS, and final state, FS, for the ethyne-ethyne coupling on Pd clean surface.

When the C-C coupling between propyne molecules is analysed, there are different coupling possibilities: head-to-head, head-to-tail, and tail-to-tail. The option head-to-tail was considered since it is statistically more likely. For C-C formation on the clean surface the barrier is 1.67 eV, and as in the case of ethyne, this barrier is larger in the presence of C (1.88 eV) and H (1.52 eV). CO lowers the C-C coupling barrier to 1.50 eV but as in the case of C2, its effect in oligomerisation primarily comes from site blocking.

| | Clean | C | H | CO |
|---|---|---|---|---|
| $\Delta E$(C2-C2) | 0.00 | 0.17/0.40 | 0.22 | -0.44 |
| $E_a$(C2-C2) | 1.38 | 1.71/1.99 | 1.52 | 0.91 |
| $\Delta E$(C3-C3) | -0.15 | -0.21/0.00 | -0.61 | -0.18 |
| $E_a$(C3-C3) | 1.67 | 1.36/1.88 | 1.52 | 1.50 |

Table 8.6: Reaction and activation energies for the oligomer formation by the ethyne-ethyne coupling, $\Delta E$(C2-C2) and $E_a$(C2-C2) in eV, and the propyne-propyne coupling, $\Delta E$(C3-C3) and $E_a$(C3-C3) in eV. In the presence of carbide, the first energy values reported correspond to the situation in which the carbide is below the oligomerisation path.

UNIVERSITAT ROVIRA I VIRGILI
THEORETICAL STUDIES OF SELECTIVE PROCESSES IN HETEROGENEOUS CATALYSIS
Mónica García Mota
ISBN:978-84-693-5424-7/DL:T-1415-2010

## 8.4 Equations for multilayered adsorption-hydride formation

The catalytic tests shown in Section 1.7 of Chapter 1, were performed on the unpretreated catalyst, and after pretreatment in alkyne, hydrogen, and in the reaction mixture. The aim of this section is to determine the equilibrium state of the surface under the different conditions. Since the description in energy terms does not account for the effect of temperatures and pressures in hydride formation, first principle thermodynamics will be employed to describe the state of the surface under different preparations. The procedure developed by Brunauer-Emmett-Teller, BET, for multilayer adsorption [206] has been used here to obtain the corresponding adsorption isotherms for the hydride formation in Pd. In this derivation $\Theta_0$, $\Theta_1$,...,$\Theta_i$ will represent the area that is covered by 0,1,..., n layers of adsorbed hydrogen, see Figure 8.9.

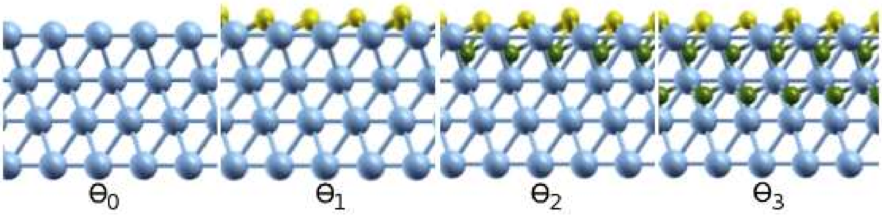

Figure 8.9: Schematic representation of the Pd structure with different i-layer coverages of hydrogen. $\Theta_0$, $\Theta_1$,...,$\Theta_i$ represent the area that is covered by 0,1,..., n layers of adsorbed hydrogen.

The equations for our conditions are as follows:

Direct adsorption on the clean surface: ($k_{1,H_2}$, $k_{-1,H_2}$)

$$H_2^{gas} + 2^* \longleftrightarrow 2H^*(1) \tag{8.7}$$

Adsorption on the already precovered surface and creation of the first subsurface layer: ($k_{2,H}$, $k_{-2,H}$)

$$H_2^{gas} + 2(1) \longleftrightarrow 2H^*(2) \tag{8.8}$$

Creation of the i-subsurface layer: ($k_{i,H}$, $k_{-i,H}$)

$$H_2^{gas} + 2(i-1) \longleftrightarrow 2H^*(i) \tag{8.9}$$

where $k_{i,H}$ describes the adsorption and $k_{-i,H}$ represents the desorption.

Since at equilibrium $\Theta_0$ must remain constant, the rate of condensation on the clean surface is equal to the rate of evaporation from the first layer

$$k_{1,H_2} p_{H_2} \Theta_0^2 = k_{-1,H_2} \Theta_1^2 \tag{8.10}$$

Extending the same argument to the second, and consecutive layers we obtain

$$k_{i,H} p_{H_2} \Theta_{i-1}^2 = k_{-i,H} \Theta_i^2 \tag{8.11}$$

The total surface area of the catalyst, $A$, and the total volume adsorbed, $v$, can be expressed as

$$A = \sum_{i=0}^{\infty} \Theta_i \tag{8.12}$$

$$v = v_0 \sum_{i=0}^{\infty} i\Theta_i \tag{8.13}$$

where $v_0$ is the volume of gas adsorbed on one square centimetre of the adsorbent surface, when it is covered with a complete unimolecular layer of adsorbed hydrogen gas. If $v_m$ is defined as the volume of hydrogen adsorbed when the entire adsorbent surface is covered with a complete unimolecular layer, $v_m = Av_0$, the relation between the total volume, $v$, and $v_m$ can be expressed as

$$\frac{v}{v_m} = \frac{\sum_{i=0}^{\infty} i\Theta_i}{\sum_{i=0}^{\infty} \Theta_i} \tag{8.14}$$

From Equation 8.10, the surface area of the first layer, $\Theta_1$, can be expressed as

$$\Theta_1 = (\frac{k_{1,H_2}}{k_{-1,H_2}} p_{H_2})^{\frac{1}{2}} \Theta_0 = (K_{1,H_2} p_{H_2})^{\frac{1}{2}} \Theta_0 \tag{8.15}$$

If in Equation 8.11, the relation $k_{i,H}/k_{-i,H}$ is the same for the resting layers, 2, 3 ... $i$, the coverage, $\Theta_i$ can be expressed as

$$\Theta_i = (\frac{k_{i,H}}{k_{-i,H}} p_{H_2})^{\frac{1}{2}} \Theta_{i-1} \tag{8.16}$$

The following relations will be defined

for $i$=1

$$Y = (K_{1,H_2} p_{H_2})^{\frac{1}{2}} \tag{8.17}$$

and for all $i \neq 1$

$$X = (K_{i,H_2} p_{H_2})^{\frac{1}{2}} \tag{8.18}$$

With the previous equations, the surface covered by $i$ layer, $\Theta_i$, can be expressed as

for $i$=1

$$\Theta_1 = Y\Theta_0 \tag{8.19}$$

for all $i \neq 1$

$$\Theta_i = cX^i\Theta_0 \tag{8.20}$$

with $c$ defined as:

$$c = \frac{Y}{X} = (\frac{K_1}{K_i})^{\frac{1}{2}} \tag{8.21}$$

where $K_1$ and $K_2$, are the equilibrium constants that can be expressed as function of the average Gibbs free energy changes when the hydrogen is adsorbed in the first layer, $\Delta G^0_H$, and in the successive $i$ layers, $\Delta G^0_{H_{ss}}$.

$$K_1(T) = \exp(\frac{-\Delta G^0_H}{k_B T}) \tag{8.22}$$

$$K_2(T) = \exp(\frac{-\Delta G^0_{H_{ss}}}{k_B T}) \tag{8.23}$$

By using infinite summations, then Equation 8.14 can be written as follows

$$\frac{v}{v_m} = \frac{cX}{(1-X)(1-X+cX)} \tag{8.24}$$

### 8.4.1 Pretreatment in alkyne

To reproduce the pretreatment in the alkyne presence, the reaction that describe the carbide formation has to be added in the model

$$\frac{1}{2}C_2H_2^{gas} + * \longleftrightarrow C^* + \frac{1}{2}H_2 \tag{8.25}$$

If the equilibrium is considered

$$k_{ads,C_2H_2}(p_{C_2H_2})^{\frac{1}{2}}\Theta_0 = k_{des,C_2H_2}(p_{H_2})^{\frac{1}{2}}\Theta_C \tag{8.26}$$

with k$_{ads,C_2H_2}$, k$_{des,C_2H_2}$ the adsorption and desorption constants for the carbide formation.

In this situation, the total catalyst surface will be the area that is covered by 0,1,..., $i$ layers of adsorbed hydrogen, $\Theta_0$, $\Theta_1$,...,$\Theta_i$, and the carbide surface, $\Theta_C$, see Figure 8.10. $\Theta_C$, by the Equation 8.26, can be expressed as

$$\Theta_C = K_{C_2H_2}\sqrt{\frac{p_{C_2H_2}}{p_{H_2}}}\Theta_0 \tag{8.27}$$

The total adsorbed volume, $v$, and the total surface area of the catalyst, $A$, assuming the exclusion area found for the carbide in Figure 8.3, are

UNIVERSITAT ROVIRA I VIRGILI
THEORETICAL STUDIES OF SELECTIVE PROCESSES IN HETEROGENEOUS CATALYSIS
Mónica García Mota
ISBN:978-84-693-5424-7/DL:T-1415-2010

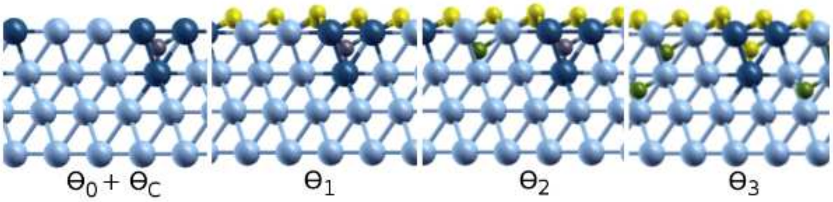

Figure 8.10: Schematic representation of the Pd structure with different i-layer coverages of hydrogen and carbide $\Theta_C$.

$$v = v_0(11\Theta_C + \sum_{i=0}^{\infty} i\Theta_i) \tag{8.28}$$

$$A = 12\Theta_C + \sum_{i=0}^{\infty} \Theta_i \tag{8.29}$$

In case of the presence of the carbide the relation $v/v_m$ is

$$\frac{v}{Av_0} = \frac{v}{v_m} = \frac{11\Theta_C + \sum_{i=0}^{\infty} i\Theta_i}{12\Theta_C + \sum_{i=0}^{\infty} \Theta_i} \tag{8.30}$$

and by using infinite summations $v/v_m$ can be written as follows

$$\frac{v}{v_m} = \frac{cX + 11(1-X)K_{C_2H_2}\sqrt{\frac{p_{C_2H_2}}{p_{H_2}}}}{(1-X)[(1-X) + cX + 12(1-X)K_{C_2H_2}\sqrt{\frac{p_{C_2H_2}}{p_{H_2}}}]} \tag{8.31}$$

With the calculated Gibbs free energy changes, $\Delta G^0_H$, $\Delta G^0_{H_{ss}}$ and $\Delta G^0_C$, compiled in Table 8.7, the relation $v/v_m$ can be represented in function of the hydrogen, and ethyne pressures, $p_{H_2}$ and $p_{C_2H_2}$ at the experimental temperature of 350 K, see Figure 8.11.

| | $\Delta G^0_H$ | $\Delta G^0_{H_{ss}}$ | $\Delta G^0_{CO}$ | $\Delta G^0_{C_2H_2}$ |
|---|---|---|---|---|
| Pd-CO | -0.76 | 0.10 | -0.77 | - |
| Pd-$C_2H_2$ | -0.76 | 0.10 | - | -0.63 |

Table 8.7: Average Gibbs free energy changes in eV, when the hydrogen is adsorbed on the first layer, $\Delta G^0_H$, and on the successive $i$ layers, $\Delta G^0_{H_{ss}}$. $\Delta G^0_{CO}$ is the average Gibbs free energy change when the CO is adsorbed, and $\Delta G^0_{C_2H_2}$ the average Gibbs free energy change for the carbide formation.

In these cases, only ethyne (propyne) and hydrogen compete for the formation of carbide and hydride structures. In Figure 8.11, $v/v_m$ larger than 1 indicates that the subsurface hydride is being formed. The corresponding experimental points employed in

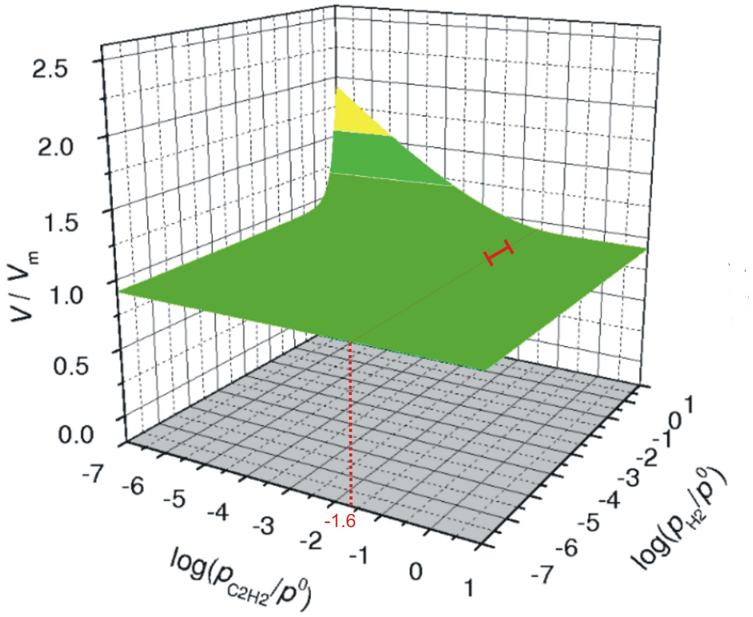

Figure 8.11: Relation $v/v_m$ in function of the hydrogen and ethyne pressures, $\log(p_{H_2}/p^0)$ and $\log(p_{C_2H_2}/p^0)$ at the experimental temperature of 350 K.

the real tests (Section 1.7 in Chapter 1) are indicated (red line) to show if the initial state of the system corresponds to an H-dense or H-lean region. Under alkyne pretreatment, carbides can be formed. This implies that a full hydrogen surface coverage is possible but carbides block the formation of subsurface hydrogen species.

### 8.4.2 Pretreatment in CO

To reproduce the pretreatment in the CO presence, the adsorption-desorption of CO on the surface is described as

$$CO^{gas} + * \longleftrightarrow CO^{*} \tag{8.32}$$

if the equilibrium is considered

$$k_{ads,CO}p_{CO}\Theta_0 = k_{des,CO}\Theta_{CO} \tag{8.33}$$

with $k_{ads,CO}$, $k_{des,CO}$ the adsorption and desorption constants for CO.

In this situation the total catalyst surface will be the area that is covered by 0,1,..., $i$ layers of adsorbed hydrogen, ($\Theta_0$, $\Theta_1$,...,$\Theta_i$) and the area covered by CO, $\Theta_{CO}$, see Figure 8.12. $\Theta_{CO}$, by the Equation 8.33, can be expressed as

$$\Theta_{CO} = (\frac{k_{ads,CO}}{k_{des,CO}}p_{CO})\Theta_0 = K_{CO}p_{CO}\Theta_0 \tag{8.34}$$

with $K_{CO}$ the CO equilibrium constant, that can be expressed as function of the average Gibbs free energy changes, $\Delta G^0_{CO}$, when the carbide is formed.

$$K_{CO}(T) = \exp(\frac{-\Delta G^0_{CO}}{k_B T}) \tag{8.35}$$

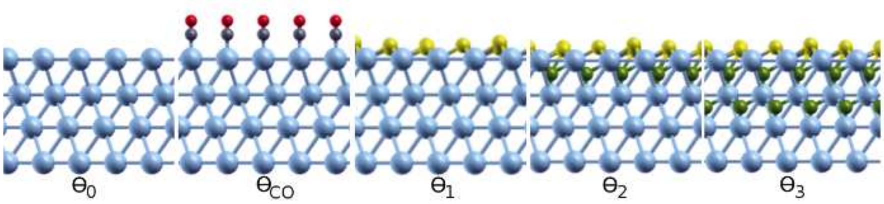

Figure 8.12: Schematic representation of the Pd structure with different i-layer coverages of hydrogen, $\Theta_0$, $\Theta_1$,...,$\Theta_i$, and one layer completely covered by CO, $\Theta_{CO}$.

The total adsorbed volume, $v$, and the total surface area of the catalyst, $A$, are

$$v = v_0 \sum_{i=0}^{\infty} i\Theta_i \tag{8.36}$$

$$A = \sum_{i=0}^{\infty} \Theta_i + \Theta_{CO} \tag{8.37}$$

With the previous equations, the relation between the total volume, $v$, and $v_m$ can be expressed as

$$\frac{v}{Av_0} = \frac{v}{v_m} = \frac{\sum_{i=0}^{\infty} i\Theta_i}{\sum_{i=0}^{\infty} \Theta_i + \Theta_{CO}} \tag{8.38}$$

By using infinite summations, then Equation 8.38 can be written as follows

$$\frac{v}{v_m} = \frac{cX}{(1-X)[(1-X) + cX + (1-X)K_{CO}p_{CO}]} \tag{8.39}$$

With the calculated Gibbs free energy changes, $\Delta G^0_H$, $\Delta G^0_{H_{ss}}$ and $\Delta G^0_{CO}$, compiled in Table 8.7, the relation $v/v_m$ can be represented in function of the hydrogen and CO pressures, $p_{H_2}$ and $p_{CO}$ at the experimental temperature of 350 K. The Figure 8.13 shows as under extremely low CO coverages, $v/v_m$ is larger than 1 indicating the formation of the hydride. But if CO is added the equilibrium structure shows a total amount of hydrogen that is not enough to form a complete a full H monolayer on the surface and no subsurface hydrogen can be formed.

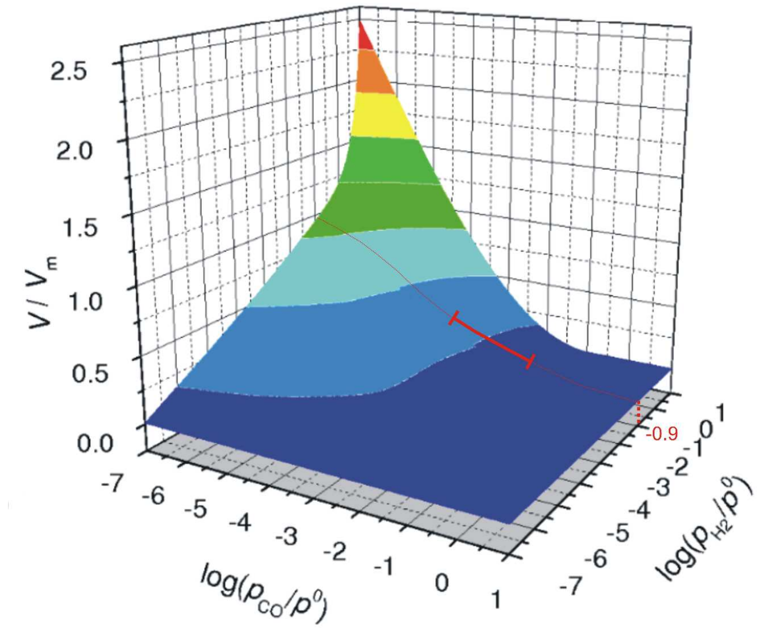

Figure 8.13: Relation $v/v_m$ in function of the hydrogen and CO pressures, $\log(p_{H_2}/p^0)$ and $\log(p_{CO}/p^0)$ at the experimental temperature of 350 K.

## 8.5 Conclusions

In the present chapter, the hydride and the carbide formation on Pd have been analysed by DFT-based simulations. The conclusions from this chapter are

- With respect to the states of the system
  - Hydride formation: $PdH_x$ shows both a low-content $\alpha$-$PdH_{0.02}$ and a high content $\beta$-$PdH_{0.7}$ phases. At low coverage, 0.25 ML, hydrogen is adsorbed exothermically, and the $H_2$ dissociation is easy even at a high hydrogen coverage. The hydrogen adsorption energy in the bulk is much smaller than that for the surface adsorption.
  - Carbide formation: carbide formation arises from the decomposition of organic moieties. The formation energy is only exothermic when it is formed from the ethyne moiety, for all the rest the carbide formation is endothermic. The most favourable positions for C atoms in Pd are the octahedral subsurface sites, penetration towards the bulk has a thermodynamic penalty cost of 0.04 eV. The carbide phase is not very dense in C atoms because the C insertion at neighbouring sites is repulsive.
  - Carbide-hydride interplay: if there is a C atom in the subsurface, only the position on top of the carbon atom is not favoured. The hydrogen average

adsorption energy of the first layer is slightly reduced compared with when C atom is not present. The insertion of H atoms on the second layer is largely restricted. The presence of carbon impedes any other H adsorption even at distances as long as 5 Å. For hydrogen adsorptions in the third layer, the standard value of the adsorption energy for subsurface H adsorption is retrieved.

- With respect to thermodynamic factors
  - The most effective way to obtain a good selectivity towards the double bound according with the calculated adsorption energies for alkynes and alkenes are by order of magnitude: CO, then hydrides, carbides and the most unselective system is the clean surface. Because it is known that hydride formation produces over-hydrogenated moieties, the thermodynamic factor can not be considered as the only selectivity descriptor when different H species are present.
- With respect to kinetic factors
  - The activation energies of the first branching reaction (vynil hydrogenation) are crucial to understand selectivity in the alkyne hydrogenation.
    - On the clean surface, formation of the ethene, and ethylidene is almost equally likely, and ethene can either desorb or be further hydrogenated. Thus, both effects are responsible for the relatively low selectivity towards ethene observed for clean Pd.
    - The presence of the carbide induces selectivity: destabilises ethene adsorbed on the surface, and improves the second hydrogenation branching ratio.
    - Low CO coverage leads to selective ethene production: the barriers for the ethene formation is reduced with respect to the clean surface, and it is lower than for the ethylidene formation.
    - In the presence of hydride, the major product is ethylidene and the final product is ethane: the first hydrogenation leaves an H-vacancy on the Pd surface with an H in the near-surface position, the attack from this almost free H atom to vinyl presents a very low barrier.
  - In the case of C3 hydrogenation, the effects of carbide, CO, and hydrides are parallel to those found in the description of C2. The main difference is that the competition between propene desorption or further hydrogenation on clean palladium is more favourable towards desorption than for its C2 counterpart.
- With respect to oligomer formation

  - The presence of oligomers affects the selectivity, activity, and lifetime of the catalyst. Oligomerisation is energetically eased in the presence of CO, but several factors must be taken into account:
    - The dense layer formed of CO blocks oligomer formation due to reduction of the effective ensembles.
    - CO can also react to the alkyne, although it is less likely to occure than other oligomerisation processes.

- With respect to the multilayered adsorption-hydride formation
  - First principle thermodynamics have been employed to describe the state of the surface under different preparations, through the procedure developed by Brunauer-Emmett-Teller.
    - Under alkyne pretreatment, carbides can be formed. The full hydrogen coverage is possible but carbides block the formation of subsurface hydrogen species. On the contrary, under hydrogen pretreatment, the hydride would be generated.
    - Under extremely low CO coverages the hydride is formed. But if CO is increased the total amount of hydrogen is not enough to form a complete a full H monolayer on the surface and no subsurface hydrogen can be formed, thus selectivity is achieved.

In general, DFT plus first principle thermodynamics and extensive kinetic determinations provide a robust platform to rationalise complex Pd:CO chemistry in selective hydrogenations.

The high unselective character of the hydride phase shown at higher $H_2$:alkyne ratio (front-end conditions) is supported in the calculations by the high activity found for nascent H atoms emerging from subsurface positions. The addition of CO to the feed presents remarkable influence on the alkyne selectivity even at very low concentrations at large $H_2$:alkyne ratios. CO forms a dense blanket that covers the surface, improves the thermodynamic factor (alkyne versus alkene adsorption), reduces the amount of available hydrogen atoms on the surface and the formation of subsurface H species, and decreases the size of active ensembles. If carbides are present they are moved away from the near-surface region. CO over-performs C in selectivity improvements since, for CO, no kinetic requirements as those found for the carbide need to be overcome to form the compact CO layer. Thus, the CO presence is a robust way to control the selectivity in Pd-containing systems.

# Chapter 9

# Concluding remarks

Advances in Density Functional Theory, DFT, have made it possible to describe catalytic reactions at surfaces with such accuracy that the theoretical results can be compared with experiments. The concluding remarks on each theme treated in the present work are:

- With respect to the CO vibrational spectra

  Monometallic systems, Pd and Au, and different PdAu alloys were characterised through the study of the CO adsorption on them. The most likely configurations in terms of thermodynamics are those where Pd atoms are surrounded by Au atoms. CO frequencies can be used to test the local Pd environment. CO is very weakly adsorbed on the Au surface sites, low coordination or high CO pressures are needed to retrieve any bonding to the surface. On Pd monometallic surfaces, the CO binding energy depends on two terms: the ensemble to which CO is bound and the *d*-band shifts of the Pd atoms in the ensemble. Pd atoms placed in the sub-surface layer provoke a increase of the binding energy of CO, but do not change its stretching frequency. Pd dimers and trimers on the surface can accept more than a CO molecule and in that case the stretching frequencies are similar to those of singleton on top adsorption. Therefore, double CO adsorption on Pd dimers can appear as shoulders at high frequencies. These bands are experimentally assigned to CO adsorbed on Au, which, according to the calculated binding energy, is unlikely. Detailed description is presented, including: CO induced segregation phenomena, multiple CO adsorption, and surface-subsurface interactions.

- With respect to catalysed CO oxidation on Au containing alloys

  The most important features in the adsorption of atomic and molecular adsorptions (O, $O_2$ and CO), are characterised on the transition metals: Ni, Pd and Pt, and on substitutional $AuM_3@M$ alloys, (M=Ni, Pd, and Pt). These properties are found to be dependent on the adsorption site. The bonds are weaker in the presence of Au with respect to that on the monometallic surfaces. The potential energy surface of atomic oxygen clarifies the role of the gold atoms on the surface reactivity; gold blocks the normal $O_2$ dissociation path observed for pure metal as consequence of the confinement on the O adsorption in sites without gold atoms in the surroundings. When the CO oxidation is inspected, on Ni the $O_2$ dissociation is likely at low temperatures, and the atomic oxygen is strongly bound on the surface. Thus, the CO reaction with active oxygen atoms in the surface is the rate-limiting step. On $AuNi_3$ surface alloy, molecular oxygen can act as oxidant at low temperatures. However, the reaction is not catalytic since remaining O atoms on the surface can not be eliminated until high temperatures are reached.

- With respect to the direct hydrogen peroxide synthesis

  The direct $H_2O_2$ synthesis was studied on Pd and Pd-containing alloys as environmentally friendly alternative to the anthraquinone process. The hydrogen dissociation is easy under normal conditions on all monometallic and bimetallic surfaces studied. $O_2$ adsorption depends on the absorption site and the bonds are weaker in the alloys than in the Pd monometallic surface. The energy barriers for the hydroperoxide intermediate formation, are lower for the $AuPd_3$ and $AgPd_3$@Pd systems than for the resting Pd and $PtPd_3$@Pd ones. The hydrogenation of the hydroperoxide species that leads to the hydrogen peroxide, presents both *anti*- and *syn*-attack. The *anti*-attack is more likely than the *syn*, with energy barriers lower than 0.15 eV in PdAu alloys. The competitive steps to the hydrogen peroxide are summarised in two categories; O-O bond splitting and over-hydrogenations. The dynamic properties of the hydroperoxide intermediate, hamper $O_2H^*$ splitting and the hydrogen attack to form a water molecule. Because the hydrogen peroxide is very weakly adsorbed to the surface, $H_2O_2$ over-hydrogenation or $H_2O_2$ splitting in two hydroxyl groups are unlikely. Therefore, $O_2$ dissociation is the most important competitive step to the formation of hydrogen peroxide. A simplified selectivity study, indicates the suitability for the direct hydrogen peroxide synthesis of each model surface, with the knowledge of the adsorption energies for atomic oxygen, $E_O$, and hydrogen, $E_H$. With this selectivity model, the gold containing alloy, $AuPd_3$@Pd, is found as the best catalyst in agreement with the experimental observations done by the Hutchings group.[65, 66, 67]

- With respect to the vinyl acetate synthesis from ethene and acetic acid on Pd-based model system

  The strong dependence on the local structure of the ensemble in the vinyl acetate synthesis was analysed with the study of the elementary steps to the VAH formation on several Pd dimer configurations on both Au(100) and (111) surfaces. The most stable ensemble corresponds to next-nearest neighbour configuration. Ethylene adsorption energies are very similar for all ensembles in both surfaces, but acetate hapticity is different depending on the Pd dimer where the acetate is adsorbed. Only on the nearest neighbour ensemble, the most stable configuration is as dihapto species, therefore, to generate the active complex: acetate-ethylene; this configuration pays an energy penalty to change the configuration. The VAH formation is the rate limiting step for the vinyl acetate with activation energy lower on the (111) surface than on (100) in any case. All previous steps need to be taken into account to explain the higher reactivity experimentally found for the next-nearest neighbour structures (100) with respect to the corresponding (111).

When the link between homogeneous and heterogeneous catalysis for the VA synthesis is investigated through theoretical tools, the main steps for the reaction mechanisms found on both version of the Pd-based catalyst are very similar: ethylene-acetate coupling (C-O formation), $\beta$-hydrogen elimination, and catalyst reoxidation, but the relative barriers are different. The reoxidation process is quite simple in the heterogeneous Pd catalyst, while several steps including a external redox pair are needed in the homogeneous version. This is due to the instability of the centre under $O_2$. With respect to the rate limiting step, for the homogeneous system it involves the $\beta$-hydrogen transfer while for the heterogeneous counterpart, hydrogen activation is relatively easy and the rate limiting step is associated to the ethylene-acetate coupling on the surface. In addition, this rate limiting step is significantly higher than that for the homogeneous system, and as consequence, the reaction takes place at lower temperatures in the homogeneous case than in the heterogeneous version of the catalyst, as seen experimentally.

- With respect to the selective homogeneous and heterogeneous gold catalysis with alkynes and alkenes

  The preference shown by alkynes to react with homogeneous and heterogeneous gold catalysis in the presence of alkenes or other functional groups is termed as alkynophilicity, but this preference is controlled by distinct mechanisms in homo- and heterogeneous gold catalysts. For heterogeneous catalysis, the origin of the selective adsorption of triple bonds is thermodynamic, while for homogeneous catalyst, alkenes are preferentially coordinated to gold than alkynes, but electro- and nucleophilic attacks are more thermodynamically favoured for the triple bonds. Therefore, alkynophilicity in homogeneous systems is not related to the relative strength of the bonding of the active alkyne species but to its activation for a desired reaction.

- With respect to the interplay between CO, hydrides, and carbides in selective alkyne hydrogenation on palladium

  The high unselective character of the hydride phase shown at higher $H_2$:alkyne ratio (front-end conditions), is supported in the calculations by the high activity found for nascent H atoms emerging from subsurface positions. The addition of CO to the feed presents remarkable influence on the alkyne selectivity even at very low concentrations at large $H_2$:alkyne ratios. CO forms a dense blanket that covers the surface, improves the thermodynamic factor (alkyne versus alkene adsorption), reduces the amount of available hydrogen atoms on the surface and the formation of subsurface H species, and decreases the size of active ensembles. If carbides are present, they are moved away from the near-surface region. CO over-performs C in selectivity improvements, since, for CO, no kinetic requirements as those found for the carbide need to be overcome to form the compact CO layer. Thus, the CO presence is a robust way to control the selectivity in Pd-containing systems.

# Appendix A

# Characterisation of transition metal surfaces: Ni, Pd, Pt and Au

This Appendix shows how the cell parameters for Ni, Pd, Pt and Au surfaces have been calculated. The study of the relative stability of each (111) surface has been analysed through different energy parameters including: surface energy and relaxation, and *d*-band centre shift.

## A.1 Bulk parameters

Calculations were performed for Ni, Pd, Pt and Au bulk in a faced-centred cubic, fcc, structure, the most stable structure for all of them. Metal bulk properties were calculated performing a Brillouin-zone integration with very dense *k*-point grids, 11x11x11, generated through the Monkhorst-Pack scheme.[130]

The cell parameter optimisation was achieved by calculating the energies for a set of values in a region close to the experimental cell parameter. As expected, the equation of state suitable for modelling solids is different from that of the ideal gas law. A solid has a certain equilibrium volume $V_0$, and the energy increases quadratically as volume is increased or decreased a small amount from that value. The simplest dependence of energy on volume would be a harmonic solid, with

$$E = E_0 + \frac{1}{2k_T}\frac{(V-V_0)^2}{V_0} \tag{A.1}$$

where $k_T$, the isothermal compressibility, is a measure of the relative volume change of a solid as a response to a pressure change at constant temperature.

$$k_T = -\frac{1}{V}\left(\frac{\partial V}{\partial p}\right)_T \tag{A.2}$$

There are equations of state in which the pressure is also considered, as the quadratic Murnaghan equation of the state,[207] or the third-order Birch-Murnaghan isothermal equation of state,[182] but we have used a third degree polynomial function for the energy as a function only dependent on the cell volume, see Figure A.1, and its minimum has been located.

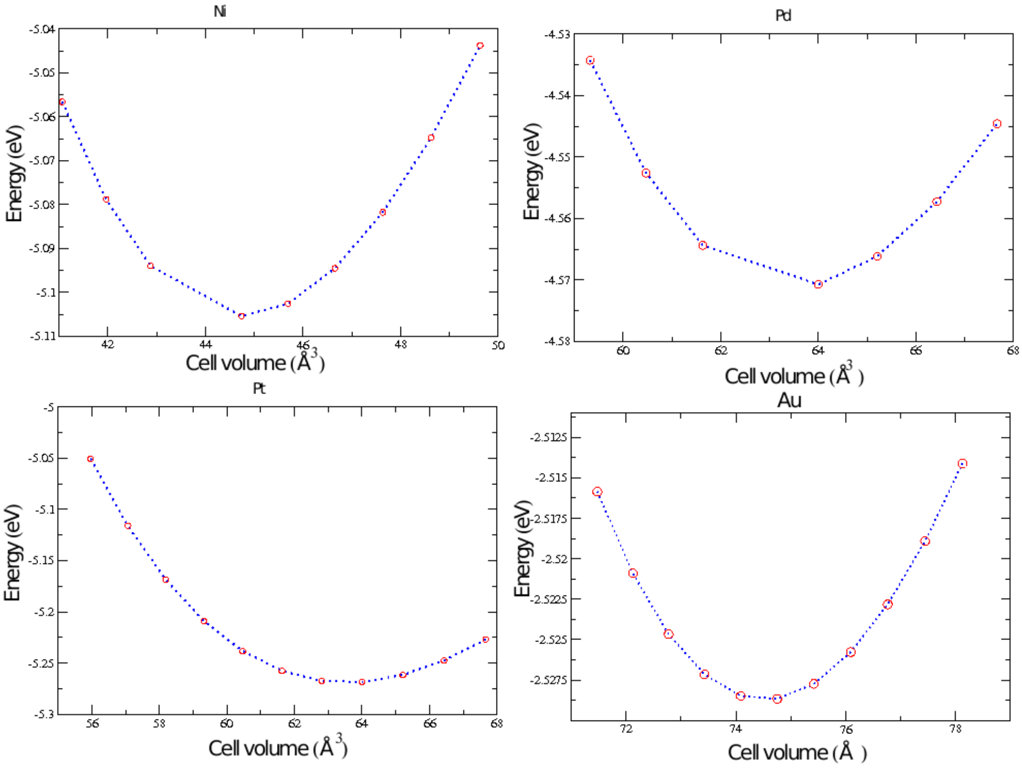

Figure A.1: The cell parameter optimisations for Ni, Pd, Pt and Au.

The calculated and experimental cell parameters are compiled in Table A.1. The theoretical cell parameters are larger than the experimental ones. This agrees with previous benchmarks with the RPBE functional.[124] The agreement with the experimental data is rather good.[172]

| | Ni | Pd | Pt | Au |
|---|---|---|---|---|
| $a$ | 3.55 | 3.99 | 3.99 | 4.21 |
| $a_{(exp)}$ | 3.524 | 3.8907 | 3.9242 | 4.0782 |
| Error(%) | 0.8 | 2.5 | 1.7 | 3.2 |

Table A.1: Theoretical and experimental cell parameter, $a$ and $a_{(exp)}$ in Å, for the transition metals, Ni, Pd, Pt and Au. Deviation in % respect to the experimetal values.

### A.1.1 Cohesive energies

The cohesive energy, $E_{coh}$, of a solid is the energy required to break the atoms of the solid into isolated species, that is

$$E_{coh} = E_{solid} - \sum_{A} E_{A}^{isolated} \tag{A.3}$$

where $E_{solid}$ is the solid energy, and the label $A$ represents the different atoms that constitute it. The results for Ni, Pd, Pt and Au are compiled in table A.2.

| | Ni | Pd | Pt | Au |
|---|---|---|---|---|
| $E_{coh}$ | -4.23 | -3.07 | -5.21 | -2.41 |
| $E_{coh(exp)}$ | -4.44 | -3.89 | -5.84 | -3.81 |
| Error ($\Delta$) | +0.21 | +0.81 | +0.63 | +1.40 |

Table A.2: Theoretical and experimental [131] cohesive energies, $E_{coh}$ and $E_{coh(exp)}$ in eV/atom, and differences respect to the experimental values, Error ($\Delta$), same units, for Ni, Pd, Pt and Au(111) surfaces.

The correlations with experimental values are not so good because the value $E_{coh}$ is severely affected by the estimation of the atomic energy. With the present approach the isolated atomic metal atoms are sometimes not properly described.

## A.2 Stability of the (111) surface

The (111) surface of fcc crystals is the one showing larger stability and as a consequence more represented in the nanoparticles forming the catalyst.[208] The (111) surface of an fcc crystal consists on triangular ensembles see Fig A.2.

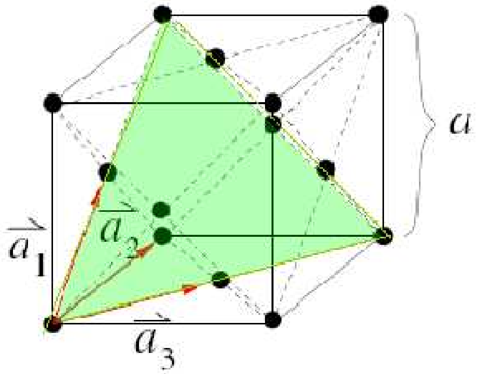

Figure A.2: Surface (111) in a faced-centred cubic structure.

The study of the relative stability of monometallic surfaces and alloys can be analysed through different energy parameters as surface energies, and $d$-band shift.

### A.2.1 Surface energy and relaxation

The surface energy, $\gamma$, defined as the surface excess free energy per unit area of a particular crystal facet, is one of the basic quantities in surface physics. The formation of surfaces is energetically costly. Surface energy quantifies the disruption of chemical bonds that occurs when a surface is created, giving an estimation of the stability of the surface. During the last decade there have been many calculations of the surface energy of metals, either from first-principles [173] or by semi-empirical methods.[209]

Surface energy, $\gamma$, can be obtained in a slab calculation as follows

$$\gamma = \gamma^{unrel} + E^{rel} \tag{A.4}$$

where $E^{rel}$ is the energy change after relaxation, and $\gamma^{unrel}$ is

$$\gamma^{unrel} = 1/2(E_{surf} - N_{atoms}E_{bulk}) \tag{A.5}$$

$E_{surf}$ is the total energy of the unrelaxed surface, $N_{atoms}$ is the total number of atoms in the slab, and $\mathrm{E}_{bulk}$ is the energy of a bulk atom. Au is found to be the metal with lower surface energy, 0.62 J/m$^2$, see Table A.3.

Relaxation is a small rearrangement of the surface layers. It involves adjustments in the layer spacings perpendicular to the surface, there is no change either in the periodicity parallel to the surface or to the symmetry of the surface. The surface relaxation has been calculated as

$$\%relax = \frac{Z_{s-relax} - Z_{s-unrelax}}{d_{(111)interplanar}} * 100 \tag{A.6}$$

where $d_{(111)interplanar}$ is the (111) interplanar distance, $\frac{a}{\sqrt{3}}$, and the difference $Z_{s-relax}$-$Z_{s-unrelax}$ is the change of the surface position after relaxation. The relaxation values are negatives for both Pd and Au metals, -0.78 and -0.38 J/m$^2$ respectively, this means that the surface layer of these atoms is pulled in towards the second layer.

| Metal | Ni | Pd | Pt | Au |
|---|---|---|---|---|
| $\gamma$ | 1.67 | 1.05 | 1.22 | 0.62 |
| % *relax* | 1.05 | -0.78 | 0.63 | -0.38 |

Table A.3: Surface energies, $\gamma$, J/m$^2$, and the rates between the surface atom and bulk atom height, % relax, for Ni, Pd, Pt and Au(111) surfaces.

### A.2.2 d-band centre variation

The centre of the *d*-band, $\varepsilon_d$, is calculated as the average of the integration of the density of states below Fermi level weighted by the energy. The presence of a second metal in the surface affects the overlap of the electronic orbitals and therefore, affects the electronic properties of the surface and its reactivity. Although the degree of the *d*-band filling remains the same, the width of the *d*-band, and the energy of its centre, $\varepsilon_d$, changes as the overlap is perturbed. Table A.4 shows how the *d*-band centre of the majority atoms is modified in the AuM$_3$@M alloy, (M=Ni, Pd, Pt).

| Surface | Ni | AuNi$_3$ | Pd | AuPd$_3$ | Pt | AuPt$_3$ | Au |
|---|---|---|---|---|---|---|---|
| $\varepsilon_d$ | -1.14 | -1.20 | -1.53 | -1.54 | -2.11 | -2.15 | -2.38 |
| $\Delta\varepsilon_d$ | 0.00 | -0.06 | 0.00 | -0.02 | 0.00 | -0.03 | 0.00 |

Table A.4: *d*-band centre, $\varepsilon_d$ in eV, and *d*-band centre shift, $\Delta\varepsilon_d$ in eV, for AuM$_3$ surface alloy, (M= Ni, Pd, Pt).

# Appendix B

# Selectivity study of direct $H_2O_2$ synthesis on Pd and Pd-containing alloys

The selectivity model employed in Chapter 5 is described in this Appendix. The following elementary reactions of the hydrogen peroxide synthesis have been considered

$$H_2^{gas} + 2* \longleftrightarrow 2H^* \qquad (k_{ads,H_2}, k_{des,2H}) \tag{B.1}$$

$$O_2^{gas} + * \longleftrightarrow O_2^* \qquad (k_{ads,O_2}, k_{des,O_2}) \tag{B.2}$$

$$O_2^* + * \longleftrightarrow 2O^* \qquad (k_{3a}, k_{3b}) \tag{B.3}$$

$$O_2^* + H^* \longleftrightarrow O_2H^* + * \qquad (k_{4a}, k_{4b}) \tag{B.4}$$

$$O_2H^* + H^* \longleftrightarrow H_2O_2^* + * \qquad (k_{5a}, k_{5b}) \tag{B.5}$$

$$O_2H^* + H^* \longleftrightarrow H_2O^* + O^* \qquad (k_{6a}, k_{6b}) \tag{B.6}$$

The corresponding rates for each step are

$$r_1(t) = k_{ads,H_2} p_{H_2}(t)\Theta_*^2(t) - k_{des,2H}\Theta_H^2(t) \tag{B.7}$$

$$r_2(t) = k_{ads,O_2} p_{O_2}(t)\Theta_*(t) - k_{des,O_2}\Theta_{O_2}(t) \tag{B.8}$$

$$r_3(t) = k_{3a}\Theta_{O_2}(t)\Theta_*(t) - k_{3b}\Theta_O^2(t) \tag{B.9}$$

$$r_4(t) = k_{4a}\Theta_{O_2}(t)\Theta_H(t) - k_{4b}\Theta_{O_2H}(t)\Theta_*(t) \tag{B.10}$$

$$r_5(t) = k_{5a}\Theta_{O_2H}(t)\Theta_H(t) - k_{5b}\Theta_{H_2O_2}(t)\Theta_*(t) \tag{B.11}$$

$$r_6(t) = k_{6a}\Theta_{O_2H}(t)\Theta_H(t) - k_{6b}\Theta_{H_2O}(t)\Theta_O(t) \tag{B.12}$$

The number of sites on a catalyst is constant and hence all coverages should always add up to unity, as expressed by the following balance of sites

$$\Theta_*(t) + \Theta_H(t) + \Theta_{O_2}(t) + \Theta_O(t) + \Theta_{O_2H}(t) + \Theta_{H_2O}(t) + \Theta_{H_2O_2}(t) = 1 \tag{B.13}$$

If reactions (B.1) and (B.2) are considered sufficiently fast that they can be considered in quasi-equilibrium, we may write its rate equations as $r_1$(t)=0, $r_2$(t)=0, and the coverages for the atomic hydrogen, $\Theta_H$(t), and molecular oxygen, $\Theta_{O_2}$(t), can be expressed as

$$\Theta_H(t) = \sqrt{K_{H_2}P_{H_2}}\Theta_*(t) \tag{B.14}$$

$$\Theta_{O_2}(t) = K_{O_2}P_{O_2}\Theta_*(t) \tag{B.15}$$

where $K_{H_2}$ and $K_{O_2}$ are the equilibrium constants

$$K_{H_2} = \frac{k_{ads,H_2}}{k_{des,2H}} \tag{B.16}$$

$$K_{O_2} = \frac{k_{ads,O_2}}{k_{des,O_2}} \tag{B.17}$$

$k_{ads,H_2}$ and $k_{ads,O_2}$ represent the adsorption for $H_2$ and $O_2$ respectively, and it can be calculated by the expressions

$$k_{ads,H_2} = \frac{1}{N_0\sqrt{2\pi m_{H_2}k_BT}} \tag{B.18}$$

$$k_{ads,O_2} = \frac{1}{N_0\sqrt{2\pi m_{O_2}k_BT}} \tag{B.19}$$

where $N_0$ is the density of active sites per area, and $m_{H_2}$, $m_{O_2}$ are the mass of $H_2$ and $O_2$, respectively. The desorption constants, $k_{des,2H}$ and $k_{des,O_2}$, describe the desorption for both species through the expressions

$$k_{des,2H} = \nu_1\exp(\frac{2E_H}{k_BT}) \tag{B.20}$$

$$k_{des,O_2} = \nu_2\exp(\frac{E_{O_2}}{k_BT}) \tag{B.21}$$

where $E_H$ and $E_{O_2}$ are the adsorption energies for the atomic hydrogen, and molecular oxygen adsorbed on the clean surface.

Under initial conditions, t=0, the coverage of all species different from molecular hydrogen and oxygen will be null.

$$\Theta_O(0) = \Theta_{O_2H}(0) = \Theta_{H_2O}(0) = \Theta_{H_2O_2}(0) = 0 \tag{B.22}$$

in that conditions the fraction of free sites can be written as

$$\Theta_* = \Theta_*(0) = \frac{1}{1 + \sqrt{K_{H_2}P_{H_2}} + K_{O_2}P_{O_2}} \tag{B.23}$$

Then, we can focus in the study of the rate for steps (B.3) and (B.4); molecular oxygen dissociation and hydrogen peroxide formation. Working in Equations (B.13), (B.14) and (B.15), $r_3$ and $r_4$ can be expressed as

$$r_3 = r_3(0) = k_{3a}K_{O_2}P_{O_2}\Theta_*^2 \tag{B.24}$$

$$r_4 = r_4(0) = k_{4a}K_{O_2}P_{O_2}\sqrt{K_{H_2}P_{H_2}}\Theta_*^2 \tag{B.25}$$

where $k_{3a}$ and $k_{4a}$ are the reaction constants for the forward molecular oxygen dissociation and hydrogen peroxide formation, respectively, being dependent of the activation energies of each reaction.

$$k_{3a} = \nu_3 \exp(\frac{-E_{a,3}}{k_BT}) \tag{B.26}$$

$$k_{4a} = \nu_4 \exp(\frac{-E_{a,4}}{k_BT}) \tag{B.27}$$

$E_{a,3}$ and $E_{a,4}$ are the activation energies for the steps (B.3), (B.4) respectively, and can be written as

$$E_{a,3} = E_{TS,3} - E_{O_2} \tag{B.28}$$

$$E_{a,4} = E_{TS,4} - E_{O_2} - E_H \tag{B.29}$$

with $E_{TS,3}$ and $E_{TS,4}$ the energies of the transition state for each reaction and $E_{O_2}$, $E_H$ the energies of molecular oxygen and hydrogen adsorbed on the surface.

Assuming the prefactors are independent of the metal,($\nu_i \simeq 10^{13}$, i=1..4) there are four metal dependent parameters determining the kinetics: $E_H$, $E_{O_2}$, $E_{TS,3}$ and $E_{TS,4}$. However, the $O_2$ adsorption energy, $E_{O_2}$, and the transition state energy for the $O_2$ dissociation, $E_{TS,3}$, scale with the adsorption energy of the atomic oxygen, $E_O$, while the transition state energy for the hydroperoxide formation, $E_{TS,4}$, scales with the sum of the O and H adsorption energies, $E_O$+$E_H$, see Figure B.1. This means that the only independent variables needed to characterise the metal in the microkinetic model are

$E_H$ and $E_O$. This simplified model allows us to represent the difference between the rates for the steps (B.4) and (B.3), $\ln(|r4 - r3|)$, as a function of the two independent variables, $E_O$ and $E_H$, through the relationship previously showed, see Figure B.2. This Figure is extensively discussed in Section 5.5 of Chapter 5. Table B.1 compiles the adsorption energies for the metals plotted in the figure.

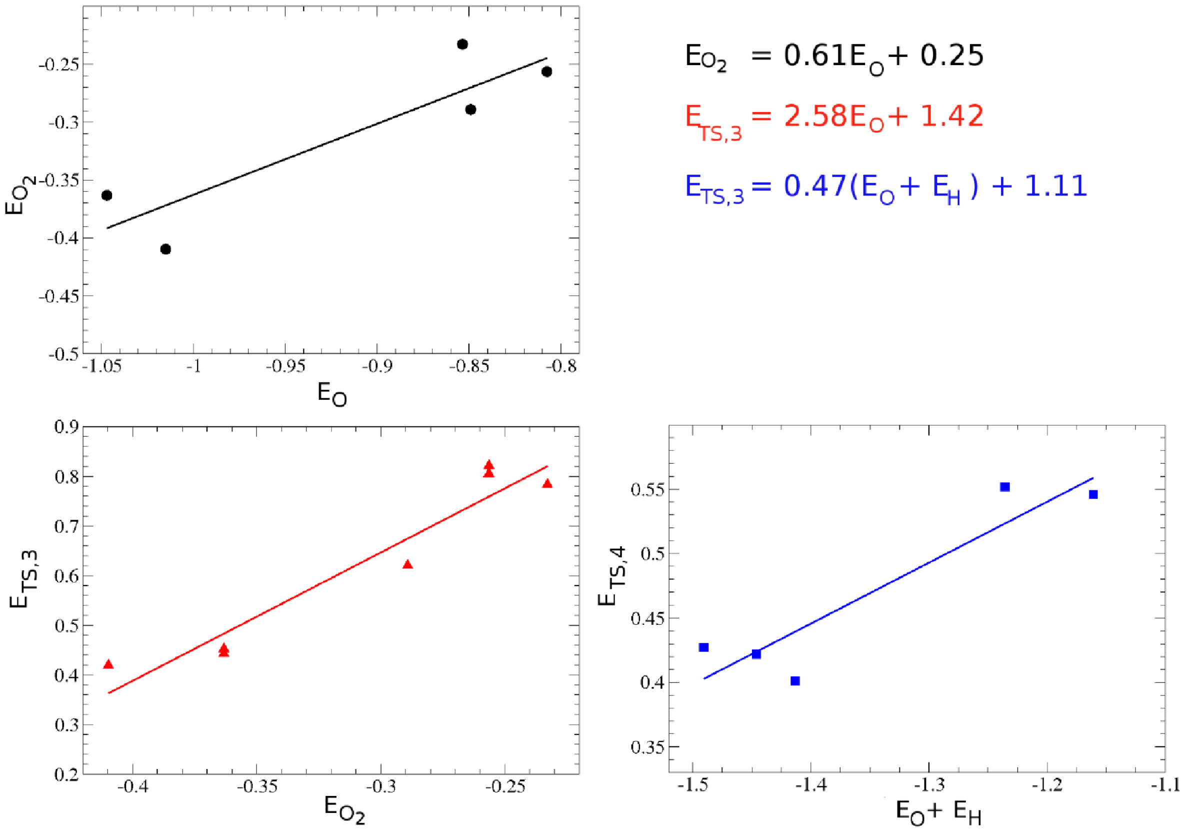

Figure B.1: Top: Relationship between adsorption energy of molecular oxygen, $E_{O_2}$, and atomic oxygen, $E_O$, (r=0.90). Bottom left: Adsorption energy of the transition state for the $O_2$ dissociation, $E_{TS,3}$, scales with the adsorption energy of molecular oxygen, $E_{O_2}$, (r=0.96). Bottom right: Adsorption energy of the transition state for hydroperoxide formation, $E_{TS,4}$, scales with the sum of the adsorption energies of atomic oxygen, $E_O$, and atomic hydrogen, $E_H$, (r=0.93). r is the correlation coefficient. The metals employed are Pd surface and alloys $MPd_3$@Pd (M=Pt, Au and Ag). The alloy with the lowest three layers corresponding to bulk Au, $AuPd_3$@Au is also included. For the $O_2$ dissociation, reaction B.3, two possible paths are studied on $PtPd_3$@Pd and $AgPd_3$@Pd alloys. All energies are expressed in eV.

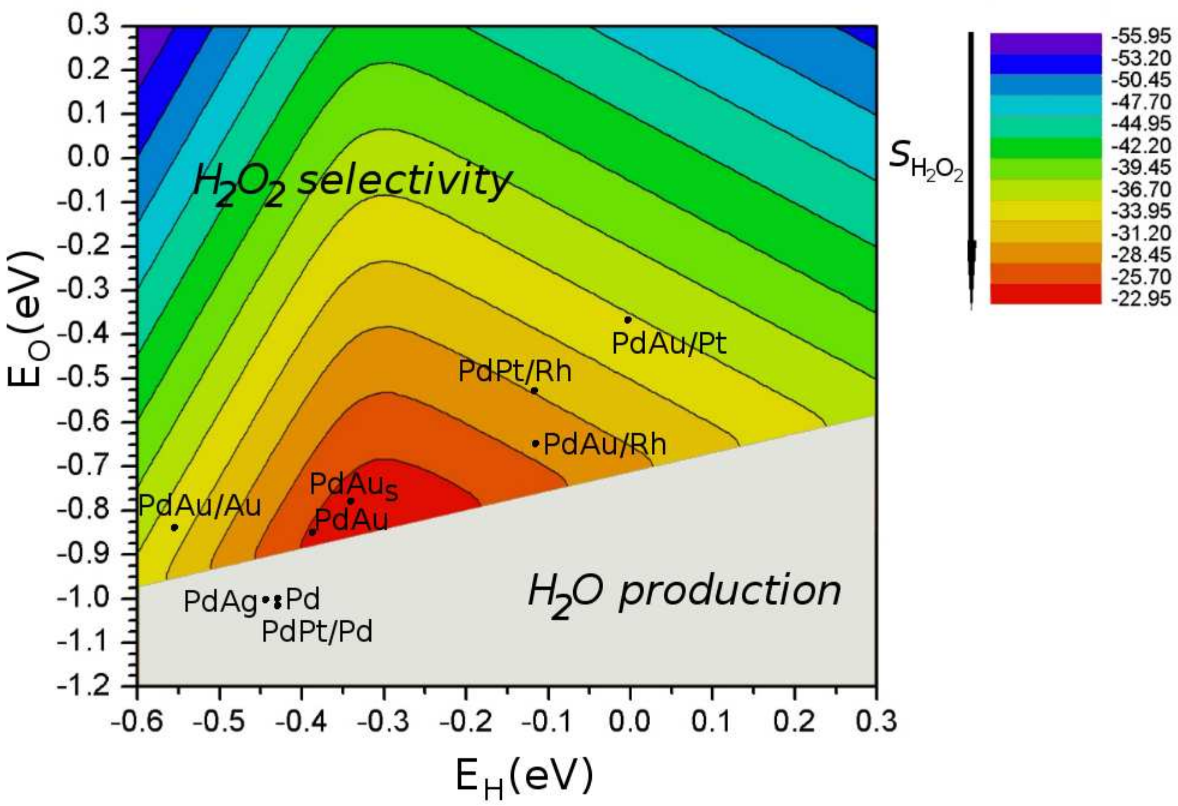

Figure B.2: Two dimensional contour of $\ln(|r4 - r3|)$ as a function of $E_O$ and $E_H$. Energies are expressed in eV.

| | $E_O$ | $E_H$ |
|---|---|---|
| **Pd** | -1.015 | -0.431 |
| **AuPd$_3$@Pd** | -0.854 | -0.382 |
| **AuPd$_3$@Au** | -0.849 | -0.564 |
| **PtPd$_3$@Pd** | -1.074 | -0.437 |
| **AgPd$_3$@Pd** | -1.047 | -0.444 |
| **AuPd$_3$@Rh** | -0.651 | -0.196 |
| **AuPd$_3$@Pt** | -0.374 | -0.017 |
| **PtPd$_3$@Rh** | -0.532 | -0.140 |
| **AuPd$_3$@Pd-strain(-1%)** | -0.787 | -0.346 |

Table B.1: Adsorption energies for atomic oxygen, $E_O$ in eV, and hydrogen, $E_H$ in eV, on the most stable site for the different surfaces $p$(2x2).

# Appendix C

# Solvent role in the direct $H_2O_2$ synthesis on Pd and AuPd alloy

The reaction mechanism that drives to the formation of hydrogen peroxide directly from its elements takes place in a three-phase system; the reagent gases, the catalyst and a solvent. In this appendix, a water layer has been modelled as solvent to study its role in the direct $H_2O_2$ synthesis.

## C.1 Computational details

DFT calculations were performed using the DACAPO code.[210] Electron-ion interactions were described by ultrasoft pseudopotential,[211] within a plane-wave basis with a cutoff energy of 350 eV. Electron exchange and correlation effects were described by the RPBE generalised gradient approximation functional.[124] The electron density of the valence states was obtained by a self-consistent iterative diagonalization of the Kohn-Sham Hamiltonian with Pulay mixing of the densities.[149, 212] The occupation of the one-electron states was calculated using an electronic temperature of $k_BT= 0.2$ eV. All the energies were extrapolated to T=0 K. The (111) monometallic surface of Pd was modelled by a four-layer slab with a (3x2) supercell, separated by a 12 Å thick vacuum layer. The alloy is represented by a substitutional model, where 0.16 ML of the surface metal is replaced by Au: $AuPd_5$. Brillouin zone integrations were performed on a grid of 3x5x1 Monkhorst-Pack $k$-points.[130] The top two metal layers were allowed to relax, and the third and fourth layers were fixed to the bulk values in order to represent the bulk of the material. The test calculations to compare VASP and DACAPO results, were modelled with a smaller p(2x2) supercell, on a grid of 4x4x1 Monkhorst-Pack $k$-points.

## C.2 DACAPO-VASP tests

The Pd and Au cell parameters were recalculated using the DACAPO code, in order to be compared with the values obtained by VASP, see Table C.1.

| Metal | Pd | Au |
|---|---|---|
| $a_{VASP}$ | 3.99 | 4.21 |
| $a_{DACAPO}$ | 4.02 | 4.22 |
| $a_{exp}$ | 3.8907 | 4.0782 |

Table C.1: Theoretical cell parameter calculated by VASP and DACAPO codes, $a_{VASP}$ and $a_{DACAPO}$ in Å, for the transition metals, Pd and Au. The experimental values for these metals are also reported, $a_{exp}$ in Å.

The differences between VASP and DACAPO cell parameters are found to be around 0.03 Å. The agreement with the experimental data is good.[172] Same test were also performed to compare energies and geometries obtained by DACAPO with respect to those obtained with the VASP code, shown in Chapter 5:

- Hydrogen adsorption on Pd, $H^*$(Pd).
- Atomic oxygen adsorption on Pd and $AuPd_3$, $O^*$(Pd) and $O^*$($AuPd_3$).
- Molecular oxygen adsorption on Pd and $AuPd_3$, $O_2^*$(Pd) and $O_2^*$($AuPd_3$).

The hydrogen adsorption energy was calculated with respect to the hydrogen energy in gas phase, $E_{H_2^{gas}}$, and the clean surface, $E_{clean}$.

$$E_{ads(H^*)} = E_{H_2^*} - E_{clean} - \frac{1}{2}E_{H_2^{gas}} \tag{C.1}$$

The energy for the molecular oxygen is not suitable calculated by DFT, thus, the oxygen adsorption energies were calculated with respect to the corrected oxygen energy, $E_{O_2^{gas}(corr)}$.

$$E_{ads(O_2^*)} = E_{O_2^*} - E_{clean} - E_{O_2^{gas}(corr)} \tag{C.2}$$

$E_{O_2^{gas}(corr)}$ was calculated by using the experimental enthalpy of water, $\Delta H_{H_2O}$. The reaction of water formation is written as

$$H_2 + \frac{1}{2}O_2 \longrightarrow H_2O \tag{C.3}$$

$$\Delta H_{H_2O} = (E_{H_2O_{(DFT)}} + ZPV) - (E_{H_2(DFT)} + ZPV) - \frac{1}{2}(E_{O_2^{gas}(corr)}) \tag{C.4}$$

therefore,

| Test | $E_{ads}$(DACAPO) | $E_{ads}$(VASP) | $\Delta E$ |
|---|---|---|---|
| $H^*$(Pd) | -0.58 | -0.56 | -0.03 |
| $O^*$(Pd) | -1.18 | -1.39 | 0.21 |
| $O^*$($AuPd_3$) | -1.06 | -1.23 | 0.17 |
| $O_2^*$(Pd) | -1.09 | -1.16 | 0.07 |
| $O_2^*$($AuPd_3$) | -0.95 | -0.96 | 0.01 |

Table C.2: Adsorption energies for atomic hydrogen on Pd, $H^*$(Pd); atomic oxygen adsorption on Pd and $AuPd_3$, $O^*$(Pd) and $O^*$($AuPd_3$); molecular oxygen adsorption on Pd and $AuPd_3$, $O_2^*$(Pd) and $O_2^*$($AuPd_3$). $\Delta E$ is the energy difference between the adsorption energies calculated by VASP and DACAPO codes. All the energies are in eV.

$$E_{O_2^{gas}(corr)} = -2\Delta H_{H_2O} + 2(E_{H_2O(DFT)} + ZPV) - 2(E_{H_2(DFT)} + ZPV) \qquad \text{(C.5)}$$

The largest energy difference between both codes, $\Delta E$, takes place for the atomic oxygen adsorption on Pd and $AuPd_3$ alloy. This difference is $\sim$ 0.2 eV, see Table C.2, and it is small enough to can compare the relative energies found with both codes.

## C.3 Water layer on Pd and AuPd surfaces

Two different configurations for a water layer on Pd are $AuPd_5$ were tested, see Figure C.1.

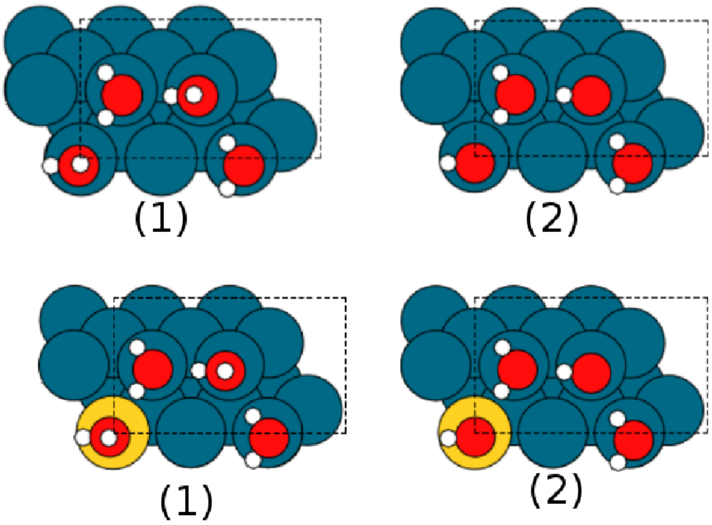

Figure C.1: Two different configurations for the adsorption of a water layer on Pd (top) and on $AuPd_5$ (bottom).

The interaction of the water layer with Pd and $AuPd_5$ surfaces is calculated as

UNIVERSITAT ROVIRA I VIRGILI
THEORETICAL STUDIES OF SELECTIVE PROCESSES IN HETEROGENEOUS CATALYSIS
Mónica García Mota
ISBN:978-84-693-5424-7/DL:T-1415-2010

$$\Delta E = E_{Pd_w} - E_{Pd} - 4E_{H_2O^{gas}} \tag{C.6}$$

$$\Delta E = E_{AuPd_{5w}} - E_{AuPd_5} - 4E_{H_2O^{gas}} \tag{C.7}$$

The energy interaction found is -1.27 and -1.12 eV for Pd and $AuPd_5$ respectively, and the average distance between the water layer and the surfaces is found to be around 4.2 Å. The energy difference between both configurations (1) and (2) in Figure C.1 was found to be less than 0.1 eV.

## C.4 $O_2$ dissociation

The $O_2$ dissociation is one of the decomposition routes that avoid the direct hydrogen peroxide formation.

$$O_2^* + * \longleftrightarrow 2O^* \tag{C.8}$$

The initial and final states for the $O_2$ dissociation have been studied on Pd clean surface, and on Pd with a layer of water, $Pd_w$, see Figure C.2. The molecular precursor, $O_2^*$, is placed on a tfcc site in the initial state. The adsorption of two oxygen atoms in the hcp sites constitutes the final state. The adsorption energy, $E_{ads}$, has been calculated respect to the corrected $O_2$(corr) energy (Equation C.5). The $O_2$ dissociation is exothermic and the reaction energy increases 0.06 eV with the presence of the water layer, see Table C.3.

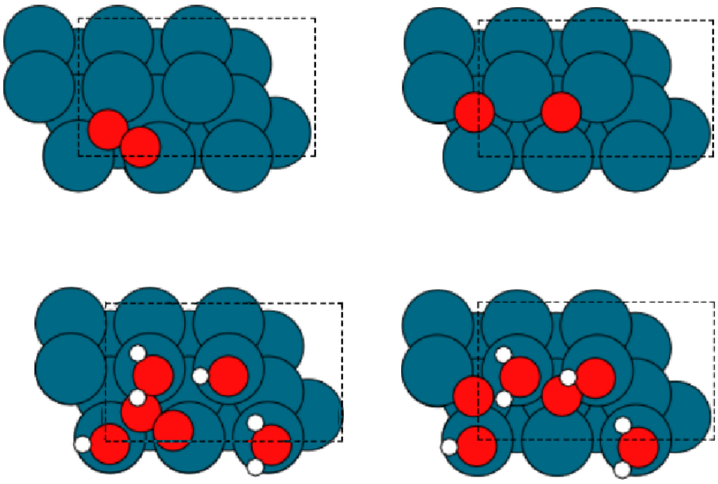

Figure C.2: Initial and final state for the molecular oxygen dissociation on Pd (top) and on a Pd surface with a water layer (bottom).

When the $O_2$ dissociation is studied on the $AuPd_5$ alloy (Figure C.3), both initial and final states are found to be stabilized by the presence of the water layer. The

| | | $E_{ads}$ | $d_{O-O}$ | $\Delta E$ |
|---|---|---|---|---|
| Pd | $O_2$ | -1.02 | 1.351 | -0.77 |
| | 2O | -1.79 | 3.141 | - |
| $Pd_w$ | $O_2$ | -0.95 | 1.357 | -0.83 |
| | 2O | -1.78 | 3.178 | - |

Table C.3: Adsorption energies, $E_{ads}$ in eV, and O-O distances, $d^{TS}_{O-O}$ in Å, at the initial and final state for the molecular oxygen dissociation on Pd and on Pd surface with a water layer, $Pd_w$. Reaction energy, $\Delta E$ in eV.

exothermicity of the reaction increases from 0.59 ($AuPd_5$) to 0.68 eV ($AuPd_{5w}$), see Table C.4.

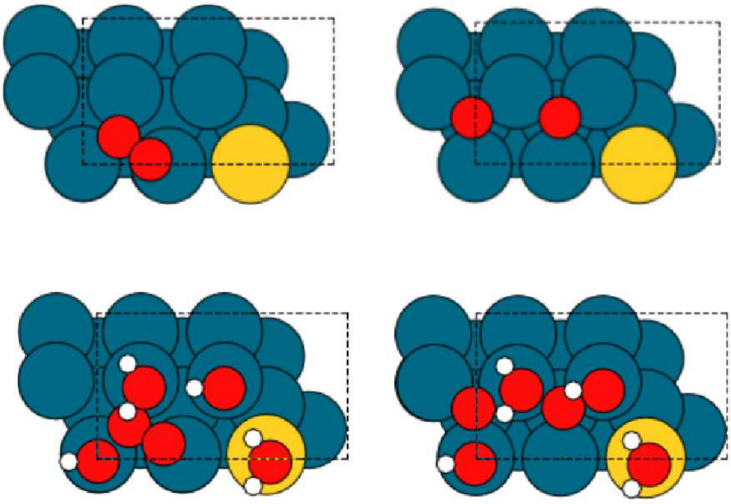

Figure C.3: Initial and final state for the molecular oxygen dissociation on $AuPd_5$ (top), and on a $AuPd_5$ surface with a water layer, (bottom).

| | | $E_{ads}$ | $d_{O-O}$ | $\Delta E$ |
|---|---|---|---|---|
| $AuPd_5$ | $O_2$ | -0.84 | 1.349 | -0.59 |
| | 2O | -1.43 | 3.066 | - |
| $AuPd_{5w}$ | $O_2$ | -0.97 | 1.357 | -0.68 |
| | 2O | -1.61 | 3.097 | - |

Table C.4: Adsorption energies, $E_{ads}$ in eV, and O-O distances, $d^{TS}_{O-O}$ in Å, at the initial and final state for the molecular oxygen dissociation on $AuPd_5$ and on $AuPd_5$ surface with a water layer, $AuPd_{5w}$. Reaction energy, $\Delta E$ in eV.

## C.5 Hydroperoxide formation

Once the molecular $O_2$ precursor is adsorbed on the surface, the first hydrogenation step leads to the formation of hydroperoxide.

$$O_2^* + H^* \longleftrightarrow O_2H^* + * \tag{C.9}$$

The tbt adsorption site of $O_2$ has been taken as starting point, and the hydrogenation takes place from a neighbouring fcc site. In the final state, the hydroperoxide, $O_2H$, is bonded to the surface in a tbt configuration, see Figure C.4. The binding energy of hydroperoxide on $Pd_w$ is found to be around 0.3 eV higher than that on Pd, and the exothermicity of the reaction increases from 0.11 (Pd) to 0.41 eV ($Pd_w$), see Table C.5. The transition state has also been calculated for the hydroperoxide formation on Pd; the energy barrier is found to be 0.15 eV higher in the presence of the water layer.

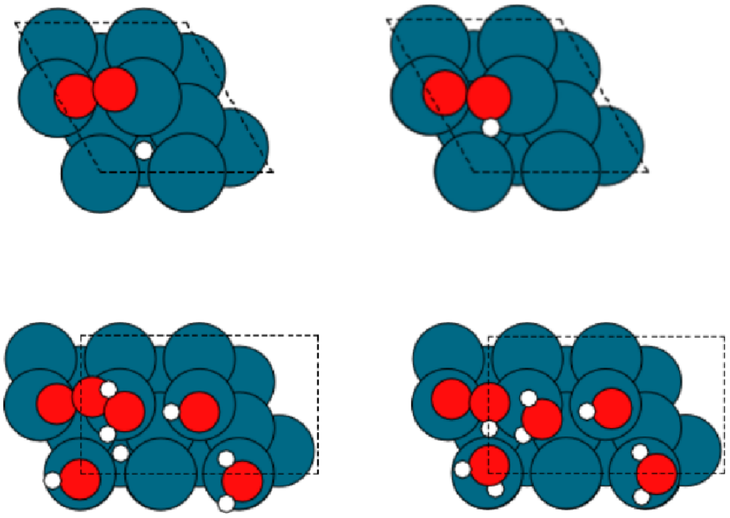

Figure C.4: Initial and final state for the molecular oxygen reacting with hydrogen on Pd (top), and on a Pd surface with a water layer (bottom).

| | | $E_{ads}$ | $d_{O-O}$ | $d_{O-H}$ | $\Delta E$ | $E_a$ |
|---|---|---|---|---|---|---|
| Pd | $O_2$+H | -1.44 | 1.297 | 2.674 | -0.11 | 0.90 |
| | $O_2H$ | -1.54 | 1.458 | 0.991 | - | - |
| $Pd_w$ | $O_2$+H | -1.42 | 1.308 | 2.792 | -0.41 | 1.05 |
| | $O_2H$ | -1.82 | 1.438 | 1.025 | - | - |

Table C.5: Adsorption energies, $E_{ads}$ in eV, and O-O distances, $d_{O-O}^{TS}$ in Å, at the initial and final state for the molecular oxygen dissociation on Pd, and on Pd surface with a water layer, $Pd_w$. Reaction energy and activation energy, $\Delta E$ and $E_a$ in eV.

When the hydroperoxide formation is analysed on the alloy, the binding energy of the final state, $O_2H$, increases by 0.26 eV because of the presence of the water layer.

UNIVERSITAT ROVIRA I VIRGILI
THEORETICAL STUDIES OF SELECTIVE PROCESSES IN HETEROGENEOUS CATALYSIS
Mónica García Mota
ISBN:978-84-693-5424-7/DL:T-1415-2010

The exothermicity of the reaction increases from 0.24 ($AuPd_5$) to 0.63 eV ($AuPd_{5w}$), see Table C.6.

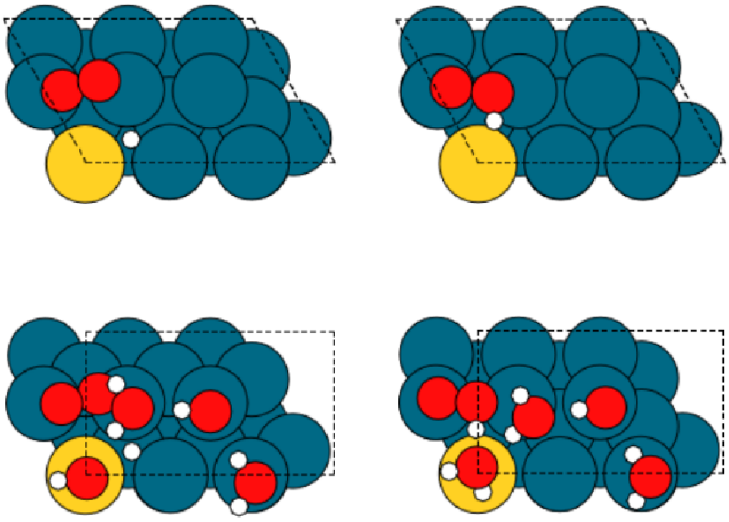

Figure C.5: Initial and final state for the molecular oxygen reacting with hydrogen on $AuPd_5$ (top), and on a $AuPd_5$ surface with a water layer, (bottom).

| | | $E_{ads}$ | $d_{O-O}$ | $d_{O-H}$ | $\Delta E$ |
|---|---|---|---|---|---|
| $AuPd_5$ | $O_2$+H | -1.22 | 1.297 | 2.681 | -0.24 |
| | $O_2$H | -1.46 | 1.450 | 0.992 | - |
| $AuPd_{5w}$ | $O_2$+H | -1.09 | 1.294 | 2.636 | -0.63 |
| | $O_2$H | -1.72 | 1.429 | 1.023 | - |

Table C.6: Adsorption energies, $E_{ads}$ in eV, and O-O distances, $d^{TS}_{O-O}$ in Å, at the initial and final state for the molecular oxygen dissociation on $AuPd_5$ and on $AuPd_5$ surface with a water layer, $AuPd_{5w}$. Reaction energy, $\Delta E$ in eV.

As summary of this appendix, when a water layer is modelled as solvent for the $O_2$ dissociation and for the hydroperoxide formation on Pd and AuPd surface alloy, the presence of water increases the exothermicity of the reactions and stabilises the products on the surface.

Even though a more extensive study would be needed to determine the effect of the solvent on the direct $H_2O_2$ synthesis, the results shown in this appendix indicate that the main conclusions in Chapter 5 would still be valid in the presence of water.

# Bibliography

[1] Hammer, B.; Nørskov, J. K. *Nature* **1995,** *376,* 238.

[2] Haruta, M. *Catal. Today* **1997,** *36,* 153.

[3] Valden, M.; Lai, X.; Goodman, D. W. *Science* **1998,** *281,* 1647.

[4] Chowdhury, B.; Bravo-Suarez, J. J.; Date, M.; Tsubota, S.; Haruta, M. *Angew. Chem. Int. Ed.* **2006,** *45,* 412.

[5] Segura, Y.; López, N.; Pérez-Ramírez, J. *J. Catal.* **2007,** *247,* 383.

[6] Corma, A.; Serna, P. *Science* **2006,** *313,* 332.

[7] Hashmi, A. S. K.; Hutchings, G. J. *Angew. Chem. Int. Ed.* **2006,** *45,* 7896.

[8] Bond, G. C. *Metal-Catalysed Reactions of Hydrocarbons;* Springer, New York: 2005.

[9] Lahr, D. L.; Ceyer, S. T. *J. Am. Chem. Soc.* **2006,** *128,* 1800.

[10] Shapovalov, V.; Metiu, H. *J. Catal.* **2007,** *245,* 205.

[11] Mingshu, C.; Dheeraj, K.; Cheol-Woo, Y.; Goodman, D. W. *Science* **2005,** *310,* 291.

[12] Mavrikakis, M.; Stoltze, P.; Nørskov, J. K. *Catal. Lett.* **2000,** *64,* 101.

[13] Besenbacher, F.; Chorkendorff, I.; Clausen, B. S.; Hammer, B.; Molenbroek, A. M.; Nørskov, J. K.; Stensgaard, I. *Science* **1998,** *279,* 1913.

[14] Vestergaard, E. K.; Vang, R. T.; Knudsen, J.; Pedersen, T. M.; An, T.; Laegsgaard, E.; Stensgaard, I.; Hammer, B.; Besenbacher, F. *Phys. Rev. Lett.* **2005,** *95,* 126101.

[15] Samanos, B.; Boutry, P. *J. Catal.* **1971,** *23,* 19.

[16] Maroun, F.; Ozanam, F.; Magnussen, O. M.; Behm, R. J. *Science* **2001,** *293,* 1811.

[17] Sakong, S.; Mosch, C.; Gross, A. *Phys. Chem. Chem. Phys.* **2007,** *9,* 2216.

[18] Christoffersen, E. Ph.D. Thesis **2001**.

[19] Nørskov, J. K.; Bligaard, T.; Rossmeisl, J.; Christensen, C. H. *Nature Chem.* **2009,** *1,* 37.

[20] Ertl, G.; Neumann, M.; Streit, K. M. *Surf. Sci.* **1977,** *64,* 393.

[21] Dabo, I.; Wieckowski, A.; Marzari, N. *J. Am. Chem. Soc.* **2007,** *129,* 11045.

[22] Rodriguez, J. A.; Goodman, D. W. *Science* **1992,** *257,* 897.

[23] Luo, K.; Wei, T.; Yi, C. W.; Axnanda, S.; Goodman, D. W. *J. Phys. Chem. B* **2005,** *109,* 23517.

[24] Wei, T.; Wang, J.; Goodman, D. W. *J. Phys. Chem. C* **2007,** *111,* 8781.

[25] Kumar, D.; Chen, M. S.; Goodman, D. W. *Catal. Today* **2007,** *123,* 77.

[26] Gao, F.; Wang, Y.; Goodman, D. W. *J. Am. Chem. Soc.* **2009,** *131,* 5734.

[27] Gao, F.; Wang, Y.; Goodman, D. W. *J. Phys. Chem. C* **2009,** *113,* 14993.

[28] Niemantsverdriet, J. W. ; IRAS. In *Spectroscopy in Catalysis*, 2nd ed., Wiley-VCH: 2007, pages 201-228.

[29] Sluiter, M. H. F.; Colinet, C.; Pasturel, A. *Phys. Rev. B* **2006,** *73,* 174204.

[30] Han, P.; Axnanda, S.; Lyubinetsky, I.; Goodman, D. W. *J. Am. Chem. Soc.* **2007,** *129,* 14355.

[31] Yi, C. W.; Luo, K.; Wei, T.; Goodman, D. W. *J. Phys. Chem. B* **2005,** *109,* 18535.

[32] Soto-Verdugo, V.; Metiu, H. *Surf. Sci.* **2007,** *601,* 5332.

[33] Pierantozzi, R. ; Carbon dioxide. In *Kirk-Othmer Encyclopedia of Chemical Technology,* Vol 5, 5th ed., Wiley: 2003, pages 803-822.

[34] López, N.; Janssens, T. V. W.; Clausen, B. S.; Xu, Y.; Mavrikakis, M.; Bligaard, T.; Nørskov, J. K. *J. Catal.* **2004,** *223,* 232.

[35] Sanchez-Castillo, M. A.; Couto, C.; Kim, W. B. Dumesic, J. A. *Angew. Chem. Int. Ed.* **2004,** *116,* 1160.

[36] Remediakis, I. N.; López, N.; Nørskov, J. K. *Angew. Chem. Int. Ed.* **2005,** *117,* 1858.

[37] Alavi, A.; Hu, P.; Deutsch, T.; Silvestrelli, P. L.; Hutter, J. *Phys. Rev. Lett.* **1998,** *80,* 3650.

[38] Zhang, C.; Hu, P.; Alavi, A. *J. Am. Chem. Soc.* **1999,** *121,* 7931.

[39] Eichler, A.; Hafner, J. *Phys. Rev. B* **1999,** *59,* 5960.

[40] Eichler, A. *Surf. Sci.* **2001,** *498,* 314.

[41] Mittendorfer, F.; Eichler, A.; Hafner, J. *Surf. Sci.* **1999,** *433,* 756.

[42] Eichler, A.; Mittendorfer, F.; Hafner, J. *Phys. Rev. B* **2000,** *62,* 4744.

[43] Xu, Y.; Mavrikakis, M. *Surf. Sci.* **2001,** *494,* 131.

[44] Xu, Y.; Mavrikakis, M. *Surf. Sci.* **2003,** *538,* 219.

[45] Nørskov, J. K.; Rossmeisl, J.; Logadottir, A.; Lindqvist, L.; Kitchin, J. R.; Bligaard, T.; Jónsson, H. *J. Phys. Chem. B* **2004,** *108,* 17886.

[46] Yim, W. L.; Klüner, T. *J. Catal.* **2008,** *254,* 349.

[47] Eul, W.; Moeller, A.; Steiner, N. ; Hydrogen peroxide. In *Kirk-Othmer Encyclopedia of Chemical Technology*, Vol 13, 3rd ed., Wiley: 2001, pages 12-38.

[48] Campos-Martin, J. M.; Blanco-Brieva, G.; Fierro, J. L. G. *Angew. Chem. Int. Ed.* **2006,** *45,* 6962.

[49] Zuwei, X.; Ning, Z.; Yu, S.; Kunlan, L. *Science* **2001,** *292,* 1139.

[50] Kamata, K.; Yonehara, K.; Sumida, Y.; Yamaguchi, K.; Hikichi, S.; Mizuno, N. *Science* **2003,** *300,* 964.

[51] Torres, D.; López, N.; Illas, F.; Lambert, R. M. *Angew. Chem. Int. Ed.* **2007,** *119,* 2101.

[52] Pospelova, T. A.; Kobozev, N. I.; Eremin, E. N. *Russ, J. Phys. Chem.* **1961,** *35,* 143.

[53] Pospelova, T. A.; Kobozev, N. I. *Russ, J. Phys. Chem.* **1961,** *35,* 262.

[54] Pospelova, T. A.; Kobozev, N. I. *Russ, J. Phys. Chem.* **1961,** *35,* 584.

[55] Dissanayake, D. P.; Lunsford, J. H. *J. Catal.* **2003,** *214,* 113.

[56] Sivadinarayana, C.; Choudhary, T. V.; Daemen, L. L.; Eckert, J.; Goodman, D. W. *J. Am. Chem. Soc.* **2003,** *126,* 38.

[57] Lunsford, J. H. *J. Catal.* **2003,** *216,* 455.

[58] Abate, S.; Centi, G.; Melada, S.; Perathoner, S.; Pinna, F.; Strukul, G. *Catal. Today* **2005,** *104,* 323.

[59] Abate, S.; Melada, S.; Centi, G.; Perathoner, S.; Pinna, F.; Strukul, G. *Catal. Today* **2006,** *117,* 193.

[60] Melada, S.; Pinna, F.; Strukul, G.; Perathoner, S.; Centi, G. *J. Catal.* **2006,** *237,* 213.

[61] Choudhary, V. R.; Samanta, C. *J. Catal.* **2006,** *238,* 28.

[62] Edwards, J. K.; Solsona, B.; Ntainjua, E.; Carley, A. F.; Herzing, A. A.; Kiely, C. J.; Hutchings, G. J. *Science* **2009,** *323,* 1037.

[63] Liu, Q.; Lunsford, J. H. *J. Catal.* **2006,** *239,* 237.

[64] Han, Y. F.; Lunsford, J. H. *J. Catal.* **2005,** *230,* 313.

[65] Landon, P.; Collier, P. J.; Carley, A. F.; Chadwick, D.; Papworth, A. J.; Burrows, A.; K., C. J.; Hutchings, G. J. *Phys. Chem. Chem. Phys.* **2003,** *5,* 1917.

[66] Edwards, J. K.; Thomas, A.; Solsona, B. E.; Landon, P.; Carley, A. F.; Hutchings, G. J. *Catal. Today* **2007,** *122,* 397.

[67] Edwards, J. K.; Hutchings, G. J. *Angew. Chem. Int. Ed.* **2008,** *47,* 2.

[68] Menegazzo, F.; Burti, P.; Signoretto, M.; Manzoli, M.; Vankova, S.; Boccuzzi, F.; Pinna, F.; Strukul, G. *J. Catal.* **2008,** *257,* 369.

[69] Han, Y. F.; Zhong, Z.; Ramesh, K.; Chen, F.; Chen, L.; White, T.; Tay, Q.; Yaakub, S. N.; Wang, Z. *J. Phys. Chem. C* **2007,** *111,* 8410.

[70] http://www.vinylacetate.org/what.shtml, retrieved January 2010.

[71] Moiseev, I. I.; Vargaftik, M. N.; Syrkin, J. K. *Dokl. Akad. Nauk SSSR* **1960,** *133,* 377.

[72] Bissot, T. 1977 U. S. Patent, 4,048,096.

[73] Nakamura, S.; Yasui, T. *J. Catal.* **1970,** *17,* 366.

[74] Nakamura, S.; Yasui, T. *J. Catal.* **1971,** *23,* 315.

[75] Moiseev, I. I. ; Catalytic Oxidation; Sheldon, R. A., Ed.; In *World Scientific*, 1995, page 203.

[76] Stacchiola, D.; Calaza, F.; Burkholder, L.; Schwabacher, A. W.; Neurock, M.; Tysoe, W. T. *Angew. Chem. Int. Ed.* **2005,** *117,* 4648.

[77] Yuan, D.; Gong, X.; Wu, R. *J. Phys. Chem. C* **2008,** *112,* 1539.

[78] Chen, M.; Kumar, D.; Yi, C. W.; Goodman, D. W. *Science* **2005,** *310,* 291.

[79] Chen, M. S.; Luo, K.; Wei, T.; Yan, Z.; Kumar, D.; Yi, C. W.; Goodman, D. W. *Catal. Today* **2006,** *117,* 37.

[80] Chorkendorff, I.; Niemantsverdriet, J. W. ; Kinetics. In *Concepts of Modern Catalysis And Kinetics* ; Wiley-VCH: 2003, pages 57-65.

[81] Smidt, J.; Hafner, W.; Jira, R.; Sedlmeier, J.; Sieber, R.; Ruttinger, R.; Kojer, H. *Angew. Chem., Int. Ed. Engl.* **1959,** *71,* 176.

[82] Smidt, J.; Hafner, W.; Jira, R.; Sieber, R.; Sedlmeier, J.; Sabel, A. *Angew. Chem., Int. Ed. Engl.* **1962,** *74,* 93.

[83] Goossen, L. J.; Rodríguez, N.; Goossen, K. *Angew. Chem., Int. Ed.* **2008,** *47,* 3100.

[84] Beccalli, E. M.; Broggini, G.; Martinelli, M.; Sottocornola, S. *Chem. Rev.* **2007,** *107,* 5318.

[85] Grennberg, H.; Simon, V.; Bäckvall, J. E. *J. Chem. Soc.,Chem. Commun.* **1994,** 265.

[86] Grennberg, H.; Bäckvall, J. E. *Chem.-Eur. J.* **1998,** *4,* 1083.

[87] van Helden, R.; Kohll, C. F.; Medema, D.; Verberg, G.; Jonkhoff, T. *Rec. Trav. Chim. Pays-Bas* **1968,** *87,* 961.

[88] Hutchings, G. J. *J. Catal.* **1985,** *96,* 292.

[89] Huber, H.; McIntosh, D.; Ozin, G. A. *Inorg. Chem.* **1977,** *16,* 975.

[90] Claus, P. *Appl. Catal., A* **2005,** *291,* 222.

[91] Landon, P.; Hutchings, G. J.; Solsona-Espriu, B.; Carley, A. F.; Herzing, A. A.; Knight, D. W.; Enache, D. I.; Kiely, C. J.; Watanabe, M.; Edward, J. K. *Science* **2006,** *311,* 362.

[92] González-Arellano, C.; Corma, A.; Iglesias, M.; Sanchez, F. *Chem. Commun.* **2005,** *15,* 1990.

[93] Nieto-Oberhuber, C.; Muñoz, M. P.; Buñuel, E.; Cárdenas, D. J.; Echavarren, A. M. *Angew. Chem. Int. Ed.* **2004,** *43,* 2402.

[94] Comas-Vives, A.; González-Arellano, C.; Corma, A.; Iglesias, M.; F. Sánchez, F.; Ujaque, G. *J. Am. Chem. Soc* **2006,** *128,* 4756.

[95] González-Arellano, C.; Corma, A.; Iglesias, M.; Sánchez, F. *J. Catal.* **2006,** *238,* 497.

[96] González-Arellano, C.; Abad, A.; Corma, A.; García, H.; Iglesias, M.; Sánchez, F. *Angew. Chem.* **2007,** *46,* 1536.

[97] Lopez-Sanchez, J.; Lennon, D. *Appl. Catal., A* **2005,** *291,* 230.

[98] Jia, J. F.; Haraki, K.; Kondo, J. N.; Domen, K.; Tamaru, K. *J. Phys. Chem. B* **2000,** *104,* 11153.

[99] Montano, M.; Bratlie, K.; Salmeron, M.; Somorjai, G. *J. Am. Chem. Soc.* **2006,** *128,* 13229.

[100] Molnár, A.; Sárkány, A.; Varga, M. *J. Mol. Catal. A: Chem.* **2001,** *173,* 185.

[101] Teschner, D.; Borsodi, J.; Wootsch, A.; Révay, Z.; Hävecker, M.; Knop-Gericke, A.; Jackson, S. D.; Schlögl, R. *Science* **2008,** *320,* 86.

[102] Studt, F.; Abild-Pedersen, F.; Bligaard, T.; Sørensen, R. Z.; Christensen, C. H.; Nørskov, J. K. *Science* **2008,** *320,* 1320.

[103] Teschner, D.; Borsodi, J.; Hävecker, M.; Knop-Gericke, A.; Schlögl, R.; Milroy, D.; Jackson, D. S.; Torres, D.; Sautet, P. *Angew. Chem. Int. Ed.* **2008,** *47,* 9274.

[104] Greenwood, N. N.; Earnshaw, A. ; In *Chemistry of the elements*, 2nd ed., Elsevier: 2008, page 1150.

[105] Borodziński, A.; Bond, G. C. *Catal. Rev. Sci. Eng.* **2006,** *48,* 91.

[106] Johnson, A. D.; Daley, S. P.; Utz, A.; Ceyer, S. T. *Science* **1992,** *257,* 223.

[107] Molero, H.; Bartlett, B. F.; Tysoe, W. T. *J. Catal.* **1999,** *49,* 181.

[108] Kovnir, K.; Osswald, J.; Armbrüster, M.; Teschner, D.; Weinberg, G.; Wild, U.; Knop-Gericke, A.; Ressler, T.; Grin, Y.; Schlögl, R. *J. Catal.* **2009,** *264,* 93.

[109] Buchele, W.; Roos, H.; Wanjek, H.; Muller, H. J. *Catal. Today* **1996,** *30,* 33.

[110] Sheth, P. A.; Neurock, M.; Smith, C. M. *J. Phys. Chem. B* **2003,** *107,* 2009.

[111] Mei, D. H.; Sheth, P. A.; Neurock, M.; Smith, C. M. *J. Catal.* **2006,** *242,* 1.

[112] Studt, F.; Abild-Pedersen, F.; Bligaard, T.; Sørensen, R. Z.; Christensen, C. H.; Nørskov, J. K. *Angew. Chem. Int. Ed.* **2008,** *47,* 9299.

[113] Mei, D. H.; Neurock, M.; Smith, C. M. *J. Catal.* **2009,** *268,* 181.

[114] García-Mota, M.; Bridier, B.; Pérez-Ramírez, J.; López, N. Under revision. J.Catalysis, 2010.

[115] Hohenberg, P.; Kohn, W. *Phys. Rev. B* **1964,** *136,* B864.

[116] Kohn, W.; Sham, L. J. *Phys. Rev.* **1965,** *140,* A1133.

[117] Dirac, P. A. M. *Proc. R. Soc.* **1928,** *A117,* 610.

[118] Teller, E. *Rev. Mod. Phys.* **1962,** *34,* 627.

[119] Gunnarsson, O.; Lundqvist, B. I. *Phys. Rev. B* **1976,** *13,* 4274.

[120] Becke, A. D. *Phys. Rev. A* **1988,** *38,* 3098.

[121] Perdew, J. *Phys. Rev. B* **1986,** *33,* 8822.

[122] Perdew, J. P.; Chevary, A.; Vosko, S. H.; Jackson, K. A.; Pederson, M. R.; Singh, D. J. *Phys. Rev. B* **1992,** *46,* 6671.

[123] Perdew, J. P.; Burke, K.; Ernzerhof, M. *Phys. Rev. Lett.* **1996,** *77,* 3865.

[124] Hammer, B.; Hansen, L. B.; Nørskov, J. K. *Phys. Rev. B.* **1999,** *59,* 7413.

[125] Lee, C.; Parr, R. G.; Yang, W. *Phys. Rev. B* **1988,** *37,* 785.

[126] Stephens, P. J.; Devlin, F. J.; Frisch, M. J. Chabalowski, C. F. *J. Phys. Chem.* **1994,** *98,* 11623.

[127] Aschroft, N. W.; Mermin, N. D. *Solid State Physics;* Saunders College Publishing: 1976.

[128] Payne, M. C.; Teter, M. P.; Allan, D. C.; Arias, T. A.; Joannopoulos, J. D. *Rev. Mod. Phys.* **1992,** *64,* 1045.

[129] Chelikowsky, J. R.; Cohen, M. L. *Phys. Rev. B* **1974,** *10,* 5095.

[130] Monkhorst, H. J.; Pack, J. D. *Phys. Rev. B* **1976,** *13,* 5188.

[131] Kittel, C. *Introducción a la física del estado sólido;* Editorial Reverté: 1998.

[132] von Barth, U.; Gelatt, C. D. *Phys. Rev. B* **1980,** *21,* 2222.

[133] Phillips, J. C. *Phys. Rev.* **1968,** *166,* 832.

[134] McQuarrie, D. A.; Simon, J. D. *Molecular Thermodynamics;* University Science Books: 1999.

[135] Chorkendorff, I.; Niemantsverdriet, J. W. *Concepts of Modern Catalysis And Kinetics;* Wiley-VCH: 2003.

[136] Hammer, B.; Morikawa, Y.; Nørskov, J. K. *Phys. Rev. Lett.* **1996,** *76,* 2141.

[137] Brønsted, J. N. *Chem. Rev.* **1928,** *V,* 231.

[138] Evans, M. G.; Polanyi, M. *Trans. Faraday Soc.* **1938,** *34,* 11.

[139] Hammond, G. S. *J. Am. Chem. Soc.* **1955,** *77,* 334.

[140] Shaik, S. S.; Pross, A. *J. Am. Chem. Soc.* **1982,** *104,* 2708.

[141] Marcus, R. A. *J. Chem. Phys.* **1956,** *24,* 966.

[142] Marcus, R. A. *J. Chem. Phys.* **1965,** *43,* 679.

[143] Deutschmann, O.; Knözinger, H.; Kochloefl, K.; Turek, T. ; Heterogeneous Catalysis and Solid Catalyst. In *Ullmann's Encyclopedia of Industrial Chemistry*; Wiley-VCH: 2009.

[144] Nørskov, J. K.; Bligaard, T.; Logadottir, A.; Bahn, S.; Hansen, L. B.; Bollinger, M.; Bengaard, H.; Hammer, B.; Sljivancanin, Z.; Mavrikakis, M.; Xu, Y.; Dahl, S.; Jacobsen, C. J. H. *J. Catal.* **2002,** *209,* 275.

[145] Abild-Pedersen, F.; Greeley, J.; Studt, F.; Rossmeisl, J.; Munter, T. R.; Moses, P. G.; Skulason, E.; Bligaard, T.; Nørskov, J. K. *Phys. Rev. Lett.* **2007,** *99,* 16105.

[146] Fernández, E. M.; Moses, P. G.; Toftelund, A.; Hansen, H. A.; Martínez, J. I.; Abild-Pedersen, F.; Kleis, J.; Hinnemann, B.; Rossmeisl, J.; Bligaard, T.; Nørskov, J. K. *Angew. Chem. Int. Ed.* **2008,** *47,* 4683.

[147] Andersin, J.; López, N.; Honkala, K. *J. Phys. Chem. C* **2009,** *113,* 8278.

[148] Kresse, G.; Hafner, J. *Phys. Rev. B* **1993,** *47,* 558.

[149] Kresse, G.; Furthmüller, J. *Phys. Rev. B* **1996,** *54,* 11169.

[150] Kresse, G.; Furthmüller, J. *Comput. Mater. Sci.* **1996,** *6,* 15.

[151] Blöchl, P. E. *Phys. Rev. B* **1994,** *50,* 17953.

[152] Kresse, G.; Joubert, D. *Phys. Rev. B* **1999,** *59,* 1758.

[153] Ruban, A. V.; Skriver, H. L.; Nørskov, J. K. *Phys. Rev. B* **1999,** *59,* 15990.

[154] Yuan, D. W.; Gong, X. G.; Wu, R. Q. *Phys. Rev. B* **2007,** *75,* 085428.

[155] http://webbook.nist.gov/chemistry, retrieved January 2010.

[156] Loffreda, D.; Simon, D.; Sautet, P. *Surf. Sci.* **1999,** *68,* 425.

[157] Roudgar, A.; Gross, A. *Phys. Rev. B* **2003,** *67,* 033409.

[158] Wang, X. G.; Chaka, A.; Scheffler, M. *Phys. Rev. Lett.* **2000,** *84,* 3650.

[159] Bollinger, M. V.; Jacobsen, K. W.; Nørskov, J. K. *Phys. Rev. B* **2003,** *67,* 085410.

[160] Łodziana, Z.; Nørskov, J. K.; Stoltze, P. *J. Chem. Phys.* **2003,** *118,* 11179.

[161] Henkelman, G.; Uberuaga, B. P.; Jonsson, H. *J. Chem. Phys.* **2000,** *113,* 9901.

[162] Henkelman, G.; Jonsson, H. *J. Chem. Phys.* **1999,** *111,* 7010.

[163] Hammer, B.; Morikawa, Y.; Nørskov, J. K. *Phys. Rev. Lett.* **1996,** *76,* 2141.

[164] Eichler, A. *Science* **2003,** *526,* 332.

[165] German, E. D.; Sheintuch, M. *J. Phys. Chem. C* **2008,** *112,* 14377.

[166] Feibelman, P. J.; Hammer, B.; Nørskov, J. K.; Wagner, F.; Scheffler, M.; Stumpf, R.; Watwe, R.; Dumesic, J. *J. Phys. Chem. B* **2001,** *105,* 4018.

[167] Greeley, J.; Nørskov, J. K. *Surf. Sci.* **2005,** *592,* 104.

[168] Hammer, B.; Nørskov, J. K. *Surf. Sci.* **1995,** *343,* 211.

[169] Hammer, B.; Nørskov, J. K. *Nature* **1995,** *376,* 238.

[170] Falsig, H.; Hvolbæk, B.; Kristensen, I. S.; Jiang, T.; Bligaard, T.; Christensen, C. H.; Nørskov, J. K. *Angew. Chem. Int. Ed.* **2008,** *47,* 4835.

[171] Beutl, M.; Rendulic, K. D.; Castro, G. R. *Surf. Sci.* **1997,** *385,* 97.

[172] http://webelements.com, retrieved January 2010.

[173] Ruban, A. V.; Skriver, H. L.; Nørskov, J. K. *Phys. Rev. B* **1999,** *59,* 15990.

[174] Mitsui, T.; Rose, M. K.; Fomin, E.; Ogletree, D. F.; Salmeron, M. *Nature* **2003,** *422,* 705.

[175] López, N.; Łodziana, Z.; Illas, F.; Salmeron, M. *Phys. Rev. Lett.* **2004,** *93,* 146103.

[176] López, N.; García-Mota, M.; Gómez-Díaz, J. *J. Phys. Chem. C.* **2008,** *112,* 247.

[177] Bernardotto, G.; Menegazzo, F.; Pinna, F.; Signoretto, M.; Cruciani, G.; Strukul, G. *Appl. Catal., A* **2009,** *358,* 129.

[178] Plata, J. J.; García-Mota, M.; Braga, A. A. C.; Maseras, F.; López, N. *J. Phys. Chem. A* **2009,** *113,* 11758.

[179] García-Mota, M.; López, N. *J. Am. Chem. Soc.* **2008,** *130,* 14406.

[180] Liu, P.; Nørskov, J. K. *Phys. Chem. Chem. Phys.* **2001,** *3,* 3814.

[181] Ruff, M.; Takehiro, N.; Liu, P.; Nørskov, J. K.; Behm, R. J. *Chem. Phys. Chem.* **2007,** *8,* 2068.

[182] Birch, F. *Phys. Rev.* **1947,** *71,* 809.

[183] Bocquet, M. L.; Rappe, A. M.; Dai, H. L. *Mol. Phys.* **2005,** *103,* 883.

[184] Kragten, D. D.; van Santen, R. A.; Neurock, M.; Lerou, J. J. *J. Phys. Chem. A* **1999,** *103,* 2756.

[185] Frisch, M. J. *et al.* “Gaussian 03, Revision C.02”, Gaussian, Inc., Wallingford, CT, 2004.

[186] López, N.; Nørskov, J. K. *J. Am. Chem. Soc.* **2002,** *124,* 11262.

[187] Pykkö, P. *Angew. Chem. Int. Ed.* **2004,** *116,* 4512.

[188] Gorin, D. J.; Toste, F. D. *Nature* **2007,** *446,* 395.

[189] Bond, G. C.; Dowden, D. A.; Mackenzie, N. *Trans. Faraday Soc.* **1958,** *54,* 1537.

[190] Hertwig, R. H.; Koch, W.; Schröder, D.; Schwarz, H.; Hrušák, J.; Schwerdtfeger, P. *J. Phys. Chem.* **1996,** *100,* 12253.

[191] Nechaev, M. S.; Rayón, V. M.; Frenking, G. *J. Phys. Chem. A* **2004,** *108,* 3134.

[192] Hargittai, M.; Schulz, A.; Réffy, B.; Kolonits, M. *J. Am. Chem. Soc.* **2001,** *123,* 1449.

[193] García-Mota, M.; Cabello, N.; Maseras, F.; Echavarren, A. M.; Pérez-Ramírez, J.; López, N. *Chem. Phys. Chem.* **2008,** *9,* 1624.

[194] Cabello, N.; Rodríguez, C.; Echavarren, A. M. *Synlett.* **2007,** *11,* 1753.

[195] Nieto-Oberhuber, C.; López, S.; Echavarren, A. M. *J. Am. Chem. Soc.* **2005,** *127,* 6178.

[196] Nieto-Oberhuber, C.; Pérez-Galán, P.; Herrero-Gómez, E.; Lauterbach, T.; Rodríguez, C.; López, S.; Bour, C.; Rosellón, A.; Cárdenas, D. J.; Echavarren, A. M. *J. Am. Chem. Soc.* **2008,** *130,* 269.

[197] Lavallo, V.; Frey, G. D.; Kousar, S.; Donnadieu, B.; Bertrand, G. *Proc. Nat. Acad. Sci. USA* **2007,** *104,* 13569.

[198] Shapiro, N. D.; Toste, F. D. *Proc. Nat. Acad. Sci. USA* **2008,** *105,* 2779.

[199] Labonne, A.; Kribber, T.; Hintermann, L. *Org. Lett.* **2006,** *8,* 5853.

[200] Hintermann, L.; Labonne, A. *Synthesis* **2007,** *8,* 1121.

[201] Nieto-Oberhuber, C.; López, S.; Muñoz, M. P.; Cárdenas, D. J.; Buñuel, E.; Nevado, C.; Echavarren, A. M. *Angew. Chem. Int. Ed.* **2005,** *117,* 6302.

[202] Rose, M. K.; Borg, A.; Mitsui, T.; Ogletree, D. F.; Salmeron, M. *J. Chem. Phys.* **2001,** *115,* 10927.

[203] Gracia, L.; Calatayud, M.; Andres, J.; Minot, C.; Salmeron, M. *Phys. Rev. B* **2005,** *71,* 033407.

[204] Ziemecki, S. B.; Jones, G. A.; Swartzfager, D. G. *J. Less-Common Met.* **1987,** *131,* 157.

[205] Horiuti, J.; Polanyi, M. *Trans. Faraday Soc.* **1934,** *30,* 1164.

[206] Brunauer, S.; Emmet, P. H.; Teller, E. *J. Am. Chem. Soc.* **1938,** *60,* 309.

[207] Murnaghan, F. *Proc. Nat. Acad. Sci.* **1944,** *30,* 244.

[208] Wulff, G. *Z. Kristallogr.* **1901,** *34,* 449.

[209] Rodríguez, A. M.; Bozzolo, G.; Ferrante, J. *Surf. Sci.* **1993,** *289,* 100.

[210] computer-code DACAPO package (v. 2.7), http://wiki.fysik.dtu.dk/dacapo.

[211] Vanderbilt, D. *Phys. Rev. B* **1990,** *41,* 1510.

[212] Pulay, P. *Chem. Phys. Let.* **1980,** *73,* 393.

# List of publications

1. **Temperature and Pressure effects in CO titration of ensembles in PdAu(111) alloys: a theoretical approach** García-Mota, M.; López, N. *Submitted* **2010**
2. **Interplay between carbon monoxide, hydrides, and carbides in selective alkyne hydrogenation on palladium** García-Mota, M.; Bridier, B.; Pérez-Ramírez, J.; López, N. *J. Catal. Under revision* **2010**
3. **Vinyl acetate synthesis on homogeneous and heterogeneous Pd-based catalyst: A theoretical analysis on the reaction mechanisms** Plata, J. J.; García-Mota, M.; Braga, A. A. C.; Maseras, F.; López, N. *J. Phys. Chem. A* **2009**, 113, 11758-11762
4. **Template effects in vinyl acetate synthesis on PdAu surface alloys: A Density Functional Theory study** García-Mota, M.; López, N. *J. Am. Chem. Soc.* **2008**, 130, 14406-14407
5. **Selective homogeneous and heterogeneous gold catalysis with alkynes and alkenes: Similar behavior, different origin** García-Mota, M.; Cabello, N.; Maseras, F.; Echavarren, A. M.; Pérez-Ramírez, J.; López, N. *Chem. Phys. Chem.* **2008**, 9, 1624-1629

The author has performed all the numerical work in the publications 1, 4 and 5, and part of the calculations in the publication 2 and 3, by using the density functional theory codes VASP and Gaussian (publication 5). She has written the first draft of publications 1 and 4, and participated actively in the writing of the rest of the publications. Furthermore, the author has contributed to the paper:

- **NH3 oxidation on oxygen-precovered Au(111): A Density Functional Theory study on selectivity** López, N.; García-Mota, M.; Gómez-Díaz, J. *J. Phys. Chem. C* **2008**, 112, 247-252

which is excluded from the thesis.

# Temperature and Pressure effects in CO titration of ensembles in PdAu(111) alloys: a theoretical approach

Mónica García-Mota, Núria López*

*Institute of Chemical Research of Catalonia, ICIQ,*
*Avgda. Països Catalans 16, 43007 Tarragona, Spain**

In Surface Science, CO is a suitable probe to test the properties of metals in different chemical environments. We have analyzed the properties of CO adsorption on different PdAu alloys at both low and medium Pd content through a theoretical approach. CO is adsorbed on several sites, and the ensemble rules both the CO stretching frequency and the binding energies. Multiple CO adsorption on large ensembles (dimers) is likely at very low temperatures or high CO pressures. As a consequence, at low temperatures, the vibrational spectra of CO on the PdAu(111) alloy can lead to the identification of dimers as singletons. Misinterpretations on the nature of the sites result in the wrong identification of ensembles that are fundamental both in chemical and electrochemical processes. According to our thermodynamic model, CO-induced segregation, is possible at moderate CO pressures, about $10^{-5}$ Torr, in reasonable agreement with experimental determinations for more open surfaces.

March 17, 2010
PACS 68.43.Bc; 68.43.Fg; 68.43.Pq; 61.66.Dk;

## I. INTRODUCTION

Since the early days of Surface Science, CO has been employed as an indirect probe to identify active sites on surfaces. [1–3] The very sensitive nature of the CO vibrational frequency to the local environment has been applied as an accurate measure of the electronic properties of a given metallic system, and serves as a fingerprint of the adsorption site. [4–7] The use of CO to determine the structure of alloys is particularly important since the surface structure and stoichiometry depend on that of the bulk but also on the gas pressure,

---

*Electronic address: `nlopez@iciq.es`

composition, and temperature. The pioneering work by Rodriguez and Goodman [8] on CO adsorption on alloys, and the theoretical explanation given by the *d*-band model, [9] have opened a robust framework for the detailed study of the local structure of alloys. Besides the fundamental interest, CO adsorption on metals and alloys is related to several technologically relevant processes such as: water-gas shift reaction, [10, 11] Fischer-Tropsch synthesis, [12] fuel-cell performance, [13] and selective hydrogenations, [14, 15] just to cite a few examples.

Recently, PdAu alloys with low Pd content were investigated regarding the role of ensembles in electrocatalysis,[16] acetoxylation of ethylene to vinyl acetate (VA), [17–19] and water peroxide synthesis.[20] In the electrochemical experiments it was found that isolated single Pd atoms (singletons) constitute the minimum ensemble needed for CO adsorption, while a larger set is needed for proton adsorption. For VA synthesis, Au has a promotional effect since it drives the formation of the preferred selective catalytic ensemble. In the case of water peroxide enhanced selectivity is found when Au is present. Thus, the detailed characterization of the local structures in PdAu is a need to understand the appealing chemical and electrochemical properties of these alloys. In order to do this, both Scanning Tunneling Microscopy, STM, and the vibrational spectra of CO on PdAu alloys, have been employed to titrate the ensembles present on differently prepared surfaces in order to establish their nature. [17, 21–26]

For instance, the surface concentration of both 5ML Pd grown on 5ML Au on Mo(110), or 5ML Au on 5ML Pd on Mo(110), was studied as a function of the annealing temperature. [22] When annnealed at 800 K (for 45'), the order of the Pd-Au metal growth was found to be irrelevant, and a surface composition of $Pd_{0.2}Au_{0.8}$ was reported. Then, the CO vibrational spectra consisted on a single band at 2088 $cm^{-1}$ with a satellite at 2112 $cm^{-1}$ that appears at low temperatures or alternatively at very high coverages. [23] If instead the 5ML Pd/5ML Au sample annealing was performed at lower temperatures, 600 K, and for shorter time 30', the surface composition was $Pd_{0.25}Au_{0.75}$, and the observed CO spectra were different. At low CO dosing temperatures (80 K), a set of bands at high frequency (around 2078 $cm^{-1}$) with a second broad band in the 1950-1850 $cm^{-1}$ region were found. When increasing the CO dosage (at 80 K) a satellite at 2103 $cm^{-1}$ appeared. A similar behavior was observed when studying different temperatures at constant pressure (i.e. low coverage corresponding to high temperatures). More recently, experiments at different CO pressures, from vacuum to near-atmospheric conditions, were performed by the same group on PdAu(100) surfaces. [25] At CO pressures of $10^{-3}$ Torr, Pd segregation to the surface was observed, the extraction process was highly enhanced by CO pressure so that dimers were present at 0.1 Torr. Several theoretical papers have dealt with the study of the structure of PdAu alloys.[27, 28] In particular, the Pd-Pd, Pd-Au and Au-Au pair interactions were obtained from calculations and employed in Monte-Carlo analysis of the ensembles. In addition, CO interacting with Pd impurities in Au was found to induce segregation of bulk Pd. [29]

In the present paper we use Density Functional Theory, DFT, coupled to *ab initio* thermodynamics to analyze the vibrational spectra of CO on different $\mathrm{Pd}_x\mathrm{Au}_{100-x}(111)$, 0<x<50, alloys under different temperatures and pressures, and compare them to experimental results available in the literature. [17, 21–26]

## II. COMPUTATIONAL DETAILS

Density Functional Theory, DFT, applied to slabs has been employed to determine the adsorption energies and the stretching frequencies of CO adsorbed on Pd(111) and Au(111) surfaces, and on different $\mathrm{Pd}_{100-x}\mathrm{Au}_x(111)$ alloys, 0<x<50. DFT calculations were performed using the Vienna ab initio simulation package, VASP. [30] RPBE exchange-correlation functional [31] was employed to obtain the energy. Monoelectronic states corresponding to the valence electrons were expanded in plane waves with a cut-off energy of 400 eV, while the inner electrons were represented by Projector Augmented Wave, PAW, pseudopotentials. [32, 33] A finite temperature of $k_BT = 0.2$ eV was employed, and the total energies were extrapolated to $k_BT = 0$ eV.

### A. Monometallic surfaces

Monometallic Pd and Au lattice constants were calculated to be 3.990 and 4.208 Å respectively, slightly larger than the experimental values, 3.8907 and 4.0782 Å. [34] Overlayers were also prepared through a similar approach with two metal layers on two of the second metal, the unit cell being that corresponding to the second metal, denoted as Pd/Au (Au cell) and Au/Pd (Pd cell). The slabs contain four layers and are interleaved by a vacuum of at least 12 Å. These systems were studied with $p(2\text{x}2)$ supercells, and the Brillouin zone sampling was set to 5x5x1 *k*-points.[35]

### B. Bimetallic models

The phase diagram of PdAu is that of a solid solution showing short range order. The mixing enthalpy for Pd in Au (bulk data) is -0.36 eV/atom. [36] In order to study the PdAu bimetallic systems, several structures were built. The first family of models is that of Pd impurities in Au and represents low Pd concentration alloys. The structures are shown in Figure 1: a subsurface Pd atom: $Pd_{ss}$@Au; surface monomers like: an isolated atom on the surface: Pd@Au; a structure formed by a surface and a subsurface Pd as nearest neighbors: Pd-$Pd_{ss}$@Au; or next-nearest neighbors: Pd+$Pd_{ss}$@Au. Surface dimers like: $Pd_2$@Au; a next-nearest neighbors configuration on the surface: Pd+Pd@Au; a dimer with a subsurface Pd atom: $Pd_2$-$Pd_{ss}$@Au; or next-nearest neighbors with a subsurface Pd atom: Pd+Pd-$Pd_{ss}$@Au. Larger ensembles consisting of three Pd atoms can be formed on the surface: like trimers, $Pd_3$@Au. All these structures where calculated on a *p*(3x3) reconstruction with 3x3x1 *k*-points.

Figure 1: (Color online) Schematic representation of the models representing the Pd impurities on Au. Yellow spheres stand for Au and gray for Pd.

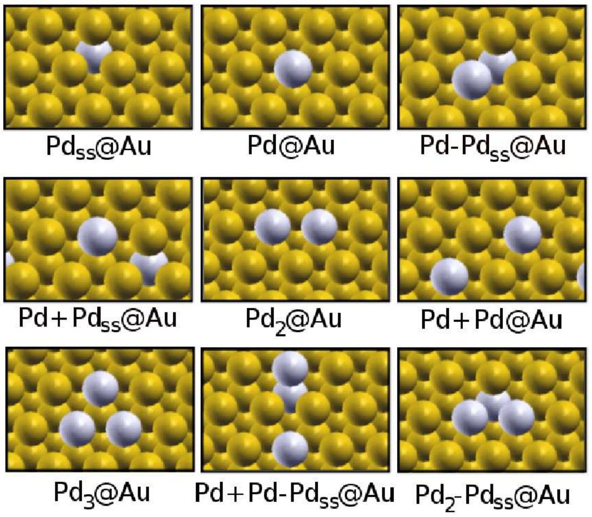

The low temperature annealing of 5ML Pd on top of 5ML Au produces an alloy with a bulk composition for the top layers close to $Pd_3Au$. The calculated cell parameter for $Pd_3Au$ is 4.043 Å. However, due to the different surface energies of Au and Pd, the $Pd_3Au$

surface is enriched in Au, formally being PdAu$_3$.[22] This surface PdAu$_3$, shows isolated Pd atoms, Figure 2, denoted as Pd@PdAu$_3$. From this structure, islands can be formed: a dimer: Pd$_2$@PdAu$_3$; and two trimers: triangular Pd$_{3t}$@PdAu$_3$ and linear Pd$_{3l}$@PdAu$_3$. These surfaces have been modeled by a $p$(4x4) supercell with 2x2x1 $k$-points.

Figure 2: (Color online) Schematic representation of the PdAu$_3$ surfaces considering Pd island formation. Color code is that of Figure 1.

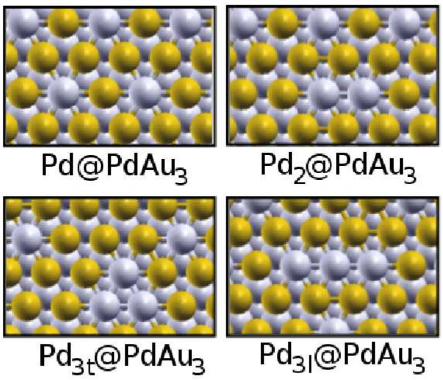

The 50:50 alloy composition has been studied with different models formed by a layer-by-layer growth allowing tridimensional rearrangements, see Figure 3. The first model consists on two Pd layers sandwiched with two external Au layers, Au/2Pd/Au denoted as PdAu (A); and the second contains two gold layers on palladium, 2Au/2Pd, indicated as PdAu (B). In both cases the average cell parameter, 4.099 Å, was employed. Different Pd ensembles can be modeled on the PdAu surface: isolated Pd atoms: Pd@PdAu; dimers: Pd$_2$@PdAu; and trimers: Pd$_3$@PdAu, on both (A) and (B) alloys. We have calculated these ensembles with a $p$(3x3) supercell and 3x3x1 $k$-points.

Figure 3: (Color online) Schematic representation of Pd$_{50}$Au$_{50}$ alloys. Top panel: PdAu (A), and lower panel: PdAu (B). Tridimensional alloys containing singletons, Pd@PdAu; dimers, Pd$_2$@PdAu; and trimers, Pd$_3$@PdAu; are represented. Color code is that of Figure 1.

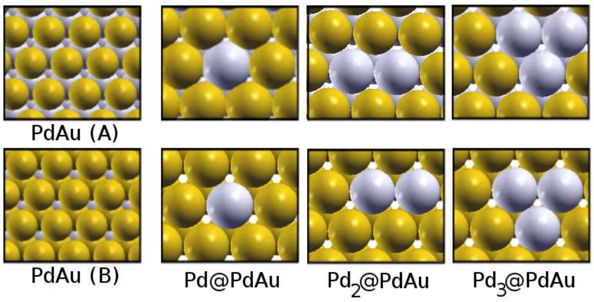

### C. CO adsorption and vibrational frequencies

To investigate adsorption, the CO molecule has been adsorbed only on one side of the above described slabs, and both CO and the two outermost metal layers have been allowed to relax. A dipole layer has been placed in the vacuum region separating the slabs in order to avoid spurious electrostatic interactions due to slab asymmetry.

The vibrational frequencies of free and adsorbed CO were determined through finite differences. Three displacements for each degree of freedom of CO were computed with a step size of 0.02 Å, then the Hessian matrix was obtained and diagonalized. In the frequency calculations, the substrate was kept fixed. With this set up the harmonic calculated gas-phase CO stretching frequency is $\nu$=2120 cm$^{-1}$, which is smaller than experimental estimate, 2170 cm$^{-1}$, but in reasonable agreement with previous theoretical results (2140-2112 cm$^{-1}$). [4, 5] In order to study the experimental spectra, calculated values have been scaled by 1.023, then denoted by $\overline{\nu}$, see Section IV C. This correction factor has been chosen such that the gas-phase calculated CO stretching frequency matches the corresponding experimental value.

## III. RESULTS

### A. Stability of the bimetallic systems

The study of the relative stability of the each alloy has been analyzed through different energy parameters including: formation, segregation and aggreation energies and $d$-band shift, that are reported in Table I. The formation energy, $\Delta E^f$, is obtained as: $\Delta E^f = (E_{alloy} - N_{Pd}E_{bulkPd} - N_{Au}E_{bulkAu})/(N_{Au} + N_{Pd})$. $\Delta E^f$ of the different alloys is always positive due to the formation of both surfaces in the slabs. $\Delta E^f$ ranges from 0.12 to 0.20 eV/atom depending on the composition and configuration of the alloy. Several structures lay in narrow energy intervals (i.e. from 0.12-0.14 eV/atom). The $d$-band shift, $\Delta\epsilon_d$, is found to be almost always positive, i.e. the surface Pd $d$-band is shifted towards the Fermi level, thus increasing its activity. This destabilization amounts between 0.02 and 0.30 eV. The only exceptions are Pd$_2$@PdAu (B) and Pd$_3$@PdAu (B) for which a small negative (stabilizing) value is retrieved.

Segregation energies, $E_{seg}$, for isolated impurities Pd@Au, and for the extraction of

Pd in the PdAu (A) or PdAu (B) layers, are obtained through the following equation: $E_{seg} = E_{Pd@X} - E_{Pd_{ss}@X}$, where $E_{Pd@X}$ and $E_{Pd_{ss}@X}$ correspond to the energies of the slabs representing with the impurity in surface and subsurface positions, respectively. While X represents the alloy. It can be seen that while for isolated impurities antisegregation is favored by 0.30 eV (i.e. bulk is a preferred state), moderated value is obtained for Pd@PdAu (A) configuration, 0.01 eV. Favored segregation is only found for Pd@PdAu (B), -0.17 eV.

Aggregation energies, $E_{agg}$, measure the ability of impurities to form islands on the surface. $E_{agg}$ from isolated impurities, Pd@Au, and from the ensembles of Pd in the PdAu (A) or (B) layers, has been computed as follows: $E_{agg} = E_{Pd_N@X} + (N_{Pd} - 1)E_X - N_{Pd}E_{Pd@X}$, where $E_{Pd_N@X}$ is the energy of the configuration with the dimer (trimer), and $E_X$ is the energy of the slab (either Au, PdAu (A) or (B)), and $E_{Pd@X}$ is that of slab with the impurity on the surface. In the case of the impurities, aggregation of isolated Pd atoms on Au(111) surfaces is endothermic: $E_{agg}$ lays in the range of 0.05-0.18 eV. This is in agreement with the negative formation energy of the alloy in the bulk, [36] with experimental observations,[24] and with recent theoretical results. [37] For the layer-by-layer surfaces, PdAu (A) and (B), the formation of aggregates is more energy demanding for the alloys with (A) configuration than for those with (B) configuration, up to 0.41 eV. This effect can be explained by the fact that the number of heterometallic (Au-Pd) contacts in the segregated structures of (B) composition is larger than that of (A).

For $PdAu_3$ models, in the normal termination more than a single Pd atom is found in the supercell surface. Aggregation energies have been calculated as: $E_{agg} = E_{Pd_N@PdAu_3} - E_{Pd@PdAu_3}$, where the first energy corresponds to the island, and the second to the initial configuration with 4 surface Pd atoms per $p$(4x4) supercell. The formation of dimer on the surface stabilizes the alloy by 0.02 eV, while the formation of larger ensembles, $Pd_{3t}@PdAu_3$ and $Pd_{3l}@PdAu_3$ is endothermic by 0.04-0.06 eV.

Finally, we want to point out that the present aggregation energies do not contain configurational entropy contributions,[29] that at low Pd coverage will increase the endothermicity of island formation.

Table I: Alloy formation energies, $\Delta E^f$, with respect to bulk Au and Pd metals, shift of the Pd *d*-band, $\Delta\epsilon_d$, and aggregation and segregation energies, $E_{seg}$ and $E_{agg}$. See text for definitions. All the energies are in eV except for $\Delta E^f$, in eV/atom.

| Alloy | $\Delta E^f$ | $\Delta\epsilon_d$ | $E_{seg}$ | $E_{agg}$ |
|---|---|---|---|---|
| Pd@Au | +0.12 | +0.07 | +0.30 | – |
| Pd-$Pd_{ss}$@Au | +0.12 | +0.08 | – | +0.11 |
| Pd+$Pd_{ss}$@Au | +0.12 | +0.05 | – | +0.07 |
| $Pd_2$@Au | +0.13 | +0.08 | – | +0.10 |
| Pd+Pd@Au | +0.13 | +0.06 | – | +0.05 |
| $Pd_3$@Au | +0.14 | +0.15 | – | +0.18 |
| Pd+Pd-$Pd_{ss}$@Au | +0.13 | +0.14 | – | +0.09 |
| $Pd_2$-$Pd_{ss}$@Au | +0.13 | +0.07 | – | +0.18 |
| Pd@$PdAu_3$ | +0.14 | +0.02 | – | – |
| $Pd_2$@$PdAu_3$ | +0.14 | +0.14 | – | -0.02 |
| $Pd_{3t}$@$PdAu_3$ | +0.14 | +0.06 | – | +0.06 |
| $Pd_{3l}$@$PdAu_3$ | +0.14 | +0.06 | – | +0.04 |
| Pd/Au (Au cell) | +0.20 | +0.30 | – | – |
| Au/Pd (Pd cell) | +0.15 | – | – | – |
| Pd@PdAu (A) | +0.08 | +0.17 | +0.01 | – |
| $Pd_2$@PdAu (A) | +0.09 | +0.10 | – | +0.12 |
| $Pd_3$@PdAu (A) | +0.09 | +0.15 | – | +0.41 |
| Pd@PdAu (B) | +0.18 | +0.05 | -0.17 | – |
| $Pd_2$@PdAu (B) | +0.17 | -0.01 | – | +0.03 |
| $Pd_3$@PdAu (B) | +0.17 | -0.04 | – | +0.12 |

### B. CO adsorption

The main features of the CO adsorption on the pure metal surfaces Pd, Au and layered structures Au/Pd (Pd cell) and Pd/Au (Au cell), are reported in Table II. On Pd, CO adsorption at low coverage takes place at the fcc site and it is very exothermic, 1.72 eV, the CO vibrational frequency being about 1800 cm$^{-1}$. At high coverage, a 3CO-Pd $p$(2x2) structure develops, the average CO adsorption energy is -1.12 eV/CO molecule, and fcc, hcp and top sites are simultaneously occupied. Three stretching frequencies are obtained: 2074, 1864 and 1798 cm$^{-1}$. Our results are in agreement with previously reported values. [5] On gold, CO is very weakly adsorbed ($|E_{ads}| < 0.05$ eV) and thus, the stretching frequency does not change significantly from the gas-phase value. A stronger binding energy is found when the CO adsorption takes place in the Au(211) step, $E_{ads}$ = -0.34 eV, then the corresponding frequency is 2038 cm$^{-1}$. With respect to the overlayer structures, for Au/Pd (Pd cell) on the Au side, the binding energy of CO is smaller than the corresponding to Au(111). This indicates that the reduction of the cell parameter and the formation of the heterometallic bonds destabilize CO adsorption. In contrast, the adsorption energy of CO on Pd/Au (Au cell) is exothermic by 1.79 eV, thus larger than for the Pd(111) surface. The increase of the binding energy can be traced back to the change in the cell parameter.

Table II: CO adsorption energies on Au, Pd, Au/Pd (Pd cell) and Pd/Au (Au cell), $E_{ads}$ in eV/CO molecule; the molecular bond length, $d_{C-O}$ in Å; the average distance of C to the surface metal atoms, $d_{C-X}$ in Å; and the intra-molecular stretching, $\nu$ in cm$^{-1}$. Metastable sites have been labeled in italics.

| | site | $E_{ads}$ | $d_{C-O}$ | $d_{C-X}$ | $\nu$ |
|---|---|---|---|---|---|
| Au | top | -0.03 | 1.151 | 2.050 | 2046 |
| Au(211) | top | -0.34 | 1.152 | 2.004 | 2038 |
| Pd | *top* | -1.18 | 1.157 | 1.864 | 2046 |
| Pd | fcc | -1.72 | 1.189 | 2.085 | 1798 |
| Pd | hcp | -1.72 | 1.190 | 2.079 | 1791 |
| Pd | *bridge* | -1.43 | 1.179 | 2.004 | 1870 |
| 3CO-Pd | fcc+hcp+top | -1.12 | 1.171 | 2.055 | 2074/1864/1798 |
| Au/Pd (Pd cell) | Au | 0.19 | 1.150 | 2.069 | 2060 |
| Pd/Au (Au cell) | fcc | -1.79 | 1.193 | 2.089 | 1770 |
| Pd/Au (Au cell) | *top* | -1.27 | 1.158 | 1.871 | 2043 |

The properties of CO adsorbed on impurities are reported in Table III. The binding energy to the singleton is 0.93 eV, lower than to the dimer (1.37 eV) and trimer (1.75 eV).

This latter value is slightly larger than that obtained for the Pd(111) surface, see Table II. Indeed CO can extract $Pd_{ss}$@Au to Pd@Au, the energy gained for this process is 0.63 eV. Kinetic limitations due to low temperatures or small CO pressures would control $Pd_{ss}$@Au extraction towards the surface. For complex ensembles, where subsurface Pd atoms are present, Pd-$Pd_{ss}$@Au or Pd+$Pd_{ss}$@Au, larger CO binding energies are obtained. In this case, extraction of Pd+$Pd_{ss}$@Au to $Pd_2$@Au with a CO in a bridging site is endothermic by 0.12 eV, further CO adsorption leading to 2CO on Pd+Pd@Au, is 0.69 eV more exothermic than the single CO adsorption on a bridge site. With respect to the CO stretching frequencies, the values obtained for the impurities are red shifted with respect to pure metal surface. For low CO coverages, the changes in binding energies and stretching frequencies are mainly due to the change of the ensemble, and three different sets are observed: top: about 2030, bridge: 1850, and three-fold: 1768 $cm^{-1}$. Pd dimers and trimers can adsorb more CO molecules. In that case, the average binding energy per CO molecule is slightly smaller than for a single molecule at the same ensemble but the total energy gain is larger. With multiple CO adsorption on large ensembles, the stretching frequencies are in the range 2049-2010 $cm^{-1}$, thus similar to on top adsorption but modified by dipole-dipole interactions, by 40 $cm^{-1}$. On isolated singletons, Pd-Au sites do not correspond to absolute minima, thus once CO is coordinated to the singletons, Pd-Au sites are effectively blocked.

In Table IV, CO adsorption properties to $PdAu_3$ models are shown. The binding energy to the singleton Pd@$PdAu_3$ is 0.96 eV, and the C-O stretching frequencies of 2027 $cm^{-1}$. Thus, the energies are similar to those found for isolated impurities, while frequencies seem more sensitive to the environment. For Pd dimers and trimers on the surface, bridge and hollow configurations are possible. Adsorption energies on bridge and fcc are smaller, by about 0.25 eV, than for the isolated ensembles $Pd_N$@Au (N=2,3). The effect on the frequencies falls within few $cm^{-1}$. For the large islands multiple CO adsorption is possible, then the binding energies are smaller than for the isolated ensembles, and stretching frequencies are also affected, in particular the highest energy band which is about 2035 $cm^{-1}$. Some of the configurations explored present CO adsorption on Pd-Au mixed bridge sites, then adsorption is slighlty lower than for the two on top Pd position, $E_{ads}$= -0.78 and -0.88 eV/CO, respectively. The frequencies corresponding to vibration on these configurations are higher than those from $Pd_2$ bridge configurations.

CO adsorption on singletons, dimers and trimers of the $Pd_{50}Au_{50}$ alloys are reported

Table III: CO adsorption energy, $E_{ads}$ in eV/CO molecule; molecular bond length, $d_{C-O}$ in Å; distance of the carbon atom to the surface metal atoms, $d_{C-X}$ in Å; and intra-molecular stretching frequency, $\nu$ in cm$^{-1}$; for CO on the available sites on the low Pd-content alloys. Metastable sites have been labeled in italics.

| Impurity | $N_{CO}$ | site | $E_{ads}$ | $d_{C-O}$ | $d_{C-X}$ | $\nu$ |
|---|---|---|---|---|---|---|
| Pd@Au | 1 | *top*$_{Au}$ | -0.04 | 1.150 | 2.016 | 2055 |
| Pd@Au | 1 | top | -0.93 | 1.156 | 1.907 | 2032 |
| Pd-Pd$_{ss}$@Au | 1 | top | -1.14 | 1.157 | 1.904 | 2030 |
| Pd+Pd$_{ss}$@Au | 1 | top | -1.17 | 1.157 | 1.903 | 2031 |
| Pd$_2$@Au | 1 | *top* | -1.11 | 1.156 | 1.891 | 2041 |
| Pd$_2$@Au | 1 | bridge | -1.37 | 1.178 | 2.026 | 1850 |
| Pd$_2$-Pd$_{ss}$@Au | 1 | bridge | -1.40 | 1.179 | 2.021 | 1850 |
| Pd$_3$@Au | 1 | *top* | -1.11 | 1.156 | 1.888 | 2035 |
| Pd$_3$@Au | 1 | fcc | -1.75 | 1.192 | 2.090 | 1768 |
| Pd$_2$@Au | 2 | top | -0.97 | 1.156 | 1.915 | 2043/2012 |
| Pd+Pd@Au | 2 | top | -1.01 | 1.156 | 1.910 | 2044/2022 |
| Pd+Pd-Pd$_{ss}$@Au | 2 | top | -1.05 | 1.156 | 1.898 | 2051/2030 |
| Pd$_2$-Pd$_{ss}$@Au | 2 | top | -1.00 | 1.156 | 1.901 | 2045/2016 |
| Pd$_3$@Au | 3 | top | -0.94 | 1.156 | 1.911 | 2049/2010/2010 |

in Table V. For all Pd ensembles the binding energy of CO depends on the second layer metal, being larger when Pd atoms are present, PdAu (A). Tridimensional alloys adsorb CO more weakly than impurities (Pd$_N$@Au) with the exception of the Pd@PdAu (A) singleton. Frequencies corresponding to on top adsorption contribute to the band at 2031 cm$^{-1}$, while bridge and three-fold hollow adsorption to the dimer, show frequencies $\sim$ 1840 cm$^{-1}$, or to the trimer, $\sim$ 1770 cm$^{-1}$. Again, ensembles rule the main position of the vibrational stretching frequency, and only a small modification is caused by the electronic structure changes in the surroundings. Multiple CO adsorption is also possible and shows similar characteristics to other alloys. In particular, the vibrational frequencies resemble those of isolated Pd atoms showing a splitting (30 cm$^{-1}$) due to the dipole-dipole interactions.

Table IV: CO adsorption energy, $E_{ads}$ in eV/CO molecule; molecular bond length, $d_{C-O}$ in Å; distance of the carbon atom to the surface metal atoms, $d_{C-X}$ in Å; and intra-molecular stretching frequency, $\nu$ in cm$^{-1}$; for CO on the available sites at the PdAu$_3$ surface. Metastable sites have been labeled in italics.

| PdAu$_3$ | $N_{CO}$ | site | $E_{ads}$ | $d_{C-O}$ | $d_{C-X}$ | $\nu$ |
|---|---|---|---|---|---|---|
| Pd@PdAu$_3$ | 1 | top | -0.96 | 1.156 | 1.904 | 2027 |
| Pd$_2$@PdAu$_3$ | 1 | bridge | -1.15 | 1.179 | 2.014 | 1857 |
| Pd$_{3t}$@PdAu$_3$ | 1 | fcc | -1.50 | 1.192 | 2.074 | 1768 |
| Pd$_2$@PdAu$_3$ | 2 | top | -0.88 | 1.156 | 1.910 | 2033/2012 |
| Pd$_2$@PdAu$_3$ | 2 | bridge | -0.78 | 1.170 | 2.101 | 1891/1864 |
| Pd$_2$@PdAu$_3$ | 3 | bridge | -0.59 | 1.169 | 2.100 | 1916/1882/1871 |
| Pd$_{3t}$@PdAu$_3$ | 3 | top | -0.83 | 1.157 | 1.909 | 2035/2006/2004 |
| Pd$_{3l}$@PdAu$_3$ | 3 | top | -0.82 | 1.177 | 1.916 | 2032/2009/2000 |
| Pd$_{3l}$@PdAu$_3$ | 2 | bridge | -1.08 | 1.174 | 2.051 | 1897/1867 |

### C. CO binding energies and d-band

We have analyzed the CO adsorption energy on different surfaces as a function of the *d*-band shift. A good correlation between the adsorption energies and the local configuration to the site to which is bound is found in Figure 4. As expected, three different sets of data are present in the figure depending on the ensemble. This is by far the most important effect since it alters binding energies by more than 0.5 eV. Thus, geometrical effects are the leading contributions to CO binding to PdAu alloys. Contrary to what is found for many cases [38, 39] for which binding energies can be roughly obtained by the interpolation of the corresponding values to the isolated metal surfaces. This effect is due to the inert nature of Au on the surface. The second factor contributing to the binding energies electronic effects. The most important are due to the change in the number of non-homogeneous metal atoms in the surroundings of the active site. In that case modulations can reach differences of about 0.2-0.3 eV. Similar results have been found by Roudgar and Gross.[40] Still a set of points falls off the lines corresponding to their ensembles. Those points show subsurface Pd

Table V: CO adsorption energy, $E_{ads}$ in eV/CO molecule; molecular bond length, $d_{C-O}$ in Å; average distance of the carbon atom to the surface metal atoms, $d_{C-X}$ in Å; and intra-molecular stretching frequency, $\nu$ in cm$^{-1}$; on the available sites on each alloy PdAu (A) and (B). Metastable sites have been labeled in italics.

| $Pd_{50}Au_{50}$ | $N_{CO}$ | site | $E_{ads}$ | $d_{C-O}$ | $d_{C-X}$ | $\nu$ |
|---|---|---|---|---|---|---|
| Pd@PdAu (A) | 1 | top | -0.94 | 1.156 | 1.910 | 2031 |
| $Pd_2$@PdAu (A) | 1 | *top* | -0.97 | 1.156 | 1.897 | 2030 |
| $Pd_2$@PdAu (A) | 1 | bridge | -1.21 | 1.180 | 2.021 | 1835 |
| $Pd_3$@PdAu (A) | 1 | *top* | -0.99 | 1.157 | 1.895 | 2023 |
| $Pd_3$@PdAu (A) | 1 | fcc | -1.69 | 1.192 | 2.077 | 1765 |
| $Pd_2$@PdAu (A) | 2 | top | -0.89 | 1.156 | 1.913 | 2040/2010 |
| $Pd_3$@PdAu (A) | 3 | top | -0.89 | 1.157 | 1.913 | 2047/2008/2008 |
| Pd@PdAu (B) | 1 | top | -0.81 | 1.156 | 1.915 | 2107 |
| $Pd_2$@PdAu (B) | 1 | *top* | -0.76 | 1.155 | 1.902 | 2042 |
| $Pd_2$@PdAu (B) | 1 | bridge | -1.06 | 1.178 | 2.032 | 1849 |
| $Pd_3$@PdAu (B) | 1 | *top* | -0.81 | 1.156 | 1.904 | 2032 |
| $Pd_3$@PdAu (B) | 1 | fcc | -1.38 | 1.190 | 2.097 | 1779 |
| $Pd_2$@PdAu (B) | 2 | top | -0.76 | 1.156 | 1.915 | 2042/2013 |
| $Pd_3$@PdAu (B) | 3 | top | -0.73 | 1.156 | 1.913 | 2048/2010/2010 |

atoms in the neighboring region to the active ensemble. The reason for such behavior is related to the changes in the Pauli repulsion that are not represented well enough by the single $\Delta\epsilon_d$ parameter.

## IV. DISCUSSION

In the following section, we illustrate the origin of the bands in the spectra reported in ref.[23] and the behavior found with annealing conditions, CO coverage and dosing temperature. In addition, we complement the previous indications of segregation induced by CO [29] and compare our calculated CO thresholds for Pd extraction to those in ref. [26]

Figure 4: (Color online) CO adsorption energy, $E_{ads}$, on different alloys as a function of the shift on the $d$-band center, $\Delta\epsilon_d$. The insets show the local configuration of the active site. Only isolated CO adsorption is considered. Lines correspond to the fitting of different ensembles discarding the structures with subsurface Pd atoms, see text for more details.

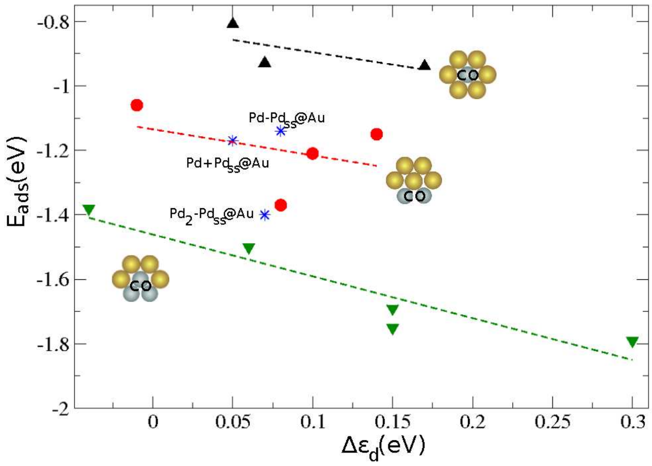

although in that case the surface chosen was PdAu(100).

## A. Surface composition

Experimental surface composition analysis indicates that 5ML Pd on 5ML Au grown on Mo(110) generate an alloy with $Pd_{0.2}Au_{0.8}$ surface composition at 800 K, and $Pd_{0.25}Au_{0.75}$ at 600 K.[22] Therefore, the alloys described in Figures 1 (impurity) and 2 ($PdAu_3$), would be suitable to simulate the spectra at 800 K and 600 K annealing temperatures, respectively .

Annealing conditions control the presence of each ensemble on the alloy surface. On a well-annealed sample, like the 800 K, equilibrium is reached, and thus a Boltzmann distribution considering ensemble formation energies, $E_f$, controls the probability for each configuration, $\mathcal{P}^{B(alloy)}_{T_{ann}} = exp(-E_f/k_B T_{ann})/\Sigma_{alloy}\exp(-E_f/k_B T_{ann})$. $E_f$ can be obtained as a combination of segregation and aggregation energies reported in Table I. Thus, Boltzmann distributions provide a 100% of monomers on the surface at 800 K, $\mathcal{P}^{B(imp)}_{800K}$. Instead for the 600 K system, two limiting distribution models can be employed to analyze surface ensembles. For the Boltzmann distribution with the energies corresponding to the $PdAu_3$, the number of dimers increases up to a 15%, while monomers represent a 78% of the sample,

$\mathcal{P}_{600K}^{B(PdAu_3)}$. Instead a random model distribution provides a different scenario where a 55% of the sites correspond to dimers and 27% to monomers, see Table VI. The probability for each ensemble in the random model is obtained as: $\mathcal{P}^{r(PdAu_3)} = m(\rho_{Pd}^{n}\rho_{Au}^{(6-n)})$,[24] where $m$ is the degeneracy of a given configuration; $n$ is the number of Pd nearest neighbors; 6 comes from the surface coordination of a Pd atom; and $\rho_{Pd}$ and $\rho_{Au}$ are the surface concentrations of Au and Pd ($\rho_{Pd} \sim 0.25$). In summary, high temperature annealed samples provide 100% monodispersed Pd atoms, while a significant fraction of dimers 15-55% is expected for the low temperature annealed samples.

Table VI: Ensemble probability calculated by a Boltzmann distribution at annealing temperature of 800 K, $\mathcal{P}_{800K}^{B(imp)}$ , or 600 K, $\mathcal{P}_{600K}^{B(PdAu_3)}$, and by random distribution with $\rho_{Pd} \sim 0.25$, $\mathcal{P}^{r(PdAu_3)}$.

| Ensemble | $\mathcal{P}_{800K}^{B(imp)}$ | $\mathcal{P}_{600K}^{B(PdAu_3)}$ | $\mathcal{P}^{r(PdAu_3)}$ |
|---|---|---|---|
| Monomers | 1.00 | 0.78 | 0.27 |
| Dimers | 0.00 | 0.15 | 0.55 |
| Trimers | 0.00 | 0.07 | 0.18 |

### B. CO adsorption

In a second step, we have employed *ab initio* thermodynamics [41, 42] to introduce the temperature and pressure effects on the CO adsorption, Tables III and IV. The excess free energy of the CO-alloy system can be written as: $\Delta G_{NCO} = [G_{slab+N_{CO}} - G_{slab} - N_{CO}\mu_{CO}]$. Due to the solid state nature of the slabs and the low frequencies of the metallic systems (and their similarity in both clean slab and CO-covered slab), the Gibbs energies can be approximated by the energies obtained from DFT calculations except for the adsorbed CO vibrational contribution. Moreover, the CO molecular potential can be written as: $\mu_{CO} = \mu_{CO}^{0} + k_B T ln(p_{CO}/p^0)$ where $\mu_{CO}^{0} = E_{CO} + ZPVE - Ts_{CO} + \Delta h$ contains entropic and enthalpic contributions and the Zero Point Vibrational Energy, ZPVE. This later term can be removed since the difference between the adsorbed ZPVE and that of the free molecule is relatively small (less than 0.02 eV). The entropic and enthalpic contributions to $\mu_{CO}^{0}$ can be obtained through the Thermodynamic Tables [43], and with the ideal gas approximation we can obtain $\Delta G_{NCO}$, as: $\Delta G_{NCO} \sim [E_{slab+NCO} - E_{slab} - N_{CO}(E_{CO} + \Delta h_{CO} - Ts_{CO} + k_B T ln(p_{CO}/p^0))]$.

The previous model allows us to indicate when CO-induced segregation is a favorable event as suggested theoretically [29] and observed experimentally on the PdAu(100).[25, 26] At low CO pressures, $\sim 10^{-5}$ Torr, $Pd_{ss}$@Au can segregate to the surface to form Pd@Au, and at moderate CO pressures $p_{CO} > 270$ Torr, $Pd_{ss}$ in Pd+$Pd_{ss}$@Au can segregate to the surface to form $Pd_2$@Au. This is in reasonable agreement with the experimental results for the PdAu(100) surface reported in ref. [25], segregation $\sim 10^{-3}$ and 0.1 Torr dimer formation. Our values are somehow different due to two different reasons, for the low pressure regime our value is smaller than the experimental because a thermodynamic limit is obtained, instead for the high pressure regime our value constitutes a maximum threshold due in part to the more open character of the (100) surface. Then, the excess free energy, $\Delta G_{NCO}$, of single and multiple CO adsorption on dimers, $Pd_2$@Au, is shown as a function of the pressure in Figure 5. At low temperature, the equilibrium configuration for CO adsorption on the $Pd_2$@Au is 2*CO molecules in all range of pressures, while at high temperature, a single CO bound to the bridge site is favored at low pressures, and CO pairs are likely only at high CO pressures. The crossing between multiple and single CO adsorption is observed at $p_{CO} \sim$ 1.3 Torr.

High CO adsorption density on the Pd patches can be traced back to the reduced number of nearest Pd neighbors in the alloy when compared to the extended Pd surface. The number of CO-CO repulsive interactions in the Pd surface on the 3CO-Pd(111) $p(2x2)$ is six for CO each molecule (for distances smaller than $2d_{Pd-Pd}$). This is reduced in the case of dimers or trimers on the alloys (to 1 or 2). In the isolated islands, in the alloys the CO-CO repulsions calculated as $\Delta E = \overline{E} - E_{isolated}$ are smaller than for the Pd(111) surface, 0.4 eV (dimer) compared to 0.6 eV. This is similar to what has been observed for the AuNi alloy at high CO pressures [44] were preferred Ni extraction due to the increase in the effective CO pressure.

## C. CO spectra

In the following we concentrate on the low CO pressure experiments reported in ref. [23] In Table VII, the Gibbs energies at high (250 K) and low (80 K) CO dosing temperature, and at experimental CO pressure, $p_{CO} = 5x10^{-8}$ Torr, are presented for the impurity and $PdAu_3$ models.

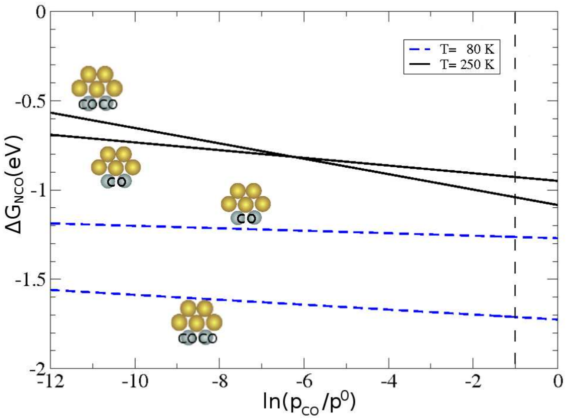

Figure 5: Most likely composition at different $p_{CO}$ and temperatures showing the single or double CO adsorption on $Pd_2$@Au. The vertical line indicates the pressure at which Pd+$Pd_{ss}$ would transform into $Pd_2$ on the Au(111) surface.

At the well-annealed sample (T=800 K), monomers are the only configuration present on the surface. At high CO dosing temperature (250 K), adsorptions take preferentially place at Pd ensembles with subsurface Pd sites, Pd-$Pd_{ss}$@Au and Pd+$Pd_{ss}$@Au, see Table VII. At low CO dosing temperature (80 K), CO adsorption is more energetically favored for all ensembles. Moreover, the presence of Pd atoms in the subsurface can not be distinguished by IRAS, and all Pd monomers will contribute with a single group of vibrations centered at 2079 $cm^{-1}$. In addition, neighboring Pd atoms: Pd+Pd@Au and Pd+Pd-$Pd_{ss}$@Au can provoke the appearance of a band at 2091-2098 $cm^{-1}$, even if the number of these ensembles is relatively small according to the Boltzmann analysis. In that case, due to the IRAS selection rules, only the high frequency, symmetric mode, is active. Thus, neighboring CO adsorption can contribute to the high frequency band in contrast to the common belief that they are due to CO on Au sites.

When the sample is annealed at low temperatures (T=600 K), both Pd monomers and dimers are present on the surface, thus, adsorption on both ensembles has to be considered. At high CO dosing temperature (250 K), single CO adsorption on the bridge site, $Pd_2$@$PdAu_3$, is favored, in agreement with the single broad signal around 1900 $cm^{-1}$ obtained at 300 K in the experiments.[23] At lower temperatures single and multiple adsorption on dimers, either at top or bridge positions (even at Pd-Au bridge sites), and adsorption

Table VII: Gibbs free energy, $\Delta G_{NCO}$ in eV, and corrected intra-molecular stretching frequency, $\overline{\nu}$ in $cm^{-1}$, for CO adsorption in low Pd-content alloys, and in $PdAu_3$ alloys.

| System | $N_{CO}$ | $\Delta G^{80K}_{NCO}$ | $\Delta G^{250K}_{NCO}$ | $\overline{\nu}$ |
|---|---|---|---|---|
| **Pd monomers** (800 K) | | | | |
| Pd@Au (topAu) | 1 | 0.06 | 0.37 | 2102 |
| Pd@Au | 1 | -0.67 | -0.01 | 2079 |
| Pd-$Pd_{ss}$@Au | 1 | -0.88 | -0.22 | 2077 |
| Pd+$Pd_{ss}$@Au | 1 | -0.91 | -0.25 | 2078 |
| Pd+Pd@Au | 2 | -1.50 | -0.19 | 2091/2068 |
| Pd+Pd-$Pd_{ss}$@Au | 2 | -1.58 | -0.27 | 2098/2077 |
| **Pd monomers** (600 K) | | | | |
| Pd@$PdAu_3$ | 1 | -0.70 | -0.04 | 2075 |
| **Pd dimers** (600 K) | | | | |
| $Pd_2$@$PdAu_3$ | 1 | -0.89 | -0.23 | 1901 |
| $Pd_2$@$PdAu_3$ | 2 | -1.24 | 0.07 | 2081/ 2060 |
| $Pd_2$@$PdAu_3$ | 2 | -1.04 | 0.27 | 1936/ 1908 |
| $Pd_2$@$PdAu_3$ | 3 | -0.99 | 0.98 | 1961/1926/1915 |

on isolated monomers can coexist, see $\Delta G^{80K}_{NCO}$ in Table VII. Therefore, the spectrum is composed by a wide group of vibrations with bridge-like character centered at 1900 $cm^{-1}$, together with the top adsorption about 2075 $cm^{-1}$, plus contributions from multiple top adsorption on dimers, 2081 $cm^{-1}$.

## V. CONCLUSIONS

We have analyzed the adsorption of CO on different PdAu alloys by means of Density Functional Theory. We have found that the most likely configurations, in terms of thermodynamics, are those where Pd atoms are surrounded by Au atoms. This indicates the better energetics of Pd-Au interactions when compared to Pd-Pd ones. Thermodynamics indicates the formation of singletons on the surface at high annealing conditions. In contrast, dimers can appear at low temperature annealings due to both the stoichiometry of the PdAu alloy and the fact that equilibrium is not completely reached. Moreover, high CO pressures can extract Pd atoms from subsurface layers to form monomers and dimers on the surface.

As suggested from the experiments, CO frequencies can be used to test the local Pd environment. Therefore, at low pressures and/or high temperatures, CO samples first either dimers or monomers on low and high annealed PdAu samples, respectively. Ensembles formed by surface and subsurface neighboring Pd atoms are more prone to adsorb CO, and thus are the ones occupied at high temperatures. When increasing the CO pressure (equivalent to lower dosing temperatures), and for high temperature annealed samples, adsorption on top sites prevails. Adsorption in neighbouring singletons can generate high frequency bands, about 2100 cm $^{-1}$, that have been traditionally assigned to adsorption on Au centers. For the low temperature annealed sample, the CO spectra are very complex, including CO adsorption and multiadsorption on Pd dimers or even at Pd-Au centers and on the available monomers. This extremely rich behavior warns about the direct description of the ensembles since in several cases, multiple CO adsorption and/or surface-subsurface dimers, Pd-Pd$_{ss}$, can provide energies or frequencies that overlap on previously identified frequency fingerprints. Finally, CO density on Pd islands on the surface is larger than that expected for an extended surface because of the reduced number repulsive interactions when compared to infinite surface.

## VI. ACKNOWLEDGMENTS

We thank the ICIQ foundation, MEC (CTQ2009-07533BQU, CSD2006-003) and GenCat for financial support, and RES-BSC for providing generous computational resources.

[1] G. Ertl, M. Neumann and K. M. Streit, Surf. Sci., **64**, 393 (1977)
[2] G. A. Somorjai, Introduction to Surface Science and Catalysis, Wiley-Interscience (1994)
[3] A. Gross, Theoretical Surface Science: A Microscopic Perspective, Springer 1st. Edition (2002)
[4] I. Dabo, A. Wieckowski and N. Marzari, J. Am. Chem. Soc., **129**, 11045 (2007)
[5] D. Loffreda, D. Simon and P. Sautet, Surf. Sci., **68**, 425 (1999)
[6] A. S. Worz, U. Heiz, F. Cinquini and G. Pacchioni, J. Phys. Chem. B, **109**, 18418 (2005)
[7] N. López, J. Chem. Phys., **114**, 2355 (2001)

[8] J. A. Rodriguez and D. W. Goodman, Science, **257**, 897 (1992)

[9] B. Hammer, Y. Morikawa and J. K. Nørskov, Phys. Rew. Lett., **76**, 2141 (1996)

[10] Q. Fu, H. Saltsburg and M. Flytzani-Stephanopoulos, Science, **301**, 935 (2003)

[11] J. A. Rodriguez, S. Ma, P. Liu, J. Hrbek, J. Evans and M. Perez, Science, **318**, 175 (2007)

[12] M. P. Andersson, T. Bligaard, A. Kustov, K. E. Larsen, J. Greeley, T. Johannessen, C. H. Christensen and J. K. Nørskov, J. Catal., **239**, 501 (2006)

[13] B. E. Hayden, M. E. Rendall and O. South, J. Am. Chem. Soc., **125**, 7738 (2003)

[14] M. Montano, K. Bratlie, M. Salmeron and G. Somorjai, J. Am. Chem. Soc., **128**, 13229 (2006)

[15] N. López, B. Bridier and J. Pérez-Ramírez, J. Phys. Chem. C, **112**, 9346 (2008)

[16] F. Maroun, F. Ozanam, O. M. Magnussen and R. J. Behm, Science, **293**, 1811 (2001)

[17] C. Mingshu, K. Dheeraj, Y. Cheol-Woo and D. W. Goodman, Science, **310**, 291 (2005)

[18] D. Kumar, M. S. Chen and D. W. Goodman, Catal. Today, **123**, 77 (2007)

[19] M. García-Mota and N. López, J. Am. Chem. Soc., **130**, 14406 (2008)

[20] P. Landon, P. J. Collier, A. F. Carley, D. Chadwick, A. J. Papworth, A. Burrows, J. K. Christopher and G. J. Hutchings, Phys. Chem. Chem. Phys. **5**, 1917 (2003)

[21] K. Luo, T. Wei, C. W. Yi, S. Axnanda and D. W. Goodman, J. Phys. Chem. B, **109**, 23517 (2005)

[22] C. W. Yi, K. Luo, T. Wei and D. W. Goodman, J. Phys. Chem. B, **109**, 18535 (2005)

[23] T. Wei, J. Wang and D. W. Goodman, J. Phys. Chem. C, **111**, 8781 (2007)

[24] P. Han, S. Axnanda, I. Lyubinetsky and D. W. Goodman, J. Am. Chem. Soc., **129**, 14355 (2007)

[25] F. Gao, and Y. Wang, and D. W. Goodman, J. Phys. Chem. C, **113**, 14993 (2009)

[26] F. Gao, and Y. Wang, and D. W. Goodman, J. Am. Chem. Soc., **131**, 5734 (2009)

[27] J. A. Boscoboinik, C. Plaisance, M. Neurock and W. T. Tysoe, Phys. Rev. B, **77**, 045422 (2008)

[28] J. A. Boscoboinik, F. C. Calaza, M. T. Garvey, and W. T. Tysoe, J. Phys. Chem. C, **114**, 1875 (2010)

[29] V. Soto-Verdugo, H. Metiu, Surf. Sci., **601**, 5332 (2007)

[30] G. Kresse and J. Hafner, Phys. Rev. B, **47**, 558 (1993); ibid. **49**, 14251 (1994); G. Kresse and J. Furthmüller, Comput. Mat. Sci., **6**, 15 (1996); G. Kresse and J. Furthmüller, Phys. Rev. B, **54**, 11169 (1996)

[31] B. Hammer, L. B. Hansen and J. K. Nørskov, *Phys. Rev. B*, **59**, 7413 (1999)

[32] P. E. Blöchl, Phys. Rev. B, **50**, 17953 (1994)

[33] G. Kresse and D. Joubert, Phys. Rev. B, **59**, 1758 (1999)

[34] http://www.webelements.com Retrieved January 2010

[35] H. J. Monkhorst and J. D. Pack, Phys. Rev. B, **13**, 5188 (1976)

[36] F. R. de Boer, R. Boom, W. C. M. Mattens, A. R. Miedema and A. K. Niessen, Cohesion in Metals: Transition metal alloys (North Holland, Amsterdam 1988)

[37] D. W. Yuan, X. G. Gong and R. Q. Wu, Phys. Rev. B, **75**, 085428 (2007)

[38] J. Greeley and J. K. Nørskov, Surf. Sci., **592**, 104 (2005)

[39] N. López and J. K. Nørskov, Surf. Sci., **447**, 59 (2001)

[40] A. Roudgar and A. Gross, Phys. Rev. B, **67**, 033409 (2003)

[41] X. G. Wang, A. Chaka and M. Scheffler, Phys. Rev. Lett., **84**, 3650 (2000)

[42] Z. Lodziana, J. K. Nørskov and P. Stoltze, J. Chem. Phys., **118**, 11179 (2003)

[43] http://webbook.nist.gov/chemistry/ Retrieved January 2010

[44] E. K. Vestergaard, R. T. Vang, J. Knudsen, T. M. Pedersen, T. An, E. Laegsgaard, I. Stensgaard, B. Hammer and F. Besenbacher, Phys. Rev. Lett., **95**, 126101 (2005)

# Interplay between carbon monoxide, hydrides, and carbides in selective alkyne hydrogenation on palladium

*Mónica García-Mota,[a,1] Blaise Bridier,[b,1] Javier Pérez-Ramírez,[b,]* Núria López[a,]**

[a] Institute of Chemical Research of Catalonia (ICIQ), Avinguda dels Països Catalans 16, 43007, Tarragona, Spain.

[b] Institute for Chemical and Bioengineering, Department of Chemistry and Applied Biosciences, ETH Zurich, HCI E125, Wolfgang-Pauli-Strasse 10, CH-8093 Zurich, Switzerland.

* Corresponding authors: Phone: +34 977 920 237; E-mail: nlopez@iciq.es

Phone: +41 44 633 7120; E-mail: jpr@chem.ethz.ch

---

[1] These authors contributed equally to the results in this manuscript.

## ABSTRACT

Alkyne hydrogenation, a widely used process in industry to purify olefin streams, comprises a prototype reaction to understand selectivity in heterogeneously catalysed reactions. The selectivity of the reaction on palladium catalysts to the alkene, alkane, or oligomers strongly depends on the state of the (sub)surface; *i.e.*, the occurrence of complex carbide or hydride phases. In practice, hydrogenation reactors in C2 and C3 cuts of steam crackers require continuous CO feeding in order to enhance the alkene selectivity of the palladium supported catalyst. In the present work, we have studied the impact of carbon monoxide on the carbide and hydride phases as a standpoint to derive structure-performance relationships under realistic process conditions. For this purpose, catalytic tests on $Pd/Al_2O_3$ and Density Functional Theory on Pd(111) were combined. The influence of (i) the alkyne (ethyne and propyne), (ii) the hydrogen:alkyne ratio (1-10), (iii) the carbon monoxide:hydrogen ratio (0-0.2), and (iv) the catalyst pretreatment on the product distribution were assessed in a continuous flow reactor at ambient pressure. In the absence of CO, subtle changes in the hydrogen:alkyne ratio activate channels towards undesired products. Carbon monoxide enables the external control of the catalyst state by suppressing the formation of (sub)surface hydride and carbide phases, thereby stabilizing a high alkene yield in a broad range of feed hydrogen:alkyne ratios. This scenario contrasts with the more fragile regime of the hydride-carbide phases under CO-free conditions. DFT calculations obtained a single Brønsted-Evans-Polanyi relationship independently of the state of the surface (carbide, hydride, CO-covered) and the nature of the alkyne-alkene-alkane set (C2, C3).

**KEYWORDS.** Palladium; selective hydrogenation; alkyne; alkene; alkane; oligomer; carbide; carbon monoxide; hydride; DFT.

# 1. INTRODUCTION

The focus of catalysis research in the 21st century should be on achieving 100% selectivity for the desired product.[1] Sharp chemical transformations, suppressing side paths, while being specific to particular functional groups in multi-functionalized molecules or to specific reactants in complex reaction mixtures are required.

In the last years, partial hydrogenation of alkynes and alkadienes in the presence of alkenes over Pd-based catalysts has been taken as one of the best playgrounds to identify the control parameters for selectivity.[2,3] This reaction, industrially referred to as hydrorefining, is widely used to upgrade olefin streams by removing highly unsaturated impurities and is carried out over Pd catalysts.[4,5] However, palladium chemistry has been found to be extremely sensitive to the presence of subsurface species. Teschner *et al.*[2,6] proposed on the basis of *in situ* XPS studies that a substoichiometric carbide phase is responsible for the selectivity towards alkenes. Palladium also forms hydrides, even at low hydrogen pressures,[7] which are reported to be unselective.[8] Such subsurface hydrogen species were also reported as very active for nickel.[9] The possible formation of carbide and hydride phases and their relationship with the selectivity of the catalysts has been speculated and discussed vividly during several decades.[4-6] It is often perceived in the open literature that the selective character of a certain catalyst in partial alkyne hydrogenation merely attends to the absence of the fully hydrogenated alkane at the reactor outlet. However, in addition to alkene and alkane production, oligomer production has to be taken into consideration. The presence of oligomers (C4+ and C6+ products in C2 and C3 hydrogenations, respectively) is known to affect the performance of the catalyst.[4] In fact, the selectivity of pure palladium catalysts is very low and therefore, in practice, promotion by a second metal like Ag or Au and CO feeding are requirements to increase alkene selectivity.[10,11] In commercial plants, average ethene selectivities of 40% have been reported in ethyne hydrogenation over promoted Pd/$SiO_2$.[12]

As for theoretical studies, the reaction pathway for hydrogenation has been studied on pure Pd surfaces,[3,13-15] gold nanoparticles,[16] copper and nickel surfaces,[17] and Pd-Ag alloys.[18] In some of these studies, [3,16] thermodynamic selectivity (*i.e.,* strong adsorption for alkynes and none for alkenes) was identified as the selectivity indicator, while the ability to form C-C bonds (oligomers) was neglected. By optimization of the thermodynamic selectivity factor, a new selective NiZn alloy was identified computationally.[3] Ethyne hydrogenation tests on NiZn/$MgAlO_2$ confirmed that over-hydrogenation to ethane was suppressed. However, in theoretical models, the presence of carbide, hydrides, and selectivity modulators has been addressed only partially. A thermodynamic study of carbide formation was reported by Teschner *et al.,*[6] showing the dependence on the alkyne nature, C2 vs. C3. In addition, the ethyne-ethene thermodynamic factors for $PdC_x$ ($x$ = 0.25-1 ML) and $PdH_{0.5}$ were calculated[15] indicating that carbon lowers the binding energies of the unsaturated pairs and that the values for $PdH_{0.5}$ are very similar to those for clean Pd. However, no analysis of the complete reaction path on the carbide or hydride phases was performed. As for CO, its positive effect on the thermodynamic factor has been reported recently for the clean surface.[19] CO reduces the size of the available Pd ensemble on the surface and inhibits C-C bond formation from the hydrocarbons. However, the interplay of CO with carbides and hydrides was not investigated.

In order to understand the selectivity of the industrial process, the overall complexity of the catalytic system under realistic experimental conditions needs to be considered. Thus, both carbide and hydride phases and selectivity enhancers (CO) should be taken into account. In addition, for any rational catalyst design, structure-selectivity relationships must be determined as close as possible to the real conditions.

The aim of the present paper is to establish new structure-selectivity relationships for alkyne hydrogenation on palladium catalysts based on the detailed knowledge of the state of the catalyst under reaction conditions, with or without CO, considering all reactants and products: alkynes, alkenes, alkanes, and oligomers. To achieve this goal the partial hydrogenation of ethyne and propyne was studied by means of systematic catalytic tests over Pd/$Al_2O_3$ and Density Functional Theory, DFT. In both cases different initial states of the catalyst were investigated.

## 2. CATALYTIC TESTS

Catalytic tests were carried out over a 1 wt.% Pd/$\gamma$-$Al_2O_3$ (Aldrich, ref: 205702). $N_2$ adsorption at 77 K was measured in a Quantachrome Autosorb-1MP analyzer. Prior to the analysis, the sample was degassed at 373 K for 16 h. Pd dispersion was determined by CO chemisorption using a volumetric apparatus (Quantachrome Autosorb-1C). Prior to CO chemisorption, the sample was heated in He at 573 K (5 K $min^{-1}$) for 30 min, reduced in $H_2$ (50 $cm^3$ $min^{-1}$) at 473 K for 2 h (3 K $min^{-1}$), evacuated at 473 K for 2 h, and cooled down to 308 K in vacuum. Based on the amount of CO adsorbed and assuming an adsorption stoichiometry CO:Pd = 1:1, the metal dispersion was calculated.

The gas-phase hydrogenation of ethyne and propyne was studied at a total pressure of 1 bar and 348 K in a MicroActivity Reference set-up (PID Eng&Tech). The catalyst (0.15 g, sieve fraction 200-400 μm) was loaded in the quartz microreactor (12 mm i.d.) and heated in He (42 $cm^3$ $min^{-1}$) at 573 K (5 K $min^{-1}$) for 30 min before each reaction. Three types of tests were carried out:

(i) Influence of the $H_2$:alkyne ratio (1-10): the inlet alkyne concentration was kept at 2.5 vol.% and the inlet $H_2$ concentration was increased from 2.5 to 25 vol.% every 2 h. This set of experiments was repeated with an inlet CO concentration of 0.1 vol.%.

(ii) Influence of the CO:$H_2$ ratio (0-0.2): the inlet alkyne and hydrogen concentrations were kept at 2.5 vol.% and 12.5 vol.%, respectively ($H_2$:alkyne = 5), and the CO concentration was gradually increased from 0 to 2.5 vol.% every 2 h.

(iii) Influence of the pretreatment in the absence or presence of carbon monoxide. The catalyst was tested without pretreatment (besides the drying step in He at 573 K) or after pretreatment in (a) 2.5 vol.% alkyne in He, (b) 5 vol.% $H_2$ in He, and (c) 2.5 vol.% alkyne and 3.75 vol.% $H_2$ in He (reaction mixture). The pretreatments were carried out at 473 K for 30 min using a total gas flow of 42 $cm^3$ $min^{-1}$. Afterwards, the catalyst was cooled down in the same gas mixture to 348K (5K$min^{-1}$) and evaluated in two feed mixtures: alkyne:$H_2$:He = 2.5:3.75:93.75 and alkyne:CO:$H_2$:He = 2.5:0.1:3.75:93.65.

In the catalytic tests, the total flow was kept constant at 42 $cm^3$ $min^{-1}$ (space velocity, $SV$ = 16,800 $cm^3$ $h^{-1}$ $g^{-1}$) by balancing the mixtures with He. Fresh catalyst was loaded in each test and for each pretreatment. Alkynes, alkenes, and alkanes were analyzed by a gas chromatograph (Agilent GC6890N) equipped with a GS-GasPro column and a thermal conductivity detector. The selectivity to the alkene (alkane) was determined as the amount of alkene (alkane) formed divided by the amount of reacted alkyne. The selectivity to oligomers was obtained as: $S$(oligomers) = 1 - $S$(alkene) - $S$(alkane).

## 3. COMPUTATIONAL TECHNIQUES

The catalytic hydrogenation of ethyne and propyne was studied by means of periodic Density Functional Theory (DFT) applied to slabs and calculated with the VASP code.[20] The Pd cell parameter was 3.987 Å in agreement with the experimentally determined.[21] The (111) slabs consist on four atomic layers and a $p(2\times2)$ reconstruction. Four different models were set up: (i) clean Pd surface, (ii) a near-surface carbide (carbon content 0.25 ML), (iii) a fully hydrogenated Pd system and (iv) a partially CO-covered surface (CO coverage 0.25 ML) (see Supporting Information S1 for a schematic representation). To study C-C coupling reactions (oligomerization) we have used a larger supercell $p(2\times4)$ where two alkyne molecules have been placed, thus keeping the same hydrocarbon coverage employed in the hydrogenation steps. In addition, both coupling between an alkyne CO and or to another, partially hydrogenated alkyne has been investigated to identify the effect of other species and the incorporation of CO to the oligomers that has been proposed in the literature.[22] k-point meshes of 5×5×1 were considered for the $p(2\times2)$ cell and reduced to 5×3×1 for the $p(2\times4)$ cell.[23] The energy profiles were studied with the GGA-PW91 functional.[24] In the calculations, inner electrons were represented by PAW pseudopotentials[25] and the monoelectronic valence states were expanded with plane waves with kinetic energies lower than 400 eV. Transition states were located by the Climbing Image version of the Nudged Elastic Band, CI-NEB, method,[26]and were proven to show a single imaginary frequency.

To obtain the chemical state of the surface under different environments, the above-described $p(2\times2)$ supercell was employed. In that case, sequential hydrogen additions, first to the surface layer and then to subsequent layers, have been introduced following the procedure by Mavrikakis *et al.* [27] To model the hydride phase, lattice enlargements were taken into account as it corresponds to the experimental observation for the β-PdH phase.[7] Since the description in energy terms does not account for the effect of temperatures and pressures in hydride formation, first principle thermodynamics were employed to describe the state of the surface under different conditions. Hydride formation in Pd can be understood as a particular case of multilayered adsorption,[28] the final equation being:

$$V/V_m = \Sigma_{i=0}^{\infty} i\theta_i/\Sigma_{i=0}^{\infty} \theta_i = cx/((1-x)(1+(c-1)x)) \tag{1}$$

where $V/V_m$ represents the number $i$ of H-multilayers adsorbed, and $c$ and $x$ are related to the partial hydrogen pressure and adsorption-desorption constants of the surface layer $k_1,k_{-1}$ or the resting layers $k,$ $k_-$, $c=(k_1\, p_{H2}/k_{-1})^{1/2}/x$ and $x=(k\, p_{H2}/k_-)^{1/2}$ and $p_{H2}$ stands for the hydrogen pressure. If some carbon or CO impurities are present then the equation is modified and reads as follows:

$$V/V_m=(cx+11(1-x)K_{C2H2}(p_{C2H2}/p_{H2})^{1/2}/((1-x)((1-x)+cx+12(1-x)K_{C2H2}(p_{C2H2}/p_{H2})^{1/2})) \tag{2}$$

$$V/V_m=cx/((1-x)((1-x)+cx+(1-x)K_{CO}p_{CO})) \tag{3}$$

where $K_{C2H2}$ and $K_{CO}$ are the adsorption constants of ethylene and CO; and $p_{C2H2}$ and $p_{CO}$ their corresponding partial pressures. Full derivation of these equations is elaborated in the Supporting Information.

## 4. RESULTS AND DISCUSSION

In the following section we first describe the effect of the hydrogen:alkyne ratio in order to analyze the role of carbide and hydride formation. In this analysis the reaction network for three systems has been considered: clean surface, carbide-containing, and hydride-containing. Next, the role of carbon monoxide, the balance between carbide and hydride, and the barriers are taken into account both for the clean and CO-covered surface.

### 4.1. Catalytic performance

The total surface area of the 1 wt.%. $Pd/Al_2O_3$ sample ($S_{BET}$) was 210 $m^2$ $g^{-1}$. CO chemisorption revealed a Pd dispersion in the catalyst of 22%, yielding an average Pd particle size of 5 nm (assuming hemispherical particle). Alkyne hydrogenation tests assessed the influence of the $H_2$:alkyne ratio and the CO:$H_2$ ratio on the product distribution. Besides, the impact of the catalyst pretreatment on the CO effect was evaluated. All tests were systematically conducted with ethyne and propyne in order to extrapolate conclusions to relevant substrates with different carbon number. Few studies in the literature include both alkynes, and since the catalyst, reaction conditions and reactor configurations employed differ substantially, a proper comparison of catalytic data is sometimes not straight forward. The different scenarios studied experimentally were compared with complementary computational results in the next section.

**$H_2$-to-alkyne ratio.** Figure 1 shows that the alkyne conversion at 348 K was complete at all $H_2$:alkyne ratios, except for values around 90% for both alkynes at the stoichiometric ratio of 1. The selectivity to ethene and propene with $H_2$:alkyne = 1 was 42% and 62%, respectively. These values decrease steadily upon increasing the inlet partial $H_2$ pressure. The same trend described for the selectivity to the olefin was followed by the selectivity to oligomers, starting at *ca.* 30-40% with $H_2$:alkyne = 1. The selectivity to the alkane exhibited an opposite trend, increasing from 10-20% at $H_2$:alkyne = 1 to 80-90% at $H_2$:alkyne = 10. At $H_2$:alkyne > 4, the selectivity to products remained essentially constant: no alkene production and *ca.* 90% to the fully hydrogenated alkane but still the selectivity to oligomers amounted to *ca.* 10%. The low alkene selectivity of unpromoted palladium catalysts has been stressed by various authors[10,11] and obviously addition of a second metal (Ag) or continuous feeding of carbon monoxide is mandatory to explain its successful implementation in industry (*vide infra*). The loss of alkene selectivity upon increasing the $H_2$:alkyne ratios has been typically explained by the formation of the β-PdH phase, which is selective to the over-hydrogenated product.[4,8] In qualitative terms, the dependences of the products distribution on the $H_2$:alkyne ratio were very similar for C2 and C3. More specifically, it can be observed that at low $H_2$:alkyne ratios, the selectivity to propene is higher than to ethene by more than 10%. This difference smoothed out when increasing the inlet partial $H_2$ pressure. The selectivity to the alkane was higher for C2 than for C3 at all $H_2$:alkyne ratios. In any case, the main outcome from Figure 1 is that, the most competitive path under H-lean conditions (hydrogen:alkyne ≤ 1) is oligomerization, whereas at hydrogen:alkyne ≥ 2 the alkane in the main product. The ratio of 1.5-1.7 corresponds to a switch for alkene:alkane selectivity. Indeed, the very narrow window under which selective hydrogenation is observed on palladium, stresses the major role of surface modifiers in the industrial process.

**$H_2$-to-CO ratio.** The increase in alkene selectivity upon addition of carbon monoxide has been demonstrated in the past; this effect is reversible, *i.e.* it disappears when CO feeding is turned off.[4,8] The influence of CO on the production of oligomers has been assessed in a less systematic way and there are contradictory statements:[22] some authors said that CO reduces the selectivity to green oil while others indicated that CO leads to the occurrence of more carbon deposits. In our experiments the influence of CO as selectivity enhancer was studied in two different regimes. First, the $H_2$:alkyne was set to 5 while gradually increasing the CO:$H_2$ ratio (Figure 2). The selected $H_2$:alkyne ratio in the feed was relatively high in order to evidence more clearly the decrease of alkane production upon CO addition. Addition of very low amounts of carbon monoxide (CO:$H_2$ < 0.002) led to a marked decrease of the alkane selectivity at the expenses of an increased production of the alkene and oligomers. A further increase of the inlet partial CO pressure (CO:$H_2$ = 0.04) completely suppressed the over-hydrogenation product and led to a maximum alkene selectivity (*ca.* 30% ethene and *ca.* 60% propene), see Figure 2. Even at CO:$H_2$=0.04 oligomers were formed extensively (more for propene than for propyne). Within this range of CO:$H_2$ ratios, the degree of alkyne conversion was >90%. Excess of carbon monoxide (CO:$H_2$ > 0.1) was detrimental, producing a decrease of the alkyne conversion (down to 30%) and alkene selectivity (*ca.* 30% propene and *ca.* 20% ethene). The pathway to the alkane was suppressed and oligomers are the major byproduct, reaching a selectivity of *ca.* 85% for C2 and *ca.* 75% for C3. Therefore, CO acts a external switch of the alkene:alkane:oligomers selectivity and, by optimization, it enables to adjust the partial hydrogenation depending on the inlet $H_2$:alkyne ratio. The yield of oligomers, determined as the product of alkyne conversion and alkene or oligomer selectivity is presented in Figure 3. The alkene yield presents a maximum in the range 0.02-0.04 allowing a pretty broad operating window (Figure 3). Interestingly, the optimal window for alkene selectivity and yield coincides with the range at which the yield to oligomers is maximal.

In the second set of experiments a constant CO content of 0.1 vol.% was employed while the $H_2$:$C_3H_4$ ratio is varied between 1 and 10. The effect of the feed hydrogen-to-propyne ratio on the propyne conversion and selectivity to products is presented in Figure 4. The product distributions over clean Pd and in the presence of CO were markedly different. Partial hydrogenation of propyne in the presence of CO was hardly affected by the inlet partial $H_2$ pressure, at a difference to the results discussed in the previous section for Pd. The selectivity to propene at very low $H_2$:$C_3H_4$ ratios was relatively low (46%) in favor of a higher selectivity to oligomers (54%). In the other extreme, i.e. at very high $H_2$:$C_3H_4$ ratios, the selectivity to propene was still remarkably high *ca.* 70% and only little propane was produced (3%). From $H_2$:$C_3H_4$ ratios=2-10, the selectivity to alkene was within the range of 60-70%, to oligomers 30-40% and that to the alkane virtually zero. Propyne conversion was practically complete at any ratio.

**Pretreatment.** A third type of experiments was dedicated to study the influence of CO on alkyne hydrogenation over differently pretreated catalysts (Figure 5). The pretreatment conditions influence the state of palladium (clean, H-rich and C-containing) prior to reaction. For ethyne and the non-pretreated catalyst, CO addition lowers the conversion, suppresses ethane production, and increases both the ethene and oligomer selectivity. When the catalyst was pretreated in ethyne, ethene selectivity did not change upon CO addition and the oligomer selectivity increased at the expense of ethane. If the sample was exposed to high $H_2$, the alkyne conversion was high and the alkane was the major product (75% selectivity), the second product being oligomers (24%), and minor ethene production. If CO was added, ethyne conversion decreases, then the major products were oligomers, ethene production was enhanced and the complete quenching of ethane was observed. When the catalyst was pretreated under the reaction mixture the effect of CO addition was very similar to the results observed for non-pretreated catalyst.

The results for C3 parallel those of C2. The main differences observed were that for C3, alkenes were more likely to appear both in presence and absence of CO, this, points out to the intrinsic properties of the insaturated C3 when compared to the C2 counterparts in terms of oligomerization. Oligomeric compounds were more likely to be formed with C2 (*ca.* 40% for C2 compared to *ca.* 20% for C3). The most striking difference appeared in regard to alkyne pretreatment. In both cases, this leaded to more selective alkene catalysts, while the introduction of CO in the feed results in no change in alkene selectivity for the C2 case and a large increase (about 30% more) for C3.

As a summary, upon CO addition, the alkyne conversion decreased by 10-20%. Under hydrocarbon pretreatment alkenes were the major product and the presence of CO improved alkene production in the case of C3. The effect of CO was much more important in the case of hydrogen pretreatment where initially over-hydrogenated products predominated (selectivity ~70%). CO blocked this process but did not completely suppress it in the case of C2. Nevertheless, after hydrogen pretreatment, CO addition improved the selectivity to the double bound even if the effect was more significant in propyne hydrogenation. Finally, if the pretreatment was carried out under reaction conditions, the hydrogenation behavior of C2 and C3 were similar to the one carried out over non-pretreated catalyst: oligomers and alkanes were obtained for C2 and alkanes were the major products for C3. After CO addition, alkene production was enhanced but the olefin was the major product only in the case of C3.

### 4.2. States of the system

By extensive use of DFT-based simulations, the interplay between the carbide, hydride, and CO-rich phases was analyzed employing models similar to those employed in first-principle thermodynamics.[29]

**Hydride formation.** The formation of hydrides and carbides has been proposed and documented under some conditions in the past.[5,8] $PdH_x$ shows both a low-H-content $\alpha$-$PdH_{0.2}$ phase, and a high content $\beta$-$PdH_{0.7}$ phase.[7] From our models, starting with the clean Pd(111) surface, hydrogen is adsorbed exothermically, by 0.58 eV/H atom, at 0.25 ML coverage. $H_2$ dissociation is easy even at a high hydrogen coverage.[30,31] The average adsorption energies per atom for the clean surface are close to

-0.5 eV/surface H atom while was much smaller for the inner octahedral sites, around -0.1 eV/bulk H atom. The low barrier for dissociation of $H_2$ and the easy incorporation along (111) surfaces indicates that the all the surface can capture and incorporate $H_2$ from the gas.

**Carbide formation.** Carbide formation arises from the decomposition of organic moieties.[32,33] According to Andersin *et al.*[34] ethene dissociation into two methylene groups is hindered by a barrier of 2.12 eV barrier on the Pd(111) surface, but it is reduced to 1.69 eV at the step. Therefore formation of C-related species takes place mainly at steps. In fact, the adsorption energy of C atoms (with respect to gas-phase $C_2H_2$ and $H_2$) is exothermic by -1.0 eV at the step (endothermic by 0.2 eV with respect to $C_2H_4$ and $H_2$). The formation of the C-containing deposits strongly depends on the chemical potential of the alkyne-alkene pairs as reported by Teschner *et al.*[6] and corroborated by us in the Supporting Information. Once carbon atoms are formed they can diffuse inside the step to the near-surface layer. The process is hindered by a barrier between 0.8-1.0 eV depending on the coverage (0.33 or 0.17 ML C atoms at the step). This agrees with the experimental observations in the group of Kiwi-Minsker, which assigned the formation of a carbide layer near defective sites to the low turn-over frequency found for small particles when compared to larger ones.[35]

The binding energy of the carbide at low coverages (0.0625 ML) is similar to the value at the step (about 1 eV with respect to gas phase $C_2H_2$ and $H_2$). Diffusion in the near-surface layer is rather easy, the activation energy for diffusion being $E_{a,diffusion}$=0.71 eV. This value is in agreement with the 0.72 eV estimate from STM experiments for the denominated β-impurities and previous computational results.[32,33] The carbide phase is not very dense in C atoms, as insertion in near subsurface carbon position is repulsive by 0.6 eV at neighboring sites (0.1 eV at second next nearest neighbors). This is compatible with the $PdC_{0.13}$ phase reported by Teschner *et al.*[2] The most favorable position for C atoms in Pd is the octahedral subsurface sites; penetration towards the bulk has a thermodynamic penalty cost of 0.04 eV for the subsurface layer (and more than 1.5 eV for bulk Pd). The reason for near-surface carbide formation is closely related to the higher *d*-band energy of the Pd atoms on the surface and to the fact that geometric relaxations are also easier for surface atoms than for bulk atoms. From the data above, the near surface positions close to the step edges are most likely *poisoned* by the formation of the carbide, the extension of the carbide depends on the diffusion from these positions towards the center of the palladium particle.

**Carbide-hydride interplay.** To analyze the interplay between the carbide and the hydride phase we started by a configuration in which a near-subsurface C atom were already present. Adsorption of H atoms on the surface takes place normally. There is an exception for the position on top of the carbon atom where adsorption is not favored. The average adsorption energy of the first H-layer is slightly reduced to -0.46 eV/H atom (-0.58 eV/atom clean Pd). The insertion of H atoms in the second layer is largely hampered as shown in Figure 6 and the presence of C in the near-surface layer impedes additional H adsorption even at distances as long as 5 Å (about 2 positions in the lattice). Thus H adsorption close to C atoms is less stable than on the surface or in a subsurface layer very far away from the C position. For H in the third layer, Pd atoms screen more effectively the presence of C and already at 4 Å (more than one lattice position) the standard value for subsurface H adsorption is retrieved (-0.11 eV/atom). On the other hand, if the initial situation consists on the PdH form, less available step sites for hydrocarbon dissociation exist thus hampering the formation of the carbide. Indeed, C incorporation to the near-surface layer at the step site under high hydrogen content results in very endothermic > 1.5 eV insertion. Thus, the hydride prevents the formation of the carbide layer both by blocking possible carbide positions and by increasing the thermodynamic requirements for insertion.

**CO-containing systems.** CO is known to adsorb on Pd(111) forming very dense layers even at low partial pressures.[36-38] At low coverage, 0.25 ML, the calculated CO adsorption energy with the present set up is -2.06 eV, which is in close agreement with previous calculations.[36] Dense structures up to *p*(2×2)-3CO are usually formed under UHV conditions. For this case, the average adsorption energy decreases to -1.43 eV/CO. At 0.25 ML CO coverage, the H binding energies are -0.40 eV/H atom on the surface and even more reduced for subsurface H, *ca*. -0.05 eV. Thus the formation of a dense CO layer implies the reduction the number of adsorption sites for $H_2$ and the decrease of the average binding energies.

Since CO is very strongly bound to the surface, it can interact with carbon impurities, as suggested by Salmeron *et al.*[32] For instance, in a $p(2\times2)$ lattice containing subsurface C, the average CO adsorption energy in the compact 3CO layer is still favorable, -1.16 eV/CO. Moreover, the dense CO layer can induce the penetration of the carbon atom deeper in the Pd structure, since this structure is 0.80 eV more favorable than the corresponding with near-surface C. Thus the CO modifier moves the carbide layer to deeper positions in the Pd particle. This is a dynamic effect since once CO is removed; the diffusion of carbide towards the near-surface position is energetically favored. In the contrary, if the CO layer is deposited first, it blocks the sites at the steps; (CO binding energy is -2.11 eV) and impedes the formation of the carbide from alkynes. The C-CO steady state would then depend both on the history of the sample and on the partial CO pressure.

## 4.3. Reaction mechanism and kinetics

In the present work, we have carried out a systematic study on the effect of the catalyst state on the reaction network for the clean Pd surface or in the presence of carbide, hydride, and CO. A complete reaction list with thermodynamic and kinetic parameters is collected in the Supporting Information. Only most relevant data will be discussed hereafter. Figure 7 shows the reaction network for the hydrogenation. Parallel paths including oligomer formation and the participation of CO in the oligomerization process will be described too. However, the extensive number of different moieties that can undergo C-C bond formation prevents from a detailed quantitative analysis of the complex oliomerization reactions.

**Hydrogenation.** The complete reaction network starts by $H_2$ dissociation and the adsorption of the alkyne on the surface. Both steps are exothermic under all conditions (clean, C, H, and CO). Then the sequential addition of H following a Horiuti-Polanyi mechanism[39] can take place. Given the symmetric nature of ethyne, the first hydrogenation leads to a single product vinyl, $HCCH_2$. Vinyl is a branching point intermediate since upon hydrogenation, two competitive products: ethene ($H_2CCH_2$) or ethylidene, ($HCCH_3$), can be formed. From $H_2CCH_2$ or $HCCH_3$ further hydrogenation leads to a common intermediate ethyl, ($H_2CCH_3$), and finally the fourth hydrogenation leads to ethane. For higher hydrocarbons such as C3, the number of possibilities grows and three branching points exist in the complete hydrogenation path. The complexity of the bifurcation points has not been considered in the majority of the hydrogenation calculations,[3] but as we will show later, all this possibilities cannot be *a priori* neglected from an energy point of view and might be the main hydrogenation path for some of catalyst states.

Analyzing the data for the clean surface during ethyne hydrogenation, its adsorption is exothermic by *ca.* 2 eV, the first hydrogenation is exothermic by 0.17 eV, and the barrier is 0.66 eV. The second hydrogenation to ethene shows a barrier of 0.81 eV, while the barrier to ethylidene is 0.79 eV. Both products are more stable than the vinyl intermediate by 0.42 eV for ethene and 0.12 eV for ethylidene. Then ethene can desorb releasing 0.82 eV. The third hydrogen addition towards ethyl has barriers of 0.74 eV (from $H_2CCH_2$) and 0.80 eV (from $HCCH_3$) while the final step is hindered by the lowest barrier, only 0.48 eV. Summarizing the results above: on the clean surface, formation of ethene and ethylidene is almost equally likely and ethene can either desorb or be further hydrogenated. Thus, both effects are responsible for the relatively low selectivity towards ethene observed for clean Pd. Indeed, our catalytic tests on the non-pretreated $Pd/Al_2O_3$ catalyst lead to selectivities of 40% (20%) to ethene (ethane) at stoichiometric ratios.

Therefore, both binding energies of ethyne and ethene pair (thermodynamic factor) (Table 1) and activation energies of the first branching reaction are crucial to understand selectivity in alkyne hydrogenation. Thermodynamic factors are known to depend on the nature of the catalyst, [3,16,19] but also kinetic contributions depend on the nature of the system. For instance, if C is present, the second hydrogenation barriers are 0.57 and 0.69 eV to $H_2CCH_2$ and $HCCH_3$, respectively. Therefore, the presence of the carbide induces selectivity, both by destabilizing ethene adsorbed on the surface ($E_{ads}$=-0.67 eV to be compared to -0.82 eV for the clean surface) and by improving the second hydrogenation branching ratio. Our results explain the observations by Teschner *et al.*[2] of improved selectivity in the presence of the carbide. If CO is present, the second hydrogenation barriers are 0.88 and 0.57 eV at low

CO coverage (0.25 ML) but already at 0.50 ML CO the barriers are reduced to 0.14 and 0.23 eV (ethene and ethylidene), leading to selective ethene production.

The situation is far more complex in the presence of the hydride phase. The first hydrogenation takes place from one of the hydrogen atoms on the surface. This leaves an H-vacancy on the Pd surface with an H in the near-surface position. This nascent hydrogen atom has a chemical potential that exceeds the surface hydrogen atom by 0.45 eV. Thus once vinyl is formed two options can be triggered, either from a H sitting on the surface (to attack the HC fragment) or an almost free H atom ($H_{subsurface}$), closer to the $CH_2$ moiety, see Figure 8. The corresponding hydrogenation barriers are 0.36 and 0.06 eV, respectively. As a consequence, under these conditions, the major product is ethylidene and the final product is ethane. This differs from the previous theoretical estimation where the presence of subsurface hydrogen was reported to induce almost no change in the barriers,[13] but in that study the direct effect of emerging H atoms was not considered. Therefore, in the case of the hydride, the alkane production is controlled by the opening of surface H-vacancies generated by the first H transfer and the subsequent ejection of near-surface H.

In the case of C3 hydrogenation, adsorption of propyne on the clean surface is exothermic by 1.57 eV. Then the first hydrogenation can take place on the primary carbon or secondary carbons, both $E_a = 0.70$ eV. From each hydrogen addition, a branching point occurs that leads to the formation of $CH_3CH_2CH$ and propene or to propene and $CH_3CCH_3$, where the corresponding barriers are 0.72, 0.71, 0.76, and 0.48 eV, respectively. Propene desorption is endothermic by 0.60 eV. Further propene hydrogenation to $CH_3CH_2CH_2$ or $CH_3CHCH_3$ is hindered by 0.75 and 0.83 eV barriers. Thus the competition between propene desorption or further hydrogenation is more favorable towards desorption than for the C2 counterpart. Therefore, propyne hydrogenation is intrinsically more selective to the alkene than ethyne hydrogenation. Any other hydrogenation from the rest of the intermediates in Scheme 1 shows hydrogenation barriers between 0.93 and 0.48 eV. The effects of carbide, CO, and hydrides parallel those found in the description of C2.

**Thermodynamic factors.** The values for the thermodynamic factors for all systems considered in the present work are reported in Table 1. According to this, the most effective model catalysts to obtain a good selectivity towards the double bound are by order of magnitude: CO, then hydrides, carbides and the most unselective system is the clean surface. Clearly, this is not the case if hydrides are present. Hydride formation produces over-hydrogenated moieties even if the thermodynamic factor is more favorable than for the clean surface. This is due to the presence of new active H species indicated in Figure 8 that opens a new path in the case of the over-hydrogenation route. Therefore, we stress that the thermodynamic factor can thus only be considered as a reliable selectivity descriptor provided that the active species are preserved.

**Brønsted-Evans-Polanyi relationships.** To compile all the results concerning the kinetic parameters for all the reactions in Scheme 1, we have plotted the corresponding Brønsted-Evans-Polanyi relationships (BEP) for C-H dissociation in all the model structures for both C2 and C3 (Figure 9). Dehydrogenations of ethylene derivatives on Pd have been found to follow this kind of linear relationships independently of the degree of unsaturation of the hydrocarbon.[34] The present results extend the use of such relationships to different carbon numbers and to all the Pd-derived substrates included in the calculations, *i.e.* clean surface, hydrides, carbides, and CO-covered surfaces. Remarkably, no individual fitting (either by carbon number or by the state of the catalysts) finds a better correlation than that including all data. The success of the present BEP linear relationship is likely to be related to the small ensemble needed for the dehydrogenation reaction: in all transition steps the H atom is activated to a on-top Pd position.

**Oligomerization**. We discuss first the oligomer formation with ethyne, the initial, transition and final states are shown in the Supplementary Information. On the clean surface, the barrier for oligomerization is 1.38 eV. However, if very dense alkyne layers exist the barrier could be reduced down to 0.86 eV. In the presence of carbide, the reaction barriers are different depending on the local configuration, however the C-C barrier increases up to 1.71 or 1.99 eV depending if the carbide is below the oligomerization path or further away from it. Oligomerization is energetically eased in the presence of CO, 0.91 eV due to both the reduction of the reactants binding energy and the smaller steric hindrance in the final structure. Instead, the coupling barrier is higher on the palladium hydride, 1.52 eV due to the difficult diffusion. However, for CO and to a lesser extent for hydride, the dense layer formed implies also the isolation of different sites and thus there is a geometric contribution that blocks preferentially oligomer formation due to reduction of the effective ensembles and blocked diffusion. In addition, C-C coupling from vinyl to ethyne shows a smaller barrier than the ethyne-ethyne coupling, 1.19 eV (*versus* 1.38 eV), which means that partially hydrogenated molecules are more energetically prone to undergo oligomerization. Finally, CO can also react to the alkyne leading to HC=CH-CO. The barrier for this process is 1.40 eV, thus incorporation of CO to the oligomer cannot be discarded.

In general, the C-C coupling barrier is higher for C3 than for C2. This explains, at least partially why lower oligomer selectivities are found for propyne. In the C3 case different possibilities for the coupling exist: head-to-head, head-to-tail, and tail-to-tail. We have considered the second option since it is statistically more likely. C-C formation on the clean surface displays a barrier of 1.67 eV. As in the case of ethyne, this barrier is larger in the presence of C (1.88 eV) but slightly reduced in the hydride case (1.52 eV). CO lowers the C-C coupling barrier to 1.50 eV but as in the case of C2.

In summary, CO significantly reduces the size of the ensembles in such a way that independent alkyne adsorption sites can be considered. While the direct CO effect in the alkyne-alkyne coupling is to lower the reaction barrier a second contribution, coming from the close-packed nature of the CO overlayer is more effective reducing the amount of alkyne coupling by alkyne isolation. However, a second source of oligomer production, the coupling of alkynes (or their derivatives) to CO, increases under CO-rich conditions.

## 4.4. Interplay of phases in selective hydrogenation

In this section we will comparatively discuss the experimental and modeling results. As summarized in Section 4.1, catalytic tests were performed on the as-received catalyst, *i.e.* non-pretreated, and after pretreatment in alkyne, hydrogen, and the reaction mixture. Then, ethyne and propyne hydrogenation were studied in the absence or presence of CO (Figures 2-5). We have determined the equilibrium state of the surface under the different conditions employed in the experiments. In order to do so, the combination of the binding energies of H, C, and CO to the surface (Section 4.2) and the pressures of the corresponding gases: $H_2$, $C_2H_2$ (or $C_2H_4$, $C_3H_4$, $C_3H_6$), and CO, are needed as an input to obtain the hydrogen volume uptake ($V/V_m$) described in Section 3 (equations 1-3). The data required for the equations is summarized in Table S2 in the Supporting Information. Two different equilibrium diagrams representing the hydrogen uptake $V/V_m$ as a function of $H_2$, $C_2H_2$ and CO pressures have been constructed to understand the formation of subsurface hydrogen species ($V/V_m > 1$), which is the main responsible for over-hydrogenation. Results are presented in Figure 10.

A first scenario consists on pretreatments that only involve the alkyne and hydrogen, the calculations can then be compared to experiments on the non-pretreated sample and the pretreatments with alkyne, hydrogen and reaction mixture. In these cases, only ethyne (propyne) and hydrogen compete for the formation of carbide and hydride structures. In Figure 10, $V/V_m>1$, indicate that the subsurface hydride is being formed and the areas corresponding to the experiments in Section 4.1 are indicated by a red line. Therefore we can assign the experiments to H-rich or H-lean regions. Under alkyne pretreatment, carbides can be formed. This implies that full hydrogen coverage is possible but carbides block the formation of subsurface hydrogen species, see Figure 10a. As pointed out in Section 4.2, the formation of the carbide is strongly dominated by kinetic aspects of hydrocarbon dissociation. Due to the kinetic control, only experiments in which the pretreatment was performed with alkyne would be prone to generate the carbide layer. Since carbides are formed in the regions close to the steps, mainly these defects and their surroundings (at least 5 Å around the defect) would be H-lean. In regions where carbides cannot be formed (either far away from steps or when lower chemical potential substrates are employed, *i.e.* propyne and other C3+, see Supplementary Figure S6) unselective-subsurface hydride species can appear. On the contrary, under hydrogen pretreatment, the hydride would be generated and carbide formation would be hindered by the presence of H in subsurface sites. According to the phase descriptions and the kinetic studies in Section 4.3, the carbide layer formed in ethyne is more selective towards the alkene than any of the other phases (see Figure 5). Over-hydrogenation leads to the alkane as the major product in three cases: hydrogen pretreatment, non-pretreatment and reaction mixture pretreatment (cases 1,3 and 4 in Figure 5).

Since the carbide is only effectively formed to a large extent in ethyne pure conditions, in Figure 10b we illustrate the interplay between $H_2$ and CO to understand the effect in the formation of subsurface hydrogen. In this case, the control variables are the partial pressures of $H_2$ and CO. Under extremely low CO coverages, $V/V_m$ is larger than 1 indicating the formation of the hydride. But if CO is increased the equilibrium structure shows a total amount of hydrogen that is not enough to form a complete a full H monolayer on the surface and no subsurface hydrogen can be formed. From the experiments, CO enhances alkene production due to the quenching of H on the subsurface region, the reduction of the total amount of hydrogen present on the surface catalyst, the thermodynamic control of the alkyne-alkene pair (see Table 1) and the isolation of the reacting molecules that can not couple to generate oligomers. However, CO could be incorporated to the oligomeric compounds and thus continuous replacement is needed.

A summary of the different scenarios that can occur under different reaction conditions is shown in Figure 11. Initially more or less clean palladium surfaces are present Figure 11a, carbon impurities coming from hydrocarbon dissociation can appear in the regions near defective areas, Figure 11b depleting H coverages from these areas. However, carbide formation depends strongly on the feed hydrogen:alkyne ratio and shows kinetic barriers of formation. Thus, it seems unlikely that large particles could form a uniform selective carbide layer and from an industrial point of view the catalysts is not robust enough since selectivity will depend on the very narrow $H_2$:alkyne window observed in Figure 1. In fact, hydrides are so labile there is a spatio-temporal dependence of the carbide-hydride palladium phases during the hydrogenation reaction, Figure 11b and 11c. A clear example on the dependence of the history of the samples can be found in the experiments in Figures 1 and 5. Under the same $H_2$:alkyne conditions two different ethene selectivities are found, *ca.* 18% in Figure 1 and *ca.* 5% in Figure 5. Indeed while the catalyst in Figure 5 was fresh the corresponding for Figure 1 was already on stream with a $H_2$:alkyne ratio of 1 for two hours. In addition, the dynamics of the hydride phase respond to different external conditions providing very different outlet products with small $H_2$:alkyne ratio variations. It is even likely that due to this flexibility different regions of the catalyst are responsible for the generation of different products. If this is the case, the extension of the hydride will control over-hydrogenation products, while alkene products would be derived from the carbide region. The situation is even worst in the case of front-end hydrogenation where $H_2$:alkyne goes from 10-25 but it can be as large as 100, there the control via the formation of carbides is way too weak to be employed under such extreme conditions. Industrially in order to have a control on the selectivity in front-end hydrogenation, the CO concentration is varied between 0.15 and 0.5 vol.%. According to our models it forms a uniform, homogeneous control layer that displaces both the hydride and the carbide resulting in a robust way of controlling the surface and near-surface Pd catalyst, Figure 11d. This opens a wide operation window, where the relative $H_2$:alkyne ratio at which the catalyst might be active and selective is enlarged by several orders of magnitude, see Figures 2-4. Thus CO resets the system by setting up a completely new scenario, which is robust in the sense that it shows a weak dependence on the feed alkyne:$H_2$ ratio and on the temperature.

## 5. CONCLUSIONS

We have studied the selective hydrogenation of alkynes (ethyne and propyne) on differently pretreated catalysts with and without the presence of CO as a selectivity enhancer. We have identified the very narrow $H_2$:alkyne window that controls the selective production of the desired alkene products ($H_2$:alkyne = 1-1.7), in the absence of CO. Under this H-poor regime oligomers are the major competitive route that diminishes the overall alkene yield. Pretreatment under ethyne-only conditions can improve alkene selectivity however, under other possible pretreatments the effect disappears.

Calculations suggest that carbides are likely formed from the steps and diffuse towards the center of the Pd particles. Thus the formation of this phase is kinetically controlled by the barrier at the step and the number of empty sites. In addition, near-surface positions are the energetically more favored for these impurities and both penetration to the bulk of the particle and formation of dense carbide structures are energetically unfavorable. At higher $H_2$:alkyne ratio (front-end conditions) the formation of PdH occurs, switching the reaction selectivity towards the production of alkanes. The hydride is easily formed and reversible since charging of the deep layers depends on the full occupation of the surface layer, and both $H_2$ dissociation and penetration are rather easy. The high unselective character of the hydride phase is clearly supported in the calculations by the high activity found for nascent H atoms emerging from subsurface positions. The addition of CO shows remarkable effects even at very low concentrations at high $H_2$:alkyne ratios. CO forms a dense blanket that covers the surface, improves the thermodynamic factor, reduces the amount of available H on the surface and the formation of subsurface H species, and shrinks the size of active ensembles. If carbides are present they are moved away from the near-surface region. In a way, CO presence overwrites the previous state of the system leading to a stable, non-dynamic and robust way to control the selectivity in Pd-containing systems.

ACKNOWLEDGMENT. This work was funded by the MICINN (CTQ2006-01562/PPQ, CTQ2006-00464/BQU, CTQ2009-07553/BQU, CTQ2009-09824/PPQ, and Consolider-Ingenio 2010 Grant CSD2006-0003), Catalan Government (2009-SGR-461, 2009-SGR-259) and the ICIQ Foundation. BSC-RES is acknowledged for providing generous computational resources. We would like to thank Prof. Jens K. Nørskov for stimulating discussions.

**Supporting Information Available**. The Supporting Information contains the reaction energies and barriers for all the hydrogenation steps considered in Scheme 1 on the clean, C, CO and hydride models together with the mathematical derivation of the hydride formation equations, the effect of different alkyne or alkene sources in carbide formation, the reaction path for oligomerization and the data employed to obtain Figure 10.

# REFERENCES

[1] G.A. Somorjai, Y. G. Borodko, Catal. Lett. 76 (2001) 1.

[2] D. Teschner, J. Borsodi, A. Wootsch, Z. Révay, M. Hävecker, A. Knop-Gericke, S.D. Jackson, R. Schlögl, Science, 320 (2008) 86.

[3] F. Studt, F. Abild-Pedersen, T. Bligaard, R.Z. Sorensen, C.H. Christensen, J.K. Nørskov, Science 320 (2008) 1320.

[4] A. Molnár, A. Sárkány, M. Varga, J. Mol. Catal. A: Chem. 173 (2001) 185, and references therein.

[5] G.C. Bond, Metal-Catalysed Reactions of Hydrocarbons, Springer, New York, 2005, p. 395.

[6] D. Teschner, Z. Revay, J. Borsodi, M. Hävecker, A. Knop-Gericke, R. Schlögl, D. Milroy, S. D. Jackson, D. Torres, P. Sautet, Angew. Chem. Int. Ed. 47 (2008) 9274.

[7] N.N. Greenwood, A. Earnshaw, Chemistry of the elements, 2nd Edition, Elsevier 2008, p. 1150; and references therein.

[8] A. Borodziński, G.C. Bond, Catal. Rev. -Sci. Eng. 48, (2006) 91.

[9] A.D. Johnson, S.P. Daley, A.L. Utz, S.T. Ceyer, Science, 257 (1992) 223.

[10] H. Molero, B.F. Bartlett, W.T.;Tysoe, J. Catal. 181, (1999) 49.

[11] K. Kovnir, J. Osswald, M. Armbrüster, D. Teschner, G. Weinberg, U. Wild, A. Knop-Gericke, T. Ressler, Y.Grin, R. Schlögl, J. Catal. 264, (2009) 93.

[12] W. Buchele, H. Roos, H. Wanjek, H.J. Muller, Catal. Today 30 (1996) 33.

[13] P.A. Sheth, M. Neurock, C.M. Smith, J. Phys. Chem. B 107 (2003) 2009.

[14] D.H. Mei, P.A.;Sheth, M. Neurock, C.M. Smith, J. Catal. 242 (2006) 1.

[15] F. Studt, F. Abild-Pedersen, T. Bligaard, R.Z. Sørensen, C.H. Christensen, J.K. Nørskov, Angew. Chem. Int. Ed. 47 (2008) 9299.

[16] Y. Segura, N. López, J. Pérez-Ramírez, J. Catal. 247 (2007) 383.

[17] B. Bridier, N. López, J. Pérez-Ramírez, J. Catal. 269 (2010) 80.

[18] D.H. Mei, M. Neurock, C.M. Smith, J. Catal. 268 (2009) 181.

[19] N. López, B. Bridier, J. Pérez-Ramírez, J. Phys. Chem. C 112 (2008) 9346.

[20] G. Kresse, J. Hafner, Phys. Rev. B 47 (1993) 558.

[21] R.W.G. Wyckoff, Crystal Structures, Interscience, New York, 1965.

[22] A. Borodziński, G.C. Bond, Catal. Rev. -Sci. Eng. 50 (2008) 379.

[23] H.J. Monkhorst, J.D. Pack, Phys. Rev. B 13, (1976) 5188.

[24] J.P. Perdew, J.A. Chevary, S.H. Vosko, K.A. Jackson, M.R. Pederson, D.J. Singh, C. Fiolhais, Phys. Rev. B 46 (1992) 6671.

[25] P.E. Blöchl, Phys. Rev. B 50 (1994) 17953.

[26] G. Henkelman, B.P. Uberuaga, H. Jonsson, J. Chem. Phys. 113 (2000) 9901.

[27] J. Greeley, W.P. Krekelberg, M. Mavrikakis, Angew. Chem. Int. Ed. 43 (2004) 4296.

[28] S. Brunauer, P.H. Emmett, E. Teller, J. Am. Chem. Soc. 60 (1938) 309.

[29] X.G. Wang, A. Chaka, M. Scheffler, Phys. Rev. Lett. 84 (2000) 3650.

[30] T. Mitsui, M.K. Rose, E. Fomin, D.F. Ogletree, M. Salmeron, Nature 422 (2003) 705.

[31] N. Lopez, Z. Łodziana, F. Illas, M. Salmeron, Phys. Rev. Lett. 93 (2004) 146103.

[32] M.K. Rose, A. Borg, T. Mitsui, D.F. Ogletree, M. Salmeron, J. Chem. Phys. 115 (2001) 10927.

[33] L. Gracia, M. Calatayud, J. Andres, C. Minot, M. Salmeron, Phys. Rev. B 71 (2005) 033407.

[34] J. Andersin, N. Lopez, K. Honkala, J. Phys. Chem. C 113 (2009) 8278.

[35] M. Ruta, N. Semagina, L. Kiwi-Minsker, J. Phys. Chem. C 112 (2008) 13635.

[36] D. Loffreda, D. Simon, P. Sautet, Surf. Sci. 425 (1999) 68.

[37] K. Honkala, P. Pirila, K. Laasonen, Surf. Sci. 489 (2001) 72.

[38] M.K. Rose, T. Mitsui, J. Dunphy, A. Brog, D.F. Ogletree, M. Salmeron, P. Sautet, Surf. Sci. 512 (2002) 48.

[39] J. Horiuti, M. Polanyi, Trans. Faraday Soc. 30 (1934) 1164.

## FIGURE CAPTIONS

**Figure 1.** Conversion (*X*) of ethyne (propyne) and selectivity (*S*) to the alkene, alkane, and oligomers over $Pd/Al_2O_3$ as a function of the $H_2$:alkyne ratio. Ethyne (propyne) and the derived products are represented by open (solid) symbols. Conditions: $T = 348$ K, $SV = 16{,}800$ $cm^3$ $g^{-1}$ $h^{-1}$, and $P = 1$ bar.

**Figure 2.** Conversion (*X*) of ethyne and propyne and selectivity (*S*) to the alkene, alkane, and oligomers over $Pd/Al_2O_3$ as a function of the $CO:H_2$ ratio. Ethyne (propyne) and the derived products are represented by open (solid) symbols. Conditions: $H_2$:alkyne = 5, $T = 348$ K, $SV = 16{,}800$ $cm^3$ $g^{-1}$ $h^{-1}$, and $P = 1$ bar.

**Figure 3.** Dependence of the yield of alkene and oligomers on the $CO:H_2$ ratio. The yield was determined as the product of alkyne conversion and product selectivity given in **Figure 2**. (◇,△) represent the C2 values and (◆,▲) the C3 ones.

**Figure 4.** Selectivity to propene (◆,◇), propane (●,○), and oligomers (▲,△) as a function of the $H_2$:propyne ratio over $Pd/Al_2O_3$ in the absence (solid symbol) or presence of CO (open symbol). Conditions: 2.5 vol.% propyne, 2.5-25 vol.% $H_2$, and 0 or 0.1 vol.% CO, balance He, $T = 348$ K, $SV = 16{,}800$ $cm^3$ $g^{-1}$ $h^{-1}$, and $P = 1$ bar.

**Figure 5.** Influence of the pretreatment of $Pd/Al_2O_3$ on the hydrogenation of ethyne (a) and propyne (b) in the absence or presence of CO. Symbols: (□,■) alkyne conversion, (◇,◆) alkene selectivity, (○,●) alkane selectivity, and (△,▲) selectivity to oligomers. Pretreatments: (1) no pretreatment, (2) alkyne, (3) $H_2$, and (4) alkyne+$H_2$. Ethyne (propyne) and the derived products are represented by open (solid) symbols. Conditions: $H_2$:alkyne = 1.5, $CO:H_2$ = 0 or 0.03, $T = 348$ K, $SV = 16{,}800$ $cm^3$ $g^{-1}$ $h^{-1}$, and $P = 1$ bar.

**Figure 6.** Adsorption energy of hydrogen, $E_{ads}$ in eV, with respect to gas-phase hydrogen to a palladium carbide model system covered by a H monolayer as a function of the distance between the incoming H and C. Position 1 stands for the surface(▲), position 2 for the subsurface, (■) and position 3 for the subsubsurface (●). The horizontal line indicates the average adsorption energy for subsurface H in clean Pd.

**Figure 7.** Reaction network for hydrogenation of ethyne (left) and propyne (right).

**Figure 8.** Schematic representation of the hydrogenation of vinyl on the palladium hydride phases. Left: transition state from a surface H atom to the formation of ethene. Right: transition state for the formation of ethylidene with a subsurface H atom. Blue spheres represent Pd atoms, yellow surface H atoms, green subsurface H atoms, and grey C atoms.

**Figure 9.** Brønsted-Evans-Polanyi relationship for the dehydrogenation of C2 and C3 compounds on the clean, carbide, hydride, and CO-covered Pd models. Ethyne (propyne) and the derived products are represented by open (solid) symbols. The regression equation is: $E_a$=0.78ΔE+0.71 r=0.90.

**Figure 10.** Hydrogen uptake, *V/V$_m$*, of Pd as a function of the relative alkyne-hydrogen-CO pressures at 350 K. (a) palladium in ethyne-hydrogen mixtures and (b) palladium in CO-$H_2$ ones. The lower panels schematically represent the clean surface $\theta_0$; carbide C or CO coverages, $\theta_C$ and $\theta_{CO}$; and multilayer H adsorption, $\theta_i$. Blue spheres represent Pd, yellow H, black C and red O. Darker blue denotes Pd atoms in contact with carbon impurities.

**Figure 11.** Schematic representation of the different possible structures under different reaction feeds: (a) clean particle, (b) carbide formation, (c) hydride formation, (d) CO-containing feeds. Same color code as in **Figure 10**.

**Table 1.** Adsorption energies, $E_{ads}$ in eV, and differential binding energy, $\Delta E_{ads}$ in eV, $\Delta E_{ads} = E_{ads}$(alkyne)- $E_{ads}$(alkene) for C2 and C3 alkynes and alkenes.

| | **Clean** | **Carbide** | **Hydride** | **CO-covered** |
|---|---|---|---|---|
| $\boldsymbol{E_{ads}}$**($C_2H_2$)** | -2.02 | -1.49 | -0.94 | -1.24 |
| $\boldsymbol{E_{ads}}$**($C_2H_4$)** | -0.82 | -0.67 | -0.15 | 0.00 |
| $\boldsymbol{\Delta E_{ads}}$**(C2)** | -1.20 | -0.82 | -0.79 | -1.24 |
| $\boldsymbol{E_{ads}}$**($C_3H_4$)** | -1.57 | -1.19 | -0.59 | -0.68 |
| $\boldsymbol{E_{ads}}$**($C_3H_6$)** | -0.60 | -0.43 | -0.01 | 0.69 |
| $\boldsymbol{\Delta E_{ads}}$**(C3)** | -0.97 | -0.76 | -0.58 | -1.37 |

**Figure**

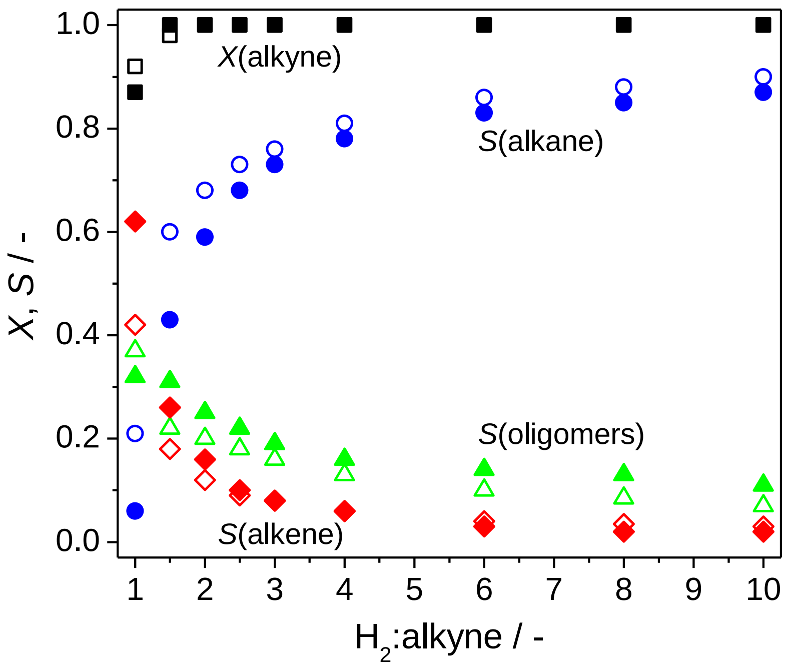
X(alkyne)
S(alkane)
S(oligomers)
S(alkene)
X, S / -
H$_2$:alkyne / -
1.0
0.8
0.6
0.4
0.2
0.0
1
2
3
4
5
6
7
8
9
10

**Fig. 1**

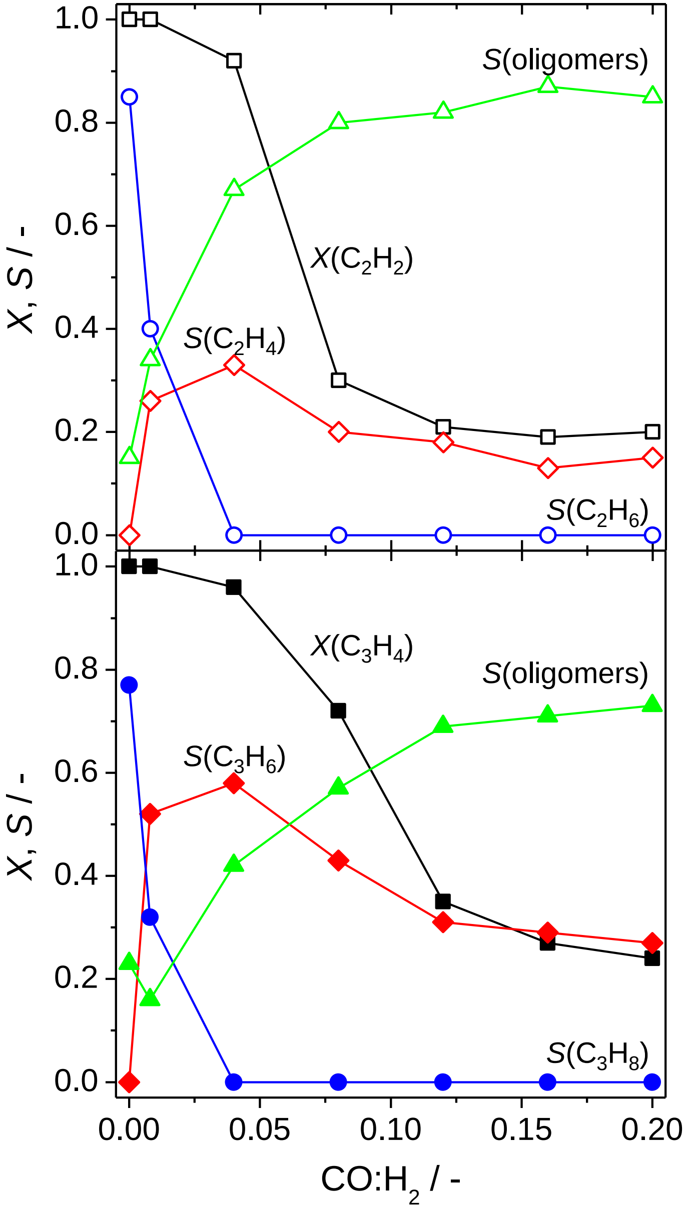
1.0
0.8
0.6
0.4
0.2
0.0
X, S / -
S(oligomers)
X(C$_2$H$_2$)
S(C$_2$H$_4$)
S(C$_2$H$_6$)
X(C$_3$H$_4$)
S(oligomers)
S(C$_3$H$_6$)
S(C$_3$H$_8$)
0.00
0.05
0.10
0.15
0.20
CO:H$_2$ / -

**Fig. 2**

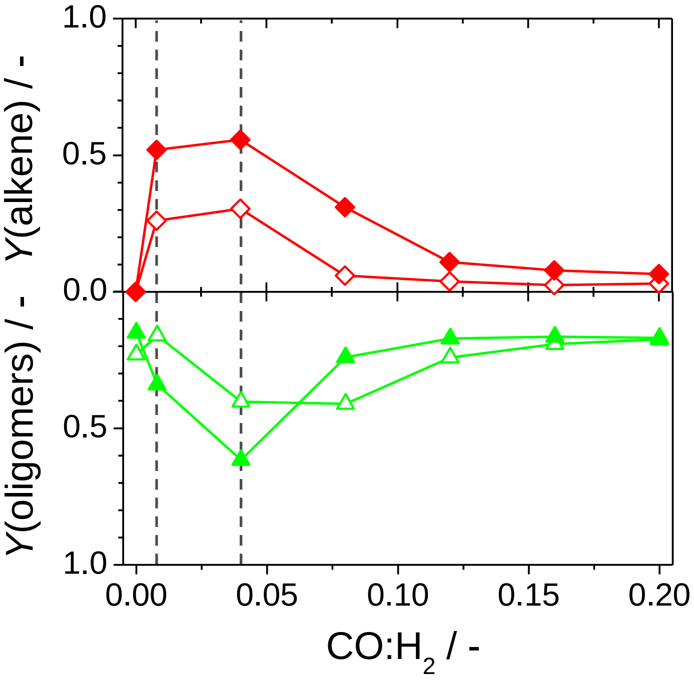

**Fig. 3**

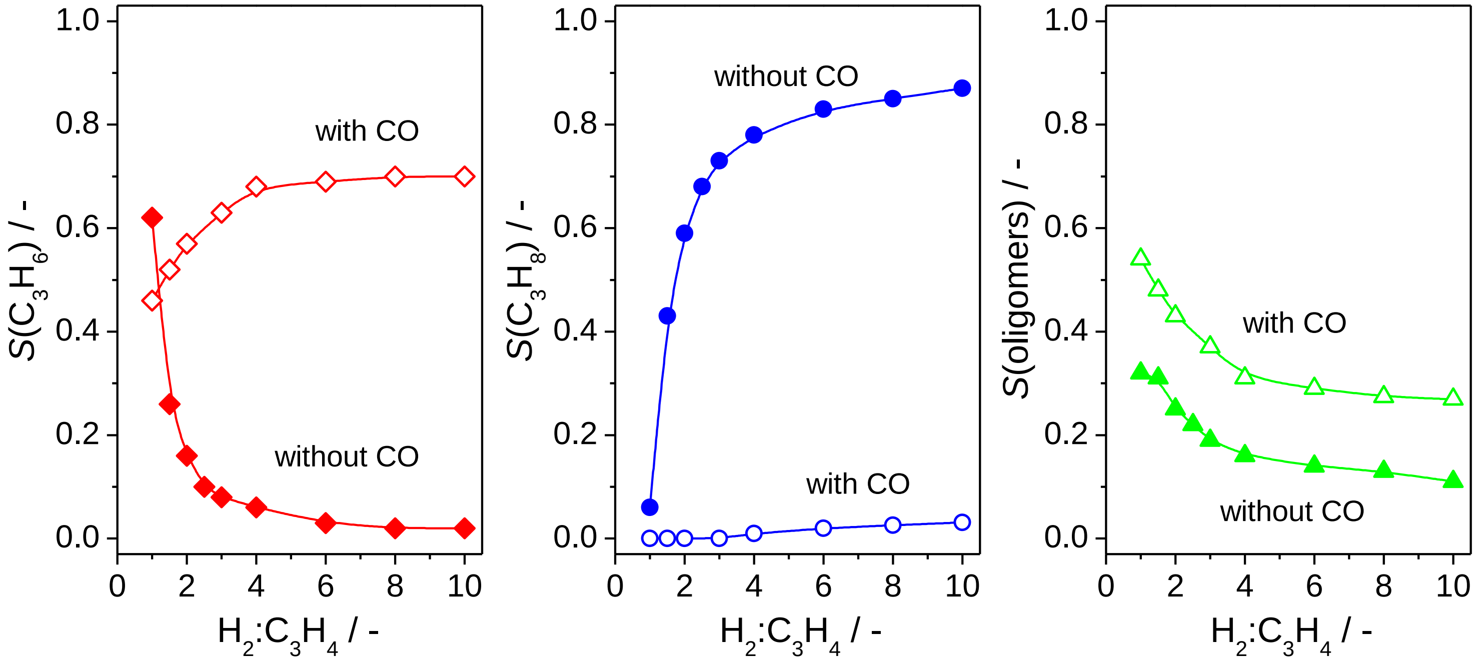
S(C3H6) / -
with CO
without CO
H2:C3H4 / -
S(C3H8) / -
without CO
with CO
H2:C3H4 / -
S(oligomers) / -
with CO
without CO
H2:C3H4 / -
0.0
0.2
0.4
0.6
0.8
1.0
0
2
4
6
8
10

**Fig. 4**

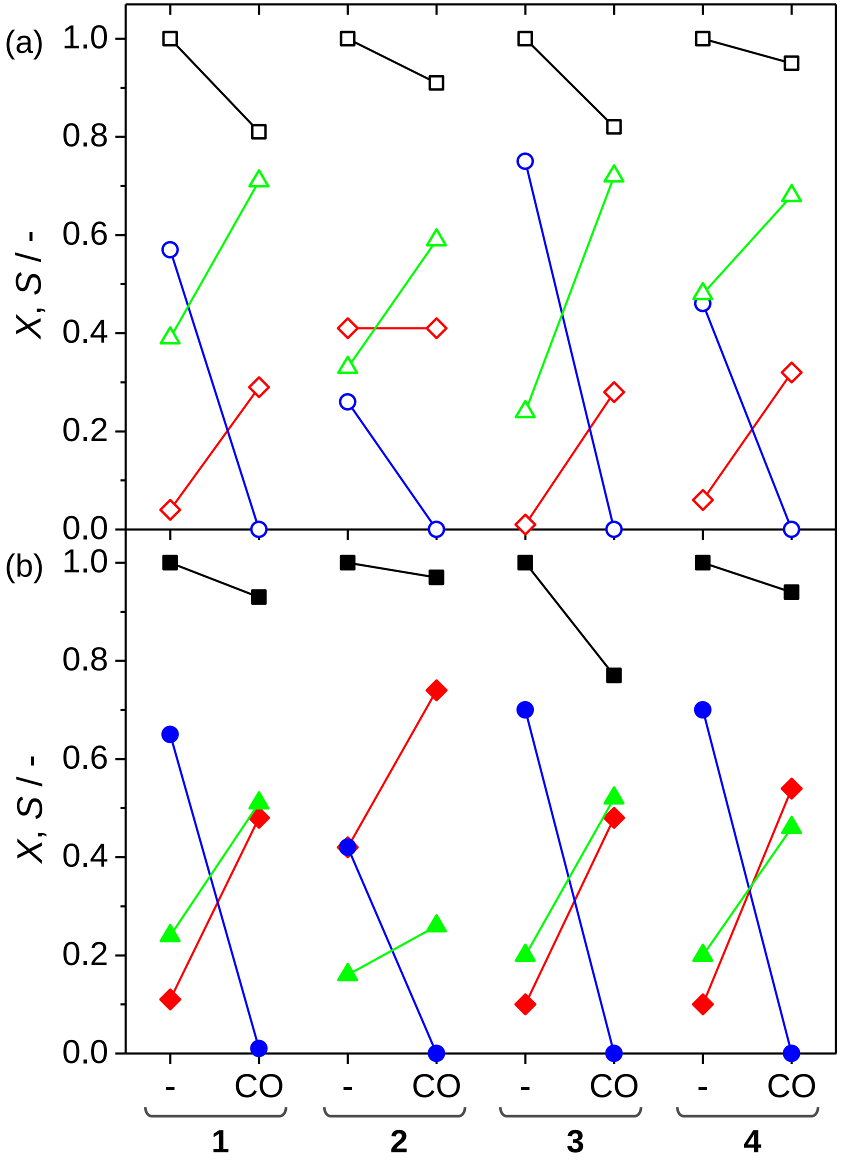

Fig. 5

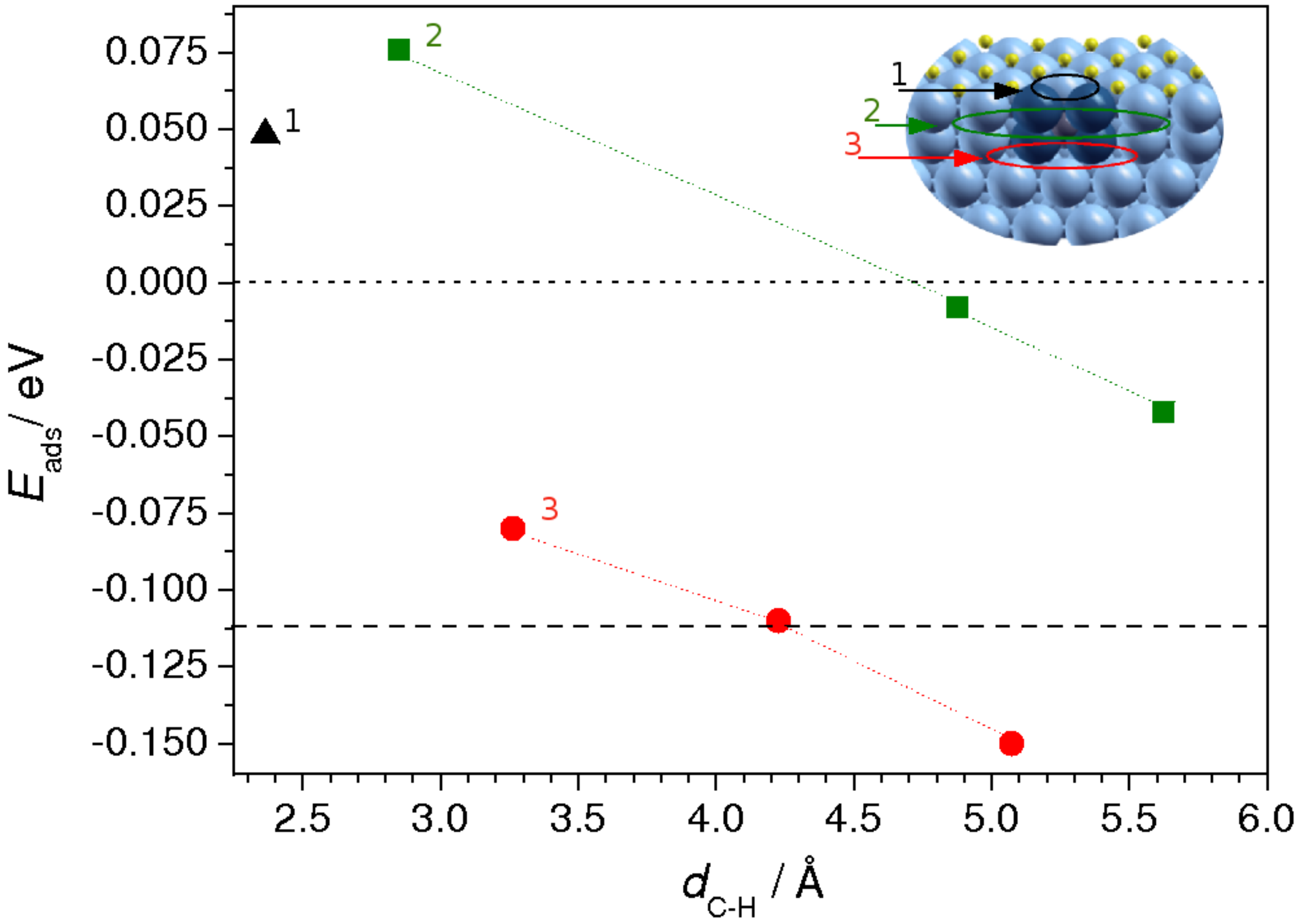
0.075
0.050
0.025
0.000
-0.025
-0.050
-0.075
-0.100
-0.125
-0.150
$E_{ads}$ / eV
2.5
3.0
3.5
4.0
4.5
5.0
5.5
6.0
$d_{C-H}$ / Å
1
2
3
1
2
3

**Fig. 6**

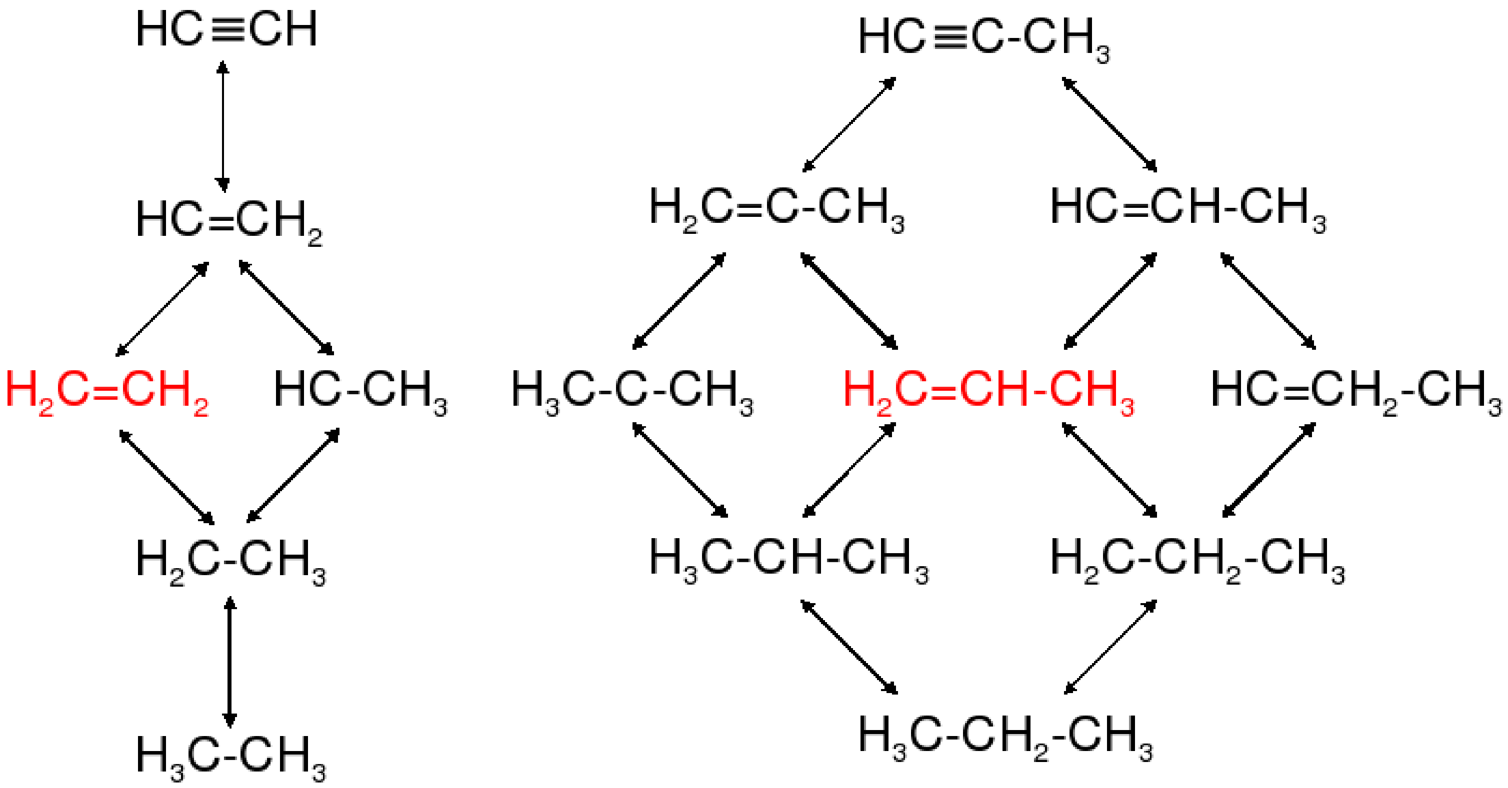
$HC\equiv CH$
$HC=CH_2$
$H_2C=CH_2$
$HC-CH_3$
$H_2C-CH_3$
$H_3C-CH_3$
$HC\equiv C-CH_3$
$H_2C=C-CH_3$
$HC=CH-CH_3$
$H_3C-C-CH_3$
$H_2C=CH-CH_3$
$HC=CH_2-CH_3$
$H_3C-CH-CH_3$
$H_2C-CH_2-CH_3$
$H_3C-CH_2-CH_3$

**Fig. 7**

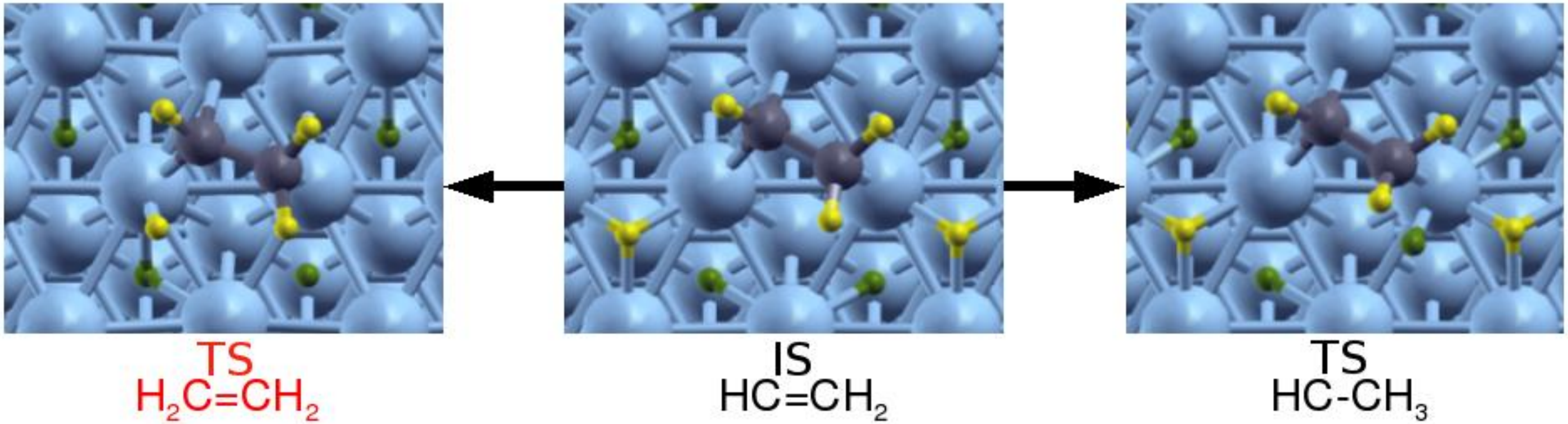

**Fig. 8**

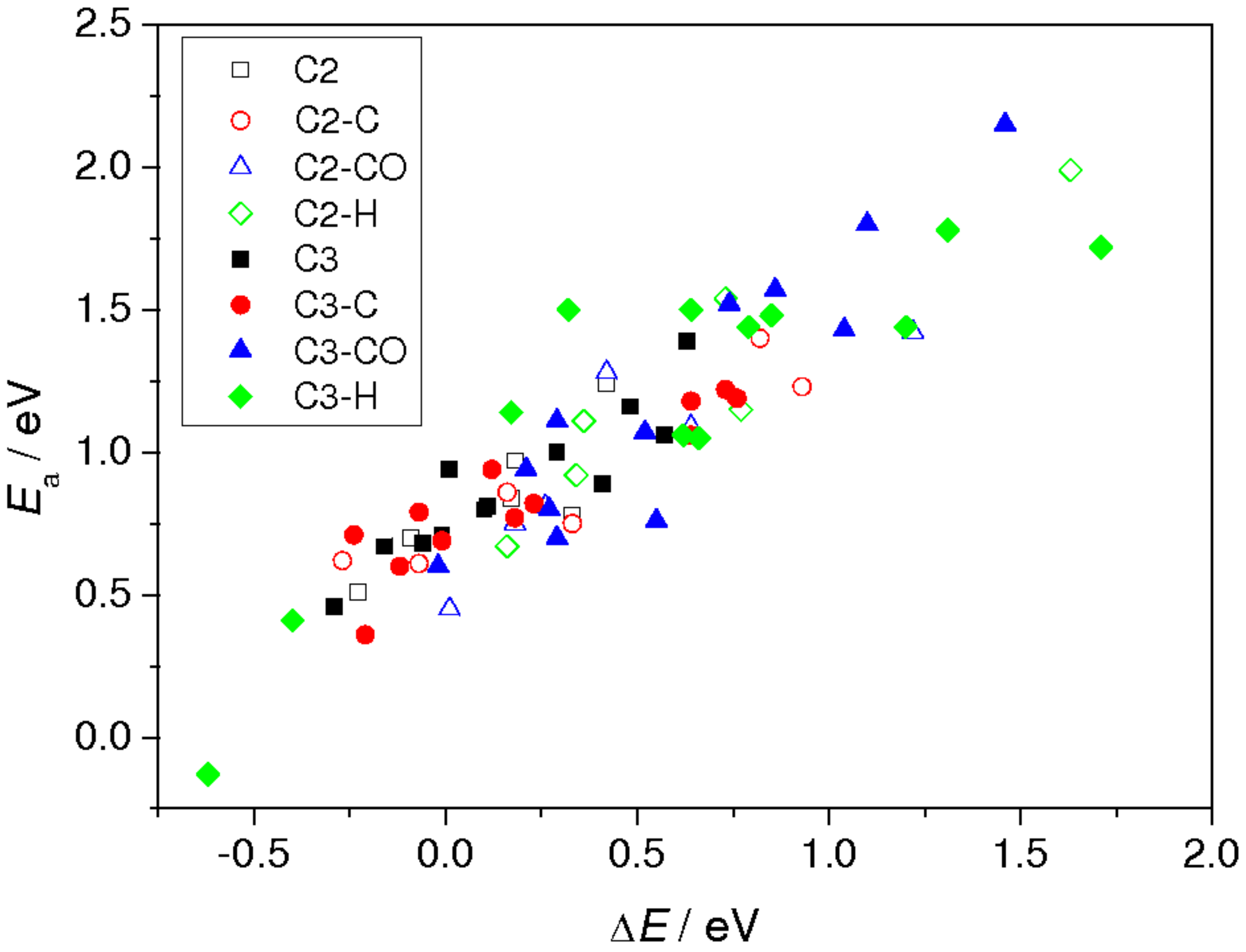
C2
C2-C
C2-CO
C2-H
C3
C3-C
C3-CO
C3-H
$E_a$ / eV
2.5
2.0
1.5
1.0
0.5
0.0
-0.5
0.0
0.5
1.0
1.5
2.0
$\Delta E$ / eV

**Fig. 9**

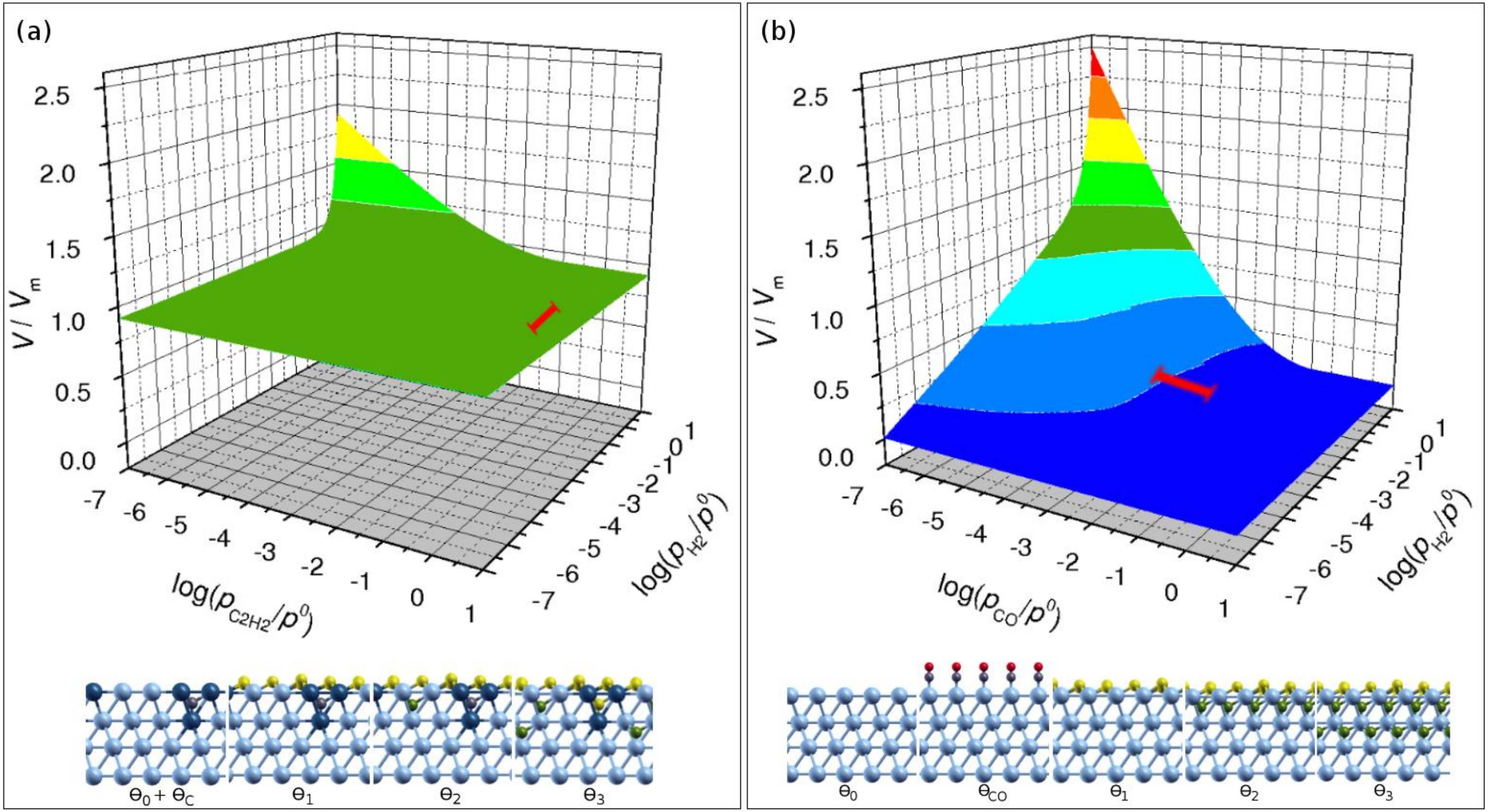
(a)
2.5
2.0
1.5
1.0
0.5
0.0
V / V_m
-7
-6
-5
-4
-3
-2
-1
0
1
log(p_C2H2/p^0)
log(p_H2/p^0)
Θ_0 + Θ_C
Θ_1
Θ_2
Θ_3
(b)
log(p_CO/p^0)
Θ_0
Θ_CO
Θ_1
Θ_2
Θ_3

**Fig. 10**

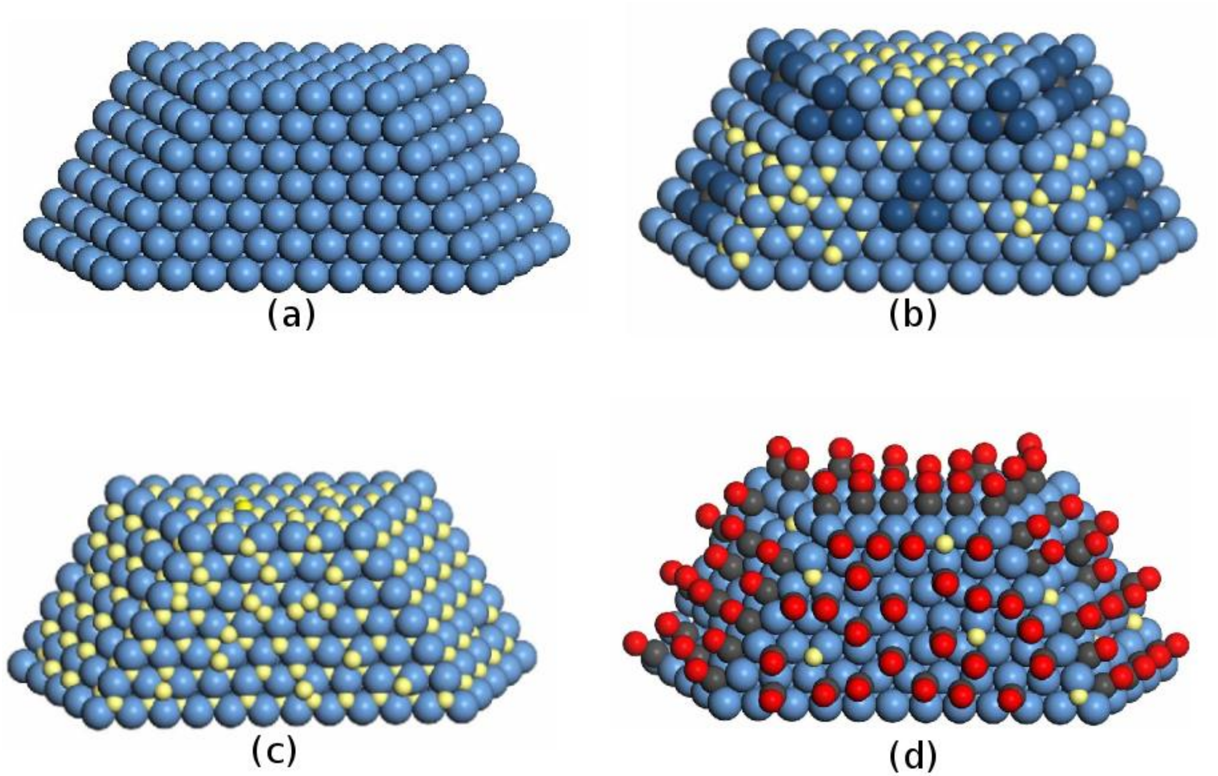

Fig. 11

11758 *J. Phys. Chem. A* **2009,** *113,* 11758–11762

# Vinyl Acetate Synthesis on Homogeneous and Heterogeneous Pd-Based Catalysts: A Theoretical Analysis on the Reaction Mechanisms[#]

**José J. Plata,[†] Mónica García-Mota,[†] Atualpa A. C. Braga,[†] Núria López,*[,†] and Feliu Maseras*[,†,‡]**

*Institute of Chemical Research of Catalonia (ICIQ), Avgda. Països Catalans, 16,
43007 Tarragona, Catalonia, Spain, and Departament de Química, Universitat Autònoma de Barcelona,
08193 Bellaterra, Catalonia, Spain*

*Received: March 31, 2009; Revised Manuscript Received: August 17, 2009*

Vinyl acetate can be synthetized by both homogeneous and heterogeneous processes involving Pd atoms as reaction centers. We have determined the reaction mechanisms by means of density functional theory applied to molecular models for the homogeneous catalyst and to slabs that model the most active heterogeneous ensemble to unravel the similarities and differences in the reaction networks under these different conditions. We find that although the reaction network is similar, the rate determining step is different. Thus, direct extrapolations from organometallic chemistry to gas-phase heterogeneous catalysis should be handled with care.

## Introduction

Vinyl acetate, VA, is an important monomer involved in the production of polymers employed as paints, adhesives, coatings, and fibers.[2] VA is synthetized from ethylene and acetic acid, and although initially the synthetic process was based on homogeneous palladium-catalysts,[3] now it has almost been completely substituted by Pd-based heterogeneous process.[4−7] The preference for the heterogeneous process is based on the better performance against corrosion and poisoning by chlorides and water. Both the homogeneous and the heterogeneous routes are reproduced in Figure 1, where the benzoquinone/hydroquinone (BQ/HQ) pair is used as external oxidant for the homogeneous reaction.

The homogeneous process was described by Moiseev around 1960,[3,8,9] and it belongs to the family of oxidative acyloxylation reactions.[10] Acyloxylations can be carried out in acetic acid at moderate temperatures (50−60 °C).[11] The mechanism shows the following steps.[12,13] First, the alkene coordinates to the Pd(II) catalyst. In the following step, the C−O bond is formed by nucleophilic addition of the acetate to the alkene. The next step is the C−H cleavage that results in formation of the C−C double bond. Finally, regeneration of the catalyst by a redox system takes place. The first description of the mechanism was developed by van Helden et al., who assumed that the elimination of the $\beta$-hydrogen atom was the rate limiting step.[14]

The industrial heterogeneous catalysts are based on silica suported Pd−Au alloys with excess of alkali acetate. The reaction takes place at 130−200 °C and 5−10 atm and the yield is 96% or higher of VA in terms of ethylene conversion.[4] Oxygen is employed in the reaction to drive acetic acid dehydrogenation, and it is released as water molecules. In the reaction mechanism oxygen is dissociated on the surface, then one of the oxygen atoms drives the dehydrogenation of acetate. Ethylene can be adsorbed in a neighboring Pd center and then the C−O coupling takes place, finally an oxygen atom or a hydroxyl group can provoke the $\beta$-hydrogen elimination leading to the product. Detailed experimental studies exist on the ensemble effects found for VA synthesis over Pd−Au alloys.[15−19]

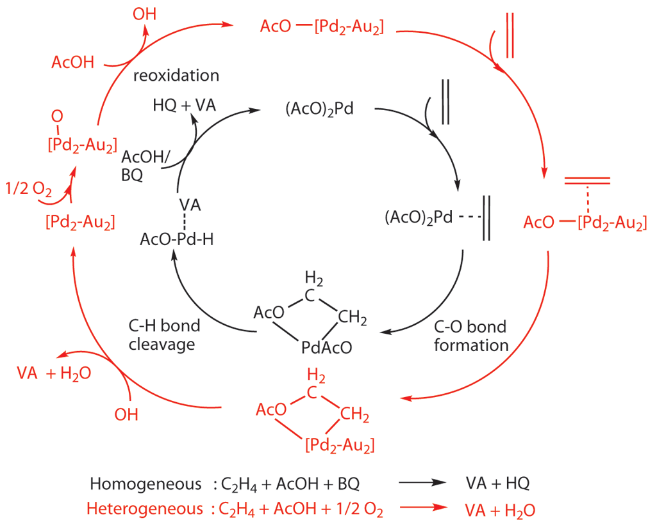

**Figure 1.** Reaction scheme for the synthesis of vinyl acetate from ethylene and acetic acid on Pd-based catalyst.

Since the same metal is employed in both homogeneous and heterogeneous versions of the catalyst, there is an interest to analyze the similarities and differences on the reaction mechanisms on both cases. Both homogeneous[20,21] and heterogeneous[22] catalysis have been intensely and successfully studied from a computational point of view, but seldom in direct comparison. In fact, the understanding of the link between homogeneous and heterogeneous catalysis constitutes a challenge in the development of new catalysts.[23,24] The present work follows our analysis for the selective activation of alkynes on gold catalysts.[25]

To this end, we have employed theoretical tools based on density functional theory (DFT). We considered for both systems the simple model reaction between ethylene and acetic acid.

---

[#] Part of the "Walter Thiel Festschrift".

* To whom correspondence should be addressed. E-mail: (N.L.) nlopez@iciq.es; (F.M.) fmaseras@iciq.es.

[†] Institute of Chemical Research of Catalonia (ICIQ).

[‡] Universitat Autònoma de Barcelona.

10.1021/jp902929x CCC: $40.75

For the homogeneous system, the catalyst employed was $[Pd(\kappa^2\text{-}O_2CCH_3)_2]$. It has been suggested that the catalyst may act in a dimeric or trimeric form, but previous studies have shown the reaction to take place in a single palladium center;[26] the monomer should thus be a good model. This previous work by Kragten et al.[26] is to our knowledge the only previous computational study on the homogeneous process. It did consider the dimeric form of the catalyst in some steps, but it did not compute the full catalytic cycle, and it applied a very simplified model system in the calculation of the transition state for the only step that was analyzed in detail. The monomeric palladium acetate model has been also applied in the theoretical study of other reactions.[27] The oxidant in our study was *p*-benzoquinone, one of many that have been found to be experimentally efficient.[11] It is transformed in hydroquinone after the reaction. As for the heterogeneous system, the PdAu alloys form a continuous solid solution; on high gold composition range, Pd atoms can be prepared to be in the surface as impurities. It has been shown experimentally that the open (100) surface with a particular Pd dimer configuration (at a distance of $\sqrt{2}d_{Pd-Pd}$) is the most active for the reaction.[15]

## Computational Methods

All calculations were performed at the DFT level. For the homogeneous reaction, we used the hybrid Becke3LYP[28-30] functional with a hybrid Becke exchange functional and a Lee-Yang-Parr correlation functional[28,29] as implemented in Gaussian03.[31] The Pd atom was described using an effective core potential for the inner electrons[32] and its associated double-$\zeta$ basis set for the outer ones. The 6-31G(d) basis set was used for the atoms H, C, and O.[33] Solvent effects were introduced in selected cases through PCM single-point calculations[34] on gas phase optimized geometries. Aniline was used as solvent due to its very similar dielectric constant compared to acetic acid ($\varepsilon_r = 6.89$ and 6.21, respectively). The structures of the reactants, intermediates, transition states, and products were fully optimized without any symmetry restriction. Transition states were identified by having one imaginary frequency in the Hessian matrix. The presented energies for the homogeneous processes correspond to potential energies corrected with zero-point energies and solvation effects. The relative gas phase potential energies with and without zero point energy corrections are collected in Table S1 (Supporting Information) and show no significant differences with the values discussed in the text. We decided against including entropic corrections because of the well-documented problems[35,36] for their accurate introduction for solvated systems through simple statistical thermodynamics based on gas phase calculations.

For the heterogeneous reaction, periodic density functional theory calculations have been performed with the VASP code.[37] A slab containing five layers represents the Au(100) surface with a p(4 × 4) reconstruction. Two of the surface Au atoms have been replaced by Pd reproducing the next-nearest neighbors local ensemble known to be the most active species.[15,25] The two outermost layers and the adsorbate degrees of freedom have been allowed to relax. The energies have been obtained within the RPBE[38] functional. Inner cores have been replaced by PAW[39,40] pseudopotentials while valence electrons have been expanded in plane waves with a cutoff energy of 400 eV. The Monkhorst-Pack scheme[41] with 2 × 2 × 1 k-points has been employed. Transition states have been located by the use of the climbing image version of the nudged elastic band algorithm[42] and in all cases a single imaginary frequency has been obtained for these structures.

The choice of the computational methods was based on the usual approaches currently applied in computational homogeneous and heterogeneous catalysis. The use of different descriptions can however hamper the comparison. In order to evaluate the effect of the use of the different computational set-ups, we carried out a systematic series of VASP RPBE single-point calculations on all the Gaussian03 B3LYP optimized structures for the homogeneous systems. A cubic box of 15 $Å^3$ was used in these periodic calculations. The results, collected in Table S2 (Supporting Information), show relative potential energy differences of 36 kJ/mol at most, and in no case modify the qualitative analysis of energetics discussed in the text.

## Complete Reaction Paths

The key features of the reaction mechanisms have been previously characterized computationally with some degree of detail for both the homogeneous[26] and heterogeneous counterpart.[43,44] However, to our knowledge, a comparison of the full catalytic cycles had not been previously reported. We carried out this calculation, and the overall profile for the reaction is presented in Figure 2 where both reaction mechanisms have been overlapped. We find both reaction mechanisms to have the three main steps that were expected, ethylene-acetate coupling (C-O formation), $\beta$-hydrogen elimination, and catalyst reoxidation. The nature of the rate-determining step is however different and the exothermicity of the reaction, due to the presence of the oxygen-water pair, is much larger for the heterogeneous process.

For the homogeneous system, the barriers for the three main steps are 74.9, 96.2, and 92.1 kJ/mol, respectively. The rate-determining step involves therefore the $\beta$-hydrogen transfer in agreement with previous experimental considerations.[14] For the heterogeneous counterpart the reaction shows a major reaction bottleneck (127.4 kJ/mol) associated to the formation of the C-O bond on the surface. Hydrogen activations are relatively easy both for acetic acid and the hydrogenated VA product. The main steps for the reaction are thus very similar, but the relative barriers are different. We will analyze in what follows in more detail each of the main three steps.

## Ethylene-Acetate Coupling

In the homogeneous reaction, the ethylene-acetate coupling consists in the formal insertion of the ethylene into one of the Pd-O bonds of $[Pd(\kappa^2\text{-}O_2CCH_3)_2]$, see Figure 3a. The $\kappa$ symbol indicates that the ligand only coordinates the metallic center by two of the three possible atoms, in this case the two O atoms. In the starting point of this step, the ethylene is coordinated $\eta^2$ to the metal, and one of the acetates is coordinated in a $\kappa^1_O$ mode with Pd-O distances of 2.202 and 2.772 Å; see hoI1. The presence of the ethylene distorts thus strongly the initial $\kappa^2$ coordination of one of the acetates in the catalyst, although this involves no insertion yet into the Pd-O bond. The insertion takes place at the transition state where a rotation takes place of both the acetate and ethylene fragments. The barrier to reach this structure is 74.9 kJ/mol, and the C-O distance is 2.163 Å. In the final state, the hydrogenated VA, VAH, is bound to the metal center by the terminal C and O atoms. The newly formed C-O distance is 1.471 and the metal-to-carbon and metal-to-oxygen distances are 2.013 and 2.085 Å, respectively. The step is mildly exothermic with the final state 6.7 kJ/mol below the initial state. This is not the rate determining step for the whole process, but the barrier of 74.9 kJ/mol is not neglectable, as had been considered in the previous computational study by

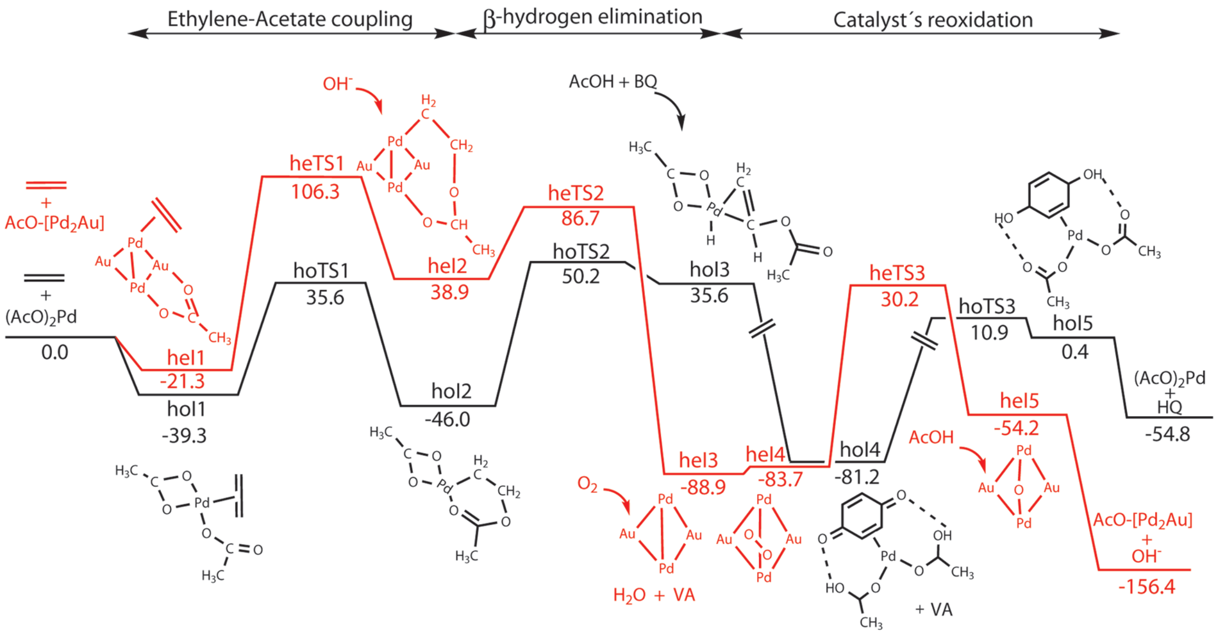

**Figure 2.** Energy profile for VA synthesis on the most active dimer of the PdAu(100) surface and with the homogeneous $Pd^{2+}$ complex. The energies are in kilojoules/mole. Origin of energies is in both cases the metal acetate complex plus ethylene.

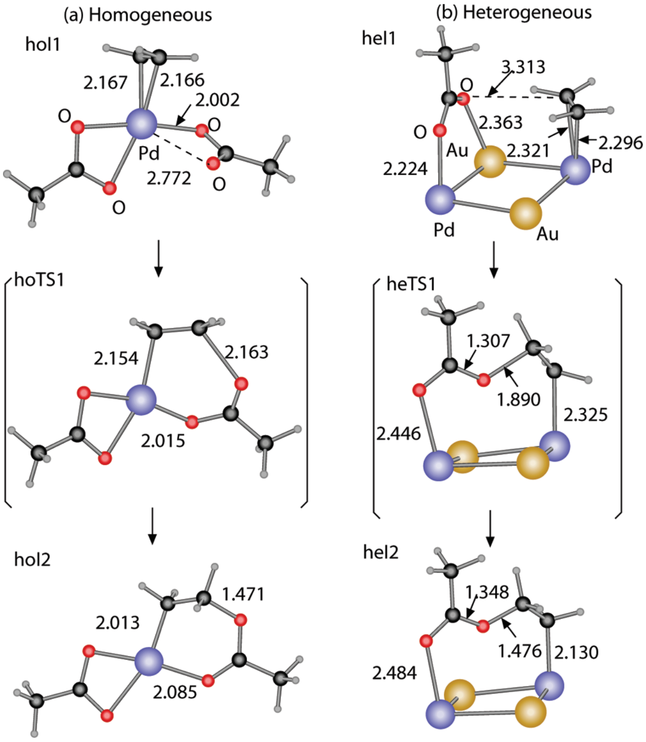

**Figure 3.** Initial, transition and final states for the formation of the C−O bond in (a) homogeneous catalyst; (b) heterogeneous catalyst.

Kragten et al.,[26] that had focused only in the barrier for the β-hydrogen elimination step.

On the heterogeneous process, in the initial structure ethylene and acetate are placed on different Pd atoms on the surface. Acetate shows a $\kappa^1_{\rm O}$ bonding configuration while ethylene is adsorbed in a π-Pd mode; see Figure 3 structure heI1. The initial C−O distance is 3.313 Å. The transition state is reached by a rotation of both reactants so that they face each other; the C−O distance at this point is 1.890 Å. In the final state, the terminal C and O atoms are bound to the active Pd centers on the surface and the new C−O bond distance is 1.476 Å. The final structure is more unstable than reactants by 60.2 kJ/mol, being the barrier 127.6 kJ/mol.

According to these results and even if the number of metal centers in the systems is different, the similarities in the initial and final states are important. The differences in the transition state structure can be linked to the Hammond−Leffler postulate[45,46] indicating that in the homogeneous case the C−O coupling is a reactant-like structure (due to the exothermicity of the reaction) while for the heterogeneous case a product-like transition state is obtained (i.e., the reaction is endothermic).

The barrier is significantly higher for the heterogeneous process. This is likely because the participation of two different metal centers stabilizes mainly the initial state thus discouraging the reaction from taking place.

***β*-Hydrogen Elimination.** β-Hydrogen elimination takes place from two different situations. In the homogeneous process, this step consists simply of the transfer of the β-hydrogen to the metal in the intermediate resulting from the C−O bond formation step; see Figure 4 structure hoI2. In the transition state, the hydrogen transfer is almost complete; Pd−H is 1.588 Å (to be compared with 1.535 Å in palladium-hydride) and C−H is 1.615 Å. This is consistent with the high endothermicity of the process. This step is endothermic by 81.6 kJ/mol, and the transition state is quite high in energy, 96.2 kJ/mol, and similar to the product. The relatively high barrier that makes this the rate-determining step is associated to the low stability of the palladium hydride complex. This barrier is very close to the value of 95 kJ/mol computed by Kragten et al. with a simplified model for the transition state.[26]

We explored also an alternative pathway where the hydrogen would not go to the palladium but to an external acceptor, which we introduced in the form of acetic acid. The energy for the transition state was higher by 13.8 kJ/mol, and we thus discarded this alternative pathway. This alternative pathway had been found to be favored in the previous work by Kragten et al., where it was labeled "outer sphere".[26] We think that the alternative pathway was heavily favored in the previous report because of the introduction of a free acetate anion without taking into account its lower abundance in the experimental glacial acetic acid conditions. The lower concentration of acetate with

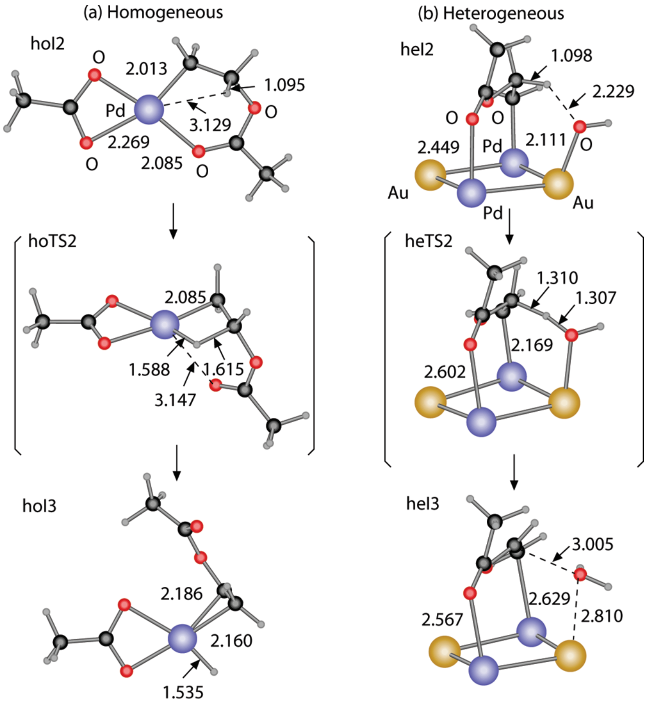

**Figure 4.** Initial, transition, and final states involved in $\beta$-hydrogen elimination. (a) Homogeneous catalyst, (b) heterogeneous catalyst.

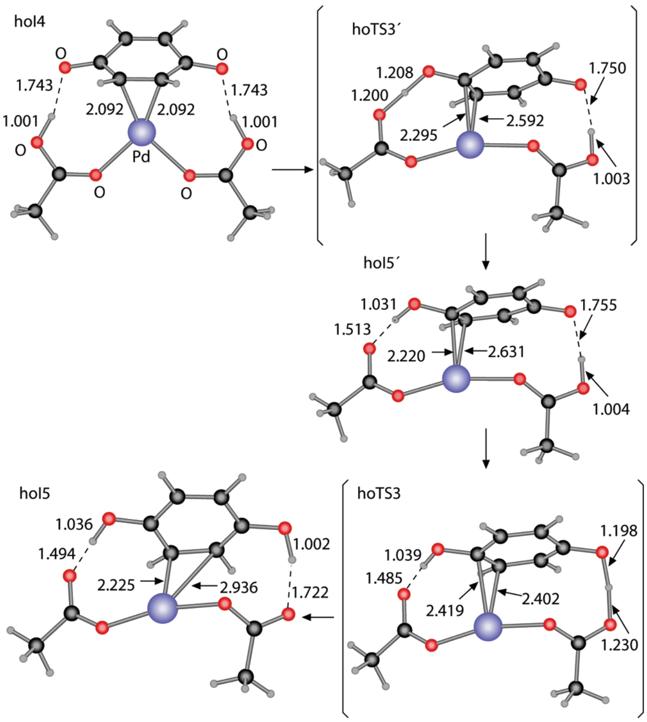

**Figure 5.** Key species involved in reoxidation of the homogeneous catalyst.

respect to acetic acid should affect the relative apparent rate constant, and the mechanism would be competitive at best with the one reported here. Moreover, if the previously reported value of 67 kJ/mol were correct, this would not be the rate determining step, which is in disagreement with the experimental observation.[14]

For the heterogeneous counterpart either oxygen or hydroxyl groups on the surface act as acceptors for the $\beta$-hydrogen atom; see Figure 4 structure heI2. In the initial state structure, VAH is adsorbed on the Pd centers through a $\kappa^2_{\mathrm{O,C}}$ configuration. OH atoms can be adsorbed on Au atoms in the neighboring region. In the initial state, the distance between the $\beta$-hydrogen and the oxygen atom in the hydroxyl group is 2.229 Å. At the transition state, the proton is close to the hydroxyl group, 1.307 Å, and finally it evolves toward the formation of a water molecule. The basicity of hydroxyl groups on Au centers is known to be large and therefore the process takes place very easily.[47] The calculated barrier is 47.8 kJ/mol and both products readily leave the surface.

The main difference in this step is thus the nature of the proton acceptor. While for the homogeneous case the metal center acts as an inefficient acceptor, the availability of oxygen or hydroxyl species facilitates this particular reaction step in the heterogeneous process.

## Catalyst Reoxidation

The reoxidation of the catalyst is done through different mechanism depending on the nature of the catalyst.

For the homogeneous version of the catalyst an external redox pair is needed.[3] In the present case, the benzoquinone-hydrobenzoquinone pair has been considered. The reoxidation does not take place directly from the final state of the previous step, the hoI3 complex, where a hydride coordinates to palladium. The reacting system must undergo some changes. First, a benzoquinone coordinates in an $\eta^2$ shape to palladium, resulting in a spontaneous movement of the hydride from palladium to the coordinated acetate, that becomes thus a $\kappa^1$ coordinated acetic acid. Next, a second acetic acid unit must come into the coordinating sphere of the metal and replace the vinyl acetate product, which is released. The rearrangements result in a complex, hoI4, where two acetic acids are coordinated $\kappa^1$ to the metal and the benzoquinone is coordinated in an $\eta^2$ shape. These steps, preliminary to catalyst reoxidation, are mechanistically complex and involve low barriers. Because of this they are not discussed in detail here, but collected in the Supporting Information, where three consecutive intermediates between hoI3 and hoI4 are presented. The highest energy transition state in this process is less than 5 kJ/mol above hoI3.

From this complex, the reoxidation takes place in two steps, shown in Figure 5. Each step consists of a hydrogen transfer from one acetic acid to the benzoquinone. The corresponding transition states have the expected shape with the hydrogen near the midpoint between the two oxygen centers involved. The O−H distances are 1.200, 1.208 Å in the first transition state and 1.230, 1.198 Å in the second. The energy of the transition states with respect to the starting point are 81.2 and 92.1 kJ/mol. Therefore, despite the complexity of the process, the barrier is still lower than for the $\beta$-hydrogen elimination. Thus, catalyst reoxidation is not the rate-determining step in the homogeneous process.

In the heterogeneous version of the catalyst, the surface can adsorb $O_2$; see Figure 6 structure heI4. The binding of $O_2$ molecular precursor is slightly endothermic by 5.2 kJ/mol and the O−O distance is 1.299 Å. The precursor is bonded to a Pd atom on the surface and the second O atom is facing a Au (thus similar to a bridge site). At the transition state, the O−O distance is elongated to 1.880 Å, and in the final state both O atoms are placed on different hollow sites on the surface. The transition state structure is higher than reactants by about 113.9 kJ/mol, thus reoxidation of the surface is not very easy due to the presence of Au on the surface. Once completed, reoxidation leads to two oxygen atoms on the surface which bear almost no magnetic moment. The final state is 29.5 kJ/mol higher in energy than the molecular adsorbed state.

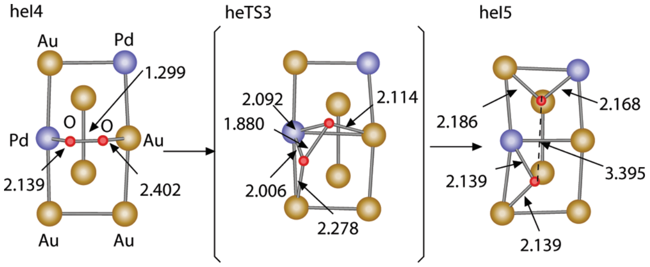

**Figure 6.** Initial, transition, and final states involved in reoxidation of the heterogeneous catalyst.

In this step the qualitative differences between the homogeneous and heterogeneous processes are the most significative. At least two steps are needed for the homogeneous process with the participation of the oxidant and those reactions are not directly transferable to the heterogeneous counterpart. However, these qualitative differences have little effect on the efficiency of the overall catalytic process, because reoxidation is never the rate-determining step.

## Conclusions

The reaction mechanisms on both homogeneous and heterogeneous catalysis for the synthesis of vinyl acetate from ethylene and acetic acid contain the same steps. However, the thermochemistry for the complete process depends on the nature of the oxidant employed, and the rate determining steps in both cases are different. For the homogeneous catalysts the most demanding step is C−H cleavage while for the heterogeneous catalyst the C−O coupling is found to be the rate determining step in agreement with the experiments. The reoxidation process is far simpler in the heterogeneous situation, but it is in no case the rate-determining step. The complexity of reoxidation in the homogeneous case may be related to the generation of nanoparticles Pd(0) that has been found to compromise the selectivity toward the product.

Finally, the reaction takes place at lower temperatures in the homogeneous case than in the heterogeneous version of the catalyst (i.e., 50−60 °C to be compared with 130−200 °C). This agrees very well with the calculated barriers for the rate determining step that are significantly higher in the heterogeneous version of the catalyst (i.e., 127 vs 96 kJ/mol for the homogeneous case). This is similar to the results for the C−C coupling in homogeneous and heterogeneous Au catalysts,[25] where organometallic compounds are able to work under softer temperature conditions.

In conclusion, we demonstrate how homogeneous and heterogeneous processes in the case of VA synthesis are closely linked. However, the direct extension of one of the process to its counterpart is not straightforward since differences in the rate determining step might be strongly dependent on the nature of the catalyst.

**Acknowledgment.** We thank the ICIQ foundation, MICINN (Consolider Ingenio 2010 CSD2006-003, CTQ2006-00464BQU, CTQ2008-06866-CO2-02/BQU), GenCat (Grants 2009SGR0259 and XRQTC), RES, and CESCA for funding support and computational resources. J.J.P. thanks the ICIQ foundation for a Summer fellowship.

**Supporting Information Available:** Full reference for Gaussian03 program, additional energy tables, and Cartesian coordinates for all optimized structures with total energies. This material is available free of charge via the Internet at http://pubs.acs.org.

## References and Notes

(1) Cordeiro, C. F.; Petrocelli, F. P. *Vinyl Acetate Polymers*. In Kirk-Othmer Encyclopedia of Chemical Technology, 5th ed.; Wiley: New York, 2005, Vol. 25, pp 557−591.

(2) http://www.vinylacetate.org/what.shtml, accessed February 23, 2009.

(3) Moiseev, I. I.; Vargaftik, M. N.; Syrkin, J. K. *Dok. Akad. Nauk SSSR* **1960**, *133*, 377–380.

(4) Bissot, T. U.S. Patent 4,048,096, 1977.

(5) Nakamura, S.; Yasui, T. *J. Catal.* **1970**, *17*, 366.

(6) Samanos, B.; Boutry, P.; Montarna., R. *J. Catal.* **1971**, *23*, 19.

(7) Nakamura, S.; Yasui, T. *J. Catal.* **1971**, *23*, 315.

(8) Smidt, J.; Sedlmeier, J.; Hafner, W.; Sieber, R.; Sabel, A.; Jira, R. *Angew. Chem., Int. Ed. Engl.* **1962**, *74*, 93.

(9) Smidt, J.; Hafner, W.; Jira, R.; Sedlmeier, J.; Sieber, R.; Ruttinger, R.; Kojer, H. *Angew. Chem., Int. Ed. Engl.* **1959**, *71*, 176–182.

(10) Goossen, L. J.; Rodríguez, N.; Goossen, K. *Angew. Chem., Int. Ed.* **2008**, *47*, 3100–3120.

(11) Beccalli, E. M.; Broggini, G.; Martinelli, M.; Sottocornola, S. *Chem. Rev.* **2007**, *107*, 5318–5365.

(12) Grennberg, H.; Simon, V.; Bäckvall, J. E. *J. Chem. Soc., Chem. Commun.* **1994**, 265–266.

(13) Grennberg, H.; Bäckvall, J. *Chem.*−*Eur. J.* **1998**, *4*, 1083–1089.

(14) van Helden, R.; Kohll, C. F.; Medema, D.; Verberg, G.; Jonkhoff, T. *Rec. Trav. Chim. Pays-Bas* **1968**, *87*, 961–962.

(15) Chen, M.; Kumar, D.; Yi, C.; Goodman, D. *Science* **2005**, *310*, 291–293.

(16) Chen, M. S.; Luo, K.; Wei, T.; Yan, Z.; Kumar, D.; Yi, C. W.; Goodman, D. W. *Catal. Today* **2006**, *117*, 37–45.

(17) Han, P.; Axnanda, S.; Lyubinetsky, I.; Goodman, D. W. *J. Am. Chem. Soc.* **2007**, *129*, 14355–14361.

(18) Wei, T.; Wang, J.; Goodman, D. W. *J. Phys. Chem. C* **2007**, *111*, 8781–8788.

(19) Kumar, D.; Chen, M. S.; Goodman, D. W. *Catal. Today* **2007**, *123*, 77–85.

(20) Vyboishchikov, S. F.; Bühl, M.; Thiel, W. *Chem.*−*Eur. J.* **2002**, *8*, 3962–3975.

(21) Ujaque, G.; Maseras, F. *Struct. Bonding (Berlin)* **2004**, *112*, 117–149.

(22) Nørskov, J. K.; Bligaard, T.; Hvolbaek, B.; Abild-Pedersen, F.; Chorkendorff, I.; Christensen, C. H. *Chem. Soc. Rev.* **2008**, *37*, 2163–2171.

(23) Somorjai, G. A.; Contreras, A. M.; Montano, M.; Rioux, R. M. *Proc. Natl. Acad. Sci. U.S.A.* **2006**, *103*, 10577–10583.

(24) Motta, A.; Fragala, I. L.; Marks, T. J. *J. Am. Chem. Soc.* **2008**, *130*, 16533–16546.

(25) García-Mota, M.; Cabello, N.; Maseras, F.; Echavarren, A. M.; Perez-Ramirez, J.; López, N. *ChemPhysChem* **2008**, *9*, 1624–1629.

(26) Kragten, D.; van Santen, R.; Neurock, M.; Lerou, J. *J. Phys. Chem. A* **1999**, *103*, 2756–2765.

(27) Biswas, B.; Sugimoto, M.; Sakaki, S. *Organometallics* **2000**, *19*, 3895.

(28) Becke, A. D. *J. Chem. Phys.* **1993**, *98*, 5648.

(29) Lee, C.; Yang, W.; Parr, R. G. *Phys. Rev. B* **1988**, *37*, 785.

(30) Stephens, P. J.; Devlin, F. J.; Chabalowski, C. F.; Frisch, M. J. *J. Phys. Chem.* **1994**, *98*, 11623.

(31) Frisch, M. J. et al. *Gaussian 03*, revision C.02; Gaussian, Inc.: Wallingford, CT, 2004.

(32) Andrae, D.; Haussermann, U.; Dolg, M.; Stoll, H.; Preuss, H. *Theor. Chim. Acta* **1990**, *77*, 123.

(33) Francl, M. M.; Pietro, W. J.; Hehre, W. J.; Binkley, J. S.; Gordon, M. S.; Defrees, D. J.; Pople, J. A. *J. Chem. Phys.* **1982**, *77*, 3654.

(34) Miertus, S.; Scrocco, E.; Tomasi, J. *Chem. Phys.* **1981**, *55*, 117.

(35) Braga, A. A. C.; Ujaque, G.; Maseras, F. *Organometallics* **2006**, *25*, 3647–3658.

(36) Robiette, R.; Aggarwal, V. K.; Harvey, J. N. *J. Am. Chem. Soc.* **2007**, *129*, 15513–15525.

(37) Kresse, G.; Furthmüller, J. *Phys. Rev. B* **1996**, *54*, 11169–11186.

(38) Hammer, B.; Hansen, L.; Nørskov, J. *Phys. Rev. B* **1999**, *59*, 7413–7421.

(39) Blöchl, P. *Phys. Rev. B* **1994**, *50*, 17953–17979.

(40) Kresse, G.; Joubert, D. *Phys. Rev. B* **1999**, *59*, 1758–1775.

(41) Monkhorst, H. J.; Pack, J. D. *Phys. Rev. B* **1976**, *13*, 5188–5192.

(42) Henkelman, G.; Uberuaga, B.; Jonsson, H. *J. Chem. Phys.* **2000**, *113*, 9901–9904.

(43) García-Mota, M.; López, N. *J. Am. Chem. Soc.* **2008**, *130*, 14406.

(44) Yuan, D.; Gong, X.; Wu, R. *J. Phys. Chem. C* **2008**, *112*, 1539–1543.

(45) Leffler, J. E. *Science* **1953**, *117*, 340–341.

(46) Hammond, G. S. A. *J. Am. Chem. Soc.* **1955**, *77*, 334–338.

(47) López, N.; García-Mota, M.; Gómez-Diaz, J. *J. Phys. Chem. C* **2008**, *112*, 247–252.

JP902929X

J|A|C|S
COMMUNICATIONS

# Template Effects in Vinyl Acetate Synthesis on PdAu Surface Alloys: A Density Functional Theory Study

Mónica García-Mota and Núria López*

*Institute of Chemical Research of Catalonia, ICIQ, Avgda. Països Catalans 16, 43007 Tarragona, Spain*

Received July 16, 2008; E-mail: nlopez@iciq.es

Vinyl acetate (VA) is a major industrial product involved in the manufacture of polymers. It is synthesized from the coupling of acetic acid and ethylene in oxygen ambient. Recently, isolated Pd dimers on Au surfaces have been found to be active and selective catalysts for the process but a strong dependence on the local structure of the ensemble is observed.[1] By means of density functional theory (DFT), we demonstrate how the most successful ensemble shows the best performance on different steps: easy adsorption of reactants, inhibited poisoning and low barrier for the rate limiting step (rls).

PdAu alloys have been revealed as new, powerful catalysts with applications in chemical and electrochemical contexts.[1,2] In particular, low Pd content PdAu surface alloys show an intrinsic high activity and pronounced structure sensitivity toward the production of VA.[1] Vinyl acetate synthesis proceeds via the oxygen-assisted dissociative adsorption of acetic acid followed by the coupling to ethylene.[3] The resulting intermediate, hydrogenated VA, (VAH in the following) evolves via $\beta$-hydrogen elimination to VA and a water molecule. This mechanism was determined both experimentally[4] and theoretically,[5] and the acetate-to-ethylene coupling was found to be the rls for Pd(100) and second nearest neighbors Pd on Au(100). However, the pronounced structure sensitivity found in the experiments[1a] cannot be understood without considering the reaction path in a full set of local structures, and this is the precise aim of our study. More generally, ensemble effects are mandatory to reach an atomistic design of new catalysts. In the following, we employ DFT to determine what drives the structure sensitivity observed for the formation of VA on different ensembles of PdAu.

To this end we have built several Pd dimer configurations on both Au(100) and (111) (see Figure 1). To obtain the reaction profiles on the Pd dimers, the VASP code has been employed[8] with RPBE as the exchange-correlation functional.[9] Valence monoelectronic states have been expanded in plane waves with a kinetic cutoff energy of 400 eV while the inner electrons have been represented by PAW pseudopotentials.[10] The slabs contain five layers for the (100) and four for the (111) surface in a $p(4 \times 4)$ supercell, and the slabs are interleaved by 12 Å of vacuum. On these surfaces two Au atoms have been replaced by Pd atoms in the configurations shown in Figure 1. Therefore, the Pd−Pd distances range from $d_{\mathrm{Pd-Pd}}$ to twice this value. The configurations have been named as nearest neighbors: NN for the $d_{\mathrm{Pd-Pd}}$ distance; next-nearest neighbors: NNN, $d\sqrt{2}$ or $d\sqrt{3}$ (for (100) and (111) surfaces, respectively); second next nearest neighbors: 2NNN, $2d$. The $k$-point sampling consists of $2 \times 2 \times 1$ Monkhorst−Pack points.[11] The two surface upper layers and the adsorbates have been optimized while the lowest layers were kept frozen at the bulk distances. With this setup, the relative energies to the most stable dimer for each surface are reported, see Figure 1. All these configurations are likely to be present on the samples at 0.1 ML Pd coverage on Au in agreement with previous experimental and theoretical results.[1,2a,6,7] The CI-NEB method has been employed[12] to locate the transition-state structures (showing a single imaginary frequency), see Supporting Information.

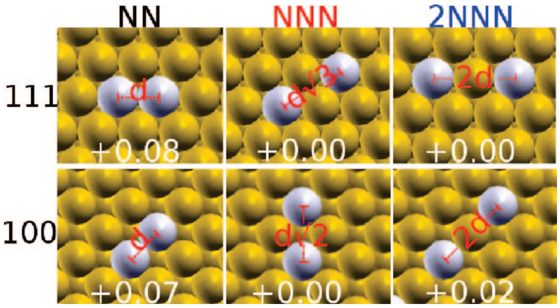

***Figure 1.*** Dimer ensembles showing different local configurations on (111) and (100) Au surfaces. Yellow spheres represent Au, and gray ones are Pd atoms. NN stands for nearest neighbors, NNN next nearest neighbors, and 2NNN second next nearest neighbors. The numbers indicate the relative energies, in eV, to the most stable dimer on each surface. The interdimer distance is expressed in $d_{\mathrm{Pd-Pd}}$ units.

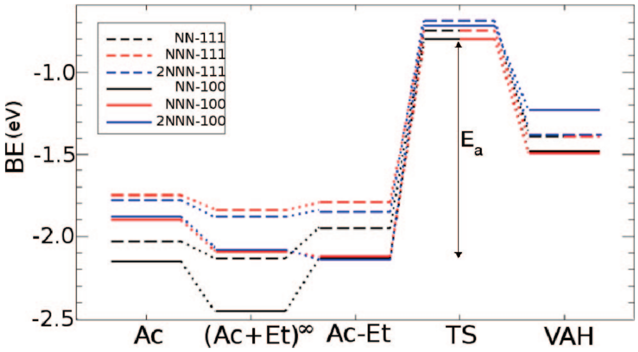

***Figure 2.*** Reaction energy profiles, BE in eV (with respect to gas-phase acetate radical, ethylene, and the clean surface), for the coupling of ethylene and acetate on the models of Figure 1. Ac states for acetate, Et for ethylene, and the infinite sign represents separated adsorption. The structures for coadsorbed Ac−Et, the intermediate VAH, and the transition state linking both can be found in the Supporting Information.

The binding energies of reactants and intermediates, BE, (with respect to gas-phase acetate radical, ethylene, and the clean surface) are shown in Figure 2 together with the barriers for the rls. Binding energies to (111) surfaces are lower than those to (100), as expected from the $d$-band model.[13] Adsorbed species can be classified according to their coordination to the surface (hapticity), $\eta^{X}{}_{\mathrm{A},\ldots}$, where $X$ indicates the number of atoms through which the adsorbate is bound to the surface and "A,..." represents these atoms.

Ethylene is weakly adsorbed to the Pd dimers, through a $\pi$−Pd bond[5] ca. −0.2 for (100) to ca. −0.1 eV for the (111) surfaces. Similarly, low binding energies have been found for ethylene on Ag.[14] Acetate can be adsorbed either as monospecies or dihapto species depending on the Pd ensemble, see Supporting Informa-

10.1021/ja805519v CCC: $40.75

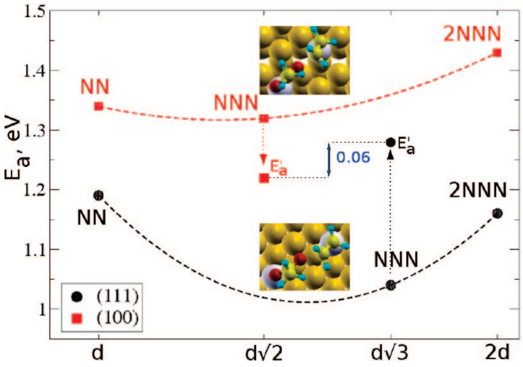

***Figure 3.*** Activation energies, $E_a$ in eV, for the rate limiting step, as a function of the template Pd−Pd distance. For the NNN dimers the apparent activation energies, $E_a'$, are also indicated. The insets show the transition state structures for NNN.

tion. For both surface orientations, acetate adsorption on NN templates results in dihapto-$\eta^2{}_{O,O}$ species (BE = −2.15 (100), −2.03 (111) eV) while for NNN and 2NNN monohaptospecies, $\eta^1{}_O$, are more stable (BE ≈ −1.90 (100), −1.75 (111) eV).

The formation of the coadsorbed state (Ac−Et) requires the approach of both acetate and ethylene adsorbates to neighboring Pd atoms in the dimer. The NN configurations on both (111) and (100) pay an energy penalty, about 0.3 eV, for changing the configuration of the acetate from the dihapto in the infinitely separated configuration to the monohapto adsorption needed to generate the active complex (Ac−Et). For NNN and 2NNN the process is almost thermoneutral, ± 0.06 eV. In fact, strong bonding of the acetate-$\eta^2{}_{O,O}$ species to the NN ensemble results in poisoning of these templates under normal conditions.

The VAH intermediate bonds the dimers in a dihapto-$\eta^2{}_{O,C}$ mode by the terminal O and C atoms to the Pd. The binding energies of these species are very similar for all dimers on the (111) surface: −1.3 to 1.4 eV. For the (100) surface, adsorption energies are more spread: −1.49, −1.44, and −1.23 eV for NNN, NN, and 2NNN, respectively. Upon VAH dehydrogenation the vinyl acetate product is easily desorbed from the surface on both (111) and (100) surfaces (not shown in Figure 2).

To shed light on the structure sensitivity, we have calculated the barriers connecting the coadsorbed state (Ac−Et) and the VAH intermediate. All the barriers, $E_a$, range in between 1.04 and 1.43 eV. From the (Ac−Et) on the different dimers the energy barrier, $E_a$, follows a Brønsted−Evans−Polanyi (BEP)-type of relationship with the reaction energy,[15] see Supporting Information. This means that the less endothermic the reaction is, the lower the barrier results. The reasons for the increased barriers at longer/shorter distances are mainly due to the energy cost of either the repulsion in the coadsorbed state structure or the strain/stress in the final VAH state.

The next step is to determine why in the experiments the NNN-(100) structures are more reactive than the corresponding (111). To understand the relative activity of NNN dimers all the elementary steps previous to the rate limiting step have to be taken into account and contribute to the apparent activation energy, $E_a'$. Working out the kinetic equations in the nearly empty surface approximation and considering constant preexponential factors,[16] $E_a'$ can be written as: $E_a' = E_a + \Sigma_i \Delta E_i$ where $\Delta E_i$ corresponds to the reaction energies of the previous steps in the reaction network. Those steps are oxygen dissociation, oxygen assisted acetic acid adsorption, ethylene adsorption, and acetate ethylene approach. When $E_a'$ are compared, the value for NNN(100) is 0.06 eV lower than that of the (111) surface. The reason for the lower $E_a'$ in (100) comes from the better adsorption of reactants. This difference in apparent activation energies, $\Delta E_a' = E_a'^{100} - E_a'^{111}$, corresponds to a relative reaction rate at the experimental temperature (453 K)[1a] of about 4−5 times faster for the (100) structure. This is in excellent agreement with experiments where the relative activities found at the (100) curve maximum are $r_{100}/r_{111} \approx 4.6$.[1a]

To summarize, the structure sensitivity for the synthesis of VA on Pd dimers on PdAu surface alloys depends on three effects. First, electronic contributions that favor the reaction on the most open surface due to better adsorption of reactants. Second, the most successful ensemble, NNN, avoids poisoning by acetate adsorption due to template effects that block the formation of the dihaptoacetate species. Third, the Pd template induces small changes, in the structure and energies, of the coadsorbed structure and the VAH product by strain/stress effects,[17] thus affecting the reaction barrier for the coupling step. These contributions follow a BEP type of relationship. A final remark is that the role of Au in these alloys is as a spacer isolating the Pd ensembles.

**Acknowledgment.** ICIQ, MEC (Consolider Ingenio 2010 CSD2006-003, CTQ2006-00464BQU), GenCat, and RES-CesViMa are acknowledged for support.

**Supporting Information Available:** Structures, imaginary frequencies, reaction energies and kinetic analysis are reported. This material is available free of charge via the Internet at http://pubs.acs.org.

## References

(1) (a) Chen, M. S.; Kumar, D.; Yi, C. W.; Goodman, D. W. *Science* **2005**, *310*, 291. (b) Kumar, D.; Chen, M. S.; Goodman, D. W. *Catal. Today* **2007**, *123*, 77. (c) Chen, M. S.; Luo, K.; Wei, T.; Yan, Z.; Kumar, D.; Yi, C. W.; Goodman, D. W. *Catal. Today* **2006**, *117*, 37.
(2) (a) Maroun, F.; Ozanam, F.; Magnussen, O. M.; Behm, R. J. *Science* **2001**, *293*, 1811. (b) Enache, D. I.; Edwards, J. K.; Landon, P.; Solsona-Espriu, B.; Carley, A. F.; Herzing, A. A.; Watanabe, M.; Kiely, C. J.; Knight, D. W.; Hutchings, G. J. *Science* **2006**, *311*, 362.
(3) Samanos, B.; Boutry, P.; Montarnal, R. *J. Catal.* **1971**, *23*, 19.
(4) Stacchiola, D.; Calaza, F.; Burkholder, L.; Schwabacher, A. W.; Neurock, M.; Tysoe, W. T. *Angew. Chem., Int. Ed.* **2005**, *44*, 4572.
(5) Yuan, D. W.; Gong, X. G.; Wu, R. Q. *J. Phys. Chem. C* **2008**, *112*, 1539.
(6) Han, P.; Axnanda, S.; Lyubinetsky, I.; Goodman, D. W. *J. Am. Chem. Soc.* **2007**, *129*, 14355. (b) Wei, T.; Wang, J.; Goodman, D. W. *J. Phys. Chem. C* **2007**, *111*, 8781.
(7) (a) Liu, P.; Nørskov, J. K. *Phys. Chem. Chem. Phys.* **2001**, *3*, 3814. (b) Martin, R.; Takehiro, N.; Liu, P.; Nørskov, J. K.; Behm, R. J. *Chem.Phys.Chem* **2007**, *8*, 2068. (c) Soto-Verdugo, V.; Metiu, H. *Surf. Sci.* **2007**, *62*, 4744. (d) Boscoboinik, J. A.; Plaisance, C.; Neurock, M.; Tysoe, W. T. *Phys. Rev. B* **2008**, *77*, 045422.
(8) (a) Kresse, G.; Hafner, J. *Phys. Rev. B* **1993**, *47*, 558. (b) Kresse, G.; Furthmüller, J. *Phys. Rev. B* **1996**, *54*, 11169.
(9) Hammer, B.; Hansen, L. B.; Nørskov, J. K. *Phys. Rev. B* **1999**, *59*, 7413.
(10) Kresse, G.; Joubert, D. *Phys. Rev. B* **1999**, *59*, 1758.
(11) Monkhorst, H. J.; Pack, J. D. *Phys. Rev. B* **1976**, *13*, 5188.
(12) Henkelman, G.; Uberuaga, B. P.; Jónsson, H. *J. Chem. Phys.* **2000**, *113*, 9901.
(13) Hammer, B.; Morikawa, Y.; Nørskov, J. K. *Phys. Rev. Lett.* **1996**, *76*, 2141.
(14) Bocquet, M. L.; Rappe, A. M.; Dai, H. L. *Mol. Phys.* **2005**, *103*, 883.
(15) (a) Brønsted, J. N. *Chem. Rev.* **1928**, *5*, 231. (b) Evans, M. G.; Polanyi, M. *Transactions of Faraday Soc.* **1938**, *34*, 11. (c) Logadottir, A.; Rod, T. H.; Nørskov, J. K.; Hammer, B.; Dahl, S.; Jacobsen, C. J.H. *J. Catal.* **2001**, *197*, 229.
(16) See Supporting Information and: Chorkendorff, I.; Niemantsverdriet, J. W. *Concepts of Modern Catalysis and Kinetics*; Wiley-VCH: Weinheim, Germany, 2003; Chapter 3 and p 38.
(17) Mavrikakis, M.; Hammer, B.; Nørskov, J. K. *Phys. Rev. Lett.* **1998**, *81*, 2819.

JA805519V

CHEMPHYSCHEM

**DOI: 10.1002/cphc.200800246**

# Selective Homogeneous and Heterogeneous Gold Catalysis with Alkynes and Alkenes: Similar Behavior, Different Origin

Mónica García-Mota,[a] Noemí Cabello,[a] Feliu Maseras,[a, b] Antonio M. Echavarren,[a, c] Javier Pérez-Ramírez,[a, d] and Nuria Lopez*[a]

*The development of new sustainable chemical processes requires the implementation of ultra-selective reaction processes. The enormous selectivity found for gold-based catalysts when applied in several reactions has opened new frontiers. For instance, the selective activation of alkynes is a common feature for both homogeneous and heterogeneous gold catalysts. Herein, we employ experimental and theoretical methods to assess the similarities and differences in the performance of homogeneous and heterogeneous gold catalysts. Alkynophilicity, the selective activation of alkynes, is found to have a thermodynamic origin in the heterogeneous case and a kinetic one for homogeneous catalysis. Complex enyne rearrangements require the more active homogeneous (single gold) catalyst because it has more electrophilic character than its heterogeneous (nanoparticle) counterpart.*

## 1. Introduction

New chemical processes with high atom efficiency and low energy demand are needed both to sustain our economies and to satisfy the increasing demand for ecologically friendly processes. In order to fulfill these requirements, chemical processes should generate less waste and reduce complex separation steps. Selectivity in chemical reactions is therefore a must. In recent years, homogeneous and heterogeneous gold catalysts have emerged as active and extremely selective in a wide range of reactions.[1,2] For several reactions, such as low-temperature CO oxidations, C–C bond formation and the hydrogenation of alkenes, both homogeneous and heterogeneous catalysts are active. As a consequence, the use of homogeneous gold catalysts has triggered the extension to the heterogeneous versions and vice versa.[3] For example, in homogeneous chemistry, $Au^{I}$ and $Au^{III}$ species are employed as catalysts for C–C and C–heteroatom bond formation from alkynes and alkenes.[1] As for heterogeneous chemistry, supported gold nanoparticles on different oxides ($CeO_2$, $Fe_2O_3$, $TiO_2$) are active and selective in the partial hydrogenation of alkynes.[4]

In homogeneous catalysis, alkynes react preferentially with homogeneous gold catalysts in the presence of alkenes or other functional groups.[1] Similar selective alkyne activation has also been observed in heterogeneous catalysis.[1a,2] This effect is known as alkynophilicity. Upon first sight, it is tempting to attribute alkynophilicity to the same mechanistic origin. However, the transferability of chemical properties from isolated single metal catalysts to nanoparticles is far from being well-established and understanding the gap between the "hetero" and "homo" catalysis worlds has been recognized as one of the major challenges in chemistry.[5] The fundamental reasons why and how the same catalytic properties, that is, selective alkyne activation, occur are unclear. Herein, we address this point by combining experiments and calculations. We also want to see whether the well-established reactivity of enynes with a variety of homogeneous $Au^{I}$ and $Au^{III}$ systems can be extrapolated to heterogeneous gold catalysts, as has been done for other reactions.[3]

## 2. Results and Discussion

In order to illustrate the nature of the selective alkyne activation in homogeneous and heterogeneous catalysis we employ DFT-based calculations together with experiments. Previous research performed in our groups concluded that Au in nanoparticle form catalyzes the hydrogenation of alkynes to alkenes in the presence of alkenes[4] while homogeneous Au excels in the formation of C–C bonds.[6] Herein, we explore the ability of nanoparticle-based heterogeneous catalysis to perform key reactions in homogeneous catalysis and from these results analyze the possible contributions to the observed differences.

---

[a] *M. García-Mota, Dr. N. Cabello, Prof. F. Maseras, Prof. A. M. Echavarren,*
*Prof. J. Pérez-Ramírez, Dr. N. Lopez*
*Institute of Chemical Research of Catalonia, ICIQ*
*Av. Països Catalans 16, 43007 Tarragona (Spain)*
*Fax: (+34) 977920237*
*E-mail: nlopez@iciq.es*

[b] *Prof. F. Maseras*
*Dept. Química, Universitat Autònoma de Barcelona*
*Bellaterra, 08193 Barcelona (Spain)*

[c] *Prof. A. M. Echavarren*
*Dept. Organic Chemistry, Universidad Autónoma de Madrid*
*Cantoblanco, 28049 Madrid (Spain)*

[d] *Prof. J. Pérez-Ramírez*
*Catalan Institution for Research and advanced studies (ICREA)*
*Passeig Lluís Companys, 23, 08010 Barcelona (Spain)*

Supporting information for this article is available on the WWW under http://dx.doi.org/10.1002/cphc.200800246.

### 2.1. Enyne Cyclation: Homo- versus Heterogeneous Au Catalysts

Under heterogeneous conditions, we first test the performance for reactions of 1,6-enynes that are known to proceed smoothly with homogeneous catalysts.[1] Thus, for example, 1,6-enyne **1** reacts with cationic Au$^I$ catalysts (2 mol%) in $CH_2Cl_2$ at room temperature in 5 min to form the skeletal rearrangement product **2** with 98% yield (Scheme 1).[6] This type of skeletal rearrangement of 1,6-enynes to give 1,3-dienes occurs readily with cationic Au$^I$ catalysts at temperatures as low as −60 °C[6b] and even proceeds with Ag$^I$ catalysts, which are much less reactive than their gold analogues.[7] Phenyl-substituted 1,6-enyne **3** gives the product of a formal [4+2] cycloaddition **4** in 86% yield under similar experimental conditions (2 mol% Au$^I$, $CH_2Cl_2$ room temperature, 1 h).[8]

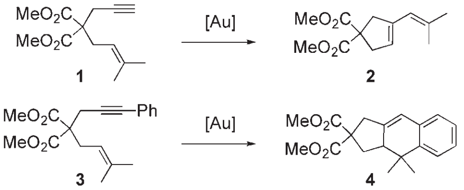

**Scheme 1.** Au$^I$-catalyzed reactions of 1,6-enynes.

Since these reactions are among the most general gold-catalyzed transformations and mechanistically reasonably well-understood,[1f,6,8] we choose them as test models. Somewhat surprisingly, reaction of **1** or **3** with heterogeneous Au/$CeO_2$ in $CH_2Cl_2$ at room temperature or at 50 °C (5% catalyst, microwave radiation, 150 W, 1 h for **1**; 5% catalyst, refluxing conditions, 24 h for **3**) lead only to unchanged starting materials. None of the expected products **2** or **4** are detected in these experiments. Thus, it is clear that there is a substantial difference in reactivity between homogeneous and heterogeneous (nanoparticle) gold catalysts, suggesting a gap in these particular C–C bond forming reactions.

### 2.2. Binding of Double and Triple Bonds to the Active Species

In order to understand the differences in the behavior described above, we analyze the coordination of substrates to the active gold species by theoretical methods. We employ DFT with the B3LYP[9] functional and localized basis sets (Gaussian03[10]). The calculated gold catalyst models include the inorganic species $Au^+$, AuCl, $AuCl_3$, and a gold nanoparticle, $Au_{10}$. The $Au_{10}$ nanoparticle is built to resemble the structure of a medium-sized nanoparticle (see computational details) as was succesfully done for the study of CO oxidation.[11] Ethylene and acetylene (C2) and propene and propyne (C3) are selected as representative models for alkenes and alkynes. Although the models might seem too simplistic, the change of ligands in the homogeneous species would only finely tune the differential energy values reported in the tables (except for very bulky ligands). For the heterogeneous models differential binding energies are similar to those calculated for $Au_{19}$ nanoparticles.[4a]

On $Au_{10}$ nanoparticles the interaction energy $\Delta E$ of $C_2H_2$ is $-112.4\ \mathrm{kJ\,mol^{-1}}$. The molecule is activated, thus the C–C distance is 1.313 Å (Figure 1). $C_2H_4$ is adsorbed much less, $\Delta E = -72.1\ \mathrm{kJ\,mol^{-1}}$ and the C–C distance is 1.454 Å, which shows that the molecule is unperturbed. The results for C3 (propyne and propene) are similar. Binding energies of −94.7 and $-63.0\ \mathrm{kJ\,mol^{-1}}$ and distances of 1.315 and 1.459 Å are found. Qualitatively, the differences in alkene and alkyne binding energies can be traced back to the position of the HOMO and LUMO energy levels in gas-phase $C_2H_2$ and $C_2H_4$ molecules with respect to the metal d band (or orbital) energies.[12] For gas-phase $C_2H_2$ ($C_3H_4$), the HOMO is situated 0.4 (0.3) eV lower than the corresponding level for $C_2H_4$ ($C_3H_6$) and it is degenerate, which leads to a larger coupling with the metal states and a larger binding energy to the nanoparticle. The differences in binding energies remain for larger $Au_{19}$ nanoparticles.[4a]

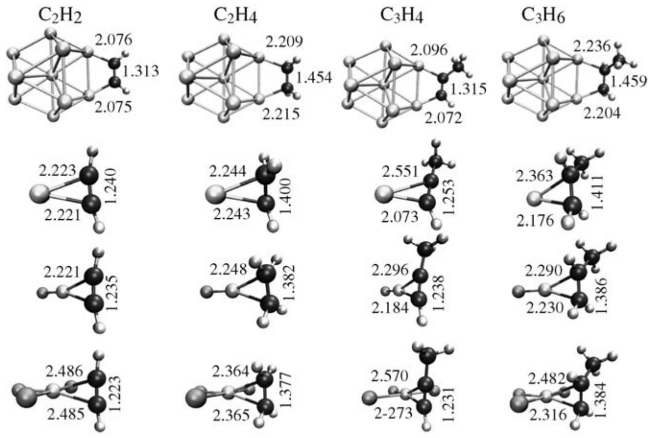

**Figure 1.** Schematic representation of the gold systems $Au_{10}$, $Au^+$, AuCl and $AuCl_3$, interacting with acetylene (left), ethylene (center left) propyne (center right) and propene (right). Grey spheres represent Au, dark grey Cl, black C, and white H. Distances are in Å.

When considering gas-phase chemistry, the interaction of $C_2H_2$ with $Au^+$ is −226.3, whereas that of $C_2H_4$ is $-263.6\ \mathrm{kJ\,mol^{-1}}$ (Figure 1). C–C distances with respect to the gas-phase molecules are elongated to 1.240 and 1.400 Å, respectively. Our results are similar to previous calculations, indicating larger stabilization for the ethylene complex over the acetylene one by $33\ \mathrm{kJ\,mol^{-1}}$.[13] The coordination of propyne–propene is similar; the binding energies are −268.8 and $-295.4\ \mathrm{kJ\,mol^{-1}}$ respectively, thus again favoring the double bond, while the C–C distances are 1.253 and 1.411 Å.

The AuCl molecule coordinates acetylene or ethylene, releasing −142.8 or $-161.1\ \mathrm{kJ\,mol^{-1}}$, repectively. Both molecules are activated and the C–C distances lengthen to 1.235 and 1.382 Å (Figure 1). If the pair propyne–propene is inspected, the binding energies to AuCl are −151.4 and $-171.0\ \mathrm{kJ\,mol^{-1}}$, again favoring the molecule containing the double bond. The relevant C–C distances are 1.238 and 1.386 Å.

$AuCl_3$ exists as the dimer $Au_2Cl_6$, both in the gas and the solid phase.[14] Upon reaction, the active moiety is $AuCl_3$, which can be coordinated to a triple or a double bond. The first process is endothermic by $+6.3\,kJ\,mol^{-1}$, while the second is marginally exothermic by $-33.1\,kJ\,mol^{-1}$, both with respect to 1/2 $Au_2Cl_6$. Again, bonding to C=C is more favorable than that to C≡C. The C–C distance for $C_2H_2$ is 1.223, and 1.377 Å for $C_2H_4$, and 1.231 and 1.384 Å respectively, for $C_3$ compounds. The interaction energies in the latter case are −13.5 and $-52.1\,kJ\,mol^{-1}$.

Table 1 shows the differential coordination energies defined as $\Delta\Delta E = \Delta E_{C\equiv C} - \Delta E_{C=C}$. From these results it is inferred that the reason for selectivity in heterogeneous systems is the selective adsorption of triple bonds (thermodynamic selectivity)[15] that leads to sharp reactions (hydrogenation, hydration) with this functional group, that is, alkenes are not adsorbed (activated) on Au nanoparticles. In contrast, the binding energies for ethylene and acetylene are comparable for AuCl and $AuCl_3$ and always higher for C=C bonds. This is also true for less electron-attracting ligands (such as $CH_3$ groups). According to the $\Delta\Delta E$, Au-based homogeneous catalysts would spend most of the time coordinated to the alkene.

**Table 1.** Differential coordination energies $\Delta\Delta E = \Delta E_{C\equiv C} - \Delta E_{C=C}$ in $kJ\,mol^{-1}$ for C2 and C3. The B3LYP and CCSD(T) results are for different gold models.

| $\Delta\Delta E$ | B3LYP | | CCSD(T) | |
|---|---|---|---|---|
| System | C2 | C3 | C2 | C3 |
| $Au^+$ | 37.3 | 26.6 | 33.0 | 29.3 |
| AuCl | 18.3 | 19.6 | 21.4 | 25.4 |
| $AuCl_3$ | 39.5 | 38.6 | 44.5 | 44.8 |
| $Au_{10}$ | −41.3 | −31.7 | – | – |

This is experimentally confirmed in the NMR spectra of a 1:1 mixture of the cationic $Au^I$ complex **5**[8] and the 1,7-enyne [dimethyl 2-(but-3-enyl)-2-(prop-2-ynyl)propanedioate, **6**] (Figures 2 and 3). For this experiment we choose 1,7-enyne **6**, which has a terminal double bond and is known to undergo cyclization reactions with $Au^I$ catalysts very slowly at low temperatures.[16] In the $^1H$ NMR spectrum of a mixture of **5** and **6**, the new signals that emerge at $\delta$ 4.3 and 6.15 are due to the alkene hydrogen atoms of the complexed $\eta^2$-alkene-gold complex.[17] Consequently, the observed selectivity in homogeneous catalysis for systems containing alkyne and alkene functions is not directly related to the thermodynamic preference in the coordination step.

## 2.3. Selectivity in Homogeneous Catalysis

Since no alkene is adsorbed on the gold nanoparticles, heterogeneous catalysis should selectively modify only the molecules containing triple bonds. Thus, no further calculations are needed to describe their selectivity. In contrast, for the homogeneous catalysts, the coordination step does not show any selectivity towards alkynes and therefore the reasons for alkynophilicity should be investigated for these reaction processes.

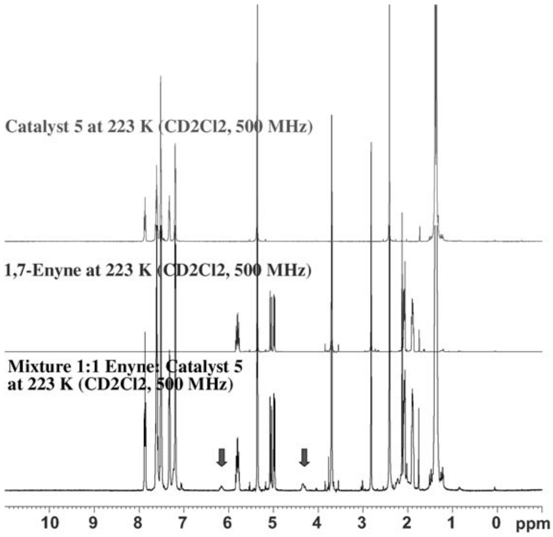

**Figure 2.** $^1H$ NMR spectra of 1,7-enyne **6** and a 1:1 mixture of **6** and the cationic $Au^I$ complex **5** (223 K, $CD_2Cl_2$, 500 MHz)

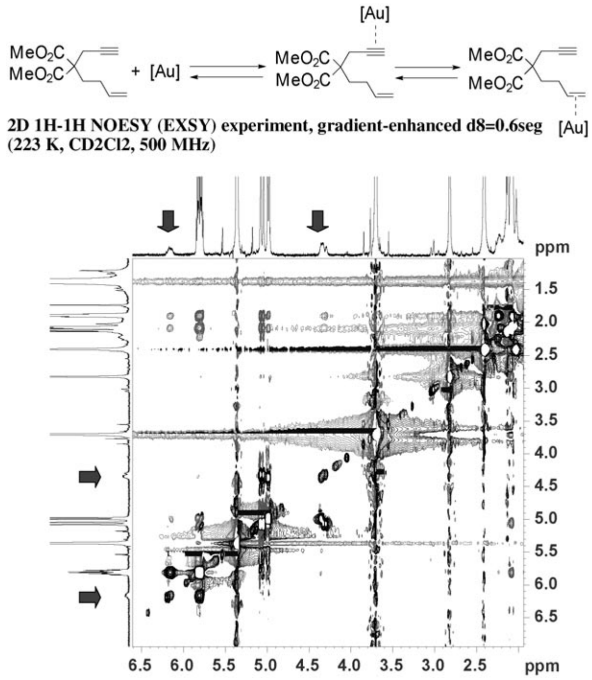

**Figure 3.** 2D $^1H$ $^1H$ NOESY experiment showing the complexation of catalyst **5** and **6** (223 K, $CD_2Cl_2$, 500 MHz).

We search further for the origin of chemoselectivity in the homogeneous systems by studying test reactions: nucleophilic ($OH^-$) and electrophilic ($H^+$) attacks and hydration ($H_2O$). For these processes, we analyze the differential reaction energy of triple bonds with respect to double bonds, $\Delta\Delta E^r$, for both free and coordinated C2 (C3) to AuCl (Table 2). For the isolated molecules, addition of $OH^-$ is exothermic by −204.8 and $-106.4\,kJ\,mol^{-1}$ ($C_2H_2$ and $C_2H_4$, respectively). When $C_2H_2$ or $C_2H_4$ are coordinated to AuCl, the reactions are exothermic by

**Table 2.** Differential reaction energies $\Delta\Delta E^r = \Delta E_{C\equiv C} - \Delta E_{C=C}$ in $kJ\,mol^{-1}$ for nucleophilic attack ($OH^-$), electrophilic attack ($H^+$) and hydration ($H_2O$) for C2 and C3 within the B3LYP approach.

| $\Delta\Delta E^r$ [$kJ\,mol^{-1}$] | C2 free | AuCl-C2 | C3 free | AuCl-C3 |
|---|---|---|---|---|
| $OH^-$ | −98.4 | −119.0 | −51.8 | −84.6 |
| $H^+$ | 35.2 | −23.0 | 13.5 | −53.8 |
| $H_2O$ | −88.0 | −148.4 | −61.3 | −128.9 |

−619.1 or −500.1 $kJ\,mol^{-1}$. The attack on the triple bond is thus intrinsically favored, but the catalyst largely increases the exothermicity of the process (>400 $kJ\,mol^{-1}$). The values are similar for C3.

With respect to electrophilic attack, interaction with a proton is exothermic for isolated $C_2H_2$ and $C_2H_4$ and more favorable for $C_2H_4$ than for $C_2H_2$, −722.8 vs −687.7 $kJ\,mol^{-1}$. Once coordinated to the AuCl catalyst, the energies for the reaction are smaller, −663.5 ($C_2H_2$) and −640.5 $kJ\,mol^{-1}$ ($C_2H_4$). Thus, proton addition to the free alkene is more favored than to the alkyne, but the reaction energy order is reversed when the catalyst is present, indicating a selective attack on the triple bond. The same is observed in the case of C3.

The results for the hydration of C=C and C≡C indicate that the latter reaction is more favorable even in the case of the isolated molecules, but that the presence of AuCl increases the differential exothermicity of the hydration reaction by more than 50% (Table 2). These results are reproduced experimentally (Scheme 2). Whereas alkyne **7** reacts with water at room temperature in the presence of catalyst **5** to form a 48:1 mixture of ketone **8** and aldehyde **9**,[18] alkene **10** is recovered unchanged.

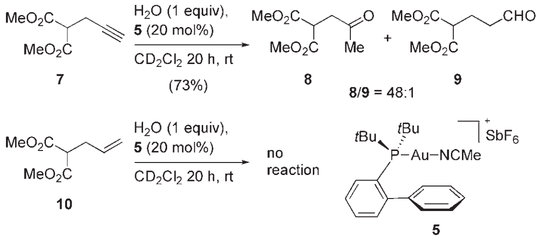

**Scheme 2.** Hydration of alkyne **7** with the gold(I) catalyst **5**.

Finally, although our models are based on gas-phase calculations, the energy differences observed for the reactions on molecules containing double and triple bonds are large enough that our conclusions do not depend on the inclusion of the solvent. Moreover, solvation would have an almost constant contribution due to the similarity of the reactants and products for acetylene and ethylene. Also, when a solvent is present, some of the reactions should show a reaction barrier that is not observed in the gas-phase calculations. The differential reaction energies $\Delta\Delta E^r$ can be employed as an indirect measure for the kinetic contributions by applying Brønsted–Evans–Polanyi (BEP)[19] relationships.

### 2.4. Enyne Cyclization

Our calculations also explain why homogeneous and heterogeneous catalysts behave differently with respect to enyne cyclization. Molecular orbital analysis is applied to rationalize these results. The differences in behavior found for cyclizations in Scheme 1 over homo- and heterogeneous catalysts are analyzed by the energy and composition of the frontier orbitals for $Au_{10}$ and AuCl-activated $C_2H_2$ and $C_2H_4$ (Figure 4). The HOMO and LUMO gas-phase $C_2H_2$ and $C_2H_4$ orbitals are shown as a reference.

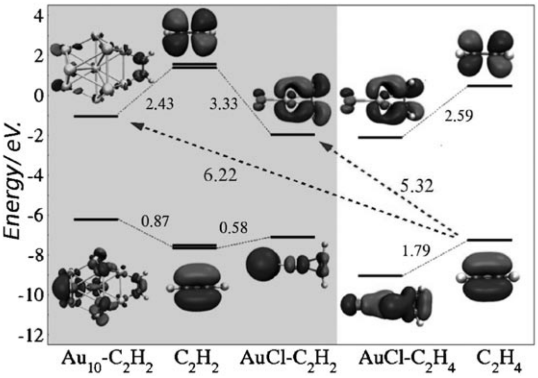

**Figure 4.** Molecular orbital diagram showing the corresponding HOMO and LUMO orbitals for $C_2H_2$ and $C_2H_4$ free and coordinated to AuCl and $Au_{10}$.

Upon AuCl interaction, the $C_2H_2$ LUMO is downshifted by more than 3.3 eV. This is how the catalyst improves the Lewis basic character of $C_2H_2$. When interacting with $Au_{10}$, the $C_2H_2$ LUMO is much less activated (downshift is only 2.4 eV), thus the system is less prone (by about 100 $kJ\,mol^{-1}$) to electron acceptance than when bound to AuCl. This can be traced back to the binding energies of $C_2H_2$ to AuCl and $Au_{10}$. The stronger the bond is, the larger the downshift in the LUMO levels. Therefore the smallest difference between the HOMO($C_2H_4$) and the LUMO($C_2H_2$) orbital energies in the AuCl-catalyzed reaction is 5.3, while it is 6.2 eV for the $Au_{10}$ system. In homogeneous systems AuCl–$C_2H_4$ units are also present, but AuCl lowers the activity of the $C_2H_4$ by lowering the position of the HOMO state, rendering it inactive. Therefore, the increase in the Lewis acidity of C≡C by AuCl, together with the intrinsic basicity of $C_2H_4$, are the driving forces for the enyne coupling. This is of course lower in the case of the nanoparticles than for the molecular compounds. The Lewis acidity of the triple bond by AuCl is the driving force for the enyne coupling, which is of course lower for the gold nanoparticles. This explains the experimental results (Scheme 1) and those in ref. [3d].

## 3. Conclusions

In summary, selective alkyne activation in complex mixtures and/or enyne compounds is controlled by distinct mechanisms in homo- and heterogeneous (nanoparticle) gold catalysts. For heterogeneous catalysis, differential reactant adsorption is the key, leading to bonded, active species that give rise to fast hydrogenation or hydration reactions. For homogeneous catalysts, alkenes rather than alkynes are preferentially coordinated to gold, but electro- and nucleophilic attacks are thermodynamically more favored for alkynes. Enyne cyclizations in homogeneous systems are mainly driven by the exceptionally low LUMO of the coordinated C≡C, which is not retrieved in the heterogeneous version of the catalyst. Therefore alkynophilicity in homogeneous systems is not related to the relative strength of the bonding of the active alkyne species, but to its activation for a desired reaction. The present results unequivocally show that fundamental differences exist between homogeneous and heterogeneous gold catalysis. This has also been shown experimentally. Thus, heterogeneous catalysts that are effective in CO oxidations and hydrogenation reactions are totally inert in the activation of enynes, a class of compounds known to react readily with a wide variety of homogeneous gold catalysts under very mild conditions.

## Experimental Section

Experimental Details: All reactions were carried out under an argon atmosphere with dry solvents using Schlenk techniques. Details on the preparation and characterization of the Au/$CeO_2$ catalyst (2.6%wt Au) can be found elsewhere.[20] The procedure employed for the reactions with this sample was as follows: to a suspension of the solid (30 mg,) in 0.25 mL of toluene or $CH_2Cl_2$, 0.08 mmol enyne **1** or **3** in 0.25 mL of the same solvent was added. The reaction mixtures were stirred at room temperature, heated at 50 °C or under microwave irradiation (150 W, 1 h) for **1** or under refluxing conditions, 24 h for **3**. The evolution of the reactions was monitored by TLC, GC/MS and $^1H$ NMR. After the time indicated in the text, the catalyst was filtered off, washed with $CH_2Cl_2$ and the solvent evaporated under reduced pressure to afford only unchanged starting material. The $^1H$ NMR experiments of complexation of gold complex **5** and 1,7-enyne **6** were carried out at 500 MHz in degassed $CD_2Cl_2$ at low temperature (223 K) to avoid the gold-catalyzed cyclization of the enyne. The complexation between catalyst **5** and enyne **6** was confirmed by $^1H$ NMR and $^1H$ EXSY experiments (Figures 2 and 3).

Finally, the hydration of the compounds was performed in a solution of 0.02 mmol (4 mg) of compound **7** or **10** (Scheme 2) in 0.5 mL of $CD_2Cl_2$ containing 0.5 µL of water with catalyst **5** (3 mg, 0.004 mmol). After 20 h at room temperature, analysis of the crude mixture by $^1H$ NMR showed formation of ketone **8** and aldehyde **9** in a 48:1 ratio (73% conversion). In the case of dimethyl allylmalonate **10**, no reaction was observed even after 48 h at room temperature.

Computational Details: With respect to the theoretical calculations, we have employed DFT with the B3LYP functional[9] and localized basis sets (Gaussian03 code[10]) to study the interaction of C2 and C3 alkenes and alkynes with gold systems including $Au^+$, AuCl, $AuCl_3$ and a $Au_{10}$ nanoparticle that represent gas-phase systems as well as homogeneous and heterogeneous catalysts. The $Au_{10}$ was built as the fcc structure showing the (111) and (100) facets. The position of the basal plane of $Au_{10}$ was kept fixed in the *z* direction and no chemistry was allowed on it.[11] The basis sets are 6-31G-(d,p) for Cl, H, C and the LANL2DZ basis set and pseudopotential for Au, which includes the scalar relativistic part crucial for the chemical properties of Au.[21] In order to check the accuracy for these systems, we have performed CCSD(T) calculations on the B3LYP structures. With the B3LYP approach, $C_2H_2$ ($C_3H_4$) has a C–C distance of 1.205 (1.207) and $C_2H_4$ ($C_3H_6$) has one of 1.331 (1.333) Å. The HOMO–LUMO gap for the C2-alkyne is 9.1 (C3 8.7) eV while it is only 7.8 (C3 7.3) eV for the C2-alkene. Geometry optimizations were full at the B3LYP level. All energy values presented correspond to potential energies. The BSSE error for the $\Delta\Delta E$ in the $AuCl_3$ case with C2 molecules (B3LYP results) amounts 1.0 kJ mol$^{-1}$.

## Acknowledgements

*This research was supported by the Spanish MEC (Consolider Ingenio 2010 Grant CSD2006-0003, CTQ2006-00464-BQU, CTQ 2006-01562PPQ, CTQ2007-60745/BQU, CTQ2005-09000-CO2-02, and Torres Quevedo Contract to N.C.) and by the ICIQ Foundation. Computing time was provided by BSC and CESCA.*

**Keywords:** alkyne-alkene mixtures · gold · heterogeneous catalysis · homogeneous catalysis · selectivity

[1] a) A. S. K. Hashmi, G. J. Hutchings, *Angew. Chem.* **2006**, *118*, 8064–8105; *Angew. Chem. Int. Ed.* **2006**, *45*, 7896–7936; b) L. Zhang, J. Sunm, S. A. Kozmin, *Adv. Synth. Catal.* **2006**, *348*, 2271–2296; c) E. Jiménez-Núñez, A. M. Echavarren, *Chem. Commun.* **2007**, 333–346; d) A. Fürstner, P. W. Davies, *Angew. Chem.* **2007**, *119*, 3478–3519; *Angew. Chem. Int. Ed.* **2007**, *46*, 3410–3449; e) A. S. K. Hashmi, *Chem. Rev.* **2007**, *107*, 3180–3211; f) E. Jiménez-Núñez, A. M. Echavarren, *Chem. Rev.* **2008**, DOI: 10.1021/cr0684319.

[2] a) A. Corma, P. Serna, *Science* **2006**, *313*, 332–334; b) T. Ishida, M. Haruta, *Angew. Chem.* **2007**, *119*, 7288–7290; *Angew. Chem. Int. Ed.* **2007**, *46*, 7154–7156.

[3] a) A. Comas-Vives, C. González-Arellano, A. Corma, M. Iglesias, F. Sánchez, G. Ujaque, *J. Am. Chem. Soc.* **2006**, *128*, 4756–4765; b) C. Gonzalez-Arellano, A. Corma, M. Iglesias, F. Sánchez, *J. Catal.* **2006**, *238*, 497–501; c) A. Abad, A. Corma, H. García, *Top. Catal.* **2007**, *44*, 237–243; d) C. Gonzalez-Arellano, A. Abad, A. Corma, H. García, M. Iglesias, F. Sánchez, *Angew. Chem.* **2007**, *119*, 1558–1560; *Angew. Chem. Int. Ed.* **2007**, *46*, 1536–1538.

[4] a) Y. Segura, N. Lopez, J. Pérez-Ramírez, *J. Catal.* **2007**, *247*, 383–386; b) J. A. Lopez-Sanchez, D. Lennon, *Appl. Catal. A* **2005**, *291*, 230–237; c) J. F. Jia, K. Haraki, J. N. Kondo, K. Domen, K. Tamaru, *J. Phys. Chem. B* **2000**, *104*, 11153–11156.

[5] G. A. Somorjai, A. M. Contreras, M. Montano, R. M. Rioux, *Proc. Natl. Acad. Sci. USA* **2006**, *103*, 10577- 10583.

[6] a) C. Nieto-Oberhuber, M. P. Muñoz, E. Buñuel, C. Nevado, D. J. Cárdenas, A. M. Echavarren, *Angew. Chem.* **2004**, *116*, 2456–2460; *Angew. Chem. Int. Ed.* **2004**, *43*, 2402–2406; b) C. Nieto-Oberhuber, S. López, M. P. Muñoz, D. J. Cárdenas, E. Buñuel, C. Nevado, A. M. Echavarren, *Angew. Chem.* **2005**, *117*, 6302–6304; *Angew. Chem. Int. Ed.* **2005**, *44*, 6146–6148; c) C. Nieto-Oberhuber, M. P. Muñoz, S. López, E. Jiménez-Núñez, C. Nevado, E. Herrero-Gómez, M. Raducan, A. M. Echavarren, *Chem. Eur. J.* **2006**, *12*, 1677–1693.

[7] S. Porcel, A. M. Echavarren, *Angew. Chem.* **2007**, *119*, 2726–2730; *Angew. Chem. Int. Ed.* **2007**, *46*, 2672–2676.

[8] a) C. Nieto-Oberhuber, S. López, A. M. Echavarren, *J. Am. Chem. Soc.* **2005**, *127*, 6178–6179; b) C. Nieto-Oberhuber, P. Pérez-Galán, E. Herrero-Gómez, T. Lauterbach, C. Rodríguez, C. López, C. Bour, A. Rosellón, D. J. Cárdenas, A. M. Echavarren, *J. Am. Chem. Soc.* **2008**, *130*, 269–279.

[9] a) C. Lee, R. G. Parr, W. Yang, *Phys. Rev. B* **1988**, *37*, 785–789; b) P. J. Stephens, F. J. Devlin, M. J. Frisch, C. F. Chabalowski, *J. Phys. Chem.* **1994**, *98*, 11623–11627.

[10] Gaussian 03 (Revision C.02), M. J. Frisch et al., Gaussian, Inc., Wallingford, CT, **2004**.

[11] a) N. Lopez, J. K. Nørskov, *J. Am. Chem. Soc.* **2002**, *124*, 11262–11263; b) I. N. Remediakis, N. Lopez, J. K. Nørskov, *Angew. Chem.* **2005**, *117*, 1858–1860; *Angew. Chem. Int. Ed.* **2005**, *44*, 1824–1826.
[12] B. Hammer, Y. Morikawa, J. K. Nørskov, *Phys. Rev. Lett.* **1996**, *76*, 2141–2144.
[13] a) R. A. Hertwig, W. Koch, D. Schroder, H. Schwarz, J. Hrusak, P. Schwerdtfeger, *J. Phys. Chem.* **1996**, *100*, 12253–12260; b) M. S. Nechaev, V. M. Rayon, G. Frenking, *J. Phys. Chem. A* **2004**, *108*, 3134–3142.
[14] M. Hargittai, A. Schulz, B. Reffy, M. Kolonits, *J. Am. Chem. Soc.* **2001**, *123*, 1449–1458.
[15] G. C. Bond, D. A. Dowden, N. Mackenzie, *Trans. Faraday Soc.* **1958**, *54*, 1537–1546.
[16] N. Cabello, C. Rodríguez, A. M. Echavarren, *Synlett* **2007**, 1753–1758.
[17] Well characterized alkyne and alkene-gold complexes: a) V. Lavallo, G. D. Frey, S. Kousar, B. Donnadieu, G. Bertrand, *Proc. Natl. Acad. Sci. USA* **2007**, *104*, 13569–13573; b) N. D. Shapiro, F. D. Toste, *Proc. Natl. Acad. Sci. USA* **2008**, *105*, 2779–2782, and references cited therein.
[18] Review on hydration of alkynes: a) L. Hintermann, A. Labonne, *Synthesis* **2007**, 1121–1150; b) Aldehyde **8** is the major product in a Ru$^{II}$-catalyzed hydration of **6**: A. Labonne, T. Kribber, L. Hinterman, *Org. Lett.* **2006**, *8*, 5853–5856.
[19] a) J. N. Brønsted, *Chem. Rev.* **1928**, *5*, 231–338; b) M. G. Evans, M. Polanyi, *Trans. Faraday Soc.* **1938**, *34*, 11–23.
[20] S. Carrettin, P. Concepción, A. Corma, J. N. Lopez-Nieto, V. F. Puntes, *Angew. Chem.* **2004**, *116*, 2592–2594; *Angew. Chem. Int. Ed.* **2004**, *43*, 2538–2540.
[21] P. Pyykkö, *Angew. Chem.* **2004**, *116*, 4512–4557; *Angew. Chem. Int. Ed.* **2004**, *43*, 4412–4456.

Received: April 16, 2008